DIGITAL IMAGE PROCESSING FOR AUTOMATIC LITHOLOGICAL MAPPING USING LANDSAT TM IMAGERY

Submitted to London University, UK
for the degree of Ph.D. and
for the Diploma of Imperial College

Liu Jian Guo
Centre for Remote Sensing / Department of Geology
Imperial College of Science, Technology and Medicine
London University, UK
May, 1991

To my wife, Zhao Qun, and

daughter, Liu Jiajia.

Abstract

This thesis presents research in the field of automatic lithological mapping in arid to semi-arid areas based on remotely sensed data. A software package with a series of new techniques has been developed to perform automatic lithological mapping in three stages: pre-classification enhancement, spectral classification and post-classification processing/analysis. The software package was used successfully for the lithological mapping and alteration detection based on a Landsat TM image for a study area in SE Spain.

The thesis is composed of eight chapters. After a general introduction in Chapter 1, a review of image interpretation and digital image processing for lithological mapping is given in Chapter 2 in order to show the development and present state level of this research field. Chapter 3 to Chapter 7 are the original work of the author. In Chapter 3, new techniques for image enhancement (band selection, contrast and spectral enhancement and shadow suppression) are introduced. Chapter 4 presents a three dimensional feature space iterative clustering algorithm using advanced decision rule, automatic seed selection and new function for cluster splitting. Chapter 5 discusses several post-classification techniques including textural reclassification, smoothing, class boundary detection, etc.. Chapter 6 and Chapter 7 report the automatic lithological mapping in SE Spain based on a Landsat TM image executed by the software package developed. The experimental processing associating with technical development was performed on the test site, a 512×512 TM subscene of the area around Rodalquilar gold deposit, as described in Chapter 6. Following the experimental processing, the similar procedure was applied to a much larger TM subscene (1792×1536) with various lithological types for regional lithological mapping. The results are presented in Chapter 7. Finally, in Chapter 8, comments and conclusions of the research project are given. The names and functions of the Fortran programmes in the software package developed in this project are listed in Appendix A for reader's reference.

Acknowledgement

This research project for the degree of Ph.D. is supported by a Technical Co-operation Award granted by the **British Council**. The **National Education Committee of P. R. China** has been providing bursary to cover my living expenses for study in UK. **China University of Geosciences** maintained my lecturer post and salary during this study program. All above deserve grateful thanks.

Mr. John McM Moore, senior lecturer of Department of Geology/Centre for Remote Sensing, Imperial College, is gratefully acknowledged, who gave an excellent supervision on my study and very kind personal help for my adapting to the study life in England.

Special thanks go to:

Dr. Jo D. Haigh Lecturer, Physics Department/Centre for Remote Sensing, Imperial College for her critical suggestions and technical verification on the image processing techniques developed in this project.

Dr. Christopher England Computer manager of Physics Department/Centre for Remote Sensing, Imperial College for his generous advice and crucial assistance on my programming for image processing software development.

I also wish to express my acknowledgement to following people for various help on my study:

Prof. Zhao Pengda President of China University of Geosciences (Wuhan), P.R. China.

Prof. Chen Zhonghui Vice President of China University of Geosciences (Wuhan), P.R. China.

Prof. Zhai Yusheng President of China University of Geosciences (Beijing), P.R. China.

Prof. Chen Huahui China University of Geosciences (Beijing), P.R. China.

Dr. M. E. Barnett Chairman of the Centre for Remote Sensing, Physics Department, Imperial College.

Dr. Alvaro P. Crosta Instituto de Geociencias, Universidade Estadual de Campinas, Brazil.

Dr. A. A. Cañas Physics Department/Centre for Remote Sensing, Imperial College.

Mrs. Lilliane Carter Secretary of Centre for Remote Sensing, Imperial College.

Mr. Adolfo Cash Photo-laboratory, Department of Geology, Imperial College.

Dr. Y. C. Robertson Former research officer of Centre for Remote Sensing, Imperial College.

Mr. J. Brunner Former research officer of Centre for Remote Sensing, Imperial College.

Mr. M. Honzak Research officer of Centre for Remote Sensing, Imperial College.

Mr. Pere Hernandez Geologist of Transaccion SA and Clough Mineral Exploration Ltd., Almeria, Spain.

Finally, I wish to thank my program officers in the British Council, **Mrs. Bibi Roye** and **Mrs. Barbara Koscia**, who very well managed the financial support of my study, including the aid for two field trips to Spain and three times international conference visiting to Canada and the United States.

Contents

1 Introduction **1**

1.1 The Structure of the Thesis 2

1.2 Lithological Information in Remotely Sensed Imagery 3

1.3 Difficulties and Potential of Automatic Lithological Mapping . 5

1.4 Approach of the Study 7

1.5 The Choice of the Study Area 9

1.6 Summary 10

2 Review of Lithological Mapping Using Remotely Sensed Data 15

2.1 General View of Remote Sensing in Geology 16

2.2 Image Visual Interpretation for Lithology 17

2.3 Digital Image Processing for Lithological Information 18

2.4 Contrast Enhancement and Colour Composition 20

2.5 Ratio and Algebra Operations 21

2.6 Principal Component Analysis and Decorrelation Stretching . . 22

2.7 IHS Transformation 24

2.8 Unsupervised Spectral Classification 25

2.9 Supervised Spectral Classification 26

2.10 Improving Classification Accuracy 27

2.11 Post-Processing of Spectral Classification 29

2.12 The Geological Study in SE Spain Using Remote Sensing . . . 30

2.13 Summary 31

3 Pre-classification Image Enhancement Techniques **33**

3.1 Index of Optimal Band-Triplet Selection (IOBS) 34

3.1.1 Review of Chavez's and Sheffield's methods 34

3.1.2 Definition of Index of Optimal Band-triplet Selection (IOBS) 35

3.1.3 Example of application using test site 38

3.2 Balance Contrast Enhancement Technique (BCET) 40

3.2.1 BCET using a parabolic function (BCETP) 41

3.2.2 BCET using a cubic function (BCETC) 45

3.2.3 BCET Fortran programmes and examples of the application 48

3.2.4 Discussion 64

3.3 Hue Image RGB Colour Composition (HRGB) 65

3.3.1 RGB-IHS Transformation 66

3.3.2 RGB false colour composition using hue images 69

3.4 Summary 72

4 A 3-dimensional Feature Space Iterative Clustering Method for Multi-spectral Imagery Classification **75**

4.1 Review of the Clustering Algorithm 76

4.2 Three Dimensional Feature Space Iterative Clustering Method 78

4.2.1 Principle of Feature Space Iterative Clustering (FSIC) . 78

4.2.2 The 3D-FSIC method 79

4.2.3 Review of optimal multiple point reassignment 82

4.2.4 The 3D-FSIC software 84

4.3 A Cluster Splitting Technique Based on the First Principal Component 85

4.4 Automatic Seed Selection Technique (ASST) 87

4.5 Classification Using Hue Images by 3D-FSIC 91

4.6 Summary 91

5 Techniques for Post-processing and Analysis of Spectral Classification **94**

5.1 Template Histogram Matching Classification (THMC) Technique 95

5.2 Iterative Majority Filtering (IMF) 98

5.3 Small Class Merging (SCM) 99

5.4 Interactive Class Editing 100

5.5 Class Boundary Detection (CBD) Technique 101

5.6 Editing Classification Images by Colour Painting 106

5.7 Intensity Modulation of Classification Imagery 107

5.8 Spectral Analysis of Classification 108

5.9 Summary 115

6 Experiment for Automatic Lithological Mapping in the Test Site **117**

6.1 The Test Site 117

6.2 Pre-classification Image Enhancement and Image Interpretation 122

6.3 Spectral Classification 126

6.4 Post-processing of Spectral classification 129

6.5 Class Identification and Appraisal of the Lithological Mapping 142

6.6 Summary 156

7 Regional Lithological Mapping in SE Spain **158**

7.1 Introduction to the Regional Geology of the Area 160

7.2 Image Processing 162

7.2.1 Pre-classification image enhancement 162

7.2.2 Spectral classification 163

7.2.3 Post-classification processing 164

7.3 Class Identification for Lithological Mapping 165

7.3.1 Editing of multi-lithology classes 173

7.3.2 Class grouping and identification 174

7.4 Discussion and Assessment of the Regional Lithological Mapping 193

7.5 Summary 196

8 Conclusions, Comments and Recommendations 200

8.1 Techniques and Software Development 200

8.1.1 Pre-processing techniques 201

8.1.2 Unsupervised classification algorithm 202

8.1.3 Post-processing techniques 202

8.2 Applications: Automatic Lithological Mapping in SE Spain . . 203

8.2.1 Processing procedure 203

8.2.2 Experimental lithological mapping of test site 205

8.2.3 Regional lithological mapping of the study area 205

8.3 Comments on Application of the Software Package 206

8.4 Recommendations for Future Study 207

8.4.1 Utilization of textural information 207

8.4.2 Knowledge based class identification 208

8.5 Conclusions 210

A Image Processing Fortran 77 Programmes Developed in the Research Project 211

References 214

List of Figures

1-1 Location of the study area in SE Spain. 12

1-2 Landsat TM band 5 image. The 1792 × 1536 subscene of the study area and the 512 × 512 subscene of the test site. 13

1-3 1:50000 scale geological maps covering the study area. 14

3-1 Correlation cube of band-triplet: band i, j and k 37

3-2 Standard parabola $Y = X^2$, $Y = -X^2$ and cubic curve $Y = X^3$. 42

3-3 BCET curves of band 1, 2, 3, 4, 5 and 7 of the TM subscene of the test site. 53

3-4 a) BCETP curve of band 6. b) BCETC1 curve of band 6. c) & d) BCETP and BCETC1 curves to compress band 7. 54

3-5 Histograms of band 1, 4 and 5 of the TM subscene of the test site before BCET processing. 55

3-6 Histograms of band 1, 4 and 5 of the TM subscene of the test site after BCET processing. 56

3-7 The colour composites of TM band-triplet 5 4 1 (RGB) of the test site. 57

3-8 Standard false colour composites of the TM subscene of the test site. 58

3-9 BCET curves of the 512 × 512 SPOT subscene of Guadix, Spain. 61

3-10 Images of 512 × 512 SPOT subscene of Guadix, Spain. 62

3-11 Histograms of the SPOT subscene of Guadix, Spain. 63

3-12 Colour cube model for RGB-IHS transformation. 67

3-13 Diagram of the procedure for producing an HRGB image . . . 70

4-1 The 3D scattergram 81
4-2 The 3D feature space partition array 82
4-3 A two dimensional example of cluster splitting. 88
4-4 An illustration of a pseudo peak caused by linear stretch. . . . 90
4-5 The data point, point $\mathbf{X}_j$, and its adjacent data point, $\mathbf{X}_l$. . . . 90
5-1 a) The mask for class boundary detection. b) The mask for class boundary thinning. 103
5-2 Illustration of the principle of the class boundary detection technique. 104
5-3 The class boundaries detected by CBD from the classification image of the test site 105
5-4 The hue wheel illustrating the value of a hue image 112
5-5 The spectral shape defined by the data in Table 5-1 113
5-6 Comparison of the class spectral shapes derived from the HRGB image and the seven TM bands of the study area 114
6-1 The regional geological map of the study area in SE Spain . . . 120
6-2 Geological map of the test site. Moore, 1989 based on IGME conventional geological maps: Frailes [1060] and Carboneras [1046],1981. 121
6-3 512 Landsat TM subscene of the test site. 123
6-4 Geological interpretation of the HRGB image of the test site. . 124
6-5 Classification image of the test site produced by 3D-FSIC. . . . 135
6-6 Classification image of the test site after THMC processing. . . 136
6-7 Smoothed classification image of the test site produced by IMF and SCM. 137
6-8 The imagery classification map of the test site painted based on the mean vectors of spectral classes. 138
6-9 The imagery classification map of the test site Painted by interactive colour editing. 139
6-10 Modulated version of Figure 6-8. 140

6-11 Modulated version of Figure 6-9. 141
6-12 TM seven band spectral shape of andesite 143
6-13 TM seven band spectral shape of andesite breccia 144
6-14 TM seven band spectral shape of dacite 145
6-15 TM seven band spectral shape of altered volcanics 146
6-16 TM seven band spectral shape of limestone 147
6-17 TM seven band spectral shape of carbonate calcrete 148
6-18 Outcrop of andesite with carbonate calcrete surface. Taken on the top of Puntazo de Piedra Negra 148
6-19 TM seven band spectral shape of volcanic debris 149
6-20 TM seven band spectral shape of old alluvial sediments 150
6-21 TM seven band spectral shape of recent alluvial sediments . . . 151
6-22 TM seven band spectral shape of fine sand 151
6-23 TM seven band spectral shape of vegetation 152
6-24 Generalized spectral signatures of vegetation, soil, rock and alteration. (Quot. from Sabins, 1986) 153
6-25 The imagery lithological map of the test site. 154
6-26 The imagery lithological map of the test site (with intensity modulation). 155
7-1 A Landsat TM colour composite image of the study area in SE Spain. TM5 in red, TM4 in green and TM1 in blue. 159
7-2 The HRGB image of the study area. 166
7-3 The classification image produced by 3D-FSIC from the HRGB image shown in Figure 7-2. 170
7-4 The smoothed classification image after IMF and SCM processing. 171
7-5 The classification image after CRED treatment. 175
7-6 TM seven band spectral shape of terrain type 1 177
7-7 TM seven band spectral shape of terrain type 2 178
7-8 TM seven band spectral shape of terrain type 3 179
7-9 TM seven band spectral shape of terrain type 4 180

7-10 TM seven band spectral shape of terrain type 5 181
7-11 TM seven band spectral shape of terrain type 6 181
7-12 TM seven band spectral shape of terrain type 7 182
7-13 TM seven band spectral shape of terrain type 8 183
7-14 TM seven band spectral shape of terrain type 9 184
7-15 TM seven band spectral shape of terrain type 10 184
7-16 TM seven band spectral shape of terrain type 11 185
7-17 TM seven band spectral shape of terrain type 12 186
7-18 TM seven band spectral shape of terrain type 13 186
7-19 TM seven band spectral shape of terrain type 14 187
7-20 TM seven band spectral shape of terrain type 15 188
7-21 TM seven band spectral shape of terrain type 16 188
7-22 TM seven band spectral shape of terrain type 17 189
7-23 TM seven band spectral shape of terrain type 18 190
7-24 TM seven band spectral shape of terrain type 19 191
7-25 TM seven band spectral shape of terrain type 20 191
7-26 TM seven band spectral shape of terrain type 21 192
7-27 TM seven band spectral shape of terrain type 22 193
7-28 TM seven band spectral shape of terrain type 23 194
7-29 TM seven band spectral shape of terrain type 24 194
7-30 The imagery lithological map of SE Spain. (Derived from Landsat TM imagery). **Note:** An enlargement of the map is in the pocket inside the back cover. 198
7-31 The imagery lithological map (with topographic background) of SE Spain. (Derived from Landsat TM imagery). 199

List of Tables

1-1 Spectral band and spatial resolution of Landsat TM and MSS images 11

3-1 Band-triplet selection based on different functions of correlation cube. 38

3-2 The correlation coefficients of the seven bands of the TM subscene of the test site. 39

3-3 IOBS of the 512 × 512 TM subscene of the test site. 39

3-4 The BCET coefficients of the TM subscene of the test site. . . 50

3-5 Statistics of the TM subscene of the test site before and after BCET processing. 51

3-6 BCET coefficients and image statistics of the 512 × 512 SPOT subscene of Guadix, Spain. 60

3-7 Correlation and IOBS of three hue image groups derived from TM band- triplets of the test site with lowest IOBS 71

3-8 The suitable band-triplets for deriving an HRGB image from Landsat TM imagery 72

5-1 A calculation example for deriving a spectral shape from HRGB data. 112

6-1 Lithological interpretation keys of the HRGB image of the test site 125

6-2 Hue DN values of the initial centres for clustering classification based on the HRGB image of the test site. 128

6-3 Iteration information of the clustering classification using three hue images (the HRGB image) of the test site. 129
6-4 Statistics of the clustering classification using the HRGB image of the test site. 130
6-5 The 3 × 3 template histogram of the textural class (relevant to the epithermal alteration in Rodalquilar) in the spectral classification image of the test site. 131
6-6 The class pixel numbers of FSIC, THMC, IMF and SCM. . . . 133
6-7 Pixel numbers of lithologies and vegetation in the imagery lithological map of the test site. 153
7-1 Hue DN values of the initial centres for clustering classification based on the HRGB image of the study area. 167
7-2 Iteration information of the clustering classification using three hue images (the HRGB image) of the study area. 168
7-3 Statistics of the clustering classification of the study area . . . 169
7-4 Class pixel numbers of FSIC, IMF and SCM of the study area. 172
7-5 New classes resulted by class regional editing (CRED) 174
7-6 Terrain types in the imagery lithological map of the study area 176

Chapter 1

Introduction

The objectives of this research project were to develop the image processing software for automatic lithological mapping and alteration identification in arid to semi-arid areas and to produce lithological image classification maps of the study area in SE Spain (Figure 1-1) from a Landsat TM image (Orbit/Frame: 199-34, Quadrant 3 scene, 19th July, 1984).

Lithological mapping is an essential task for geological mapping as well as mineral exploration. Remote sensing technology is an effective tool for lithological mapping at low cost and high accuracy. So far, most successful applications of remote sensing for lithological mapping have been based on image interpretation and image enhancement. There are few documented cases of automatic or semi-automatic lithological classification using remotely sensed data. The spectral and spatial resolution of commonly used images, such as Landsat TM and MSS images, SPOT HRV images, *etc.*, are not significant for detailed classification. Also there are other reasons that prevent better mapping results from these images:

- Commonly used image processing systems are designed for general purposes. They are good for general applications but not for specialized tasks like lithological mapping.

- Geological users do not understand the software well. Thus the available

functions may not be used in the most effective way.

A series of new image processing techniques, as well as the software, for automatic lithological mapping have been developed in this study, in the light of the author's knowledge and experience of geology. These techniques and the application results will be presented in this thesis.

This chapter is a brief introduction to the structure of the thesis, lithological information in remotely sensed imagery, difficulty and possibility of automatic lithological mapping, the approach of the study and the choice of the study area.

1.1 The Structure of the Thesis

The thesis is composed of eight chapters. After a general introduction in Chapter 1, a review of image interpretation and digital image processing for lithological mapping is given in Chapter 2 summarizing recent developments in this research field. Chapters 3, 4 and 5 introduce a series of new processing techniques for image enhancement, multi-spectral classification and post-classification processing. Chapter 6 and Chapter 7 present two examples of automatic lithological mapping in SE Spain based on Landsat TM imagery using the thesis techniques. The experimental processing associating with technical development was performed on a 512×512 TM subscene of Rodalquilar gold mine area (Figure 1-2), the test site, in SE Spain, which is reported in Chapter 6. Following the experimental processing, similar procedures were applied to a larger TM subscene (1792×1536) (Figure 1-2), which includes the test site plus more lithological types, for regional lithological mapping. The results are presented in Chapter 7. There is a summary at the end of each of these seven chapters to highlight the key points. Chapter 8 includes comments and conclusions of this research project.

In Appendix A, the names and functions of the Fortran programmes developed in this project are listed.

1.2 Lithological Information in Remotely Sensed Imagery

Lithological information in remotely sensed imagery can be considered in terms of three phenomena: spectral information, such as colour and tone; spatial information, such as texture and pattern; and geometric information, such as size, shape and location. These different types of information, or image characteristics, are not constant or unique for lithologies. The image feature of a rock type may vary from place to place depending on environmental and geological factors, such as climate, vegetation, attitude of the rock, topography, *etc.*.

Spectral information characterized by colours or tones is the fundamental data source in multi-spectral imagery and is relatively systematically related to lithology. Generally, rock types with different mineral composition have unique spectral signatures if the spectral resolution of the measurement is sufficiently high. However, in the practical terms, image spectral signatures for rock types do not well coincide with those from laboratory measurements of fresh rock samples even if the spectral bands used are precisely matched. This is because there are almost no fresh outcrops of any rock types in the natural environment. Natural outcrops of rock are usually covered by residual soils and rock fragments or weathering veneers. As the practical spatial resolution of multi-spectral imagery is not very high, a pixel without any vegetation influence is not common in most areas including semi-arid areas. The spectral character of a rock type in imagery is a composite of the spectral signatures of several different materials. As long as the vegetation is sparse, the spectral character

of a rock type is fundamentally controlled by its lithology because the mineral composition of the residual soil and debris and the weathering varnish are dependent on the lithology and weathering processes. The style of weathering is decided by the climate of an area, which varies regionally. Thus in arid to semi-arid areas, spectral information is applicable and reliable for lithological discrimination on a local scale.

The image texture and pattern related to lithology are formed by topographic features, including drainage pattern, of different scales. Both texture and pattern are concepts relating to image scale and spatial resolution. Pattern in a large scale and high resolution image will become a kind of texture in the small scale and low resolution image of the same area. The topographic feature, especially the micro-topographic feature, of a rock type largely depends on the erosion process which is controlled by the attitude of the strata, the landform, the climate and the vegetation. These factors influence erosional process and, in the long term, are controlled by tectonic movement and global environmental change. For the same natural conditions, various rock types tend to show different textures and patterns on the imagery of the same scale because of their different erosion features. However, attitude of strata and landform are not stable even in a small area if the area is disturbed by geological structure, which is a general case of an area favourable to mineral exploration. In such a case, the variation of texture and pattern of a rock type caused by the sharp change of attitude of strata and landform may be much more significant than the difference of the textures and patterns among several rock types in the same attitude and landform. This is not a big problem for visual image interpretation but a real challenge to automatic discrimination by computer based on mathematic models.

The geometric information, size, shape and location, is very useful for locating certain rock types, such as igneous intrusion bodies, volcanic craters, *etc.*,

and superficial deposits like alluvial fans, deltas, river beds and terraces, *etc.*. In visual interpretation, geometric information is used for either recognition or discrimination based on user's knowledge of the relevant ground objects. Such interpretation based on geometric information is generally difficult for mathematical modelling and computer simulation.

1.3 Difficulties and Potential of Automatic Lithological Mapping

To understand the difficulties of automatic lithological mapping, let us examine the process of visual interpretation first. The visual interpretation is a process of knowledge based discrimination and recognition based on all the information available in the image. Lithological interpretation is often begun from a known area and then extended to unknown areas by tracing identical or gradual changes of colours/tones and textures/patterns, associating the sizes of certain features and evaluating their shapes. For the areas with different landform and geological structures, different textures/patterns and conceptions of size and shape may be applied to the same rock types based on man's judgement.

The interpretation solely based on spectral information (colour and tone) can be as simple as direct comparison, if not considering the shadow effects, because the spectral information is regionally stable. Such a job can be simulated by computers using proper classification algorithms. However, the situation is much more complex for interpretation based on spatial and geometric information, which needs feedback for consulting interpreter's knowledge and comprehensive decision. Such a sophisticated task is not very difficult for well trained people with relevant knowledge but, for a computer to perform the task, dynamic self training, a knowledge base (the mathematic models and decision

rules for different kind of image information) and great processing capacity are necessary. For instance, it is easy for a man to recognize an irregular shape of certain size at certain location (*e.g.* an alluvial fan) but very difficult to configure a workable mathematic model to do the same job by a computer. The computer simulation of the interpretation based on spatial information can be partially realized by resolving the complex task into several simpler parts. As reviewed in Chapter 2, some effort has been made on texture classification. Compared with spectral classification, however, the computer costs of most textural techniques are too high to practical application, and the performance is generally poor.

It is possible to realize automatic lithological mapping based on spectral classification for those rock types having different spectral signatures in the wavelength bands of the imagery used if they are well exposed on the ground (*e.g.* arid to semi-arid areas). Theoretically, the higher the spectral and spatial resolutions of imagery, the more detail and accurate lithological discrimination can be achieved. However, with the increasing of the spectral and spatial resolution, a imagery data set will become very large. To obtain and process such data set for regional lithological mapping could be unacceptable expensive at recent time.

Landsat TM imagery is an ideal data set for regional lithological mapping because of its extensive coverage and much higher spatial and spectral resolution compared with Landsat MSS imagery, as shown in Table 1-1. Landsat TM imagery is available for almost all the regions of the Earth. The techniques developed based on the study area of this project are therefore applicable in other areas with conditions similar to SE Spain.

The seven TM bands may not be adequate for detailed lithological mapping but the discrimination of rock types can be improved significantly by well de-

signed classification techniques based on the data set derived from the original seven TM bands by proper image enhancement, incorporating by simple textural and contextual re-classification and other post classification processing techniques.

1.4 Approach of the Study

The approach of automatic lithological mapping of this project will be largely based on multi-spectral classification of TM imagery.

There are two basic types of classification algorithms: supervised and unsupervised classification. For lithological classification using multi-spectral imagery, supervised classification needs prior knowledge of the lithology in the area to be mapped. This knowledge may not be available or adequate for practical applications. Unsupervised classification can reveal important lithological information that was previously unknown before even in a well mapped area. However, the image classes may not be directly related to rock types. Lithological identification of the classes needs to be done by post-classification processing and analysis based on existing geological field and map information.

In this study, the automatic lithological mapping is based on unsupervised classification. A new classification method, 3 dimensional feature space iterative clustering, has been developed to perform classification based on three hue images.

As many failures of classification are caused by low spectral separability of the terrain types in raw image data, pre-classification processing (spectral enhancement) is an important part of automatic lithological mapping. Several new techniques have been developed to enhance the spectral information to achieve balanced colour composites containing maximum information and to

concentrate the spectral information of seven TM bands into three hue images. The shadow effects, a main obstacle for spectral classification, are removed at the same time.

A classification image is far from a clear and concise map for practical application. Post-classification processing is an essential part of the lithological mapping based on unsupervised classification. Several techniques have been introduced to simplify a spectrally classified image based on spatial context and statistical similarity, to edit and identify the classes based on user supervision and paint them in meaningful colours and to detect and add class boundaries. To remedy the limitation of spectral classification, a simple technique to perform supervised texture re-classification on a spectral classification image has been developed to detect class patterns rather than the original image textures. The advantage of such a strategy is to benefit the multi-spectral texture information of all the images (bands) used for spectral classification.

The research was executed in two stages: firstly, the technique and software development; and then, image processing for the automatic lithological mapping of the study area in SE Spain using the software package developed at the first stage. The auto-lithological mapping includes the following steps:

1. Enhancement of the spectral information of multi-spectral imagery to maximize the spectral differences and to minimize the influence of the factors that may degrade the accuracy of spectral classification, such as shadows.

2. Spectral clustering analysis (unsupervised classification) to symbolize the spectral differences.

3. (Optional) Supervised re-classification based on the class spatial texture/pattern.

4. Post-classification processing to smooth and simplify the classification

image and paint colours.

5. Field checks, study of published geological maps and analysis of class spectral characteristics for lithological identification of the spectral classes.

6. Interactive class edit to unite those classes corresponding to one terrain type and to split those classes each representing more than one terrain types based on the study of step 5.

7. Final mapping procedure including: detect and add class boundaries and edit colours of classes.

8. (Optional) Modulate the final lithological classification map by an intensity image to add topographic background to the map.

Geological knowledge is not used until the 5th step.

1.5 The Choice of the Study Area

SE Spain (Almeria Province) was selected as the study area as shown in Figure 1-1. A 512 × 512 TM subscene covering hydrothermal alteration zones with gold deposits around Rodalquilar was used as the test site for technique development and experimental processing. Then a large subscene with 1792 × 1536 pixels, which includes the test site, were processed for regional lithological mapping (Figure 1-2). The area has been chosen for following reasons:

1. It is a semi-arid area (one of the most arid regions in Europe) with sparse vegetation. The land surface is dominated by outcrops of rock and residual soils and debris. Therefore spectral information relevant to lithology can be recorded by remotely sensed imagery data. Various types of sedimentary, volcanic, metamorphic and igneous rocks are well exposed in the area. The area also contains mineral deposits.

2. Image data of the area was supplied through the Centre for Remote Sensing and Department of Geology, Imperial College, including Landsat TM, MSS and RBV images, and SPOT HRV panchromatic band image. Black and white and true colour aerial photos and airborne 11 band ATM data is also available for part of the area. Though the study is mainly based on Landsat TM imagery, other data are used for local reference and field work guidance.

3. The area has been studied by remote sensing geologists for many years. A field excursion of the inter-collegiate MSc remote sensing course of London University has been carried out by teaching staff from Department of Geology, Physics Department and the Centre for Remote Sensing, Imperial College, since 1983. The study has been of mutual benefit to the author and MSc teaching activity. The techniques developed in this project have been widely used by MSc students.

4. The area is quite well mapped geologically (Figure 1-3). The existing geological maps can be used as reference for ground truth.

1.6 Summary

This chapter is a general introduction to this thesis.

The structure of the thesis is described at the beginning of the introduction.

Three kinds of image information relating to geological study, spectral information, spatial information and geometric information, are discussed.

Automatic lithological mapping based on spatial and geometric information is difficult and not practical while that based on spectral information is feasible.

Table 1-1: Spectral band and spatial resolution of Landsat TM and MSS images

TM			MSS		
Band	Spectral Range	IFOV	Band	Spectral Range	IFOV
TM1	0.45 - 0.52 μm	30m	MSS4	0.5 - 0.6 μm	79m
TM2	0.52 - 0.60 μm	30m	MSS5	0.6 - 0.7 μm	79m
TM3	0.63 - 0.69 μm	30m	MSS6	0.7 - 0.8 μm	79m
TM4	0.76 - 0.90 μm	30m	MSS7	0.8 - 1.1 μm	79m
TM5	1.55 - 1.75 μm	30m			
TM6	10.4 - 12.5 μm	120m			
TM7	2.08 - 2.35 μm	30m			

The approach of the automatic lithological mapping reported in this research project is based on unsupervised multi-spectral classification of Landsat TM data. The pre-classification spectral enhancement and post-classification processing are regarded as necessary parts of the mapping. The research comprises two stages: technique and software development and image processing for lithological mapping.

An area in SE Spain (in Almeria Province) is selected as the study area for its well exposed lithology, plentiful imagery data and good ground control.



Figure 1-1: Location of the study area in SE Spain.

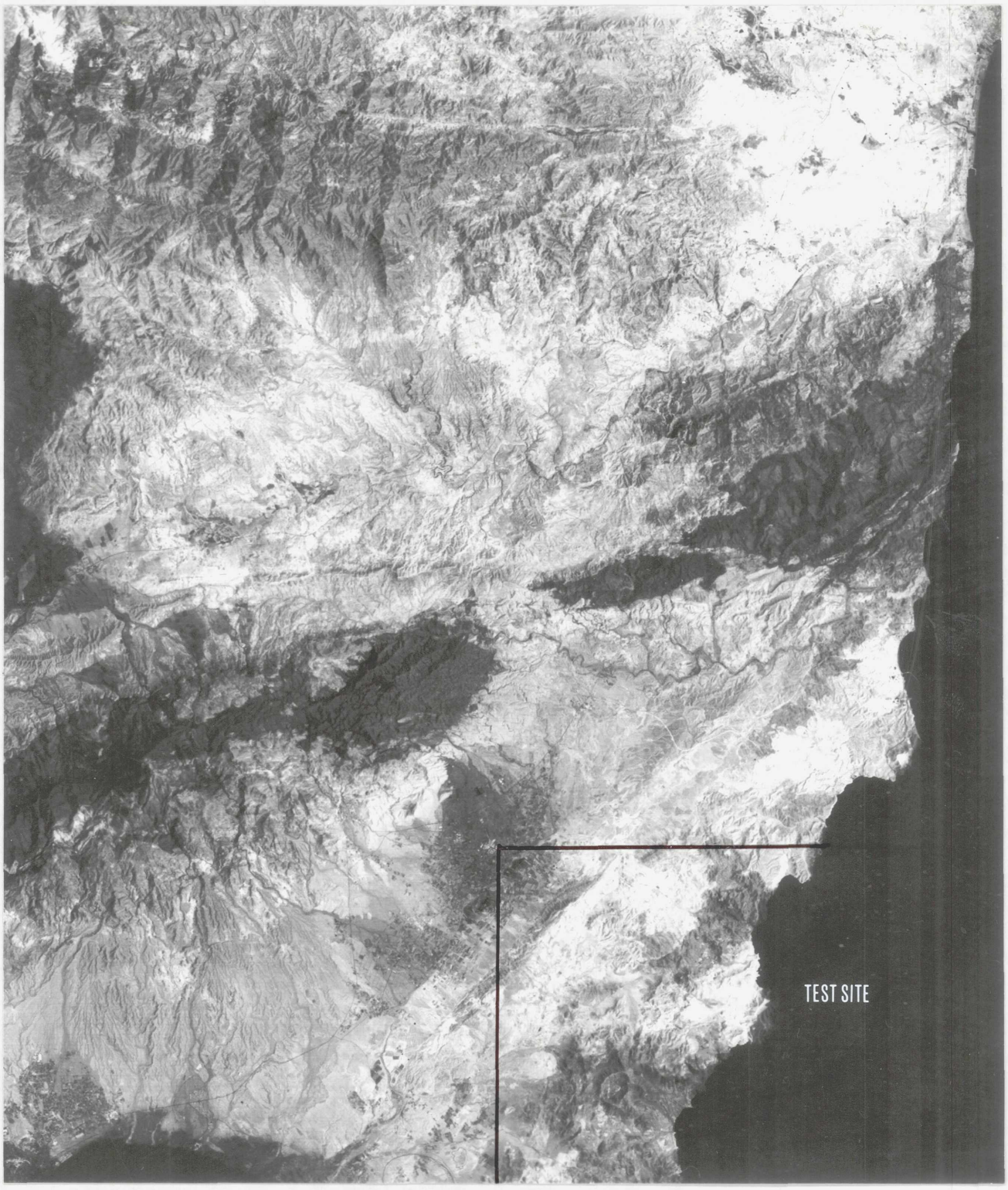


Figure 1-2: Landsat TM band 5 image. The 1792×1536 subscene of the study area and the 512×512 subscene of the test site.

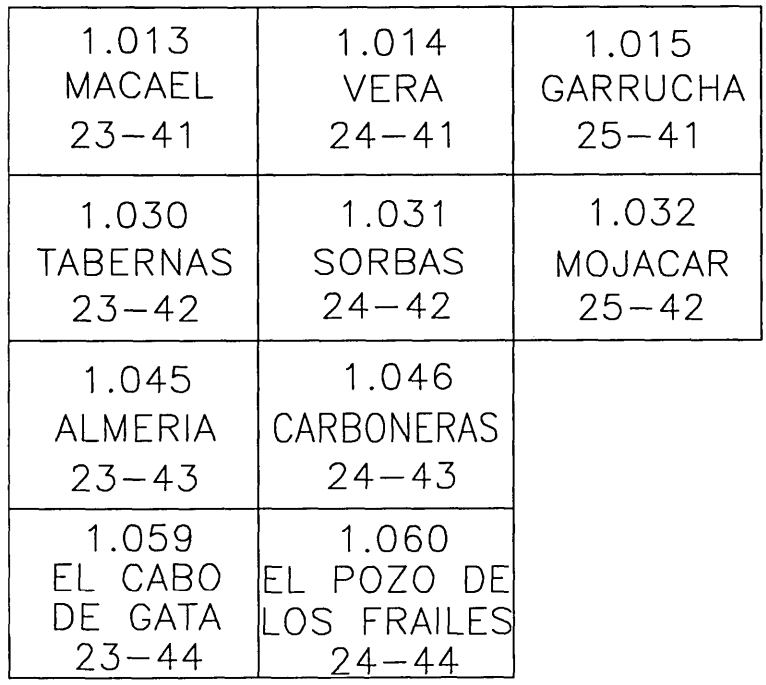


Figure 1-3: 1:50000 scale geological maps covering the study area.

Chapter 2

Review of Lithological Mapping Using Remotely Sensed Data

This chapter presents a brief review of the applications of remote sensing for lithological mapping so as to show from where the author started his research work. The chapter cannot cover all the important topics of this study field, but will try to demonstrate the technical development from visual interpretation, image enhancement to image classification followed by a review of recent geological studies using remotely sensed data in SE Spain.

General introduction to the topic and summaries of earlier work can be found in several books (*e.g.* Sabins, 1987; Lillesand and Kiefer, 1987). Abrams gave more specialized descriptions focused on the remote sensing techniques for lithological mapping as one chapter in 'Remote Sensing in Geology' (1980). Drury's book 'Image Interpretation in Geology' (1987) is another reference which concentrates on geological applications of remote sensing.

2.1 General View of Remote Sensing in Geology

Remote sensing technology can be traced back to 1858 (Lillesand and Kiefer, 1987) when the first known aerial photograph of land surface was taken from a balloon. During World War I, aerial photography was established as an operational military reconnaissance tool. In the two decades between World War I and World War II, the technology spread to civilian applications including timber surveys and mineral exploration. Since then, geology has been an important application for remote sensing. Aerial photography was for long the only form of remote sensing. The interpretation of aerial photo stereo pairs became an essential technique for regional scale geological mapping ($\geq 1:200000$ scale).

A significant advance of remote sensing technology was the launching of the Landsat 1 on 23rd July, 1972. The technical term 'remote sensing' was then defined as the technology of recording spectral radiant energy of objects as an imagery by sensors in distance. Geologists found that the MSS images taken by The Landsat 1, with 80 metre spatial resolution, four spectral bands and $185km \times 185km$ coverage, were extremely useful for the study of global tectonic features and regional geological survey. The false colour composites of MSS imagery enable geologists to view the geological structure and lithological distribution synoptically. Thus a general and comprehensive understanding of regional geology can be obtained directly and used to control local geological surveys. With the aid of Landsat MSS data, the small to medium scale geological mapping and mineral exploration have been improved significantly, especially in those areas difficult of access.

Landsat 4 (16th July, 1982) was another important step in the development of remote sensing technology. It carried a new sensor system, the Thematic Mapper (TM), with much improved spatial and spectral resolution (30m, seven

bands and the same area coverage as MSS). TM imagery is especially useful for geological study as two of its seven bands (TM5 and TM7) are designed for geological applications (Abrams *et al.*, 1977). TM imagery can be used for more detailed geological study up to 1:50000 scale.

Imaging spectrometry is a relatively new technology, currently under development. The sensor of the Airborne Imaging Spectrometer (AIS) and the Airborne Visible and Infrared Imaging Spectrometer (AVIRIS)) have very high spectral resolution (63 - 224 bands). This will make more accurate and quantitative geological study possible (Goetz, 1987).

In geological applications, remote sensing technology is used to provide information on tectonics and geological structure, lithology and superficial deposits for geological mapping, mineral exploration, hydrological survey and environmental study.

2.2 Image Visual Interpretation for Lithology

Visual interpretation is the fundamental and necessary technique for extracting lithological information from remotely sensed images. Conventional vertical panchromatic aerial photography (black and white) dominated in remote sensing before 1970s. The use of aerial photography is so well established in geology that the terms 'photogeology' (Miller, 1961) or 'aerogeology' (Von, 1962) were proposed to describe the geological photo-interpretation (Lo, 1986). Interpretation skills have been developed to permit identification of the major sedimentary and igneous rock types as well as some metamorphic lithologies under various climate and environmental conditions (Allum, 1966; Mekel, 1978). The interpretation techniques of photogeology have been adapted to space-borne and air-borne multi-spectral imagery, such as Landsat MSS, RBV and TM, SPOT HRV, ATM, *etc.* (Drury, 1987; Lillesand, 1987; Lo, 1986; Abram,

1980).

The early geological applications of space-borne imagery largely depended on visual interpretation. One example is presented by Viljoen *et al.* (1975) who produced excellent geological map of south west Africa using a Landsat MSS standard false colour composite image. Another example is the geological interpretation of Skylab photographs by Lee and Weimer (1975).

Visual interpretation is a subjective procedure. Different people may produce very different results from the same image depending on experience and interpretation skill. Errors in interpretation can be great. With improved spectral resolution, the problem becomes more complex as it is not easy to achieve similar interpretations from different bands or colour composites of different band combinations. It is impossible for visual interpretation to make full use of the great information capacity of multi-spectral imagery.

2.3 Digital Image Processing for Lithological Information

Multi-spectral digital images came into use after the launching of the Landsat 1 in 1972. Since then, digital image processing technology has become a major part of remote sensing and developed rapidly. There are many subtopics of digital image processing, such as contrast enhancement, colour composition, multi-spectral arithmetic operations ($+, -, \times, \div$), feature coordinate transformation (*e.g.* principal component analysis, IHS transformation), band or feature selection and classification. The systematic introduction of image processing of remotely sensed data can be found in Gonzalez and Wintz (1987), Mather (1987), Richards (1986) and Schowengerdt (1983).

Digital image enhancement is the most effective and essential tool for geological application of remote sensing and also the most active research topic of remote sensing. With the help of various image enhancement techniques, the quality of an image can be improved significantly and specific spectral information, based on the spectral signature, can be highlighted. Thus the interpretation of enhanced images is much easier than that of the original images. For specially enhanced image features, such as certain type of rock or alteration correlated with iron oxides or hydrated minerals, the interpretation may be simplified to direct recognition. Image information cannot be increased by any enhancement techniques. However, enhancement processing can clearly display the information of specific targets at the cost of suppressing other information.

Image enhancement is powerful, but the final value of images for geology still rest on visual interpretation. High accuracy image classification for lithology is one step on the way leading to automatic lithological mapping and is one frontier of remote sensing in geology.

Digital image classification , as a subtopic of pattern recognition, is a very active research field. Many classification techniques have been developed and used for lithologic discrimination and mapping since the early 1970s. Compared with image enhancement techniques, however, the practical results of classification are limited. Rock types are not simple targets; their image features change with environmental factors and are difficult to characterize by unique spectral signatures and textures. Research in this field is challenging and the recent developments encouraging.

2.4 Contrast Enhancement and Colour Composition

Contrast enhancement is also referred as point operation (Castleman 1979, Richards, 1986) or histogram manipulation (Gonzalez and Wintz, 1987; Hummel, 1974). The main function of contrast enhancement processing is to adjust the data distribution (the histogram) of an image so as to make proper use of the value range of the image and display system for particular purposes, such as improving the image quality and highlighting or suppressing (even removing) certain features. Contrast enhancement is often used as the first step and the last step of more sophisticated processing for preparing initial data set or final output.

The commonly used contrast enhancement techniques are linear stretch, Gaussian stretch, piecewise linear stretch, logarithm operation, exponential operation, histogram equalization (Hall *et al.*, 1971; Hall, 1972; Hummel, 1974; Gonzalez and Fittes, 1977; Woods and Gonzalez, 1981), local enhancement, *etc.* (Ketcham, 1976; Harris, 1977; Narendra and Fitch, 1981).

A new technique, the balance contrast enhancement technique (Liu Jian Guo, 1990) forms part of this thesis. The technique is especially useful for preparing high quality unbiased colour composites. A full description will be given in the section 3.2 of Chapter 3.

Any three bands of a multi-spectral imagery or three features derived from an imagery can be registered and displayed in three primary colours, red, green and blue, to form a colour composite image. The technique is simple but most useful for lithological interpretation (Moore and Liu, 1990; Rothery and Milton, 1981). In order to produce high quality and informative colour composites from multi-spectral imagery, many band selection techniques have been developed. Basically, these techniques fall into two categories: statistical procedures

(Chavez, 1982, Sheffield, 1984; Crippen, 1989; Liu and Moore, 1989) and target specific procedures (*e.g.* Crosta, 1989). For TM imagery, band combinations 7 4 1 and 5 4 1 (RGB) are suggested as the best for lithological interpretation by different researchers using different techniques in different areas (Sheffield, 1984; Crippen, 1989; Liu and Moore, 1989). When three bands are selected for colour composition, the choice of colour for each band is not simple as the eyes are not equally sensitive through out the spectrum (Cañas and Barnett, 1985). In practice, the decision is often based on visual judgement as suggested by Rothery (1987) and Moore and Liu(1990).

Band and feature selection is becoming an important topic with the development and application of high spectral resolution large data set imagery such as AVIRIS.

2.5 Ratio and Algebra Operations

Image ratio is the most popular and effective technique for spectral enhancement. The technique was developed based on the work of Kriegler *et al.* (1969) and Cutts (1971). Later, the ratio image colour composition came into use for revealing the lithological differences first on the moon (Billingsley, 1972) and then on the earth (Goetz *et al.*, 1973). Based on the basic structure of two bands simple ratio, more complex ratios with algebra operations of two or more bands were developed for particular purposes and are often referred as index, such as the Normalized Difference Vegetation Index (NDVI) (Mather, 1987; Tuker, 1977, 1979; Justic *et al.*, 1985; Perry, 1986). In the study of Gillespie *et al.* (1987), a new ratio technique was introduced to perform colour enhancement of highly correlated images and referred to as chromaticity transformation which may achieve similar results to that produced by a decorrelation stretch but with a much simpler operation.

Two attractive properties of ratio techniques are shadow suppression and selective enhancement of interesting spectral features. The effect of shadows is one major factor degrading the accuracy of spectral classification. Simple ratios often fail to eliminate shadows completely because of the additive items in the recorded radiance DN values caused by atmospheric scattering. Several techniques for atmospheric correction have been developed to relief the problem (see Crippen, 1988). On the other hand, many researchers, when using the ratio images almost without shadow effects, have realized that such images are difficult for geological interpretation because of the lack of topographic information (Kowalik, 1983; Segal, 1983). With reversed logic, Crippen *et al.* (1988) designed a directed band ratioing technique in which a controllable constant is added back to the image bands for ratioing deliberately after the atmospheric correction. Topographic information is therefore retained in a systematic way.

Ratio techniques have been applied very successfully for lithological discrimination and alteration detection in Landsat MSS images (Vincent, 1972; Rowan *et al.*, 1974; Goetz *et al.*, 1975; Blodget, 1975). In recent studies based on TM imagery, ratio techniques have also been used with other techniques to achieve effective discrimination of lithology and alteration (Kaufmann, 1988; Amos, 1989; Campos-Marquetti and Rocwell, 1989). For high spectral resolution imagery, such as AVIRIS and AIS, ratioing is an effective technique for general lithological discrimination (Barnaby, 1989).

2.6 Principal Component Analysis and Decorrelation Stretching

Principal component analysis (PCA) is a standard technique for handling correlated multi-variable data sets. Mathematically, it is a linear space transformation to convert data in a correlated multi-dimension space to an uncor-

related space with lower dimensionality. For multi-spectral imagery, PCA is used to compress data set and condense the information. Theoretically, more than 90% information of a multi-spectral imagery may be concentrated into the image of the first principle component (PC1). However, as many researchers indicated, the useful information for lithological discrimination and alteration identification is often occurs in high order PC images (William, 1983; Chavez *et al.*, 1984; Crosta, 1989).

A PC colour composite can be made by displaying three co-registered PC images in red, green and blue (Taylor, 1974). For TM image, different PC colour composites were found useful for enhancing lithological information and alteration zones in different areas (Amos, 1989; Kaufmann, 1988; Crosta, 1989; Moore and Liu, 1990). Caution must be applied in PC colour composition because the signal noise ratios (SNR) of the PC images of different orders are very different. The SNR decreases sharply with the increasing of the order of PC images. In this case, the noise of high order PC images may be improperly exaggerated by contrast enhancement and colour composition. Recognizing the problem, Chavez *et al.* (1984) proposed a selective PCA technique that performs PCA on highly correlated band pairs or subgroups rather than using all the bands together. Thus the information in high order PC images will be maximized and the colour composites of the PC1s derived from different band groups will have high and equivalent SNR in each colour channel. Further more, in the recent work of Chavez and Kwanteng (1989), selective PCA was used in an opposite way to extracting spectral contrast in Landsat TM data . Instead of using PC1 derived from a band pair, the PC2 is used to highlight the spectral difference of the two bands. The selective PCA was used successfully for lithological discrimination in the test site in northern Arizona (Chavez, 1989, Davis *et al.*, 1987).

Another important and creative application of PCA is decorrelation stretch-

ing which was introduced by Soha and Schwartz (1978) based on the earlier work of Taylor (1974). The techniques stretches the three image bands for colour composition along three PC axes to make full utilization of RGB colour space. Quite colourful composites can be produced with not significant distortion of the perceived hues and image character. The interpretation of decorrelation stretched images is straightforward. The technique has been used widely for lithologic discrimination. Many results on this topic have been published during the last decade (Kahle *et al.*, 1980; Kahle and Rowan, 1980; Kahle and Goetz, 1983; Gillespie *et al.*, 1984; Abrams, 1984; Abrams, 1986; Rothery, 1987; Drury and Hunt, 1988; Kaufmann, 1988; Crosta, 1989).

2.7 IHS Transformation

The IHS transformation is a standard technique for numerically describing colours in the image domain, using spherical coordinates roughly analogous to the conventional perceptual attributes hue (H), saturation (S) and lightness or intensity (I) (Gillespie, 1975; Soha *et al.*, 1976; Raines, 1977; Ruiz *et al.*, 1977; Gillespie, 1980; Gillespie, 1986). IHS transformation has been used to enhance multi-spectral imagery in several ways.

In Haydan's work (1981, 1982, 1983, 1984), different bands or band ratios or multi-sensor data sets are assigned to hue, saturation and intensity and then transformed back to RGB system for display. Such a strategy was applied to integrate magnetic data and radar imagery by Harris and Murray (1989 a, b). The resulting images revealing regional structural patterns were used for gold exploration and lithological discrimination.

Gillespie *et al.* (1986) introduced the IHS contrast stretch to perform decorrelation stretch based on IHS transformation. Firstly, three highly correlated image bands are transformed from RGB to IHS coordinates. Then, the satu-

ration image and intensity image are stretched. Finally, the H, S and I images are transformed back to RGB system for display. IHS contrast stretch can achieve very similar results to those produced by decorrelation stretch based on PCA. As an advantage, IHS contrast stretch is scene independent, while PCA decorrelation stretch is not. Both decorrelation techniques distort the spectral information of the original image.

Yamaguchi's work (1987, 1988, 1989) represents a quite different application of IHS transformation which is useful for highlighting mineral alteration. In the IHS coordinate system, hue is the angle (0-360) around the grey line and often described as the 'colour wheel'. Conventionally, zero, the starting point of the colour wheel, represents pure red. In Yamaguchi's method, zero is assigned to a hue according to the character of the clusters of specific targets so as to show them in remarkable colours.

A new technique based on IHS transformation for producing hue image colour composites (Liu Jian Guo and Moore 1990) forms part of this thesis as 3.3, Chapter 3.

2.8 Unsupervised Spectral Classification

Unsupervised spectral classification is an automatic procedure based on clustering analysis, which will segment image pixels into different clusters according to the statistics of their spectral properties. The classes will be identified as different terrain types by users, based on experience.

Unsupervised classification does not need prior knowledge of the terrain types. This is very attractive for lithological mapping and mineral exploration because important and unknown rock types and mineralization may be revealed. The clusters generated by clustering analysis may not be uniquely

relevant to specific terrain types. Indeed, several clusters may correspond to one terrain type, or several terrain types may be included in one cluster. How the clusters are identified with terrain types depends on user knowledge.

Two examples of unsupervised classification using MSS data for lithological discrimination are given by Sabins (1986). A recent successful application was presented by Rockwell (1989) who indicated that the unsupervised classification using six TM bands (not including the thermal band) was good for general discrimination of rock units, while that based on TM ratios 3/1, 5/7 and 4/3 can identify alteration zones even though it discriminates fewer rock units.

It seems that many remote sensing geologists have neglected unsupervised classification techniques compared with supervised classification which permits full user control. As shown in this thesis, with proper classification and post classification techniques, unsupervised classification can be controlled in two stages: the statistical control by user input parameters during the automatic clustering; and supervision based on user knowledge during post-classification processing.

2.9 Supervised Spectral Classification

Supervised spectral classification is the procedure most often used for quantitative analysis of remote sensing image data (Richards, 1986). It classifies the image pixels into known classes based on the spectral statistics derived from the training areas defined by users. The classification results thus mainly depend on training area selection. Supervised spectral classification has been used for lithological discrimination using Landsat MSS and TM data (Rothery, 1981). However, as indicated by Abrams (1980), the accuracy, especially for MSS data, is generally low. Incorrect supervision (training) is one of the major sources of error. Training areas selected by users are often not representative and ex-

clusive. The training areas for a rock type may not represent all variations of its image feature, while, the spectral statistics derived from these training areas may not be unique to this rock type. Moreover, it is impossible to select the training areas for all the possible classes in an image without classification! Thus a hybrid classification strategy has been used, in which unsupervised classification is performed to guide the selection of training areas before supervised classification (Schowengert, 1983; Richards, 1986).

2.10 Improving Classification Accuracy

Many efforts have been made to improve the accuracy of lithological classification.

Shadow effects impede to spectral classification. To suppress shadow effects (as well as topography), ratio images are used instead of the original bands (Rothery, 1981). However, ratio images must be used with caution as the data distribution of ratio images may not suitable for classification (Chalmers and Harris, 1981). Swan (1978) indicated that the ratio of two normal distributions will result in a Cauchy distribution which has no mean value and standard deviation. A more advanced technique is to convert the image radiance DN values to spectral reflectance values based on orbit parameters (Campos-Marquetti and Rockwell, 1989; Barker and Gunther, 1983; Forster, 1984), ground measurement (Roberts and Yamagushi, 1985; Elvidge, 1988) or statistical procedures (Kruse *et al.*, 1988, 1990). Campos-Marquetti and Rockwell (1989) presented a study of lithological mapping in a semi-arid area based on ratios of reflectance images derived from TM data.

The foundation of the accuracy of image classification lies on the spectral and spatial resolutions of the imagery used. New generations of sensors, such as AVIRIS, can provides up to 224 spectral bands within the wavelength

$0.4 - 2.45\mu$. This revolutionary improvement of spectral resolution has great potential for direct recognition of minerals and terrain types and has triggered the development of new techniques to handle large data sets. For such data sets, traditional statistical procedures are beyond the capacity of commonly used computers for digital image processing. A technique of binary encoding and spectral matching with a reference library, introduced by Mazer *et al.* (1987, 1988), has been used quite satisfactorily for mineral identification (*e.g.* Kruse, 1990; Barnaby, 1989). Low SNR is a major problem of such very high spectral resolution data, which prevents the information of the data being fully used for regional applications. At present, in geological applications, the data are used for mineral identification rather than lithological mapping. Techniques have been developed to reduce the noise (Lee *et al.* 1990; Green *et al.*, 1988; Berman, 1985). However, significant improvement of SNR largely depends on the sensor technology.

Many rock types are similar in spectral signature but different in texture. That is a major reason that visual interpretation can discriminate different rock types effectively from black and white imagery. The accuracy of lithological classification can be improved by using textural information. There are quite a lot of texture extraction and classification techniques (*e.g.* Gillespie, 1980; thomas, 1977; Thomas *et al.*, 1981; Moses, 1988). Many techniques have been used since 1973 (Haralick, 1973). With the improvement of image spatial resolution and the development of radar technology, the methodological research of textural classification has become more active and many experimental results for lithological discrimination have been reported (*e.g.* Wang and He, 1990). Nevertheless, there is still a long way to go in practical applications. Textural classification for lithological discrimination is an especially difficult and computationally expensive task. To make practical use of textural information for lithological discrimination, simple and effective techniques, wise strategy and powerful computers are needed.

2.11 Post-Processing of Spectral Classification

Post-processing of spectral classification was systematically described in many books on digital image processing (*e.g.* Schowengerdt, 1983). The main purpose of the processing is to remove, based on contextual information, isolated class pixels or small pixel patches. Though many classification algorithms incorporating both spectral and contextual information simultaneously have been developed (Landgrebe, 1980; Kittler and Forlein, 1984; Saeb0 *et al.*, 1985), the simplest methods of using contextual information, as indicated by Mather (1986), are those which are applied after pixel by pixel spectral classification. An excellent summary of the topic is given by Gurney and Townshend (1983).

So far, the most popular and successful contextual techniques are those for classification smoothing. A very simple and effective technique is the majority filtering (Goldberg *et al.*, 1975; Schowengerdt, 1983; Townsend, 1986), in which a central pixel is re-assigned to the majority class among all the pixels in a window used to scan the classification image. Based on the principle of majority filtering, some modifications have been made (Mather, 1986; Wharton, 1982; Thomas, 1980). The minimum area rationale (Davis and Peet, 1977) is another simple technique. More sophisticated contextual filtering technique based on probabilistic relaxation model have been presented by Rosenfeld (1976), Peleg (1980), Harris (1981, 1985) and Kittler (1983). Unfortunately, the technique is not practical for commonly used computers because of high cost of processing. Contextual techniques have been applied mainly for land use/cover mapping.

Apart from classification smoothing, those techniques which perform gen-

eral mapping procedures like detecting class boundaries, painting colours, *etc.* should also be considered as post-processing.

2.12 The Geological Study in SE Spain Using Remote Sensing

Among the institutions and people involved in the geological study in SE Spain using remote sensing imagery, the Geology Department / Centre Remote Sensing research group at Imperial College is a very important one. The review in this section will focus on the work of the group.

The Geology Department and Centre for Remote Sensing at Imperial College have engaged for some years in a continuous programme of study of the geological applications of various remote sensing data sets in SE Spain.

The research for mineral exploration has been concentrated in the Rodalquilar area. A successful commercial application of TM imagery was presented by Huckerby, *et al.*, 1986. The Landsat TM images prepared by contrast enhancement, colour composition, ratioing and ratio colour composition and edge enhancement were interpreted to identify different rock types, alteration zones and to locate faults. The colour composites: 7 5 4 and 5 7 1 (in RGB) and ratio colour composite image: 5/4 R, 7/4 G and 3/4 B were recommended for lithological discrimination.

Another interesting aspect of geological mapping in the Tabernas region using Landsat TM image was reported by Crosta and Moore (1989). Filtering, contrast enhancement and colour composition techniques were performed to enhance both spectral and textural information. As a result, lithological discrimination based on image interpretation was much improved.

Dr A.A.D Cañas, Physics Department of Imperial College, has carried out successful research on image processing in SE Spain during his teaching activity on digital image processing for MSc students. Colour composites of PC images derived from TM bands 1, 3, 4, 5, 7 were found effective for detecting kaolinization, bentonization and gypsum (Cañas, *personal com.*; Moore and Liu, 1990).

Their research work has provided a good foundation for this project.

2.13 Summary

A brief review of lithological mapping using remotely sensed data has been given in this chapter. After a general introduction to the development of remote sensing in geology and visual image interpretation for lithology, the review focussed on various image processing techniques for lithological discrimination.

Digital image enhancement techniques, which are used most successfully for improving the visual interpretation of lithological information, are discussed in four subtopics: contrast enhancement and colour composition; ratioing and algebraic operations; principal component analysis and decorrelation stretching; and RGB-IHS transformation.

Classification techniques, as the core of automatic lithological mapping, are reviewed in three aspects: unsupervised spectral classification; supervised classification and the efforts for improving classification accuracy, such as shadow suppression, textural classification and the improvement of spatial and spectral resolutions of remotely sensed imagery data. The practical results obtained from image classification are limited, but promising.

Several techniques for smoothing classification images are discussed under

the topic of post-processing of spectral classification. Contextual information is used to simplify classified images and suppress noise.

A geological study of SE Spain using remotely sensed images is briefly discussed based on the research work of the Geology Department and the Centre for Remote Sensing, Imperial College.

Chapter 3

Pre-classification Image Enhancement Techniques

Image enhancement as pre-processing for classification is different from that for highlighting particular targets. The purpose of preprocessing is to increase the spectral differences among all the terrain types to be classified in the image. Target enhancement separates the interesting targets from other terrain types. The spectral variations among irrelevant terrain types can be sacrificed to achieve the enhancement of specific targets during target enhancement.

Colourful and shadow free images are generally favoured for lithological mapping based on multi-spectral image classification, especially when different colours represent various rock types. A series of new techniques for producing high quality shadow free colour images has been developed and will be introduced in this chapter. These techniques are to be used sequentially as preparation for spectral classification even though they are individual techniques and can be used independently for spectral enhancement.

Firstly, the Index of Optimal Band-triplet Selection (IOBS) is presented. Then, there is a detailed derivation and discussion of the Balance Contrast Enhancement Technique (BCET) which eliminates colour bias and improves

the quality of colour composite images significantly. Finally, a new kind image, the Hue image RGB composite (HRGB), is introduced. An HRGB image is shadow free and spectrally well enhanced.

3.1 Index of Optimal Band-Triplet Selection (IOBS)

Generally, bands with low inter-band correlation contain more information and therefore tend to produce colourful colour composites. Based on this principle, two widely used band selection techniques were developed by Chavez, *et al.*, 1982 and Sheffield, 1985.

3.1.1 Review of Chavez's and Sheffield's methods

Chavez's technique, the Optimal Index Factor (OIF), was initially designed for selecting Landsat MSS ratios for ratio colour composites and applied later to more advanced multi-spectral imagery (*e.g.* Landsat TM and ATM) for band selection.

OIF is defined as below:

$$OIF = \frac{SD_i + SD_j + SD_k}{|r_{ij}| + |r_{ik}| + |r_{jk}|}$$

where SD_i is the standard deviation for band i and r_{ij} the correlation coefficient of band i and j.

The largest OIF is considered to indicate the best band-triplet for colour composition.

Sheffield's method is more general for selecting M bands from $N(> M)$ bands. The selection is based on the volume of the ellipsoid defined by covariance matrix. The band-triplet having the ellipsoid of maximum volume is considered to contain the maximum information. As the value of the determinant of the covariance matrix of a band-triplet is equivalent to the volume of the ellipsoid of the covariance matrix, the band-triplet selection is performed by computing and ranking in order the determinants of each 3×3 principle submatrix of the covariance matrix of M bands. To select M bands from N bands, the same operation is performed on the determinant of each $M \times M$ principle submatrix.

In both methods, the variances of image bands are considered as indicators of information content and are used as a basis for band selection. In fact, the variance of an image can be easily changed by linear stretch that does not change the information of the image. Linear stretch may therefore affect the band selection as it will increase the standard deviation in Chavez's method and the volume of the ellipsoid defined by the covariance matrix of three bands in Sheffield's method. As linear stretch can improve image contrast without changing the information content, it is often performed before colour composition. A good band selection technique should not be affected by linear stretch.

3.1.2 Definition of Index of Optimal Band-triplet Selection (IOBS)

Correlation coefficients among different bands are independent of linear operations. Let r_{ij} represent the correlation coefficient between two image bands, X_i and X_j, then,

$$r_{ij} = \frac{S_{ij}}{\sqrt{S_{ii}S_{jj}}}$$

where S_{ii} and S_{jj} are the variances of band i and j and S_{ij} is the covariance of the two bands.

If band X_i is enhanced by a linear stretch,

$$Y_i = k_i X_i + b_i$$

and band X_j,

$$Y_j = k_j X_j + b_j$$

Then the variance and covariance of Y_i and Y_j are:

$$a_i^2 S_{ii} \qquad a_j^2 S_{jj} \qquad a_i a_j S_{ij}$$

Thus the correlation coefficient between Y_i and Y_j, R_{ij}, is

$$R_{ij} = \frac{a_i a_j S_{ij}}{\sqrt{a_i^2 S_{ii} a_j^2 S_{jj}}} = \frac{S_{ij}}{\sqrt{S_{ii} S_{jj}}} = r_{ij}$$

Thus a band selection technique based on band correlation coefficients will not be affected by linear contrast enhancement. IOBS has been designed based on this principle.

Suppose that r_{ij}, r_{ik} and r_{jk} are the correlation coefficients of any three bands i, j and k of a N band image then we define the index of optimal band-triplet selection (IOBS) as:

$$IOBS = F(r_{ij}, r_{ik}, r_{jk}) \Rightarrow minimum \qquad (3-1)$$

Imagine a correlation cube with the absolute values of r_{ij}, r_{ik} and r_{jk} as length, width and height (Fig. 3-1) the following functions can be formed.

a). Sum of the length, width and height:

$$F1 = |r_{ij}| + |r_{ik}| + |r_{jk}|$$

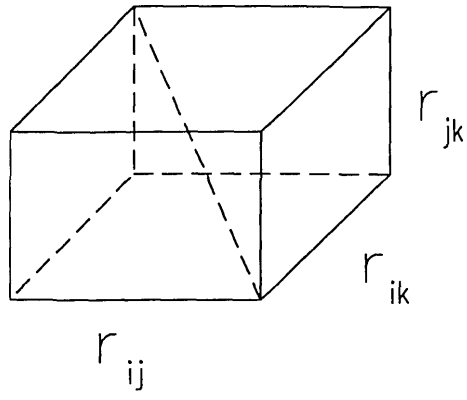


Figure 3-1: Correlation cube of band-triplet: band i, j and k

$F1$ is not sensitive to the variation among r_{ij}, r_{ik} and r_{jk} and fails to indicate the best triplet by the smallest value as shown in Table 3-1, case A and B.

b). Volume of the cube:

$$F2 = |r_{ij} \times r_{ik} \times r_{jk}|$$

For a fixed $F1$, $F2$ becomes the maximum for the best possible choice that satisfies:

$$| r_{ij} | = | r_{ik} | = | r_{jk} |$$

and thus gives larger value to a better choice (Table 3-1, case A and B).

c). Length of the major diagonal line of the cube:

$$F3 = \sqrt{r_{ij}^2 + r_{ik}^2 + r_{jk}^2}$$

For a fixed $F1$, $F3$ becomes minimum for the maximum $F2$. $F3$ is much better than $F1$ and $F2$ as an index of optimal band-triplet selection but it may fail to indicate a better band-triplet when there is a very high correlation between two bands and these two bands both have low correlation with the third band such as the cases A and C in table 3-1.

Table 3-1: Band-triplet selection based on different functions of correlation cube.

Case	r_{ij}	r_{ik}	r_{jk}	F1	F2	F3	IOBS
A	0.1	0.1	0.8	1.0	0.008	0.812	0.381
B	0.3	0.3	0.4	1.0	0.036	0.583	0.135
C	0.5	0.5	0.4	1.4	0.100	0.812	0.235

Based on the analysis above, IOBS is finally defined as below:

$$IOBS = Max(r_{ij}, r_{ik}, r_{jk})\sqrt{(r_{ij}^2 + r_{ik}^2 + r_{jk}^2)/3} \Rightarrow minimum \qquad (3-2)$$

Number 3 is used to standardize the IOBS value within 0-1. For the same F3, IOBS becomes minimum when F2 becomes the maximum. In other words, for N given bands, IOBS gives the smallest value only to the band-triplet having a correlation cube with the shortest major diagonal line and the largest volume under this major diagonal line. Calculating and ranking IOBS for every three bands of N bands, the smallest IOBS indicates a band-triplet having relatively lowest correlation between every band pair among the three bands. This generally means maximum information. IOBS indicates case A as the best, C the second and B the third in Table 3-1.

3.1.3 Example of application using test site

Table 3-2 shows the correlation coefficients of the seven bands of the 512 × 512 TM subscene of the test site in SE Spain. The IOBS values of all triplets of the seven TM bands are in Table 3-3. If the thermal band is not included, the band-triplet 5 4 1 was found to be the best, 7 4 1 the second and 5 3 1 the third. Colour composite of TM5 in red, TM4 in green and TM1 in blue has been appraised as the best composite image for geological interpretation by several geologists working in the area.

Table 3-2: The correlation coefficients of the seven bands of the TM subscene of the test site

CORRELATION COEFFICIENTS MATRIX

	BAND 1	BAND 2	BAND 3	BAND 4	BAND 5	BAND 6	BAND 7
BAND 1	1.0000						
BAND 2	0.9634	1.0000					
BAND 3	0.9091	0.9674	1.0000				
BAND 4	0.8767	0.9398	0.9512	1.0000			
BAND 5	0.7485	0.8170	0.8564	0.8737	1.0000		
BAND 6	0.3134	0.3587	0.4143	0.3567	0.2076	1.0000	
BAND 7	0.7696	0.8463	0.8970	0.8837	0.9636	0.2984	1.0000

Table 3-3: IOBS of the 512 × 512 TM subscene of the test site (the integers represent band-triplets and the decimal numbers are IOBS values)

IOBS OF 3-BAND GROUPS

123	0.9161	124	0.8934	125	0.8167	126	0.5978	127	0.8319
134	0.8683	135	0.7643	136	0.5496	137	0.7827	145	0.7321
146	0.5046	147	0.7467	156	0.3620	157	0.8026	167	0.3923
234	0.9210	235	0.8538	236	0.6210	237	0.8754	245	0.8254
246	0.5791	247	0.8372	256	0.4321	257	0.8460	267	0.4722
345	0.8910	346	0.6025	347	0.8667	356	0.4814	357	0.8738
367	0.5345	456	0.4874	457	0.8749	467	0.5095	567	0.5730

3.2 Balance Contrast Enhancement Technique (BCET)

The colours in an image may change in either hue, intensity or saturation. If the average brightness (mean DN value) of each band of the three bands used for colour composition are balanced, the resulting colour image will show large variation in hue. If the average brightness of one band is significantly higher than the other two, the colour composite will show obvious colour bias to that band. In this case, the hue variation degrades, in a certain degree, to intensity and saturation variations and a less colourful composite will be produced. As inter-band correlations are independent of the variances that are related to means and value ranges of the image bands, even the best band-triplet selected by IOBS may produce a poor colour composite if the means and value ranges of the three bands are very different. As a result, the hue image derived in turn will possess a narrow value range or discontinuous data distribution.

To get rid of colour bias, we need a contrast enhancement technique to stretch/compress each image band for colour composition to a user specified maximum, minimum and mean without changing the basic shape of the histogram (thus the information) of the image. More formally: the function to perform the contrast enhancement must be defined by at least three parameters; it must be monotonically increasing within the value range used and have a relatively straight graphic shape. Also, the calculations should be computer efficient.

There are many techniques for contrast enhancement. None, however, can fully satisfy the above requirements. Linear contrast enhancement stretches an image to a given maximum and minimum (Linear Scale) or to a given mean and standard deviation (Mean and SD Adjustment), but cannot do both simultaneously. Logarithmic and exponential stretching techniques can only move the mean to one direction (larger or smaller) but do not guarantee the maximum

and minimum. Histogram matching which is based on histogram equalization technique can adjust the maxima and minima and means of input images to given values but only at the cost of changing (sometimes significantly) the shapes of the histograms of at least two of the three bands in a colour composite. When the shape of the histogram of an image is changed, the information structure of the image is also changed. This may cause information loss. The same problem also occurs to the Gaussian stretch which forces an image histogram to fit a Gaussian distribution.

Thus a new technique called balance contrast enhancement technique (BCET) has been developed (Liu Jian Guo, 1989). In BCET, a segment of a parabola or cubic curve, derived from the image to be enhanced, is used as the point operation function to stretch or compress the image to a user defined value range and mean. The BCET using a parabolic function (BCETP) is simple and fast; while the BCET using a cubic function (BCETC) is more tolerant and flexible as explained later.

3.2.1 BCET using a parabolic function (BCETP)

Definition of BCETP

The parabolic function used in BCETP is as follows:

$$Y = A(X - B)^2 + C \qquad (3-3)$$

where X is an input image and Y an output image.

The property of the function is controlled by three coefficients: A, B and C. $1/2A$ is the distance between the directrix and the focus point of a parabola. The smaller the magnitude of A, the wider open the two branches of a parabola. The parabolic function is an even function. B and C are the coordinates of the

turning point of the parabola which determine the section of the parabola to be used by BCETP.

The first derivation of the parabolic function (3-3) is:

$$Y' = 2A(X - B) \qquad (3-4)$$

When $Y' = 0$ (*e.g.* $X = B$) the function has a maximum if $A < 0$ and a minimum if $A > 0$. Two parabolic curves with $A = 1$ or $A = -1, B = 0$ and $C = 0$ are shown in Figure 3-2. In order to satisfy the requirements of BCET, the turning point and the nearby curve section should be avoided and only the section of the monotonically increasing branch of a curve used. This is possible for most cases in image contrast enhancement, if the coefficients A, B and C of formula (3-3) are derived from an input image X and the maximum, minimum and mean given for the relevant output image Y.

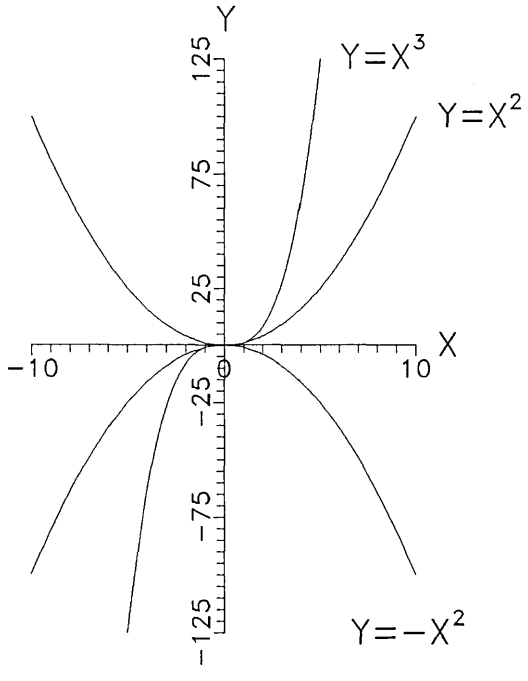


Figure 3-2: Standard parabola $Y = X^2$, $Y = -X^2$ and cubic curve $Y = X^3$.

Solution of coefficients A, B and C for a parabolic function

Let x_i represent any pixel of an input image X then the maximum, minimum and mean of X are as following:

$$h = Max(x_i) \qquad l = Min(x_i) \qquad i = 1, 2, ..., N$$

$$e = \frac{1}{N}\sum_{i=1}^{N} x_i$$

where N is the total number of pixels of the input image X.

Suppose the maximum, minimum and mean given for the output image Y are H, L and E then we have following equations:

$$L = A(l - B)^2 + C \tag{3-5}$$

$$H = A(h - B)^2 + C \tag{3-6}$$

$$E = \frac{1}{N}\sum_{i=1}^{N}[A(x_i - B)^2 + C] \tag{3-7}$$

From (3-7)

$$E = C + \frac{A}{N}\sum_{i=1}^{N}(x_i - B)^2 \tag{3-8}$$

Solve B from (3-5), (3-6) and (3-8),

$$B = \frac{U}{2V} \tag{3-9}$$

where

$$U = h^2(E - L) - s(H - L) + l^2(H - E)$$

$$V = [h(E - L) - e(H - L) + l(H - E)]$$

where

$$s = \frac{1}{N}\sum_{i=1}^{N} x_i^2$$

Further, A and C can be derived from the formulae below:

$$A = \frac{H - L}{(h - l)(h + l - 2B)} \tag{3-10}$$

$$C = L - A(l - B)^2 \qquad (3-11)$$

A solution for the equation group (3-5),(3-6) and (3-7) is finally obtained. Three cases may occur in the solution:

- If $B < l$ then $A > 0$, the parabola is open upward and a section of the right (monotonically increasing) branch of the parabola will be used by BCETP;
- If $B > h$ then $A < 0$, the parabola is open downward and a section of left (monotonically increasing) branch of the parabola will be used by BCETP;
- If $l < B < h$, then BCETP fails to avoid the turning point of the parabola derived.

The first two cases satisfy the requirements of BCET. Experimental processing has confirmed that they are far more common than the third case in image balance contrast enhancement.

After the coefficients A, B and C have been derived, the balance contrast enhancement is performed pixel by pixel on the input image X:

$$y_i = A(x_i - B)^2 + C \qquad i = 1, 2, ..., N \qquad (3-12)$$

where x_i is any pixel of the input image, X, y_i any pixel of the output image Y and N the number of total pixels of the input image.

Finally, an output image Y with exactly the given value range $[L, H]$ and mean E will be produced by BCETP.

3.2.2 BCET using a cubic function (BCETC)

Definition of BCETC

The cubic function used in BCETC is defined as following:

$$Y = A(X - B)^3 + C \qquad (3-13)$$

where X is an input image and Y an output image.

The first deviation of the cubic function of formula (3-13) is:

$$Y' = 3A(X - B)^2 \qquad (3-14)$$

If $A > 0$, then $Y' \geq 0$ and the function is monotonically increasing. B and C are the coordinates of the point of inflection (also the central symmetric point) of a cubic curve which determine the section of the cubic curve to be used by BCETC. A standard cubic curve with $A = 1, B = 0$ and $C = 0$ is shown in Figure 3-2. The shape of the curve is quite straight except the section around the point of inflection where the curve changes its shape from convex to concave. Generally the point of inflection and the nearby curve section can be avoided in balance contrast enhancement if the coefficients: A, B and C in formula (3-13) are derived in a similar way to that described in section 3.2.1.

Solution of coefficients A, B and C for a cubic function

The meanings of the symbols used are as before. Then we have following equations:

$$L = A(l - B)^3 + C \qquad (3-15)$$

$$H = A(h - B)^3 + C \qquad (3-16)$$

$$E = \frac{1}{N}\sum_{i=1}^{N}[A(x_i - B)^3 + C] \qquad (3-17)$$

From (3-17)

$$E = C + \frac{A}{N}\sum_{i=1}^{N}(x_i - B)^3 \qquad (3-18)$$

Solve B from (3-15),(3-16) and (3-18),

$$B = (-v \pm \sqrt{v^2 - 4uw})/2u \qquad (3-19)$$

where

$$u = 3[h(E-L) - e(H-L) + l(H-E)]$$

$$v = -3[h^2(E-L) - s(H-L) + l^2(H-E)]$$

$$w = h^3(E-L) - t(H-L) + l^3(H-E)$$

where $s = \frac{1}{N}\sum_{i=1}^{N} x_i^2, \quad t = \frac{1}{N}\sum_{i=1}^{N} x_i^3$

Formula (3-19) can be rewrite as below:

$$B1 = (-v + \sqrt{v^2 - 4uw})/2u \qquad (3-20)$$

$$B2 = (-v - \sqrt{v^2 - 4uw})/2u \qquad (3-21)$$

If $v^2 - 4uw \geq 0$, $B1$ and $B2$ are real solutions. This condition is satisfied in most cases of image enhancement. Further, A and C can be derived from the formulae below:

$$A = \frac{H-L}{(h-B)^3 - (l-B)^3} \qquad (3-22)$$

$$C = L - A(l-B)^3 \qquad (3-23)$$

Finally, two solutions for the equation group (3-15), (3-16) and (3-17) are obtained:

Solution 1.

$$\begin{aligned} B1 &= (-v + \sqrt{v^2 - 4uw})/2u \\ A1 &= \frac{H-L}{(h-B1)^3 - (l-B1)^3} \\ C1 &= L - A1(l-B1)^3 \end{aligned} \qquad (3\text{-}24)$$

Solution 2.

$$\begin{aligned} B2 &= (-v - \sqrt{v^2 - 4uw})/2u \\ A2 &= \frac{H - L}{(h - B2)^3 - (l - B2)^3} \\ C2 &= L - A2(l - B2)^3 \end{aligned} \tag{3-25}$$

Although algebraically fairly complex, these solutions are numerically very fast for a computer.

Selection of the appropriate solution for BCETC

The two solutions, (3-24) and (3-25), define two cubic functions,

$$BCETC1 \qquad Y = A1(X - B1)^3 + C1 \tag{3-26}$$

$$BCETC2 \qquad Y = A2(X - B2)^3 + C2 \tag{3-27}$$

There are three cases:

- if $B < l$ then $C < L$, the upper section of the cubic curve is used;
- if $B > h$ then $C > H$, the lower section of the cubic curve is used;
- if $l < B < h$ then $L < C < H$, the middle section with the point of inflection of the cubic curve is used.

The first two cases satisfy the requirements of BCET as the point of inflection is avoided and the shape of the curve section used is quite straight. The shape of the histogram will be changed significantly if an image is processed by the function of the third case. This case is certainly not qualified for balance contrast enhancement.

According to the experimental processing, the solution 1 was always either the first two cases (whether stretching or compressing) and BCETC1 performed excellent contrast enhancement while solution 2 was always the third case and

BCETC2 failed to produce any rational results. It is not clear from the mathematics that $B1 < l$ or $B1 > h$ and $l < B2 < h$ are always true; so far, however, no exceptional cases have been revealed among the images processed by BCETC.

The output images produced by BCETP and BCETC are almost exactly the same for the same parameters given. As BCETP is much simpler and faster than BCETC, it is generally preferred to BCETC. However, with higher flexibility, BCETC permits a wider range of choices for parameters and can thus perform balance contrast enhancement in those case not suitable to BCETP. A more detailed discussion will be given with the following examples.

3.2.3 BCET Fortran programmes and examples of the application

Fortran programmes have been developed based on the mathematical concepts of BCETP and BCETC. Both programmes have five user defined parameters to control output images. These parameters are the minimum, maximum and mean (L, H and E) given for an output image and the lower and upper clipping limits ($CLPL$ and $CLPH$) for saturation. $CLPL$ and $CLPH$ are given by users as percentage numbers. For an input image, the DN values of accumulated pixel number up to the percentage of $CLPL$ will be set to the user defined minimum; while that higher than the percentage of $CLPH$ will be set to the maximum. Thus the case of few pixels occupying wide value range will be avoided and the value range defined by the maximum and minimum can be fully utilized. A 512×512 TM subscene of the test site and a 512×512 SPOT subscene of Guadix city, Spain were processed by the BCET programmes.

Example 1. A 512×512 TM subscene of the test site

The image was processed by both BCETP and BCETC with parameters: $L = 0, H = 255, E = 100, CLPL = 1\%$ and $CLPH = 99\%$. The coefficients, A, B and C of BCETP and BCETC for each band are shown in Table 3-4. The necessary statistics are shown in Table 3-5. The effective value range of each band of the input image is narrow. This resulted in poor image contrast. After the balance contrast enhancement, all the bands were stretched to an equal value range, [0, 255] and average brightness, 100. For BCETC, as mentioned before, only BCETC1 satisfied the conditions: $B < l$ or $B > h$ and was used for balance contrast enhancement. Figure 3-3 shows the BCETP curves and BCETC1 curves for band 1, 2, 3, 4, 5 and 7. The right branches of upward open parabola for BCETP and the upper sections of cubic curves for BCETC1 were used for these bands. The shapes of the BCETP and BCETC1 curves for each band are almost identical. Thus the output images produced by BCETP and BCETC1 are virtually no different.

Figure 3-4, a and b are the BCETP and BCETC1 curves for band 6. BCETP, which failed to derive a parabola with its turning point out of the value range of band 6, is not suitable to perform balance contrast enhancement of this band. With higher flexibility, BCETC1 succeeded in this case.

BCET can also be used to compress an image if the value range given for an output image is narrower than that of the input image. As an experiment, the band 7 (after BCETP stretching) was compressed to a narrow value range [10, 120] with mean=60 by both BCETP and BCETC1. The relevant curves are shown in Figure 3-4 (the two curves, c and d, merge into one as they are almost identical).

In the following discussion of this example, only the images produced by

Table 3-4: The BCET coefficients of the TM subscene of the test site. ($L = 0$, $H = 255$, $E = 100$, $CLIPLOW = 1\%$, $CLIPHIGH = 99\%$).

Band	BCET	A	B	C
	BCETP	0.008571150	-121.91	-407.03
TM1	BCETC1	0.000005779	-368.34	-580.38
	BCETC2	0.004706758	125.01	114.88
	BCETP	0.035942517	-12.95	-75.88
TM2	BCETC1	0.000084405	-83.18	-132.37
	BCETC2	0.008140285	57.29	116.66
	BCETP	0.019339362	-13.41	-34.78
TM3	BCETC1	0.000038994	-94.44	-73.35
	BCETC2	0.001985154	67.63	114.40
	BCETP	0.027755048	2.97	-6.26
TM4	BCETC1	0.000081765	-51.08	-26.95
	BCETC2	0.001837289	57.04	109.28
	BCETP	0.007180939	-15.97	-6.89
TM5	BCETC1	0.000010677	-123.23	-28.20
	BCETC2	0.000247427	91.29	109.86
	BCETP	0.143021214	136.53	-2.94
TM6	BCETC1	0.001263531	120.18	-2.08
	BCETC2	0.009471489	152.88	86.23
	BCETP	0.020722043	-14.11	-10.13
TM7	BCETC1	0.000050669	-79.71	-34.19
	BCETC2	0.001345605	51.48	110.61

Table 3-5: Statistics of the TM subscene of the test site before and after BCET processing.

Band	Input image				Saturation		Output image					
					1 - 99 %				BCETP		BCETC1	
	Min	Max	Mean e	SD	l	h	min	Max	Mean	SD	Mean	SD
TM1	93	232	120.78	16	96	156	0	255	100.00	66	99.99	66
TM2	31	132	55.47	15	33	83	0	255	99.90	70	99.96	70
TM3	27	153	66.47	24	29	109	0	255	99.99	71	99.99	71
TM4	17	137	59.00	26	18	100	0	255	100.05	73	99.99	73
TM5	8	253	94.33	52	15	175	0	255	99.96	75	100.02	74
TM6	128	185	157.88	16	132	179	0	255	not used		100.06	76
TM7	5	145	52.63	29	8	99	0	255	100.02	75	99.95	74

BCETP are used and referred to as BCET.

The most dramatic result was achieved by BCET for colour composites of TM band 1, 4 and 5, the best band-triplet selected by IOBS. Figure 3-5 and Figure 3-6 show the histograms of TM band 1, 4 and 5 before and after BCET processing. The histograms of these bands are satisfactorily stretched by BCET without changing their basic shapes. The only exception is the higher frequency at minimum, 0, and maximum, 255, caused by clipping saturation. Figure 3-7 illustrates the colour composites, TM 5 4 1 in RGB, before and after BCET processing. The composite of the original bands (Figure 3-7a) shows a very strong colour bias to blue and red because the average brightness of TM4 is much lower than those of TM1 and TM5. After BCET processing, a high quality colour composite was produced as shown in Figure 3-7b. The colour composite of Landsat TM band 5 4 1 in RGB produced by BCET is considered as the best image for general geological interpretation in SE Spain by many geologists and students working in the area.

Figure 3-8 shows the standard false colour composites (TM4 in red, TM3 in green and TM2 in blue) processed by BCET and other techniques. The original composite (Figure 3-8a) possesses a strong colour bias to green and poor contrast because the average brightness of TM3 is much higher than those of TM2 and TM4 and the effective value ranges of these bands are narrow. The contrast of the image is improved after linear stretch but the colour bias is not corrected (Figure 3-8b). The composite produced by histogram equalization (Figure 3-8c) is fairly good and colour bias is well suppressed. However, the contrast of the image is so high that the subtle information in the areas with light tone, such as basin areas, is overwhelmed by excessive high value saturation. The composite produced by BCET (Figure 3-8d) is the best of the four images. It is richly coloured and has excellent contrast because the three bands have the same mean and are properly stretched to utilize the full dynamic range of the display system (0-255) without changing their basic histogram shapes. The image provides an unusual amount of information. This is especially true in very light and very dark areas. The subtle texture in these areas, which is lost in Figure 3-8c, are clearly displayed in Figure 3-8d.

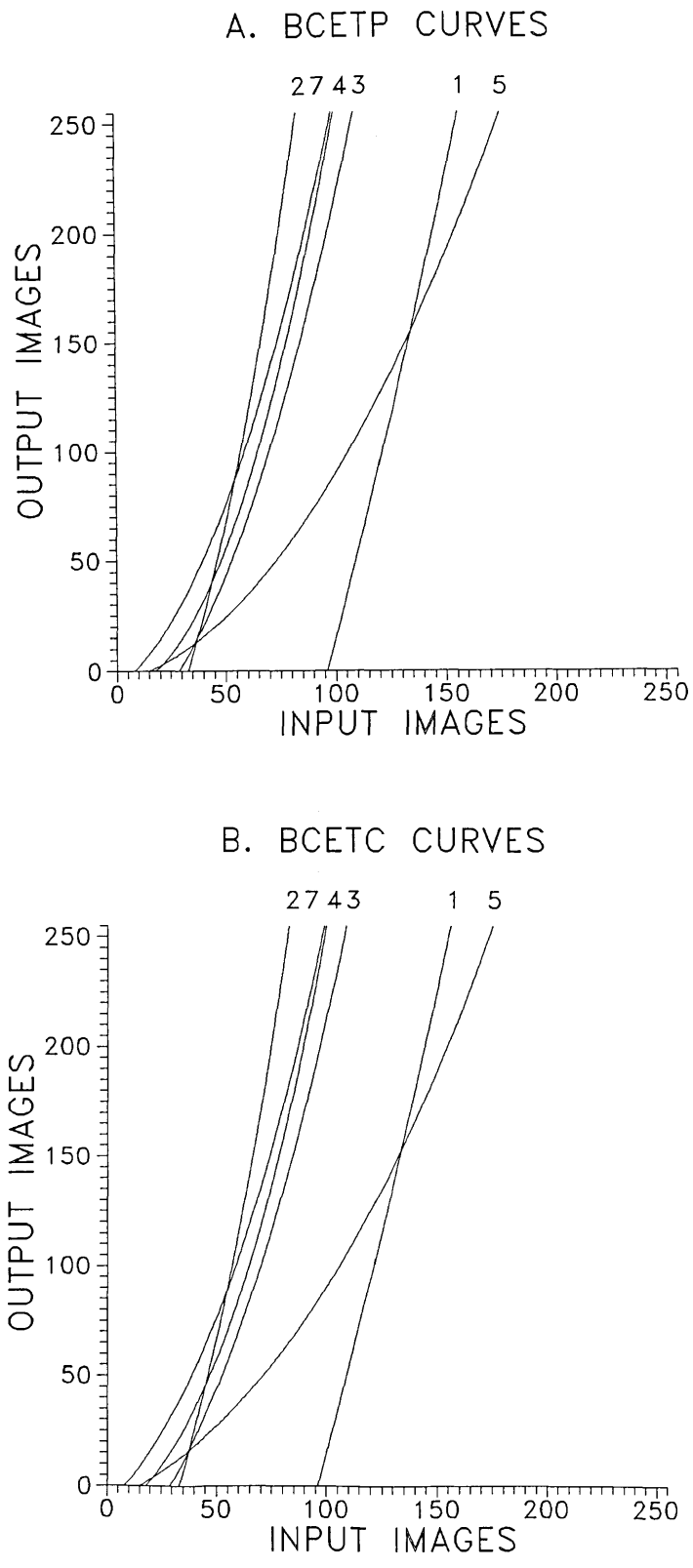


Figure 3-3: BCET curves of band 1, 2, 3, 4, 5 and 7 of the TM subscene of the test site. ($L = 0$, $H = 255$, $E = 100$, $CLPL = 1\%$, $CLPH = 99\%$).

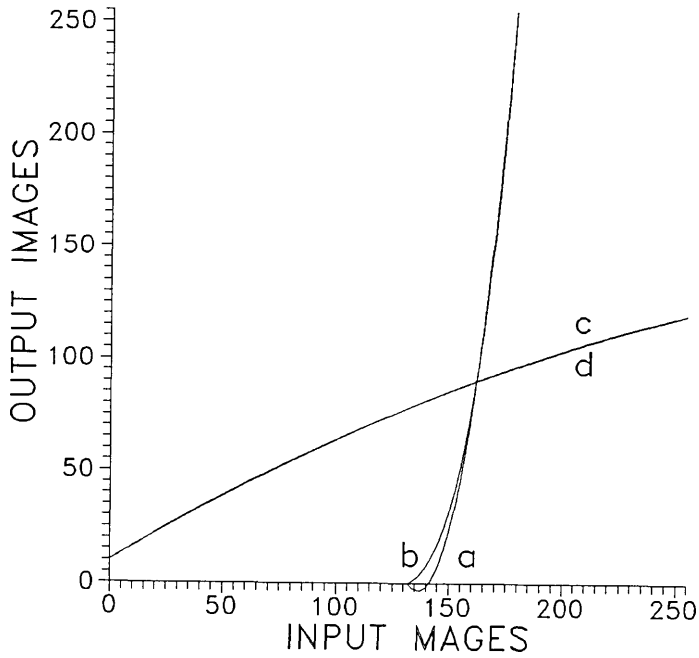


Figure 3-4: a) BCETP curve of band 6. b) BCETC1 curve of band 6. c) & d) BCETP and BCETC1 curves to compress band 7 with parameters: $L = 10, H = 120$ and $E = 60$ after BCET stretching.

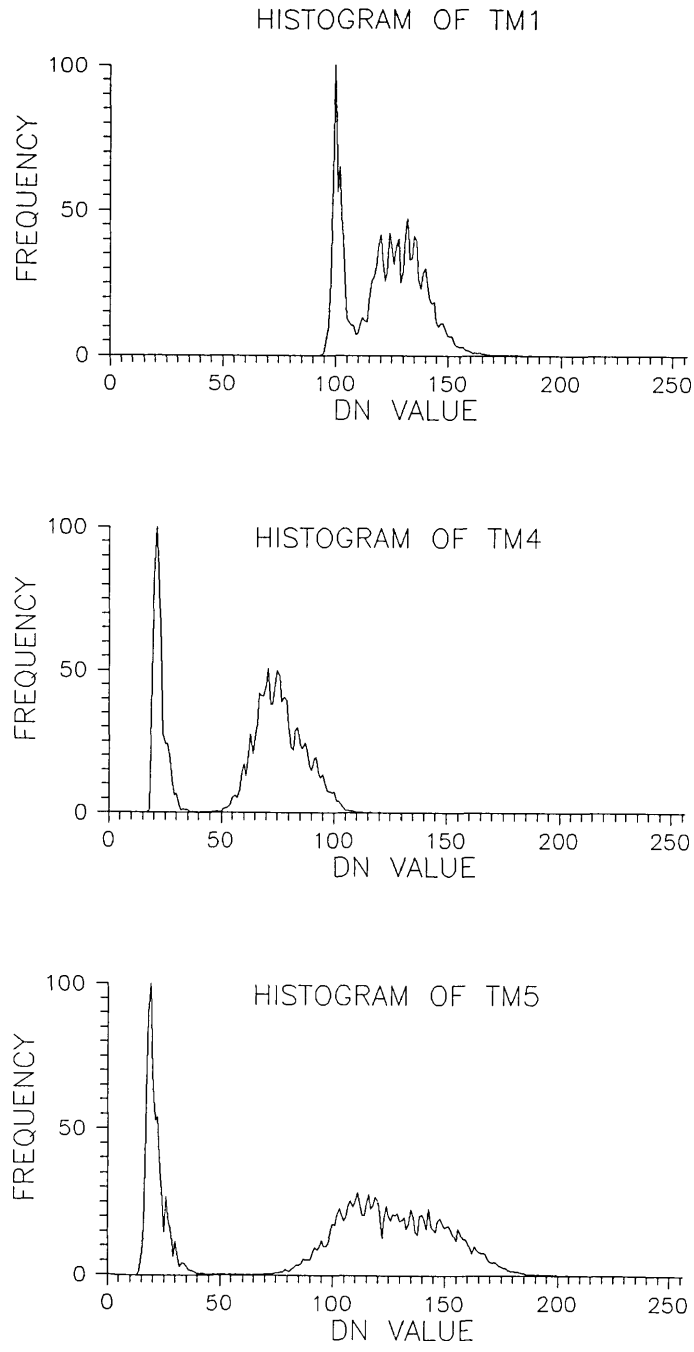


Figure 3-5: Histograms of band 1, 4 and 5 of the TM subscene of the test site before BCET processing.

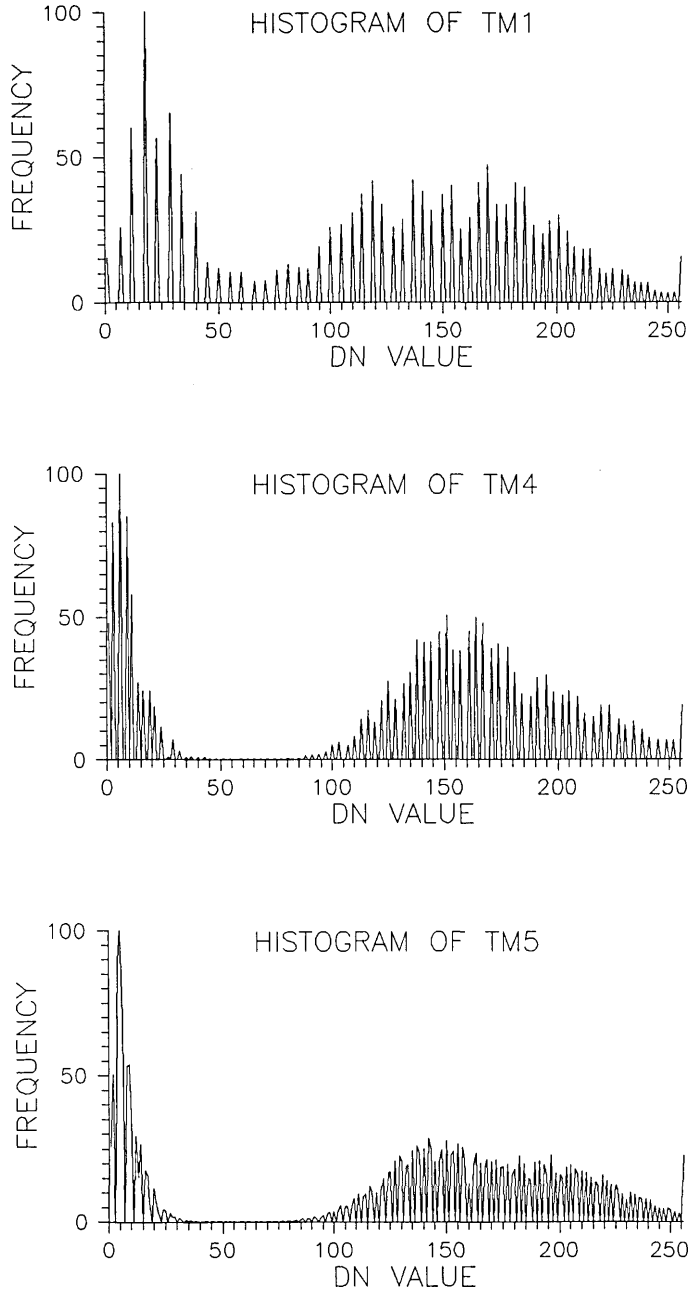
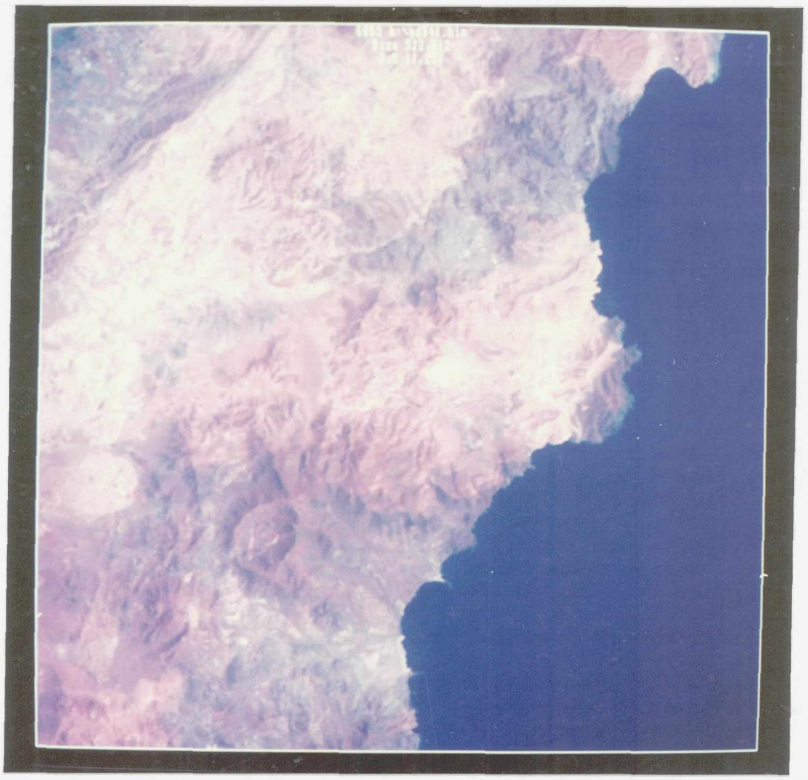
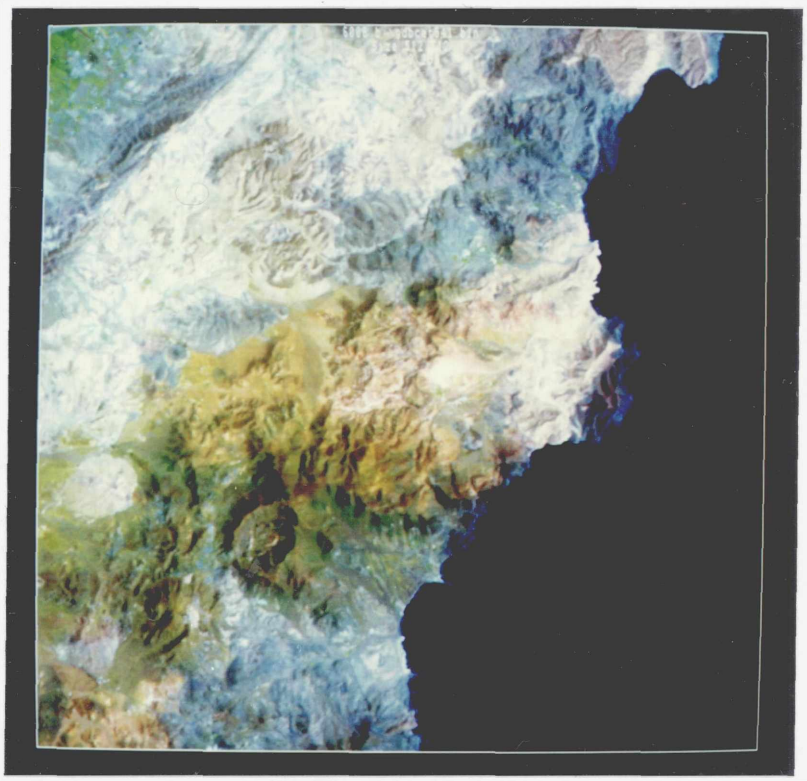


Figure 3-6: Histograms of band 1, 4 and 5 of the TM subscene of the test site after BCET processing.



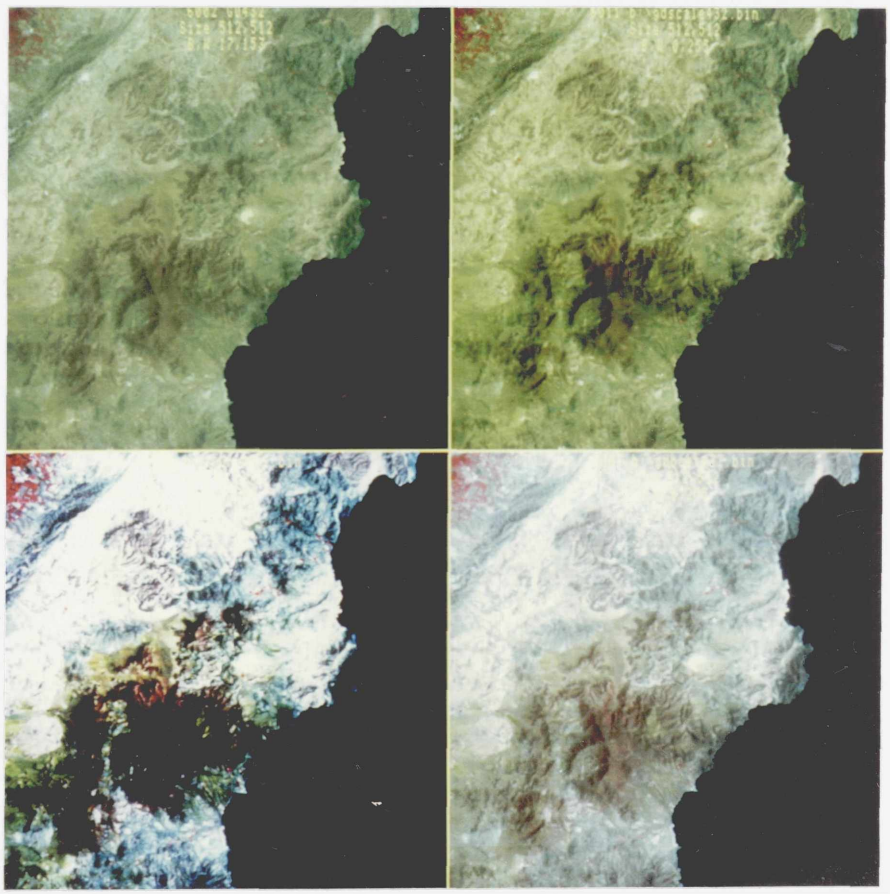
a)



b)

Figure 3-7: The colour composites of TM band-triplet 5 4 1 (RGB) of the test site. a) Before BCET processing. b) After BCET processing

a b



c d

Figure 3-8: Standard false colour composites of the TM subscene of the test site. a) Original composite. b) Linear stretch. c) Histogram equalization. d) BCET.

Example 2. A 512×512 SPOT subscene of Guadix, Spain

A 512×512 subscene of SPOT image (panchromatic band) of Guadix city, Spain was processed to test different parameters for BCETP and BCETC as well as the difference between the images produced by BCETC1 and BCETC2.

The two sets of the parameters used, the coefficients of BCETP and BCETC and the relevant statistics are shown in Table 3-6. The lower sections of the cubic curves ($B1 > h$) for BCETC1 and the left branches of the downward open parabola ($A < 0, B > h$) for BCETP were used as shown in Figure 3-9 (the BCETP and BCETC1 curves derived from the same parameters merge into one because of very high similarity). The value range of the original image seems wide: [33,167]; but the effective value range is only about [37,63] (Table 3-6, columns of $CLPL$ and $CLPH$) because a few high DN value pixels occupy wide value range. For this kind of data distribution, the clipping saturation of the value range of the input image is necessary. Otherwise, no real solutions can be found for BCETC ($v^2 - 4uw < 0$) and BCETP fails to avoid the turning point of the parabola derived.

Figure 3-10 shows the images before and after BCETC processing. The relevant histograms are shown in Figure 3-11. The contrast of the original image is very low (Figure 3-10a) as the effective value range is very narrow. Figure 3-10b is much improved. However, excessive contrast causes loss of subtle information in light and dark areas. This can be explained by Figure 3-11b. The basic shape of the histogram of the input image was changed in some extent by too large value of mean and clipping limits. Figure 3-10c is of the best quality; the contrast of the image was much improved without losing information in light and dark areas as the histogram of the input image was stretched without changing its basic shape (Figure 3-11c) by properly chosen parameters.

Table 3-6: BCET coefficients and image statistics of the 512 × 512 SPOT subscene of Guadix, Spain. The value range of the input image is [33, 167], mean 45.00 and standard deviation 16.

	BCET	BCET coefficients			CLPL	CLPH				
Parameter	functions	A	B	C	(l)	(h)	Min	Max	Mean	SD
Saturation	BCETC1	0.00731	71.88	284.26	38	56	0	255	127.98	66
3 - 97%	BCETC2	0.17330	47.50	148.47			not used			
E=128	BCETP	-0.55832	59.69	262.59	38	56	0	255	127.08	66
Saturation	BCETC1	0.00036	144.43	451.72	37	63	0	255	90.13	50
1 - 99%	BCETC2	0.05740	49.21	104.56	37	63	0	255	90.02	32
E=90	BCETP	-0.10473	96.82	374.81	37	63	0	255	89.98	50

One may notice that both B for BCETP and $B1$ for BCETC1 are within the original value range of the input image,[33,167] (Table 3-6). But after the clipping saturation, the maximum of the input image (h) becomes 56 for the first group of parameters and 63 for the second. Therefore, $B > h$ (BCETP) and $B1 > h$ (BCETC1) are true for both Figure 3-10b and c.

Figure 3-10d was processed by BCETC2 with the same parameters as Figure 3-10c. The contrast of the image is very poor. The histogram of the image (Figure 3-11d) is totally different from the original one. The high frequency pixel values were improperly compressed to occupy very narrow value range by using the flat cubic curve sections with the point of inflection. A heavy information loss resulted.

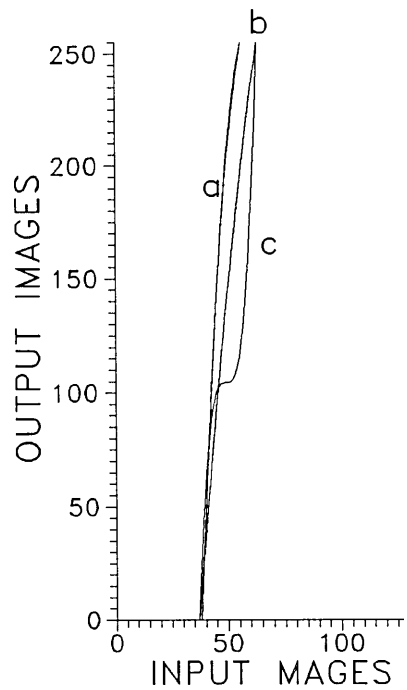


Figure 3-9: BCET curves of the 512 × 512 SPOT subscene of Guadix, Spain. a) BCETP and BCETC1: $L = 0$, $H = 255$, $E = 128$, $CLPL = 3\%$, $CLPH = 97\%$. b) BCETP and BCETC1: $L = 0$, $H = 255$, $E = 90$, $CLPL = 1\%$, $CLPH = 99\%$. c) BCETC2: $L = 0$, $H = 255$, $E = 90$, $CLPL = 1\%$, $CLPH = 99\%$.

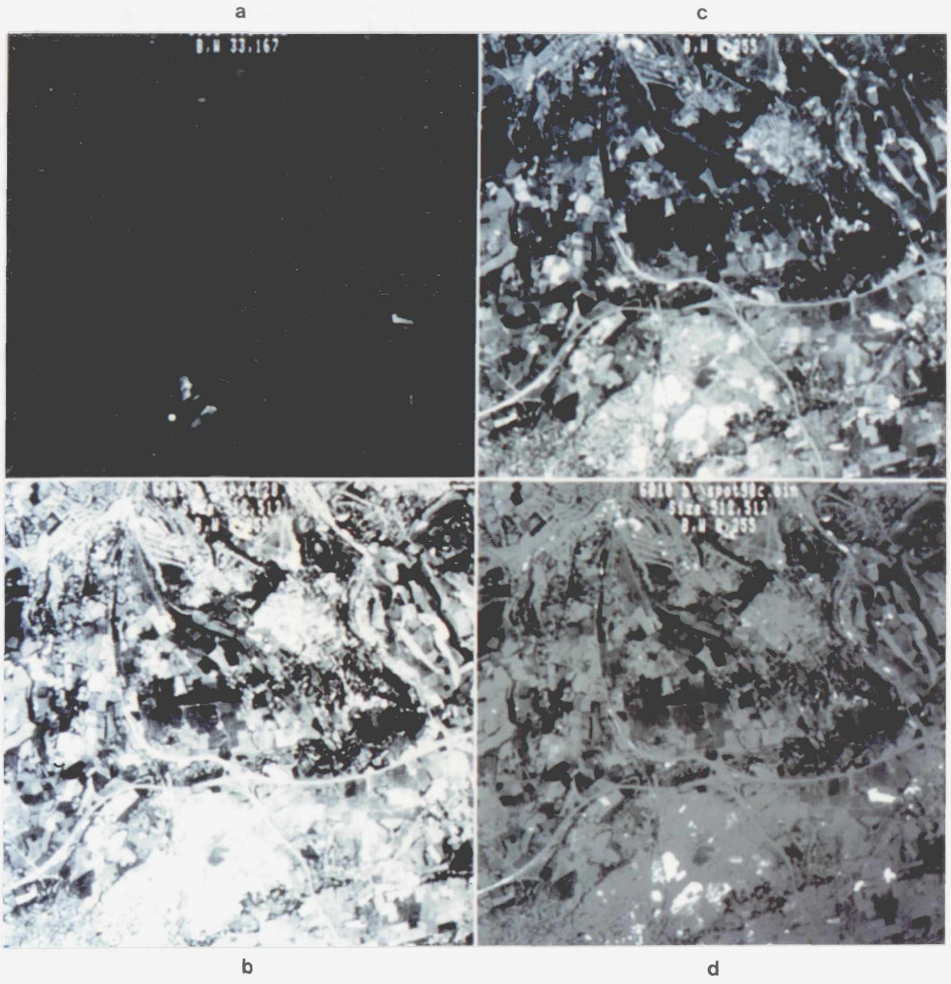


Figure 3-10: Images of 512×512 SPOT subscene of Guadix, Spain. a) Original image. b) BCETC1: $L = 0$, $H = 255$, $E = 128$, $CLPL = 3\%$, $CLPH = 97\%$. c) BCETC1: $L = 0$, $H = 255$, $E = 90$, $CLPL = 1\%$, $CLPH = 99\%$. d) BCETC2: $L = 0$, $H = 255$, $E = 90$, $CLPL = 1\%$, $CLPH = 99\%$.

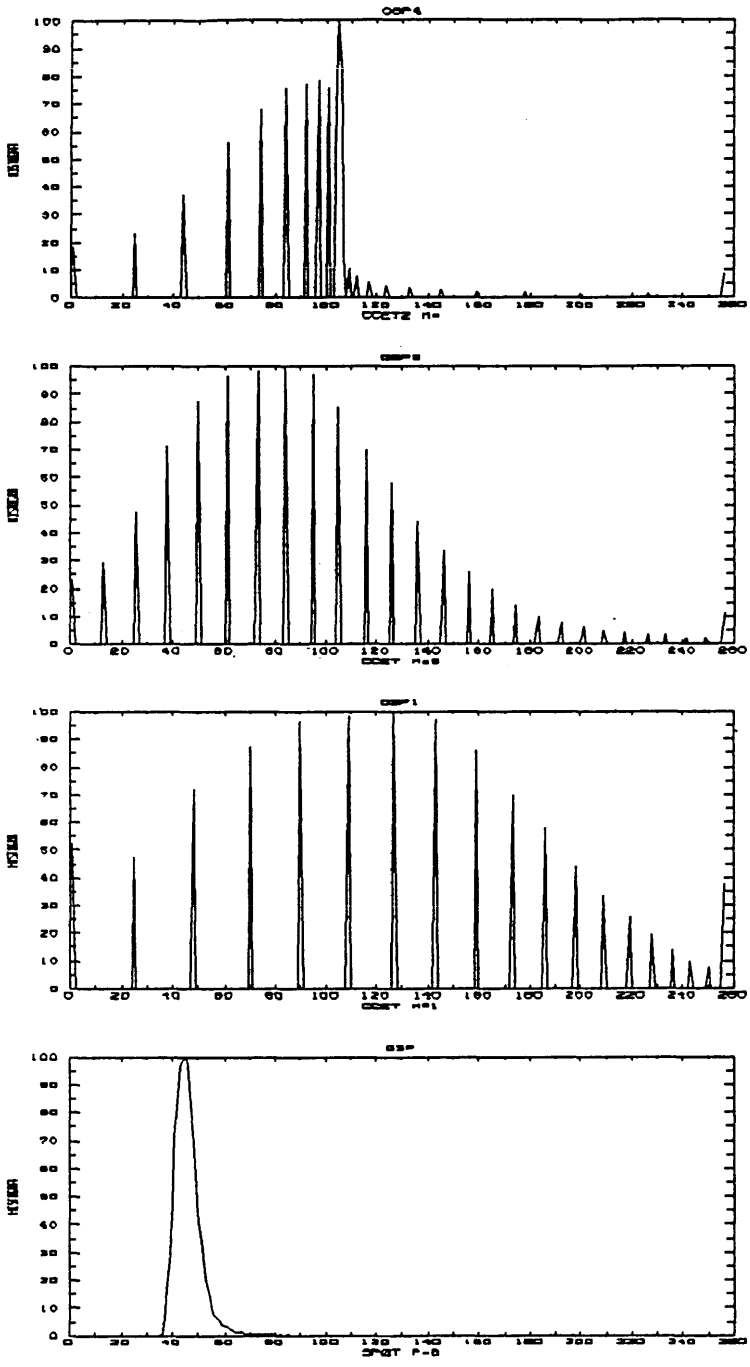


Figure 3-11: Histograms of the SPOT subscene of Guadix, Spain. a) Original image. b) BCETC1: $L = 0$, $H = 255$, $E = 128$, $CLPL = 3\%$, $CLPH = 97\%$. c) BCETC1: $L = 0$, $H = 255$, $E = 90$, $CLPL = 1\%$, $CLPH = 99\%$. d) BCETC2: $L = 0$, $H = 255$, $E = 90$, $CLPL = 1\%$, $CLPH = 99\%$.

3.2.4 Discussion

The above examples demonstrate that both BCETP and BCETC are excellent methods for contrast enhancement (stretch or compression). The contrast of an input image can be controlled easily by adjusting the five user input parameters: minimum, maximum and mean for the output image and lower and upper clipping limits for saturation. They are especially useful to improve the quality of colour composites. The BCET has been widely used by the Ph.D. and MSc students of the Department of Geology and Centre for Remote Sensing, Imperial College, since it was installed in the I2S/TAE image processing system. BCET has consistently produced the best colour composites from various images in different areas.

When using BCET, one important point must be understand. Colour balance is scene dependent. A small subscene within a colour balanced large scene may show colour bias as the proportion of the terrain types with different spectral signatures in the large scene is generally different from that in the small subscene. Thus, for colour composition, the balance contrast enhancement does not necessarily recover the original colours though it often does. Rather it illustrates spectral information in a most colourful form. Colour balance does not exist in a spectrally homogeneous image or in an image of an area dominated by one terrain type. For instance, the true colour image of deep sea should be blue. If the three bands for the true colour composition are forced to fit to a same value range and mean, the image will become grey. For such a case, BCET should be used to stretch/compress different bands to different mean values according to the knowledge of the terrain types in the image, *i.e.* the mean of blue band should be higher than green and red bands for the case of true colour composite of sea. Generally, the smaller is an image subscene, the more it is spectral homogeneous. Thus BCET should be performed on the image with reasonable spectral variations. On the other hand, balance contrast enhancement in a small subscene may effectively separate the spectrally similar

terrain types by different colours.

3.3 Hue Image RGB Colour Composition (HRGB)

Shadow suppression and spectral enhancement of rock, soil and vegetation are particularly important for lithological discrimination using multi-spectral images. Band ratio colour composites have been used widely for this purpose (Sabins, 1986; Drury, 1986). However, the relationship between ratios and spectral character is not well understood and ratio techniques cannot completely eliminate shadows for two main reasons (Drury, 1986). Firstly, natural terrain is not a perfect Lambertian surface. The reflectance of the surface depends on both the surface structure and the angle between the surface and the incident illumination from the sun (Suits, 1983). Secondly, atmospheric effects change the ratios from different slopes in an unpredictable and subtle fashion (Drury, 1986).

In fact, ratio images are angle tangent images in the view of the two dimensional transformation from a Cartesian coordinate system to a polar coordinate system:

$$RATIO = \frac{X}{Y} \qquad (3-28)$$

$$M = \sqrt{X^2 + Y^2} \qquad (3-29)$$

where X and Y are two bands for ratio, $RATIO$ is the ratio image and M is the magnitude image.

A colour can be expressed as a composite of three primaries: red, green and blue. By allocation to separate image bands, the primaries can be used to display three bands of a multi-spectral image as a colour (RGB) composite. Colour is quantitatively defined in terms of three variables: intensity, hue

and saturation, which give a numerical description of the brightness, spectral range and purity of a colour. Based on a simplified model, a colour cube model (Smith, 1978; Schowengerdt, 1983), the RGB-IHS (red, green and blue to intensity, hue and saturation) transformation is a three dimensional Cartesian-polar coordinate transformation. Thus three image bands displayed as a RGB colour composite can be converted to three images representing intensity, hue and saturation respectively by RGB-IHS transformation. Furthermore, if three hue images derived from three band-triplets (up to nine bands) are displayed in red, green and blue as a colour composite, a new kind image termed a hue RGB (HRGB) colour composite is formed. This image, as explained later, is shadow free and can encode the spectral information of up to nine bands of original multi-spectral image data.

3.3.1 RGB-IHS Transformation

As shown in Figure 3-12 (Schowengerdt, 1983), any colour in a three band colour composite of a remotely sensed image (Landsat MSS and TM, SPOT HRV, *etc.*) is a vector $\mathbf{OP}_i = (r_i, g_i, b_i)$ within a colour cube with edge length of 255. The major diagonal line connecting the origin and the furthest vertex is called grey line because the pixels lying on this line have equal components in red, green and blue. The intensity of a colour vector $\mathbf{OP}_i$ is defined as the length of its projection on the grey line, OD, and the hue the azimuthal angle around the grey line, α. The saturation is a measurement of the relative distance between vector $\mathbf{OP}_i$ and grey line under the intensity of the colour. It can be defined as the ratio of the difference of the maximum and minimum of r_i, g_i and b_i against the maximum of r_i, g_i and b_i (Smith, 1978). Let the hue angle of pure blue be zero, then we have following RGB-IHS transformation:

$$I(r_i, g_i, b_i) = \frac{1}{\sqrt{3}}(r_i + g_i + b_i) \qquad (3-30)$$

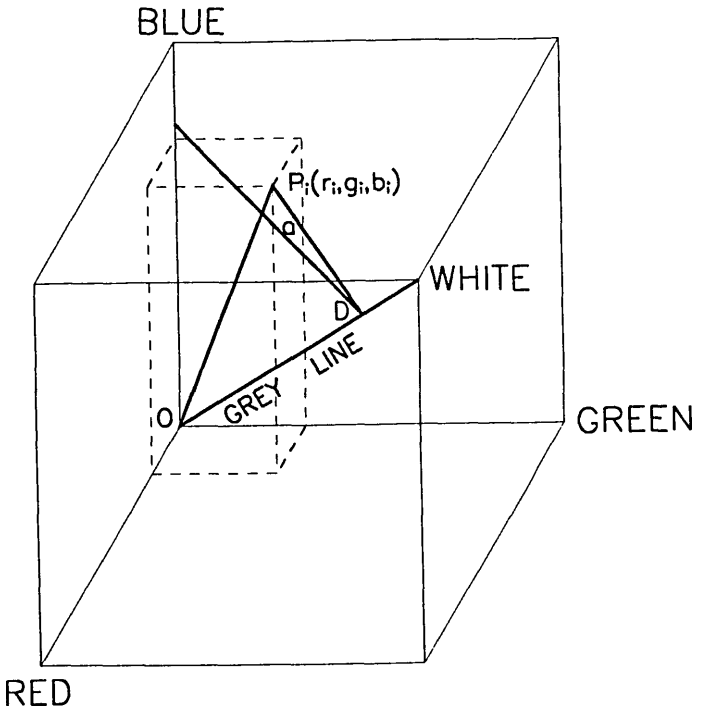


Figure 3-12: Colour cube model for RGB-IHS transformation.

$$H(r_i, g_i, b_i) = cos^{-1} \frac{2b_i - g_i - r_i}{2V_i} \qquad (3-31)$$

$$S(r_i, g_i, b_i) = \frac{max(r_i, g_i, b_i) - min(r_i, g_i, b_i)}{max(r_i, g_i, b_i)} \qquad (3-32)$$

where

$$V_i = \sqrt{(r_i^2 + g_i^2 + b_i^2) - (r_i g_i + r_i b_i + g_i b_i)}$$

The value range of the hue image derived from formula (3-31) is [0, 360]. It should be re-scaled into [0, 255] for colour display.

Suppose the irradiance upon the surface toward the sun of a terrain slope, E_t, is n times of the irradiance upon the surface backward the sun of the terrain slope (the slope in shadow), E_b, then:

$E_t = nE_b, \quad R_t = nR_b, \quad G_t = nG_b, \quad B_t = nB_b$

where R, G and B represent the irradiance of the three bands used for RGB colour composition.

From formula (3-31), we can easily prove:

$$H(R_t, G_t, B_t) = H(R_b, G_b, B_b) \qquad (3-33)$$

as follows:

$$V_t = \sqrt{(R_t^2 + G_t^2 + B_t^2) - (R_tG_t + R_tB_t + G_tB_t)}$$

$$= \sqrt{[(nR_b)^2 + (nG_b)^2 + (nB_b)^2)] - (n^2R_bG_b + n^2R_bB_b + n^2G_bB_b)}$$

$$= n\sqrt{R_b^2 + G_b^2 + B_b^2 - (R_bG_b + R_bB_b + G_bB_b)}$$

$$= nV_b$$

then,

$$H(R_t, G_t, B_t) = cos^{-1}\frac{2B_t - G_t - R_t}{2V_t}$$

$$= cos^{-1}\frac{2nB_b - nG_b - nR_b}{2nV_b}$$

$$= cos^{-1}\frac{2B_b - G_b - R_b}{2V_b}$$

$$= H(R_b, G_b, B_b)$$

Thus hue is independent of illumination. The hue of a terrain slope will not differ between direct illumination and shadow. As a result, a hue image is not affected by shadow. More generally, in the same way, we can prove:

$$H(r_i, g_i, b_i) = H(r_j, g_j, b_j) \qquad (3-34)$$

if $E_j = nE_i + a$ where a is a constant.

This equation means that if a hue image is derived from three spectrally adjacent bands (thus the atmospheric effects on each bands are almost the

same), it will not be much affected by either shadow or atmospheric scattering. This is not generally true for ratio images since:

$$\frac{band_i}{band_j} \neq \frac{n \times band_i + a}{n \times band_j + a}$$

if $band_i \neq band_j$

In fact, the value of a pixel in a hue image depends only on the shape of the original 3-band spectral shape of this pixel according to formula (3-31).

3.3.2 RGB false colour composition using hue images

Three separate hue images can be derived from three different band-triplets of a multi-band imagery. In each hue image, the brightness (the pixel DN value) changes with hue which is determined by the spectral shape of the source band-triplet. If the three hue images are displayed in red, green and blue using a RGB additive colour display system, a hue RGB (HRGB) false colour composite image is produced (Figure 3-13). Different colours in a HRGB image are controlled by the variations in brightness among the three component hue images. A HRGB image can therefore incorporate spectral information from up to nine image bands. Pixel colours in a HRGB image are unique representations (codes) of the shapes of the spectral signatures of all the original image bands used.

Selecting three band-triplets for HRGB colour composition is not as simple as selecting three bands, directly based on IOBS, for ordinary colour composition. For producing a colourful and informative HRGB colour composite, we need to select three band-triplets from which three hue images with low IOBS can be derived. For Landsat TM imagery, as there are only seven bands, it is inevitable to re-use some bands in different band-triplets for producing a HRGB image. This may cause high correlation among three hue images derived from

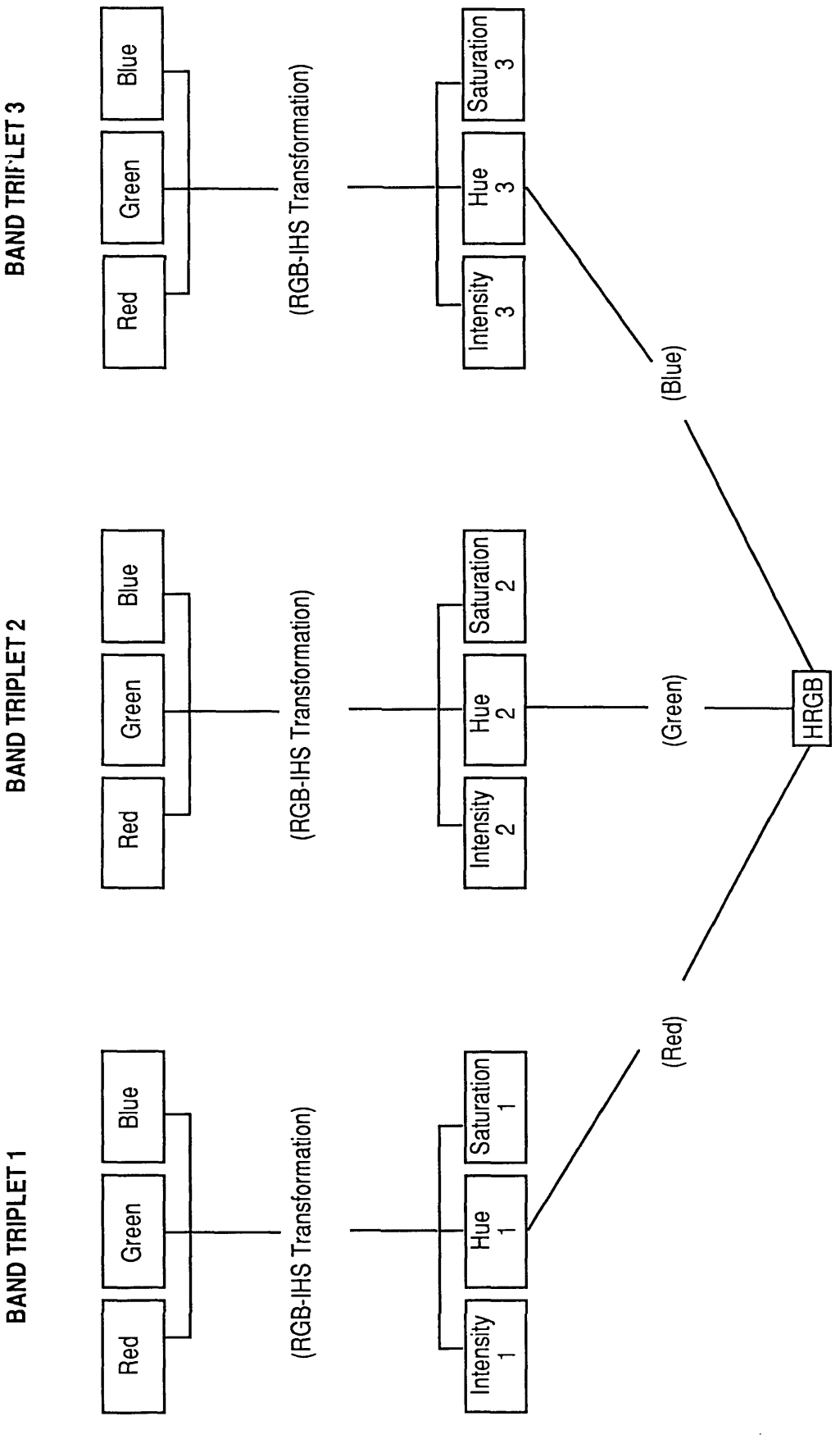


Figure 3-13: Diagram of the procedure for producing an HRGB image

Table 3-7: Correlation and IOBS of three hue image groups derived from TM band- triplets of the test site with lowest IOBS

Correlation coefficients		IOBS
H651 & H671	0.7754	
H651 & H652	0.9523	0.7937
H671 & H652	0.7589	
H541 & H741	0.5299	
H541 & H531	0.9411	0.6480
H741 & H531	0.5059	

three band-triplets even though the IOBS of each triplet is low. As shown in Table 3-3, the three band-triplets with lowest IOBS of the TM subscene of the test site are 1 5 6, 1 6 7 and 2 5 6 or, if not including the thermal band, 1 4 5, 1 4 7 and 1 3 5. In each case, only five of the seven TM bands are used and the derived hue images are highly correlated (Table 3-7). To use all the seven TM bands with the minimum band re-use, three spectrally continuous band-triplets each comprising three spectrally adjacent bands: 6 7 5, 5 4 3 and 3 2 1 are recommended for deriving three hue images for HRGB colour composition (Table 3-8). As the effects of atmospheric scattering in adjacent bands are similar, very effective elimination of shadows can be achieved. The band re-use among these band-triplets also makes it easy to derive spectral shapes from three hue image values as discussed in Chapter 5. The hue images derived from these band-triplets of the TM subscene of the test site have a very low IOBS (0.3507) and produce the best HRGB image for lithological interpretation and classification in the study area as presented in Chapter 6.

BCET enhancement is a necessary preparation for producing a high quality HRGB image as the balanced colours in a colour composite of a band-triplet will result in a hue image with a wide value range. Such a wide value range

Table 3-8: The suitable band-triplets for deriving an HRGB image from Landsat TM imagery

RGB-IHS transformation			HRGB composition	
R	G	B	Hue image	Colour
TM6	TM7	TM5	Hue675	R
TM5	TM4	TM3	Hue543	G
TM3	TM2	TM1	Hue321	B

is the result of more of the spectral information of the source bands being concentrated in the hue component rather than the intensity and saturation components. It is fundamentally different from the wide value range achieved by stretching the hue image itself because the stretching cannot increase the spectral information of the hue image.

3.4 Summary

Three new image processing techniques, IOBS, BCET and HRGB, are presented in this chapter. Initially, these techniques were developed for preprocessing to prepare shadow free and spectrally well enhanced imagery for spectral classification. However, these techniques can be used independently for general image enhancement.

The index of optimal band-triplet selection (IOBS) is an effective statistical procedure for selecting optimal band-triplet from a multi-band imagery for colour composition. IOBS is based only on the inter-band correlation, thus it is stable under linear stretch and reliable for predicting the optimal band-triplets for colour composition. The best band-triplet of the TM image of the study area in SE Spain selected by IOBS is TM5, TM4 and TM1.

The balance contrast enhancement technique (BCET) is an excellent technique for contrast enhancement. It stretches or compresses an image to a user specified value range and mean without changing the information of the image, thus the contrast and average brightness of the enhanced image can be fully controlled. Processing speed of BCET is high (faster than histogram equalization). An advantage of BCET is that it can remove colour bias in a colour composite by stretching/compressing three bands to an equal value range and mean. As the result, high quality colour composites can be achieved easily by BCET.

Two BCET techniques, BCETP and BCETC, have been developed. BCETP is based on a parabolic function derived from the statistics of the input image and the minimum, maximum and mean for the output image. BCETC is based on a cubic function derived in a similar way. The images produced by BCETP and BCETC are virtually no different. BCETP is preferred in most cases as it is much simpler and faster than BCETC. BCETC permits a wider range of choices for parameters and therefore can perform balance contrast enhancement in those cases for which BCETP fails.

Hue image RGB false colour composite (HRGB) is a simple and practical technique for multi-band image enhancement and shadow suppression. A colour in a HRGB image is a coding of the shape of a spectral signature of all the image bands used (up to nine). The correspondence between the colours of a HRGB image and the shapes of the spectral signatures of the original bands is unique. HRGB images are shadow free and the spectral discrimination among pixels in a HRGB image is significantly more delicate than can be achieved by colour composite, ratio or band difference images.

HRGB images can only show the difference of the shapes of the spectral signatures of ground objects. They cannot discriminate spectral signatures

with exactly the same shape but different albedos. The shadow suppression capability of HRGB image is base on this property. As a result, HRGB images cannot be used to distinguish among the objects with the same hue but different intensities and saturations under the same illumination.

For Landsat TM imagery, the HRGB image derived from three spectrally adjacent band-triplets: 6 7 5, 5 4 3 and 3 2 1 is recommended for lithology interpretation and classification. HRGB imagery is also potentially useful for other applications where the spectral information is relevant, *e.g.* land use, vegetation, *etc.*.

Chapter 4

A 3-dimensional Feature Space Iterative Clustering Method for Multi-spectral Imagery Classification

Multi-spectral image classification is the core of automatic lithological mapping based on remotely sensed imagery. Unsupervised classification has been used for this study. The accuracy of unsupervised classification is largely dependent on the algorithms and decision rules used. Kittler and Pairman (1986) proposed an advanced decision rule, the Optimal Multiple Point Reassignment (OMPR), in which the cluster size and pixel frequency are taken into account for improving classification accuracy. In Pairman's work (1986), a detail theoretical analysis and comparison between OMPR and other algorithms were presented to prove that OMPR guarantees better convergence to local optimum and thus produces a more accurate classification than other commonly used techniques such as minimum distance, maximum likehood, *etc.*. Unfortunately, Pairman did not use OMPR for his research into cloud classification using AVHRR images (Pairman, 1986) because of the difficulty of adapting OMPR into the traditional pixel by pixel processing method.

This chapter will introduce a new classification technique, Three Dimensional Feature Space Iterative Clustering (3D-FSIC). 3D-FSIC performs clustering iteration in three dimensional feature space rather than by scanning the images pixel by pixel, thus OMPR can be used without difficulty. The 3D-FSIC also includes several new features: a simple procedure for splitting a cluster based on the first principal component without performing principal component transformation and Automatic Seed Selection Technique (ASST). A discussion of clustering classification using hue images is given, after the technical approach.

4.1 Review of the Clustering Algorithm

Iterative clustering is a well established tool for image classification. Let $\mathbf{X}$ be a n-dimensional feature space of n variables $(\mathrm{x}_1, \mathrm{x}_2, ..., \mathrm{x}_n)$, Y_i be an object of an object set Y defined by measurement of the n variables, $(y_{i1}, y_{i2}, ..., y_{in})$, $i = 1, 2, ..., N$. N is the total number of the objects in Y. In the feature space $\mathbf{X}$, the object Y_i is represented by an observation vector, *i.e.* a data point $\mathbf{X}_j$ at the coordinates $(x_{j1}, x_{j2}, ..., x_{jn})$, $j = 1, 2, ..., M$. M is the total number of the data points representing N objects and $M \leq N$. If $\mathbf{X}$ is an Euclidean space then $x_{jh} \sim y_{ih}$, $h = 1, 2, ..., n$. The goal of the clustering process is to identify the objects of set Y in m clusters. This is equivalent to the partition of the relevant data points in feature space $\mathbf{X}$ into m spatial clusters (Devijver & Kittler, 1982). Diday (1976) summarized two principal iterative clustering algorithms labeled α and β.

Algorithm α

1. **Initialization** Let m elements Y_q of Y, chosen at random, be the 'representation' of the m clusters. Let us call them $\omega_1, \omega_2, ..., \omega_k, ..., \omega_m$.

2. **Clustering** For all i, assign any element Y_i ($Y_i \in Y$) to cluster ω_k, if $\delta(Y_i, \omega_k)$ (the dissimilarity measurement) is minimum.

3. **Update Statistical representation** For all k, new statistics of cluster ω_k are computed as the renewed representation of cluster ω_k.

4. **Stability** If no ω_k has changed stop, else go to 2.

Algorithm β

1. Same as *Step 1* of α.

2. One element Y_i ($Y_i \in Y$) is assigned to cluster ω_k, if $\delta(Yi, \omega_k)$ is minimum.

3. A new representation of ω_k is computed based on all the elements of cluster ω_k, including the last element.

4. If all elements Y_i ($Y_i \in Y$) have been put into a cluster then stop, else go to 2.

For image classification, the clustering in both algorithms is executed on object set Y, *i.e.* the image. The processing is done pixel by pixel by scanning the image.

One of the most popular clustering algorithms for image classification, the ISODATA algorithm (Ball, 1965; Ball & Hall, 1967) is a particular case of algorithm α in which the dissimilarity measure $\delta(Y_i, \omega_k)$ in *step 2* is the square Euclidean distance:

$$d(Y_i, \mu_k) = (Y_i - \mu_k)^t (Y_i - \mu_k)$$

where μ_k is the mean vector of cluster ω_k.
Cluster splitting and merging functions can also be added in ISODATA after *step 3* of algorithm α.

The assumption underlying this simple and efficient technique is that all the clusters have an equal variance and population. However, this is generally not true in image classification, which results in low classification accuracy in many cases. To improve ISODATA, more sophisticated measures of dissimilarity, such as maximum likehood estimation and population weighted measurement (Sclove, 1983; Pairman, 1986), have been introduced. For all these different decision rules within the ISODATA frame, the processing is realized by image scanning. This processing method is infeasible for OMPR because all the pixels having the same DN values in each band must be considered simultaneously. To handle this problem, a 3 Dimensional Feature Space Iterative Clustering method (3D-FSIC) has been developed.

4.2 Three Dimensional Feature Space Iterative Clustering Method

4.2.1 Principle of Feature Space Iterative Clustering (FSIC)

Both algorithm α and β can be realized in feature space $\mathbf{X}$ rather than object set Y by handling data point $\mathbf{X}_j$ instead of object Y_i at each step of the two algorithms, which are then called as feature space iterative clustering (FSIC) algorithms. For image classification, the object set Y is a multi-spectral image and an object Y_i a pixel with DN values $(y_{i1}, y_{i2}, ..., y_{in})$. All the pixels with equal DN values in each band (no matter their locations in the image) will be represented by one data point in feature space $\mathbf{X}$. Such a point is called a multiple point. If a multiple point $\mathbf{X}_j$ is assigned to a cluster ω_k, all the pixels sharing this point will be assigned to cluster ω_k simultaneously.

The processing speed of FSIC is almost unaffected by the image size because

the image size generally changes only the frequencies of the multiple points not the number of effective data points. However, increasing the number of dimensions and the number of quantisation levels of each band will increase the memory space requirement dramatically and slow down the processing speed. Thus the algorithm is probably only practical for no more than three dimensions (bands) with 7 bits or less quantisation. Fortunately, three band classification is generally preferred in the classification of remotely sensed images as the result can be compared directly with the colour composite of the three bands used. The effective value range of commonly used remote sensing images (*e.g.* MSS, TM, SPOT, *etc.*) can generally be adjusted into a 7 bits value range even though the theoretical value range of TM and SPOT is much wider.

4.2.2 The 3D-FSIC method

A practical Three Dimensional FSIC (3D-FSIC) method based on algorithm α has been developed and used successfully for image classification (Liu and Haigh, 1990). The structure of the 3D-FSIC is as below:

Step 1. Create a 3D scattergram of the input image

Read the input image Y pixel by pixel and record the pixel frequencies in a 3D scattergram, *i.e.* a 3D array:

$$G(d1 \times d2 \times d3)$$

where $d1, d2$ and $d3$ are the array sizes of the 3 dimensions or the maximum DN values of the 3 bands of the image Y.

The value of any element g_j in G indicates how many pixels share the point $\mathbf{X}_j$ at the coordinates (x_{j1}, x_{j2}, x_{j3}) in the 3D feature space $\mathbf{X}$ or the number of pixels with the same DN values as pixel Y_i in the image Y, where $y_{ih} \sim x_{jh}, h = 1, 2, 3$ (Figure 4-1).

Step 2. Initialization

Select m points in the 3D feature space $\mathbf{X}$ as the "seeds" (initial kernels) of m clusters and call them ω_k, $k = 1, 2, ...m$. The choice could be made at random. In this study, however, an automatic seed selection technique (see 4.4) based on 3D peak frequency point selecting (Letts, 1978; Richards, 1986) is used in the 3D-FSIC programme in order to speed up the convergence of the clustering.

Step 3. Feature space clustering

For all j, assign any point $\mathbf{X}_j$ ($\mathbf{X}_j \in \mathbf{X}, j = 1, 2, ..., m$) to cluster ω_k if the dissimilarity $\delta(\mathbf{X}_j, \omega_k)$ is minimum. Thus all the pixels sharing the point $\mathbf{X}_j$ are assigned to cluster ω_k simultaneously. N_k, the size of cluster ω_k increases by the value of g_j while, if it is a reassignment, the size of the cluster to which $\mathbf{X}_j$ was formerly assigned decreases by the same value. The cluster sequential number k of point $\mathbf{X}_j$ is recorded by a 3D feature space partition array:

$$P(d1 \times d2 \times d3)$$

in the element p_j at the coordinates (x_{j1}, x_{j2}, x_{j3}) (Figure 4-2).

Step 4. Update the statistical representation of each cluster

For all k ($k = 1, 2, ..., m$), statistical parameters, such as mean vector μ_k, covariance matrix Σ_k, *etc.*, are calculated. These parameters are the new representation of cluster ω_k.

Step 5. Stability

For all k ($k = 1, 2, ..., m$), if the maximum spatial migration of the mean vector μ_k (the kernel of the cluster) is less than a user controlled criterion, go to *Step 7*, else go to *Step 6*.

Step 6. Cluster splitting and merging

Split the over large and elongated clusters and merge the clusters too close to each other according to user controlled criteria and update the statistical

representations of the new clusters. Go to *Step 3.*

Step 7. Transfer the clustering result from feature space to an image
Read the image Y pixel by pixel. For all i, assign a pixel $Y_i(Y_i \in Y, i = 1, 2, ..., N)$ to cluster ω_k if its relevant data point $\mathbf{X}_j$ in feature space $\mathbf{X}$ is assigned to this cluster according to the record in the feature space partition array P, *i.e.*

$$Y_i \longrightarrow \omega_k \qquad if \qquad p_j = k$$

where p_j is at the coordinates (x_{j1}, x_{j2}, x_{j3}) in P and $y_{ih} \sim x_{jh}$, $h = 1, 2, 3$.

The 3D-FSIC can also be configured in the similar way based on the algorithm β.

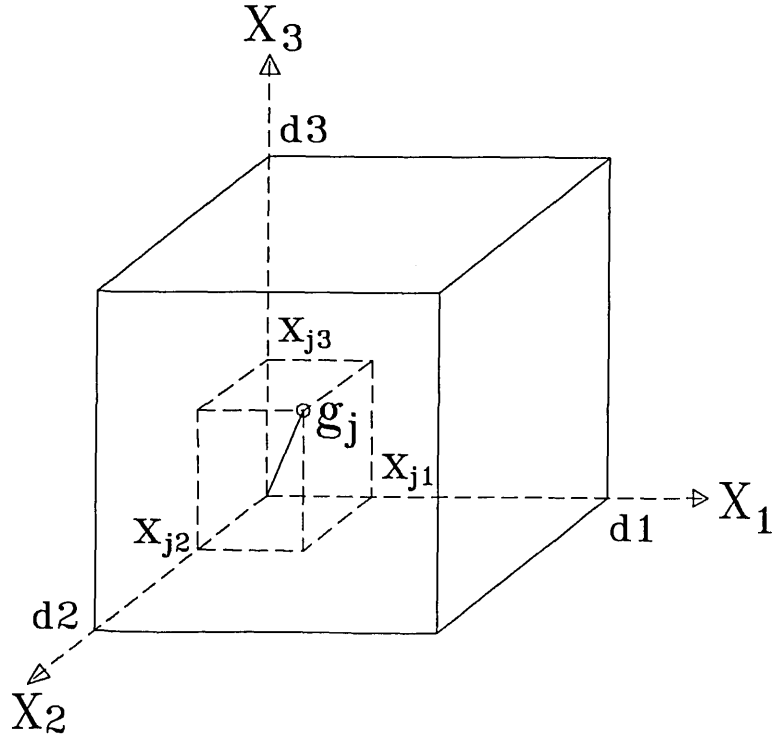


Figure 4-1: The 3D scattergram

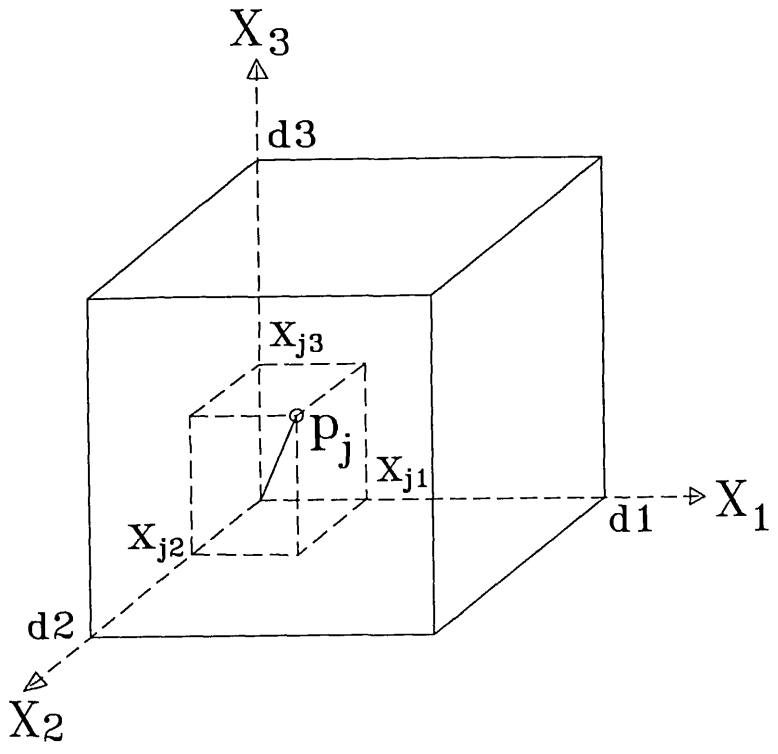


Figure 4-2: The 3D feature space partition array

4.2.3 Review of optimal multiple point reassignment

An advantage of 3D-FSIC is that the optimal multiple point reassignment (OMPR) rule can be used in a practical way if we let $\delta(\mathbf{X}_j, \omega_k)$ be an OMPR dissimilarity measurement at the *Step 3* of 3D-FSIC. The OMPR was developed by Kittler and Pairman (1986) based on the optimal point assignment rule (Macqueen, 1967). By using OMPR, the cluster sizes and the number of the pixels sharing the same point in feature space are taken into account when a reassignment of these pixels is made. Thus the accuracy of the clustering partition can be reasonably improved.

Suppose point $\mathbf{X}_j$ currently allocated to cluster ω_l is shared by h pixels, the OMPR based on square Euclidean distance (Euclidean OMPR) for all these pixels from cluster ω_l to cluster ω_k will be achieved if ω_k satisfies:

$$\frac{N_k}{N_k + H} d(\mathbf{X}_j, \mu_k) = \min_{r \neq l} \frac{N_r}{N_r + H} d(\mathbf{X}_j, \mu_r) < \frac{N_l}{N_l - H} d(\mathbf{X}_j, \mu_l) \qquad (4-1)$$

where N_r is the pixel number of any a cluster ω_r.

If the clusters are assumed to have a normal distribution (Gaussian model), the Gaussian OMPR is:

assign $\mathbf{X}_j$ in ω_l to cluster ω_k if

$$\begin{aligned}\delta(\mathbf{X}_j,\omega_k) &= \min_{r\neq l}\delta(\mathbf{X}_j,\omega_r)\\ &< log|\Sigma_l| - \frac{N_l-H}{H}log[1-\frac{H}{N_l-H}\Delta(\mathbf{X}_j,\omega_l)]\\ &- 2log\frac{N_l}{N} - (D+2)\frac{N_l-H}{H}log\frac{N_l}{N_l-H} \qquad (4\text{-}2)\end{aligned}$$

where

$$\begin{aligned}\delta(\mathbf{X}_j,\omega_r) &= log|\Sigma_r| + \frac{N_r+H}{H}log[1+\frac{H}{N_r+H}\Delta(\mathbf{X}_j,\omega_r)]\\ &- 2log\frac{N_r}{N} + (D+2)\frac{N_r+H}{H}log\frac{N_r}{N_r+H} \qquad (4\text{-}3)\end{aligned}$$

$$\Delta(\mathbf{X}_j,\omega_r) = (\mathbf{X}_j-\mu_r)^t\Sigma_r^{-1}(\mathbf{X}_j-\mu_r) \qquad (4-4)$$

Σ_r is the covariance matrix of cluster ω_r,

$|\Sigma_r|$ is the determinant of Σ_r,

D is the dimensionality of the feature space $\mathbf{X}$ or the number of the bands of the image Y.

Pairman (1986) proposed that OMPR be used within the frame of algorithm β. However, OMPR was not used in the image classification in that work because of the difficulty of realizing it with the pixel by pixel processing method.

In the FSIC method, OMPR technique can easily be adapted into either the α or β frameworks. The 3D-FSIC uses the algorithm α as this allows cluster splitting and merging functions which give more user control and guarantee more optimal convergence (Devijver & Kittler, 1982) in an unsupervised classification.

4.2.4 The 3D-FSIC software

The general features of the 3D-FSIC software are as following:

1. An automatic seed selection procedure is performed by ASST (see 4.4 for detail) before clustering to provide the initial centres of clusters ('seed') for clustering.

2. To speed up the classification and save memory space, a parameter enables users to compress the quantisation of the images to be classified. The image quantisation should not higher than 7 bits (0-127) and 6 bits (0-63) is recommended.

3. A cluster will be split if the length of the major diagonal line of the cube defined by the three standard deviations (SD) of this cluster is longer than a user specified criterion (SPLIT):

split cluster ω_r if

$$\sqrt{S_{(r)11} + S_{(r)22} + S_{(r)33}} > SPLIT \qquad (4-5)$$

where $S_{(r)11}$, $S_{(r)22}$ and $S_{(r)33}$ are the variances of the cluster ω_r in its three dimensions.

4. The clusters will be united if the Euclidean distance between the centres of two clusters is less than a user specified criterion (UNITE):

unite cluster ω_k and ω_l if

$$d(\mu_k, \mu_l) = (\mu_k - \mu_l)^t(\mu_k - \mu_l) < UNITE \qquad (4-6)$$

An advantage of such a simple judgement for cluster merging is that it only permits small clusters to be united because the centres of two large clusters generally cannot be very close to each other. The splitting and uniting functions enable user to control the maximum and minimum spatial sizes of the

clusters generated by 3D-FSIC.

5. Users can use either minimum Euclidean distance, Euclidean OMPR or Gaussian OMPR to perform the iterative clustering classification. The processing speed of Gaussian OMPR is much slower than Euclidean OMPR which is almost as fast as minimum Euclidean distance. Thus, for reasonable accuracy and high processing speed, Euclidean OMPR is generally preferred. The software also permits the hybrid iteration procedure. A user can start the classification with minimum distance iteration and then Euclidean OMPR and finally Gaussian OMPR.

6. The clustering iteration will be terminated when either the maximum iteration times has elapsed or the maximum migration of cluster centres is less than the user specified criterion. The DN values in the resulted classification image are the class label numbers.

7. A class statistical file will be generated, in which the mean vector, covariance matrix, pixel number and the inter-band correlation coefficients of each class are provided.

4.3 A Cluster Splitting Technique Based on the First Principal Component

In unsupervised clustering partition, very large clusters may result. Such a large cluster may contain several objective classes. Thus a function for cluster splitting is necessary to achieve more optimal convergence (Devijver and Kittler, 1982). In ISODATA, an over large and elongated cluster ω is split according to the variable with largest standard deviation. The objects of cluster ω are reassigned to either of two new clusters $\omega 1$ and $\omega 2$ depending on

whether their values of the splitting variable are above or below the mean of the splitting variable (Anderberg, 1973). As shown by the two dimensional case in Figure 4-3, splitting in this way may cause incorrect assignments of those objects in the shaded area in Figure 4-3. They are assigned to a new cluster further from them rather than closer. This error can be avoided if the cluster ω is split according to its first principal component ($PC1$). As $PC1$ can be found without performing a principal component transformation, not too many calculations are involved. This new technique for cluster splitting includes two steps: finding the $PC1$; and cluster splitting based on $PC1$.

Find the first principal component $PC1$

If the cluster ω is a normal distribution, its covariance matrix Σ is positive. Thus the first eigenvalue and eigenvector of Σ, λ_1 and $\mathbf{a} = (a_1, a_2, ..., a_n)^t$, can be found by the iteration defined below.

$$\Sigma \mathbf{a}^{(s)} = \lambda_1^{(s+1)} \mathbf{a}^{(s+1)} \tag{4-7}$$

$$\mathbf{a}^{(0)} = \mathbf{I} \tag{4-8}$$

where s is the iteration number and $\mathbf{I}$ is the unit vector. the $\mathbf{a}$, as an eigenvector, is orthogonal; thus for all s

$$(\mathbf{a}^{(s)})^t \mathbf{a}^{(s)} = 1 \tag{4-9}$$

Let

$$\Sigma \mathbf{a}^{(s)} = \lambda_1^{(s+1)} \mathbf{a}^{(s+1)} = \mathbf{b}^{(s)} \tag{4-10}$$

thus

$$\lambda_1^{(s+1)} = \sqrt{(\mathbf{b}^{(s)})^t \mathbf{b}^{(s)}} \tag{4-11}$$

$$\mathbf{a}^{(s+1)} = \frac{\mathbf{b}^{(s)}}{\lambda_1^{(s+1)}} \tag{4-12}$$

After 5-6 iterations the convergence with accuracy higher than 10^{-5} will be achieved and the first eigenvalue (λ_1) and eigenvector (a) are found. Thus in the n dimensional feature space $\mathbf{X}$, the first principal component of cluster ω is

$$PC1 = (\mathbf{a})^t\mathbf{X} = \sum_{h=1}^{n} a_h x_h \qquad (4-13)$$

Cluster splitting

According to formula (4-13), the $PC1$ coordinate of the mean vector $\boldsymbol{\mu} = (\mu_1, \mu_2, ..., \mu_n)^t$ of cluster ω is

$$\mu_{PC1} = (\mathbf{a})^t\boldsymbol{\mu} = \sum_{h=1}^{n} a_h \mu_h \qquad (4-14)$$

For every data point $\mathbf{X}_j \in \omega$ calculate its $PC1$ coordinate:

$$x_{j,PC1} = (\mathbf{a})^t\mathbf{X}_j = \sum_{h=1}^{n} a_h x_{jh} \qquad (4-15)$$

Assign $\mathbf{X}_j$ to $\omega 1$ if $x_{j,PC1} > \mu_{PC1}$ otherwise assign $\mathbf{X}_j$ to $\omega 2$.

Cluster splitting can also be performed on the objects instead of data points by replacing $\mathbf{X}_j$ by $Y_i, (i = 1, 2, ..., N)$ in formula (4-15).

After the cluster splitting, the statistics of the two new clusters are calculated as their representations for the next clustering iteration.

4.4 Automatic Seed Selection Technique (ASST)

The ASST is developed based on the principle of Letts' histogram peak selection clustering method (Letts, 1978; Richards, 1986)).

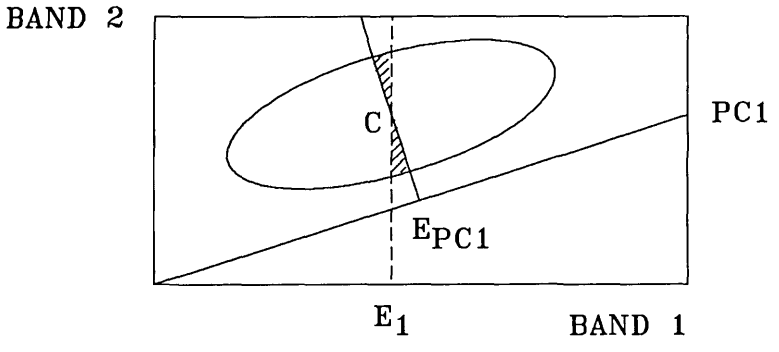


Figure 4-3: A two dimensional example of cluster splitting. C is the centre of the cluster, E_1 the mean of band 1 and E_{PC1} the mean of $PC1$. The dashed line splits the cluster according to band 1 while the solid line splits the the cluster according to the $PC1$.

In the 3D scattergram of the three images for classification, data will exhibit peaks or the points of high frequency at the locations of spectral clusters. It is thus reasonable to use these points as the initial kernels of clusters to start iterative clustering.

Such a peak point has two properties: 1) higher frequency than all its adjacent neighbour points in the feature space and 2) relatively high frequency in the 3D scattergram. The two properties are to be used to locate peak points. It is important to keep in mind that the data and scattergram of multi-spectral imagery are discrete and, even more, the increment of DN value of an image may not necessarily be unity especially after enhancement processing. For instance, when an image of 7 bits DN value range [0, 127] is linearly stretched to 8 bits DN value range [0, 255], the increment of DN values will become to 2. In this case, any non-zero frequency DN value in the original image will have two adjacent zero frequency DN value as shown in Figure 4-4. Fortunately, such

pseudo peaks can be easily prevented by compressing the image value range (*i.e.* reducing image quantisation). With these considerations, ASST includes following operations:

1. Reduce image quantisation of the three images for classification by a user defined scaling factor. For an 8 bit (0-255) image, a scaling factor 4 is proper. It reduces the image quantisation to 6 bits (0-63).

2. Locate first N points of highest frequency from 3D scattergram. N can be decided by setting a criterion frequency or based on experience and experiment. For a 6 bits image, 256 is suggested. This operation will prevent selection of isolated low frequency points (often representing noise) as seeds and thus satisfy property 2.

3. For each of the 256 points, $\mathbf{X}_j$, check all of its 26 adjacent points, $\mathbf{X}_l$, and locate it as a seed if its frequency, g_j, is higher than that of its neighbours (g_l) (Figure 4-5). *i.e.*

$\mathbf{X}_j = (x_{j1}, x_{j2}, x_{j3})$ is a peak if $g_j > g_l$ for all $\mathbf{X}_l = (x_{l1}, x_{l2}, x_{l3})$ where

$x_{l1} = x_{j1} - 1, x_{j1} + 1;\ x_{l2} = x_{j2} - 1, x_{j2} + 1;\ x_{l3} = x_{j3} - 1, x_{j3} + 1$

This operation is based on the property 1.

4. Convert the coordinates of seeds to the same quantisation as the one applied in 3D-FSIC.

There is no user input parameter to control the seed number in ASST. How many seeds can be selected by ASST is dependent on the data distribution of the image used for classification.

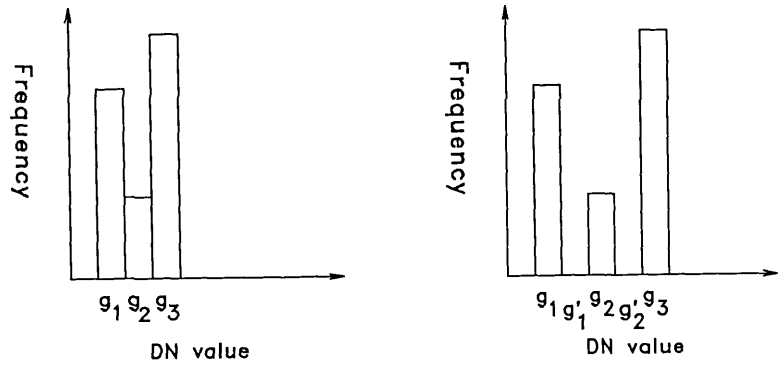


Figure 4-4: An illustration of a pseudo peak caused by linear stretch. *Left:* The histogram before linear stretch: g_2 is a dip as $g_2 < g_1$ and $g_2 < g_3$. *Right:* The histogram after linear stretch: g_2 becomes a pseudo peak as $g_2 > g_{1'}$ and $g_2 > g_{2'}$.

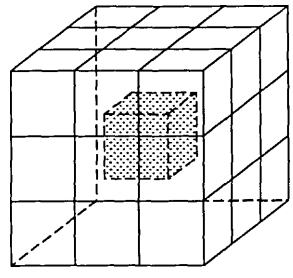


Figure 4-5: The cell in the centre (shaded) represents the data point $\mathbf{X}_j$, and all the other cells in the cube are its adjacent data point, $\mathbf{X}_l$.

4.5 Classification Using Hue Images by 3D-FSIC

For multi-spectral image classification, a limitation of 3D-FSIC is that only three bands can be used. This limitation can be partly remedied by using hue images derived from original image bands instead of using the bands directly.

A hue image derived from three bands by RGB-IHS transformation is shadow (a major obstacle of multi-spectral classification) free because the pixel values of the hue image are independent of illumination and related only to the spectral shapes of the three bands used (Liu Jian Guo, 1990). Thus a hue image incorporates the spectral information of its three source bands. A classification of three hue images derived from three band-triplets (up to nine bands) is actually based on the spectral information of up to nine bands.

The saturation component is related to both illumination and spectral information. Thus some residual shadow effects will be shown in saturation images. For this reason, the saturation component is not considered for classification even though it contains some spectral information.

The automatic lithological mapping in this research project is based on the classifications of HRGB images derived from a Landsat TM image by the pre-classification enhancement described in Chapter 3.

4.6 Summary

In commonly used iterative clustering techniques for image classification, processing is executed pixel by pixel. The advantage of this processing style is that it can handle images with many bands and high data quantisation. However, it is difficult to take the cluster size and pixel frequency into account

and therefore cannot use a more advanced technique, the optimal multiple point reassignment (OMPR). The problem is solved by carrying on the iterative clustering in feature space but in practice, feature space iterative clustering (FSIC) is feasible only for image data of no more than three bands and with relatively low quantisation (less than 8 bits).

A practical three dimensional feature space iterative clustering (3D-FSIC) method for image classification is introduced after a general discussion of the FSIC algorithm. In 3D-FSIC, an image (three bands) is read into a three dimensional scattergram thus the information of the image is stored as data points in the 3-D feature space. The iterative clustering based on the scattergram is then performed. In the clustering, all the pixels sharing the same data point in feature space (the pixels having corresponding DN value in each band) are assigned to a cluster by one action. Thus the OMPR decision rule can be easily realized in 3D-FSIC. The cluster assignment for each point is recorded by a 3-D feature space partition array and updated every iteration. When the iterative clustering is terminated, the result is converted back to an image by reading the input image and assigning each image pixel to a cluster according to the record in the element allocated by the three DN values of this pixel in the partition array. The processing speed of 3D-FSIC is almost unaffected by image size. It is fast and economic especially for large and low quantisation images.

As an improvement, a new technique of cluster splitting has been developed. It splits an elongated cluster according to the first principal component ($PC1$) of this cluster. As the first eigenvalue and eigenvector of the covariance matrix of the cluster can be found by a simple iteration method, the $PC1$ can be derived without performing the computationally expensive PC transformation. Then, the $PC1$ values of the mean vector (mean of $PC1$) and all the data points (or pixels) of the cluster are calculated. Finally, the cluster is split into

two according to whether the $PC1$ value of a data point (or a pixel) is greater or less than the mean of $PC1$.

An automatic seed selection technique (ASST) is also introduced, which locates high frequency points in 3D scattergram as the initial cluster centres for iterative clustering classification.

To remedy the dimension limitation of 3D-FSIC and get rid of shadow effects, three hue images derived from original image bands can be used instead of the original bands. In this way, the classification performed by 3D-FSIC will incorporate the spectral information from up to nine bands.

Chapter 5

Techniques for Post-processing and Analysis of Spectral Classification

Multi-spectral classification techniques have been used to abstract thematic information from remotely sensed multi-spectral imagery for various applications such as land use, forestry, meteorology and geology. A classification image cannot generally be used as a thematic map, directly, for practical applications because it includes too much spatial detail and thus lacks spatial continuity.

A thematic map should not be a precise copy of the phenomena of the mapped terrain types. It is an artificially simplified product derived from raw data based on specific knowledge and application requirements such as accuracy and simplicity. A class patch in a map must be large enough to be easily recognized by the eye and different classes must be clearly separated by boundaries. A good map of a certain scale should include no more details than necessary and, at the same time, should be objective and accurate enough for applications at the corresponding map scale. To produce practical thematic maps from classified images, proper post-processing of spectral classification is necessary.

The importance of post-processing has been emphasized by many authors (Schowengerdt, 1983; Mather, 1986). The most popular techniques are those based on contextual information, such as majority filtering (Goldberg *et al.*, 1975) and the minimum area rationale (Davis and Peet, 1977). This chapter will describe a series of techniques for post-processing in a sequence for thematic mapping. Applications of these techniques will be illustrated in Chapter 6 and Chapter 7.

New techniques will be introduced, including the template histogram matching and class boundary detection. Iterative majority filtering and small class merging techniques will be presented, based on the review of contextual filtering and re-classification. For further simplification of a classification image based on user knowledge, interactive class editing programmes are provided together with a colour painting technique which is used as a map editing tool rather than simply for colour display. To add topography back to a classification image, an intensity modulation technique based on Crippen's method (1988) is discussed. Spectral analysis is essential for class identification and editing of unsupervised classification. Two simple methods for deriving class spectral shapes are presented as the final part of this chapter.

5.1 Template Histogram Matching Classification (THMC) Technique

In a multi-spectral classification image, different classes may occur in regular spatial frequency and form certain textures or patterns. This spatial information is useful for discriminating those terrain types corresponding to textures or patterns rather than to individual spectral classes but not utilized during the multi-spectral classification. It is relatively simple and very beneficial to use the spatial information to re-classify a classification image so as to increase

the thematic information for the mapping. Template histogram matching classification (THMC) is a simple technique to detect textures/patterns formed by the combinations of different DN values with certain spatial frequencies. The technique is based on the principle of template matching (Duda, 1973) and can be used on either classification images or original images. The THMC comprises two steps: template histogram training and matching classification.

Template histogram training

Training areas representing the textures of interested terrain types are selected from an image Y. For any training area $Y_k(\in Y)$ of a texture k, the histogram $H_k(h)$ ($h = 0,1,2,...,NC$; NC is the maximum DN value of the image or the number of classes in a classification image.) is calculated over all the pixels in the training area Y_k. $H_k(h)$ is then standardized for a given template window which is used to scan the image for detecting texture k:

$$SH_k(h) = \frac{H_k(h) \times ws \times wl}{S_k \times L_k} \qquad (5-1)$$

$$h = 0,1,2,...,NC$$

where SH is the standard histogram, ws and wl are the numbers of the samples and lines of the window and S_k and L_k are the numbers of the samples and lines of the training area Y_k.

$SH_k(h)$ will be used as a standard histogram of texture k in matching process. For a classification image, $SH_k(h)$ defines how the texture k is composed by different classes.

Template histogram matching

For every pixel $y(i,j)$ of image Y, the histogram $H_{ij}(h)$ is calculated over all the pixels in the $ws \times wl$ window centred at $y(i,j)$. Then the cumulative

difference between $H_{ij}(h)$ and $SH_k(h)$ is obtained from the formula below:

$$D_k(i,j) = \sum_{h=0}^{NC} |H_{ij}(h) - SH_k(h)| \qquad (5-2)$$

The values of $D_k(i,j)$ vary from 0 to $2 \times ws \times wl$ indicating perfect matching to irrelevant. For all the n possible textures represented by $SH_k(h)$ ($k = 1,2,...,n$), calculate $D_k(i,j)$ and pixel $y(i,j)$ will be assigned to a texture l if:

$$D_l(i,j) = \min_{k=1,2,...n} D_k(i,j) \leq cr \qquad (5-3)$$

where cr is a user control criterion.
The pixels which cannot satisfy the formula (5-3) will remain unchanged.

Discussion

Since the matching is based on the shapes of the histograms, no numerical calculation of DN values is involved. This property is especially suitable for classification images in which the DN values are simply the labels of classes without numerical meaning.

The window size ws and wl are very important since they control the spatial frequency of the texture to be detected. The larger the window, the lower frequency texture can be detected. By using a large window, all the textures formed by the same group of DN values (or classes) in the different spatial frequencies not less than the window size may be recognized as one texture. To solve the problem, windows of increasing size can be used, with proper logic operations, to perform THMC several times on the image. For example: if there are three pixel lines each with a particular pattern:

(a) 123123123123123123
(b) 112233112233112233
(c) 12345123451234512345

Pattern (a) will be detected if $ws = 3$. But several pixels of pattern (c) will be mistaken as a). Pattern (b) will be detected when $ws = 6$. But all the pixels of (a) will be mistaken as (c). Pattern (c) will be detected unambiguously when $ws = 5$. The mis-classification can be avoided by using the three window sizes sequentially. Firstly, let $ws = 3$. The pattern (a) is detected with several mis-classified pixels of pattern (c). Then let $ws = 5$ and for all the pixels belong to both (a) and (c), re-assign them to (c), thus the mistakes made by last step are corrected and pattern (c) is detected. Finally, let $ws = 6$ and all the pixels belong to (b) only will be assigned to (b), and pattern (b) is detected.

5.2 Iterative Majority Filtering (IMF)

Multi-spectral classification images often have a broken and noisy appearance because of many isolated class pixels that usually caused by noise. As indicated by Schowengerdt (1983), it is reasonable to expect some degree of spatial correlation in land surface cover from pixel to pixel. This correlation can be used to eliminate the isolated mis-classifications and produce a smoothed map. The majority filtering (MF), introduced by Goldberg *et al.* (1975), is a simple technique for smoothing classification images. The principle of MF is to re-assign a pixel at the centre of a window used for scanning the classification image to a majority class of all the pixels in the window. If there is no a majority class, then the centre pixel will remain unchanged. The majority class can be determined as the class with the maximum number of pixels within a window or the class with more pixels than a user specified criterion. For a 3×3 window, 5 is the least absolute majority number. There are several modifications of MF (Thomas, 1980; Mather, 1986). An iterative 3×3 window majority filtering (IMF) technique is used in this study. With a basic 3×3 window, the majority filtering will be performed several iterations by IMF to smooth a classification image. Thus, with a simple program structure, IMF can somewhat simulate the MF with the windows of increasing sizes (*e.g.* 3,5,7,...)

without excessive loss of image detail as large windows do. Generally, if the criterion for majority is not less than 6, the smoothing will converge (the image will no longer be affected by majority filtering except for the single pixel width linear feature) after few iterations. Otherwise, the IMF will keep smoothing zigzag boundaries and removing small class patches.

5.3 Small Class Merging (SCM)

In a classification image, some classes may be composed mainly of scattered noise pixels. Such classes may become very small after IMF even if they used to be quite large classes. If a small class does not represent an important terrain type for the thematic mapping and if its spatial distribution does not form class patches large enough for easy visual recognition on the scale of the mapping, it is reasonable to eliminate it. A contextual and spectral small class merging (SCM) procedure is introduced in this study. It includes following steps:

1. Input the classification image Y, the file of mean vectors of all the classes and the criterion for determining a small class.

2. Calculate the distance d_{ij} between every class pair (class i and class j) and store the distance data in a distance table.

3. Scan the image by a 3×3 window, if the centre pixel belongs to a small class i according to the criterion, re-assign the pixel to a large class j of its neighbour pixels if d_{ij} is minimum among all the distances between this small class i and the large classes of the pixels in the window. If none of the pixels in the window belongs to a large class, the centre pixel is simply re-assigned to a spectrally nearest large class according to the distance table. If the centre pixel belongs to a large class, move to next pixel.

SCM processing must be applied after majority filtering or installed in IMF at the final iteration. The processing is very fast as it uses a look up table of

between class distances. Generally, if the criterion for small classes is appropriate, there will be little difference (undetectable to the naked eye) between the images with and without SCM processing. The pixels of small classes will be locally merged with large classes.

5.4 Interactive Class Editing

IMF and SCM are automatic techniques to simplify a classification image based on statistics. In the following cases, which are not unusual in thematic mapping based on classification, interactive class editing with the supervision of user knowledge is necessary.

The correlation between terrain types and spectral classes is often not simple. For the case of several spectral classes corresponding to the same terrain type (this occurs when the inner variation of a terrain type is larger than the splitting criterion in clustering classification), the problem can easily be solved by amalgamating these spectral classes into one class based on field or map information and analysis of class spectral shapes derived from the mean vectors of the classes. In the case where a single spectral class corresponds to several terrain types, the classification has failed to distinguish these terrain types. This should be avoided if possible but such a case may occur in the classification of a large image because some terrain types may be spectrally very similar. If a spectral class corresponds to different terrain types in separate regions, the situation can be remedied somewhat by regional class editing. This procedure is equivalent to regional control based on prior knowledge.

Programmes entitled Class Grouping (CGR) and Class Regional Editing (CRED) were designed to handle the above two cases.

In CGR processing, class labels in a classification image can be changed

to the user specified labels from the key board. Thus if different classes are given the same label, they will be grouped into one class in the output image. The CGR also enables users to re-label classes according to their thematic significance. For instance, for the case of lithological mapping, 5 classes corresponding to different volcanic rocks labelled as class 1, 3, 5, 7 and 8 might be re-labelled as class 1, 2, 3, 4 and 5, while 3 classes of sedimentary rock, class 2, 4 and 6, would be re-labeled as class 6, 7 and 8.

With CRED, a class in a user defined rectangular region defined by Start Line, Start Sample, Number of Lines and Number of Samples (SL, SS, NL, NS) will be re-labeled as a new class by the user. Thus a class corresponding to several terrain types in different regions can be regionally split into several classes. Unfortunately, CRED is not able to split a class representing several terrain types as a spatially interlaced mixture in a small region.

5.5 Class Boundary Detection (CBD) Technique

Boundary detection is an important topic of image segmentation. Many techniques have been developed for detecting edges and boundaries in an image (Gonzalez and Wintz, 1987). Generally, as the first step, the image discontinuity (points, lines and edges) is detected based on the high frequency information (*e.g.* gradient and second-order derivative) derived from a window mask (Fram and Deutsch, 1975; Robinson, 1978; Marr, 1982). Then, edge linking and boundary detection and thinning are implemented by local and global analysis involving neighbour comparison, direction encoding and graphic searching (Martelli, 1972 and 1976; Rosenfeld and Kak, 1982; Gesù, 1984; Fu *et al.*, 1987). Thresholding techniques have also been effectively used for boundary detection (Chow and Kaneko, 1972; Weska, 1978; White and Rohrer, 1983).

In a classification image, DN values are simply the labels for different classes thus without any numerical meaning. Those boundary detection techniques involving numerical calculations are not applicable to a classification image. In a classification image smoothed and simplified by spatial post-processing, any a class patch in the image likes a plate at the DN level corresponding to the class label and therefore has a continuous and closed boundary. Boundaries exist between any adjacent pixels with different labels. The boundary detection in this case is an easy task which can be implemented quickly by a simple raster technique, Class Boundary Detection (CBD). CBD includes two steps: boundary detection and boundary thinning. The detected boundaries are stored in the same classification image as pixels of a new class (or recorded as a boundary image).

Boundary detection

A classification image Y is scanned by a mask shown in Figure 5-1a from top left to bottom right. Let $y_b(i,j)$ represent a pixel of the image Y_b produced by boundary detection and DN_b the DN value of boundary pixels which should not equal any existing values of the classification image Y. Thus the classification image with boundaries, Y_b, is produced by following:

$$y_b(i,j) = \begin{cases} DN_b & \text{if } y(i,j) \neq y(i,j+1) \text{ or } y(i,j) \neq y(i+1,j) \\ y(i,j) & \text{otherwise} \end{cases} \qquad (5-4)$$

As shown in Figure 5-2a and b, the boundary detected in this way is two pixel thick in the direction from top left to bottom right. Thus boundary thinning is necessary.

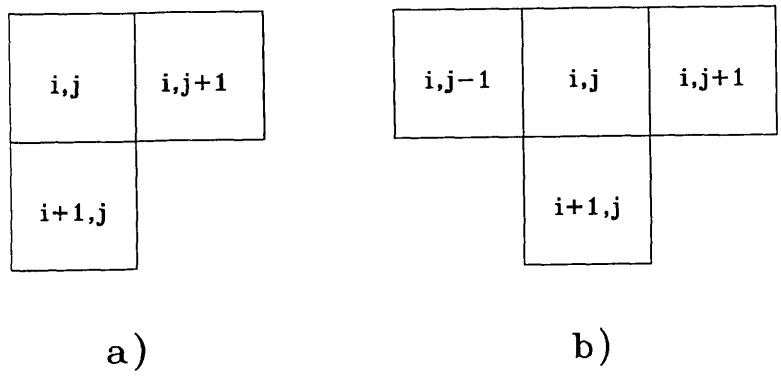


Figure 5-1: a) The mask for class boundary detection. b) The mask for class boundary thinning.

Boundary thinning

Boundary thinning is performed by scanning the images Y_b and Y simultaneously in the opposite direction, *i.e.* from bottom right to top left, using a mask shown in Figure 5-1b. Let $y_t(i,j)$ be a pixel of the image Y_t produced by boundary thinning, then,

$$y_t(i,j) = \begin{cases} y_b(i,j) & \text{if } y_b(i,j) \neq DN_b \\ y(i,j) & \text{if } y_b(i,j) = y_b(i,j-1) = y_b(i+1,j) = DN_b \\ & \text{and } y(i,j) = y(i,j+1) \\ y_b(i,j) & \text{otherwise} \end{cases} \qquad (5-5)$$

After boundary thinning processing, a boundary pixel will become to a non-boundary pixel if its left and underlying neighbour pixels are both boundary pixels, except if the pixel is a junction of more than two classes, where $y(i,j) \neq y(i,j+1)$, as shown in Figure 5-2c. To change a boundary pixel back to a non-boundary pixel will result in a break of the boundary at such a junction.

With the two steps of CBD processing, a classification image with perfect single pixel width class boundaries can be achieved (Figure 5-3).

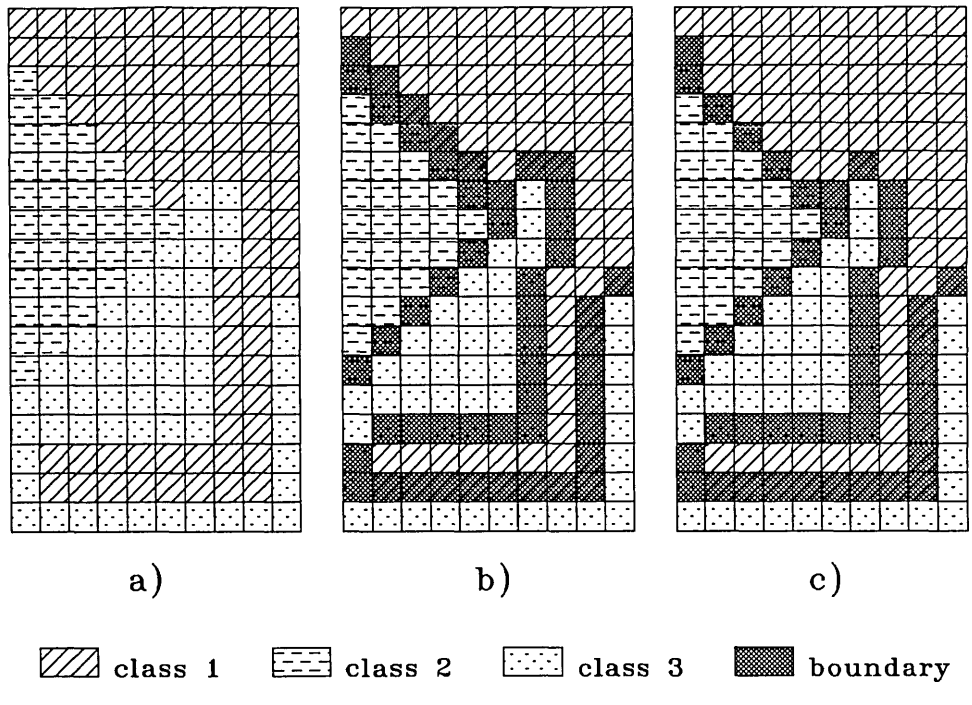


Figure 5-2: Illustration of the principle of the class boundary detection technique. a) A classification image, Y, with three classes. b) The classification image with boundaries, Y_b. The class boundaries of Y are detected by boundary detection but the boundary in the direction of top left to bottom right is two pixel thick. c) After boundary thinning, single pixel boundaries are achieved in any direction in image Y_t. Note: the pixel at the 7th line and the 6th column is a junction of three classes.

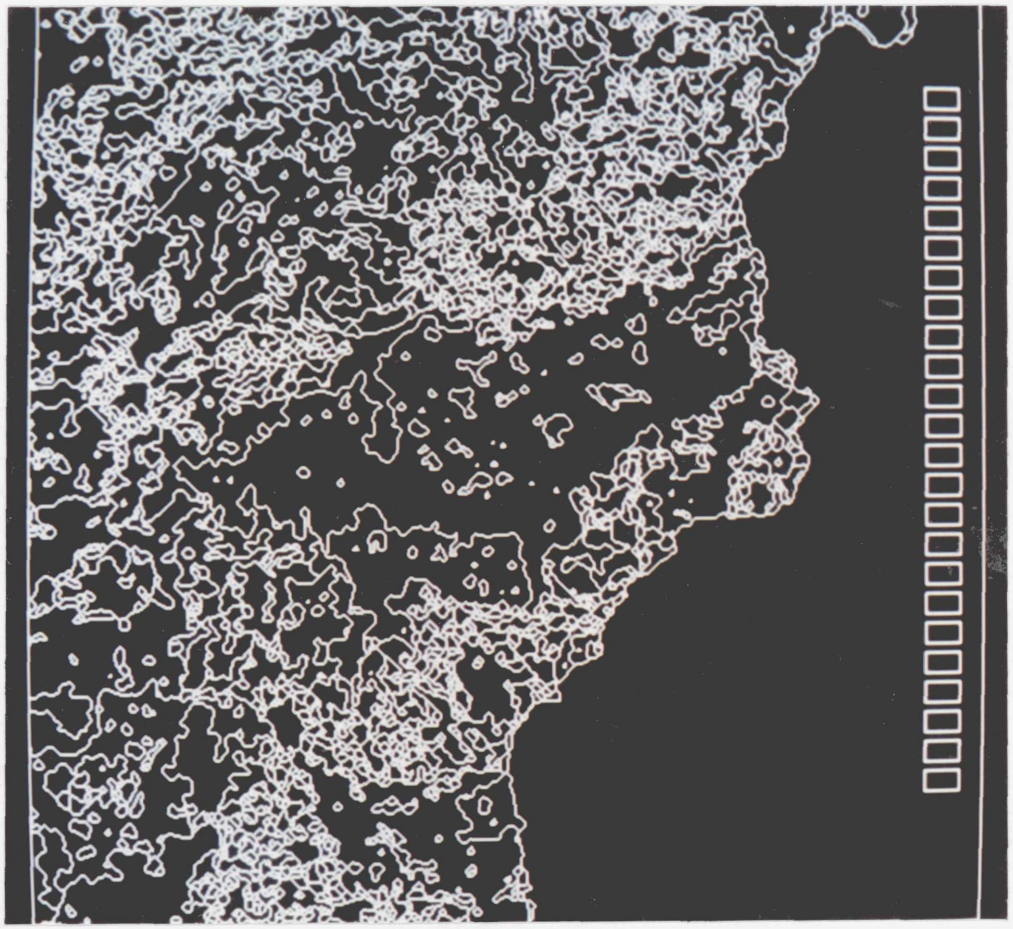


Figure 5-3: The class boundaries detected by CBD from the classification image of the test site

5.6 Editing Classification Images by Colour Painting

The importance of colour painting for a classification image is often undervalued as an aspect of colour display. Many colour paining techniques using fixed colour sequences have been developed for this simple purpose (*e.g.* colour density slice, pseudo colouration). The results are convenient for preliminary study but may not suitable for a final map product. In thematic mapping, colour painting should be regarded as an important step in class editing. The colours for various classes should be allocated according to their thematic significance, cartographic conventions and statistical similarity instead of class labels. Highly flexible interactive colour editing techniques are needed, which are already available in many image processing system. In this study, a colour painting (IPAINT) programme has been developed based on I2S/TAE system. It enables a user to paint a 512×512 image interactively from a terminal and display system. The programme generates an image with 125 colour keys and store it in a refresh imagery channel. A user can then select any colours from the colour key image to paint any grey levels of an image stored in another refresh imagery channel by simple control operations from the terminal. The colour of a grey level (class) can be easily re-allocated until a satisfactory result is achieved. Several classes may be painted in the same colour if they represent the same terrain type. Classes representing similar terrain types can be painted in similar colours. Small and important classes can be highlighted by bright colours. The programme also permits the user to input the data file of the three band mean values of the classes and start the painting with the colours coded by these data. In this case, a classification image can be painted very similar to the colour composite of the three bands used for the classification. It is convenient to carry on the further colour editing based on such an initial painting. A file of colour codes of all the grey levels (classes) will be output when the colour editing is terminated. This can then be used to paint scenes larger than 512×512 pixels.

Only with thoughtful colour editing, after a series of post-classification processes, can the final product present the thematic information as concisely, clearly and accurately as a high quality map.

5.7 Intensity Modulation of Classification Imagery

Crippen (1987) designed a very simple and useful technique to modulate a colour composite of three images by a fourth image. The information of four images can thereby be displayed simultaneously on an RGB colour display system as a modulated colour composite. The technique can be used to modulate a colour painted classification image by an intensity image so as to generate a coloured classification image with topographic background. The result is very easy to understand in relation to topography.

The intensity modulation of a classification image includes the following operations:

1. Generate three images, RC, GC and BC, from a classification image based on its colour code file. The colour composite of RC, GC and BC will restore the classification image painted according to the file. Thus the coloured classification image is stored as a colour composite.

2. Derive the average image, AVE, from the original image bands. Such an average image is equivalent to an intensity (or panchromatic) image containing the maximum topographic information of the spectral wave bands involved.

3. Compress the average image, AVE, into a narrow value range and high mean value using BCET so as to avoid too much colour distortion and maintain proper contrast in the modulated classification image.

4. Modulate RC, GC and BC by multiplying AVE as below.

$$MRC = RC \times AVE$$

$$MGC = GC \times AVE$$

$$MBC = BC \times AVE$$

5. Scale MRC, MGC and MBC to [0, 255] value range. The colour composite of the three image will then be a coloured classification image with topographic background.

5.8 Spectral Analysis of Classification

Spectral analysis is very important for spectral class identification in terms of lithology and terrain types. The seven TM band DN values of a pixel in a TM image are distorted (by atmospheric scattering and sensor gain parameters) records of average spectral energy of $30m \times 30m$ land surface. Such a $30m \times 30m$ area is usually, for most cases of geological study, covered by several different materials, such as weathered surface of rock outcrops, soils and vegetation. Therefore, the pixel spectral shapes derived from DN values of seven TM spectral bands do not really match the spectral profiles obtained from laboratory measurements based on pure samples using instruments with very high spectral resolution and are also difficult to compare with the field spectral measurements without careful atmospheric correction and spectrometric calibration. A direct comparison is even more difficult between a class spectral shape defined by seven TM band means of the spectral class and those non-imagery measurements because class means are the average band DN values of all the pixels in the class.

On the other hand, imagery spectral shapes do correspond to those significant reflection and absorbtion spectral features of vegetation and major minerals in rocks, superficial deposits and soils thus can be qualitatively used

as a reference for spectral class identification. In an image, similar terrain types will have comparable imagery spectral shapes because the sensor gain parameters are constants and atmospheric effects and the natural environment is regionally stable. Class spectral shapes can, therefore, be used directly for class grouping during interactive class editing as was done in this study.

As the spectral classification in this study was based on HRGB images, specific techniques are needed to derive class spectral shapes.

A technique for deriving spectral shapes from HRGB images

The three DN values of a pixel in an HRGB image are determined by the spectral shape (of all the bands used) of this pixel but these DN values do not directly give the spectral shape of the pixel. A simple technique for deriving spectral shapes from an HRGB image derived from the TM band-triplets: 6 7 5, 5 4 3 and 3 2 1, is introduced below.

The hue DN value of any a pixel in a hue image is initially determined by the three DN values of the pixel in the three bands from which the hue image has been derived. Such a hue DN value locates a position on the hue wheel shown in Figure 5-4. The portions of red, green and blue in the hue of this pixel can thus be derived to configure a three-band spectral shape of this pixel in two steps.

1. Re-scale the hue image from $[0, 255]$ value range to $[0, 360]$ value range:

$$Hue = HDN \times 360/255$$

where HDN is a DN value in the hue image and Hue the hue angle on the hue wheel.

2. Calculate the portions of red, green and blue:

If $0 \leq Hue < 120$ Then

$$Red = 0$$

$$Green = \frac{Hue}{120}$$

$$Blue = 1 - Green$$

If $120 \leq Hue < 240$ Then

$$Red = \frac{Hue - 120}{120}$$

$$Green = 1 - Red$$

$$Blue = 0$$

If $240 \leq Hue < 360$ Then

$$Red = 1 - Blue$$

$$Green = 0$$

$$Blue = \frac{Hue - 240}{120}$$

To obtain the spectral shape of seven TM bands of an image pixel, from an HRGB colour composite derived from band-triplets 6 7 5, 5 4 3 and 3 2 1, the above two step operation should be performed on each of the three hue values respectively. As TM3 is used as red component in triplet 3 2 1 and blue component in triplet 5 4 3, the *Red* of triplet 3 2 1 must be equal to the *Blue* of triplet 5 4 3. In other words, the spectral shape of the hue value of triplet 5 4 3 should be shifted to connect that of 3 2 1. Similarly, the spectral shape of the hue value of triplet 6 7 5 should be shifted to connect that of triplet 5 4 3. Thus a continuous spectral shape of seven TM bands is derived from the HRGB colour

composite. Finally, if the minimum value of the spectral shape is less than 0, shift the whole spectral shape upward to make the minimum 0. An example of calculation is illustrated by Table 5-1 and Figure 5-5.

This very simple technique can only be used for qualitative analysis. The red, green and blue components derived from a hue value show the relative spectral shape of the three source bands but are generally not linear proportion to the DN values of these bands because the RGB-IHS transformation is not a linear one. The spectral shapes derived from the hue values of the hue images of band-triplets 3 2 1, 5 4 3, 6 7 5 are connected simply by upward or downward shifting (adding or subtracting constants) in the above operations. The same job can be done by multiplying by appropriate factors if no zero value is involved. More generally, the connection can be performed by a linear transformation: $y = kx + b$, because hue value is not affected by such a linear transformation according to formula 3-34. However, with one band re-used in each band-triplet above, there is a family of linear transformations that can perform the connection and each of the transformations will result in a slightly different spectral shape. Thus the spectral shapes derived by the technique introduced above do not correspond uniquely to the original data. Even though, as the operations performed on each HRGB data point are the same, the results obtained from different data points are generally comparable. The spectral shapes derived by the technique are therefore reliable for spectral class grouping. For interpretation purpose, the spectral shapes must be used with caution as the shapes may not be correct among band-triplets: 3 2 1, 5 4 3 and 6 7 5. For instance, the relationship among band 1, 2 and 4 may not coincide with that of the original data.

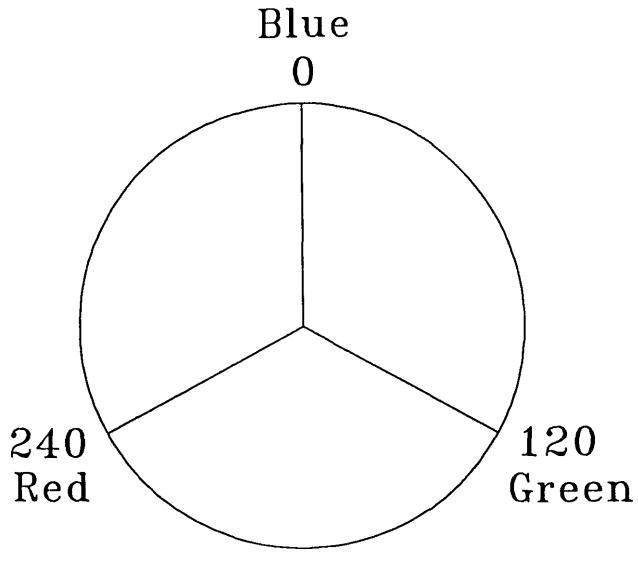


Figure 5-4: The hue wheel illustrating the value of a hue image

Table 5-1: A calculation example for deriving a spectral shape from HRGB data. (1) Calculate blue, green and red portions for each band-triplet from the hue angle value; (2) make re-used bands have equal values in different band-triplets; (3) shift the values of all the bands to prevent negative values.

	Hue321			Hue543			Hue675		
Hue DN	127.5			51.1			210.9		
Hue angle	180.1			72.1			297.8		
Band-triplet	TM1	TM2	TM3	TM3	TM4	TM5	TM5	TM7	TM6
Colours	B	G	R	B	G	R	B	G	R
(1)	0	0.50	0.50	0.40	0.60	0	0.48	0	0.52
(2)	0	0.50	0.50	0.50	0.70	0.10	0.10	-0.38	0.14
(3)	0.38	0.88	0.88	0.88	1.08	0.48	0.48	0	0.52

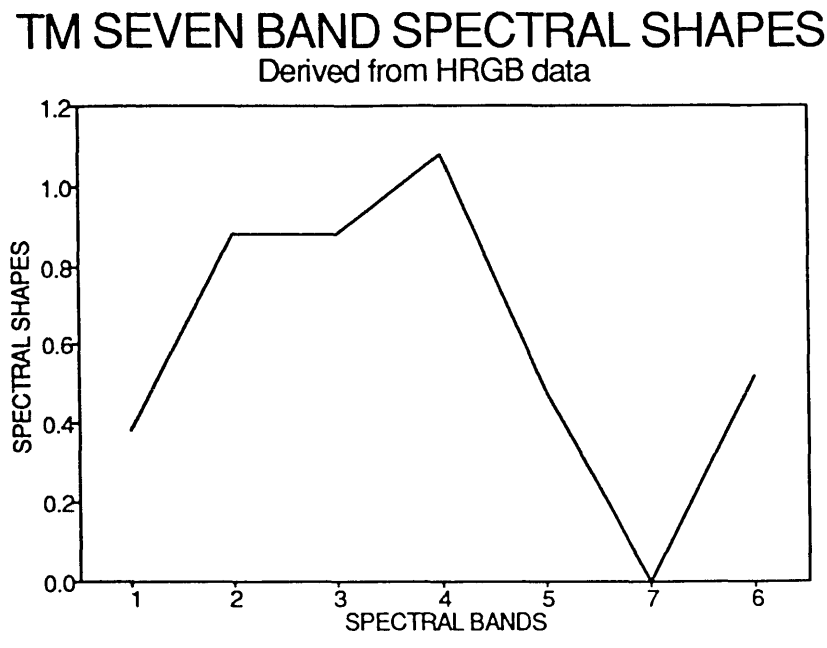


Figure 5-5: The spectral shape defined by the data in Table 5-1

Deriving class spectral shapes from seven TM bands

Class spectral shapes of the classification based on an HRGB image can be derived directly from the seven TM bands from which the HRGB image is derived. A Fortran program (CLSMV, Appendix A) was written to perform the task. It reads the classification image together with seven TM band images and calculates the mean values of seven TM bands for each class.

The class spectral shapes defined by class mean values of seven TM bands provide quantitative spectral descriptions of the classes in the classification based on HRGB images. The class spectral shapes derived by CLSMV from seven TM bands (with BCET processing) were used for class identification and grouping in the lithological mapping in this study as discussed in Chapter 6 and 7. Any contrast enhancement can change imagery spectral shapes but generally does not change the spectral similarities among image pixels. Imagery spectral shapes derived from the image with BCET processing can clearly illustrate the spectral character of various terrain types as colour bias is eliminated.

The class spectral shapes derived from class mean values of the HRGB image of the study area match those derived from the TM bands quite well as shown in Figure 5-6. This fact confirms that the technique for deriving spectral shapes from HRGB images is usable for preliminary spectral analysis.

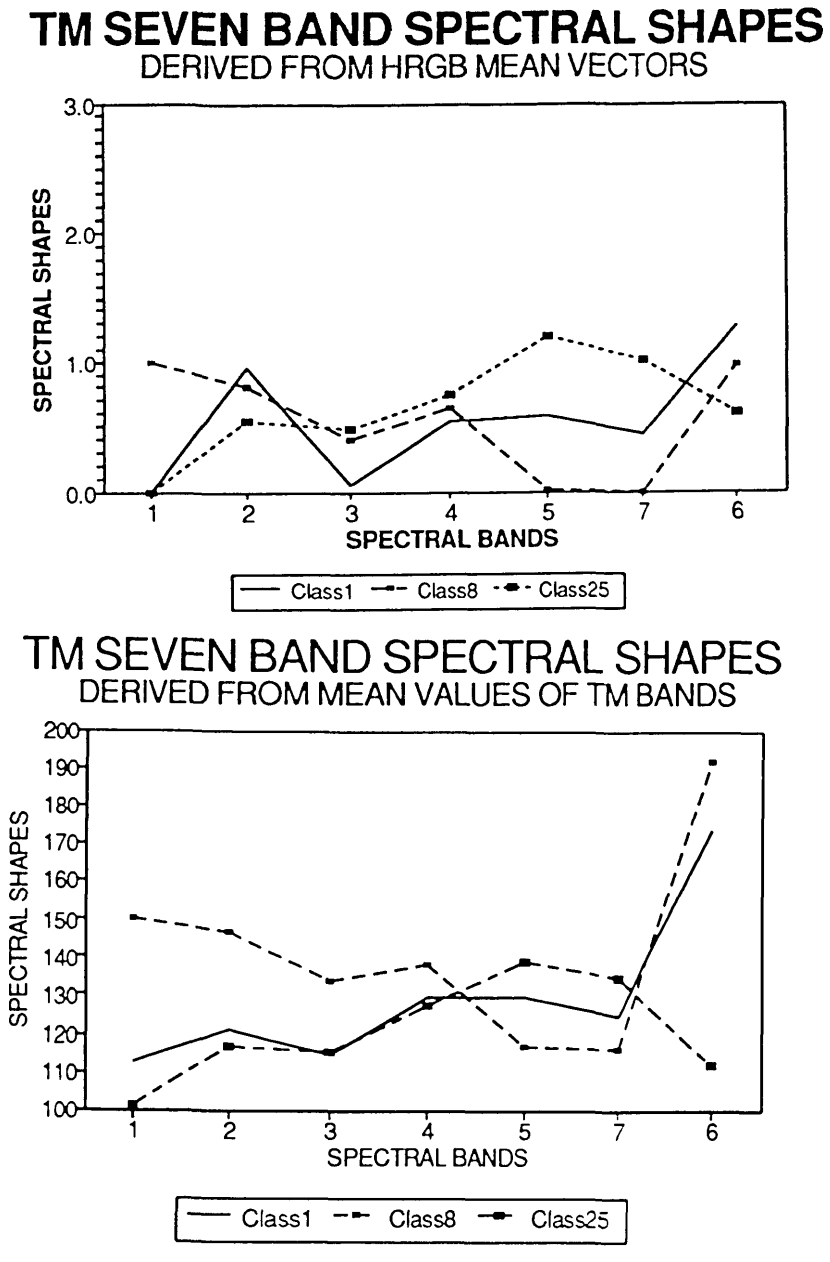


Figure 5-6: Comparison of the class spectral shapes derived from the HRGB image and the seven TM bands of the study area

5.9 Summary

Post-processing and analysis of spectral classification is a necessary step towards producing a practical thematic map using remotely sensed multi-spectral imagery based on spectral classification. Several post-processing techniques are discussed in this Chapter.

Spatial information, which is not used during multi-spectral classification, can be used to improve the classification quality and to smooth a classification image.

Template histogram matching classification (THMC) is a technique developed to detect textures and patterns formed by certain spatial configurations of several classes in a classification image.

Iterative majority filtering (IMF) and small class merging (SCM) techniques can be used after THMC processing to produce a smoothed and simplified classification image with much improved spatial continuity.

To handle the cases of several classes corresponding to one terrain type and one class representing several terrain types, interactive class editing programmes, class grouping (CGR) and class regional editing (CRED), have been introduced. CGR and CRED enable users to edit classification images based on empirical field and map information.

To make a classification image into a practical thematic map, techniques for adding class boundaries, painting colours and intensity modulation are presented.

A simple and effective technique for detecting class boundaries (CBD) has been developed. By scanning a classification image in opposite directions with

a three pixel mask and a four pixel mask, class boundaries of single pixel width will be detected and added into the classification image by CBD.

A colour painting programme (IPAINT) is introduced. The programme performs an interactive painting procedure to enable a user to colour an image as he wishes. The colours of a classification image can thus be edited to convey thematic information more efficiently than unsupervised colouring techniques using an automatic colour scheme.

Intensity modulation for adding topographic background into a colour painted classification image is discussed.

As the class means of the classification based on an HRGB image do not directly define the class spectral shapes, simple methods for deriving class spectral shapes from class mean vectors in the HRGB image and from seven TM bands are introduced. The method for deriving class spectral shapes from HRGB mean vectors is not reliable thus will not be used. The class spectral shapes derived directly from seven TM bands will be used for analysing the classification results and class identification in Chapter 6 and Chapter 7.

Chapter 6

Experiment for Automatic Lithological Mapping in the Test Site

A 512×512 TM subscene of Cabo de Gata area, including the Rodalquilar gold mine, was selected from a TM image of SE Spain (Figure 1-2) as the test site for technique development and experimental processing. Some details of the image processing of this subscene have been presented in the previous chapters to illustrate the techniques introduced in these chapters. In this chapter, the image processing of the subscene will be briefly discussed in a logical sequence for automatic lithological mapping and alteration detection. The class identification for lithology and terrain types and assessment of the mapping quality will be given based on field work, spectral analysis and published 1:50000 scale geological maps.

6.1 The Test Site

The test site is in the Cabo de Gata peninsula in Almeria Province, Spain, covering a $15.36km \times 15.36km$ area from Punta Javana in the north to Punta

de Loma Pelada in the south (Figure 6-1).

As shown in Figure 6-2 (Moore, 1990) andesitic and dacitic eruptions occurred in later Miocene times to form an arcuate volcanic belt extending along the eastern coast as a range of Sierra de Gata. The Miocene volcanics contain swarms of epithermal gold and silver-lead-zinc veins and associated alteration. The most important of these is the Rodalquilar gold deposit in the central part of the subscene. This orebody supports an open-pit and heap leach mining operation (Arribas, *et al.*, 1989). At Rodalquilar, gold occurs in quartz veins and silicified (chalcedonic) wall-rocks with associated alunite and jarosite. Surrounding a quartz-alunite zone with small areas of propylitic alteration, are concentric kaolinitic, illitic and vermiculite zones (Hernandez, 1989). The silicic and kaolinite-illite alteration covers an area of some 15 square kilometres around the mine site and extends eastward to the coast beneath a cover of younger Miocene limestone.

Surrounding the hydrothermal alteration zones are relatively unaltered but weathered dacite and andesitic pyroclastic volcanics. The volcano-clastic strata west and south of the mine area contain altered tuff horizons which have been worked for bentonite (montmorillonite).

The test site is semi-arid and thinly vegetated. The terrain surface comprises approximately 60% regolith, dominated by lithic clastic debris, 20% outcropping bedrock and 20% vegetation as scattered bushes and thin undergrowth, particularly in dry valleys and on north and west facing hill slopes. Rock outcrops are commonly obscured by weathering veneers and, locally, by lichen.

The spectral character of pixels of Landsat TM imagery used for this study is dominated by information from rock fragments and soil with contributions

from vegetation and outcropping bedrock. The only pixels dominated by the spectral signature of vegetation are those representing areas of small-scale, irrigated horticulture mainly in the northwestern corner of the subscene.

The geological objectives of the image processing of the test site are to discriminate the main rock types and superficial deposits, to detect and define the epithermal alteration zones related to gold deposits and finally to produce a lithological map of the area. The image processing was implemented in three stages: pre-classification image enhancement, spectral classification and post-classification processing.

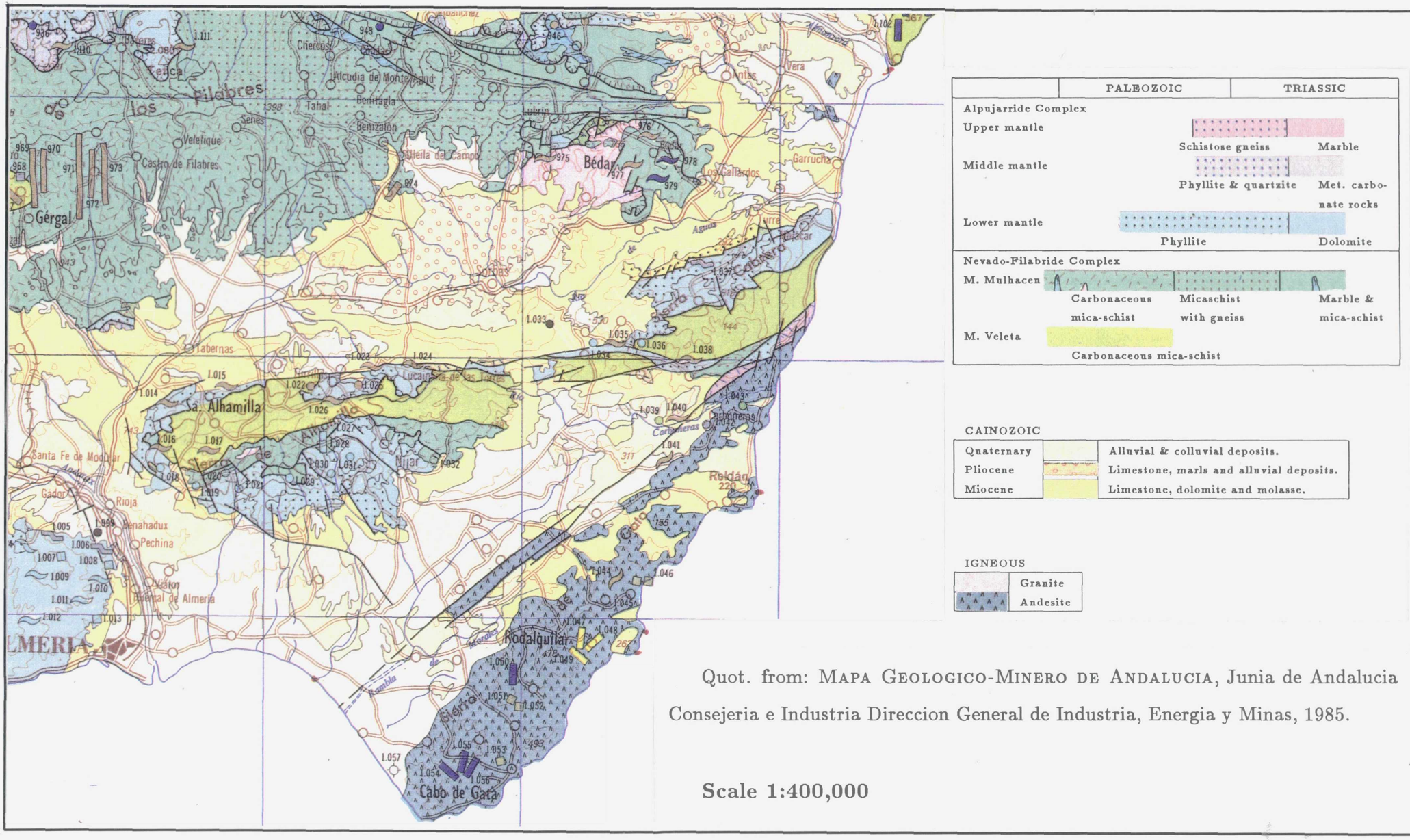


Figure 6-1: The regional geological map of the study area in SE Spain

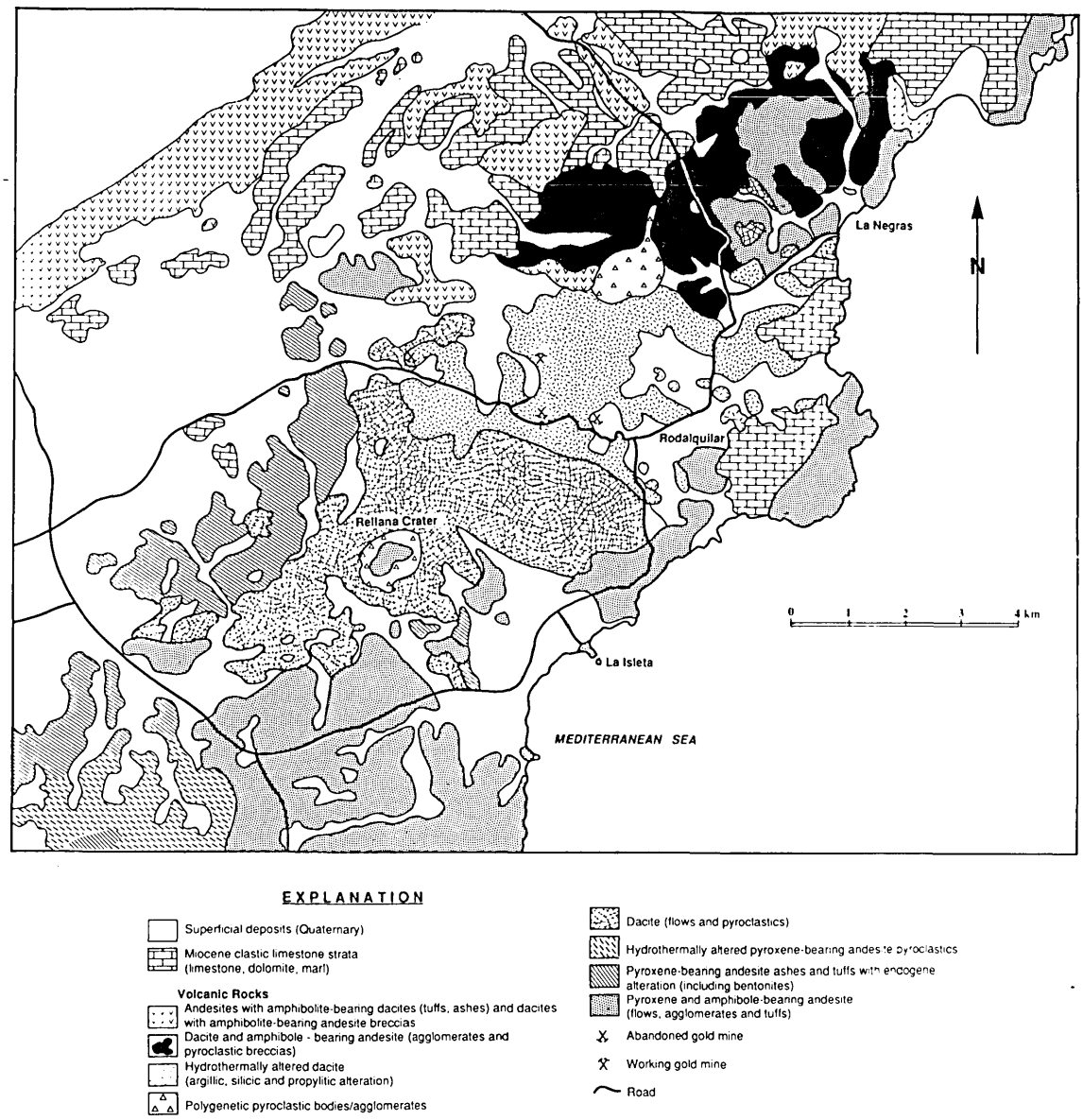


Figure 6-2: Geological map of the test site. Moore, 1989 based on IGME conventional geological maps: Frailes [1060] and Carboneras [1046],1981.

6.2 Pre-classification Image Enhancement and Image Interpretation

As discussed in Chapter 3, the purpose of the image enhancement as the pre-processing of spectral classification is to provide enhanced images with good discrimination of specified terrain types and minimum topographic shadow effects. Three techniques were used: IOBS, BCET and HRGB. Firstly, all the seven bands of the TM subscene were stretched to an equal value range (0-255) and mean (100) by BCET and then RGB-IHS transformation were performed on the band-triplets: 6 7 5, 5 4 3 and 3 2 1 (Table 3-8) to derive three hue images for producing the HRGB image of the test site (Figure 6-3). The thermal band: TM6 was used with TM5 and TM7 to form a colour composite (Figure 6-3c) though its physical properties and spatial resolution are different from those of reflective spectral bands. The advantage of using TM6 in the colour composite is that it brings inverse albedo information into the subsequent hue image (Figure 6-3d) because the thermal emissivity of objects under the same irradiance is proportional to the inverse albedo of these objects. Such information is not present in the hue images derived from band-triplets of reflective spectral bands.

Shadow effects, seen in the colour composites of the three band-triplets (Figure 6-3a, b and c) have been removed almost completely from the HRGB image (Figure 6-3d) and the major rock types as well as vegetation are displayed in distinctive colours (Table 6-1). Comparing the HRGB image with the published 1:50,000 scale geological maps (ref. Figure 6-2), the accuracy of lithological information provided by the image is remarkable. The interpretation map (Figure 6-4) of the HRGB image shows good agreement with the lithological information in the published geological maps (Figure 6-2) and was confirmed by field checks at selected locations. The dacite terrain shown on 1:50,000 scale geological maps can be sub-divided into three units using the HRGB image and one of them precisely matches the epithermal alteration zones related to gold deposits (Table 6-1).

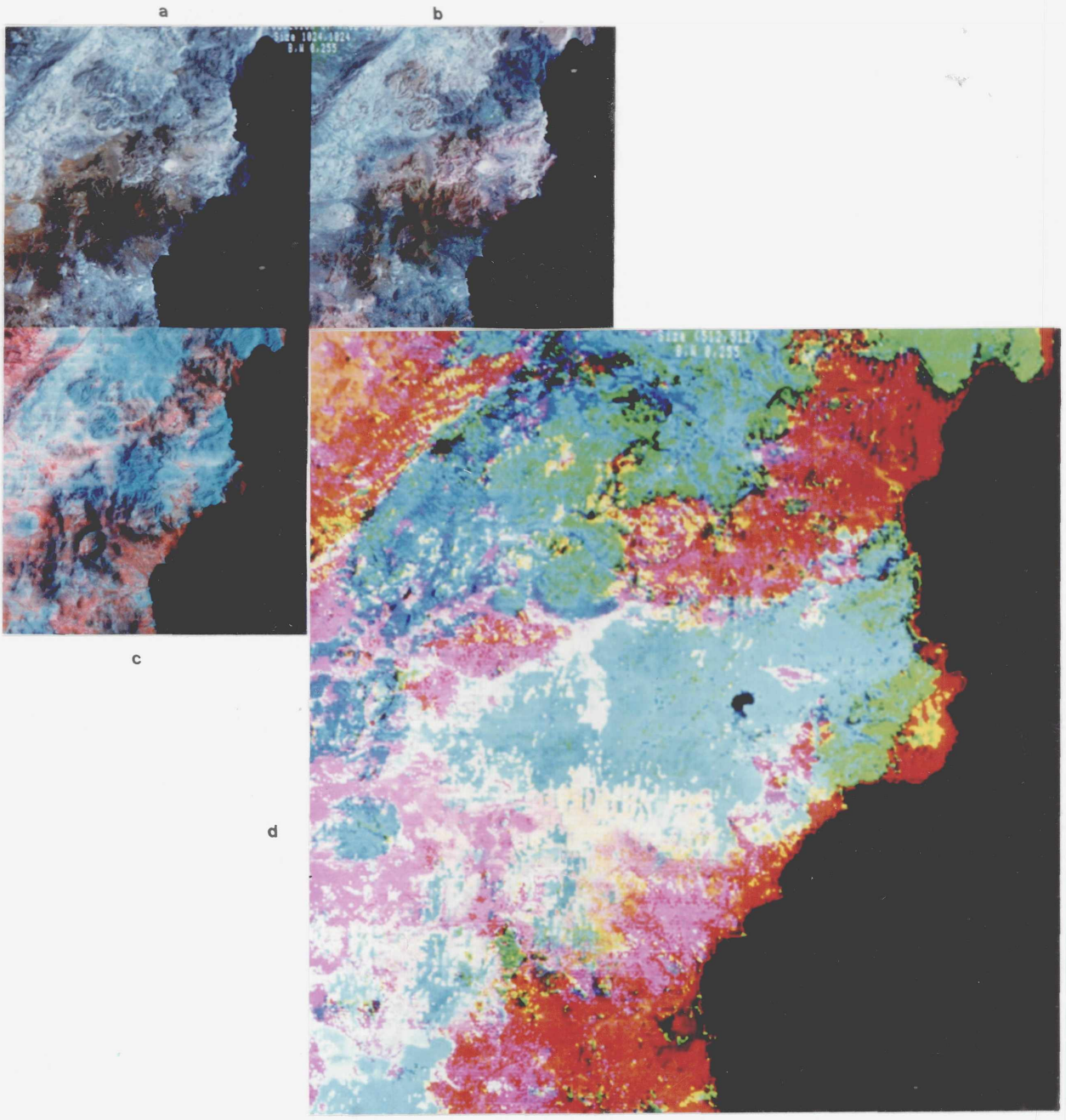


Figure 6-3: 512 Landsat TM subscene of the test site. a) Colour composite of TM band triplet 3 2 1 in RGB; b) Colour composite of TM band triplet 5 4 3 in RGB; c) Colour composite of TM band triplet 6 7 5 in RGB; d) HRGB colour composite produced by displaying the hue image derived from composite a) in red, the hue image from the composite b) in green and the hue image from composite c) in blue.

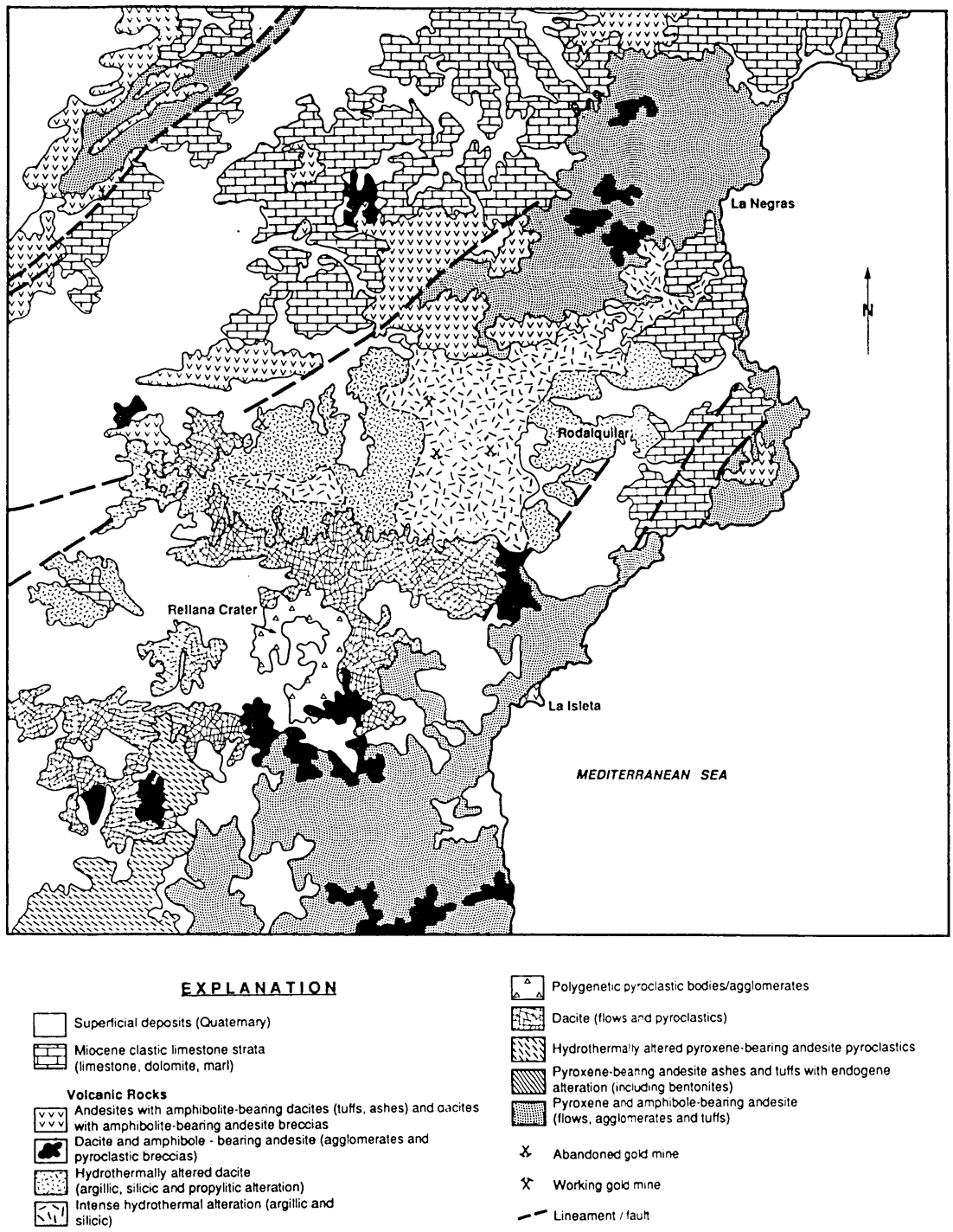


Figure 6-4: Geological interpretation of the HRGB image of the test site.

Table 6-1: Lithological interpretation keys of the HRGB image of the test site

Geological description	Colours on image
Volcanic rock	
Andesite lava and agglomerate	Red
Andesite breccia agglomerate	Red and yellow mixture
Andesite and dacite agglomerate	White, cyan and pink mixture
Dacite	Yellowish white with cyan
Altered volcanics	Cyan
Strongly altered dacite	Cyan with green spots
Tuff	Fresh green with yellow spots
Miocene carbonate rock	
Limestone, dolomite and marl	green
Quaternary deposits	
Debris from andesite	Pink
Sand deposits from volcanics (alluvial terraces)	Cyan surrounding dark blue
Debris from carbonate rock (slope wash) or dry river beds	Dark blue
Salt, carbonate or clay rich deposits (lake deposits, gypsum, etc.)	Black
Red soil	Cyan-white
Recent alluvial fan	Light pink with clear edge
Others	
Vegetation	Orange
Cultured areas	Multi-colour mixtures

6.3 Spectral Classification

The HRGB colour composite resembles a classification image as the topography is suppressed almost completely and different terrain types are displayed in distinctive colours. This phenomenon implies that the three hue images forming the HRGB colour composite are suitable for spectral classification of terrain types. The unsupervised classification using the three hue images were carried out by 3D-FSIC programme. In order to speed up the processing and save memory space, the quantisation of the hue images of the test site was reduced to 64 by factor 4. To start the clustering, twenty 'seeds' (Table 6-2) were selected from the 3D scattergram of the three hue images by ASST as the initial centres for clustering.

Different parameters were tested during the experimental classification processing, to investigate the best convergence and discrimination of the major lithologies in the area.

SPLIT and UNITE are very important parameters controlling the optimal convergence of iterative clustering. The larger the values of SPLIT and UNITE, the larger the clusters which can be formed and fewer clusters will result. Generally, SPLIT and UNITE should be kept reasonably small to permit small but possibly important classes to survive. In this case, a major rock or terrain type may be split into several classes. As discussed in section 5.3, however, it would be better to achieve a classification with several classes equivalent to the same terrain type rather than that with one class equivalent to several terrain types.

If the spectral clusters in feature space of the three hue images obey Gaussian distributions, theoretically, the Gaussian OMPR is the most appropriate decision rule among the three installed in 3D-FSIC, but the processing speed of Gaussian OMPR is almost ten times slower than the Euclidean OMPR. Thus hybrid iterations were used to reach reasonable optimal convergence at much

higher speed and lower cost. Relatively, the best result was achieved when the control parameters are as follows:

SPLIT=13, UNITE=4,
ITERATION: 1 Euclidean, 3 Euclidean OMPR and 2 Gaussian OMPR.

As the quantisation of the hue images had been reduced by factor 4, the value of SPLIT was equivalent to 52 DN levels and that of UNITE 16 DN levels. The iteration information is shown in Table 6-3. The cluster splitting and merging ceased after the second iteration and the maximum migration of class centres was small and kept decreasing steady during the iteration process except the one after the first iteration which was caused by class splitting and merging. This means that the initial cluster centres for clustering were properly located in the 3D feature space by the ASST technique. A spectral classification image (Figure 6-5) with 23 classes resulted after 6 iterations. The image was coloured in such a way that the red, green and blue portions of the colour of a cluster is determined by the three mean values of this cluster. It is a precise and simplified representation of the colour composite of the three hue images used in classification (Figure 6-3d). The relevant statistical data are shown in Table 6-4.

Table 6-2: Hue DN values of the initial centres for clustering classification based on the HRGB image of the test site.

	PIXEL VALUES OF SEEDS FOR CLUSTER		
	Hue675	Hue543	Hue321
1	86.00	2.00	2.00
2	90.00	86.00	2.00
3	86.00	2.00	170.00
4	94.00	86.00	2.00
5	90.00	86.00	170.00
6	210.00	74.00	190.00
7	210.00	82.00	190.00
8	210.00	70.00	54.00
9	210.00	74.00	54.00
10	210.00	70.00	70.00
11	210.00	78.00	190.00
12	206.00	70.00	190.00
13	214.00	66.00	54.00
14	210.00	70.00	58.00
15	206.00	70.00	198.00
16	210.00	74.00	58.00
17	210.00	78.00	70.00
18	210.00	70.00	62.00
19	210.00	66.00	62.00
20	206.00	70.00	194.00

Table 6-3: Iteration information of the clustering classification using three hue images (the HRGB image) of the test site.

Decision rules	Iteration times	Class born	Class died	Total class	Maximum migration
Seed file	0	-	-	20	-
Euclidean	1	5	2	23	26.9663
Euclidean	2	0	0	23	4.9528
OMPR	3	0	0	23	4.2263
	4	0	0	23	2.3675
Gaussian	5	0	0	23	1.9523
OMPR	6	0	0	23	1.3560

6.4 Post-processing of Spectral classification

The spectral classification image of the test site has a rather broken and noisy appearance. The known epithermal alteration zones with gold deposits (area near Rodalquilar) is not classified as an individual class. Instead, it is characterized by a spatial pattern of several classes. Post-classification processing including spatial re-classification and smoothing, boundary detection and colour editing was applied to detect the epithermal alteration zones and to produce a practical lithological map from the spectral classification image. Furthermore, the resulting image classification map was modulated by intensity image to add back the topography.

Alteration detection using THMC technique

The template histogram matching classification (THMC) is a supervised spatial (textural) classification technique. The texture/pattern training areas are defined by users. The epithermal alteration zones with gold deposits in the test site had been defined by the interpretation map (Figure 6-4) of the HRGB image. They are within the dacite terrain and show a colour pattern of cyan

Table 6-4: Statistics of the clustering classification using the HRGB image of the test site.

STATISTICAL DATA OF CLASSIFICATION

No.	MEAN VALUES			SD			CORRELATION			PIXEL
	H675	H543	H321	H675	H543	H321	CR_{12}	CR_{13}	CR_{23}	
1	79.0	16.7	39.3	22.4	15.3	32.6	-0.40	-0.23	0.65	2408
2	75.7	204.0	77.9	19.0	18.3	20.8	0.05	0.28	-0.23	13424
3	101.6	34.6	196.1	33.6	23.2	28.9	0.26	0.13	0.37	2677
4	82.2	204.1	36.3	10.3	18.3	14.0	0.10	0.14	-0.10	6088
5	77.1	203.8	183.2	23.0	20.2	26.3	0.16	0.12	0.28	39224
6	210.9	51.1	127.5	9.4	19.0	13.8	-0.01	-0.02	-0.09	1931
7	210.9	201.7	183.2	21.9	24.9	23.2	-0.24	-0.18	0.25	18573
8	209.0	72.5	31.3	9.9	10.1	11.7	-0.01	-0.03	-0.02	4523
9	215.4	120.2	50.3	12.7	17.1	17.1	-0.15	0.12	-0.04	3110
10	208.2	76.1	100.1	12.0	10.7	13.2	0.04	0.03	0.30	6345
11	206.3	77.5	157.3	13.0	12.2	12.4	-0.01	-0.02	-0.13	5718
12	217.1	53.1	53.0	11.8	8.1	7.1	0.19	0.42	0.11	2959
13	213.1	21.5	47.8	15.8	11.9	20.1	-0.04	0.07	-0.54	1426
14	208.1	74.2	232.2	10.3	24.5	13.8	0.05	0.03	0.03	3758
15	209.6	75.9	63.8	8.1	10.0	9.2	0.12	0.03	0.05	11837
16	217.6	206.8	65.6	20.0	26.4	29.0	-0.14	0.05	-0.05	5062
17	200.2	49.7	70.0	19.1	13.7	10.8	-0.59	0.49	-0.38	2945
18	204.4	66.8	191.9	11.4	22.8	9.1	-0.02	-0.03	-0.01	16378
19	72.2	118.4	74.1	36.8	27.9	29.6	0.50	0.03	-0.17	2973
20	102.5	72.1	58.1	25.2	15.4	31.3	-0.05	0.20	-0.25	6637
21	95.5	101.6	186.1	21.2	24.2	23.3	-0.24	-0.09	-0.04	14317
22	210.1	125.4	175.5	13.2	16.8	17.2	0.01	0.01	0.04	6557
23	216.5	124.2	102.5	8.9	14.7	18.8	0.20	-0.03	0.09	4677
0	Pixels masked off (sea area)									78597

Table 6-5: The 3 × 3 template histogram of the textural class (relevant to the epithermal alteration in Rodalquilar) in the spectral classification image of the test site.

Class	0	1	2	3	4	5
Frequency	0	0	0.64	0	0.48	7.88
Class	6	7	8	9	10	11
Frequency	0	0	0	0	0	0
Class	12	13	14	15	16	17
Frequency	0	0	0	0	0	0
Class	18	19	20	21	22	23
Frequency	0	0	0	0	0	0

background with green spots in the HRGB image. This spatial information appears in the classification image as a pattern of class 5 as background containing spots of class 2 and 4. Field observation and published 1:50000 scale geological maps show that the cyan in HRGB image (class 5 in the classification image) represents altered dacite and green (classified as class 2 and 4) defines limestone.

The particular feature of the epithermal zones is possibly caused by the weathering veneers of the strongly silicified dacite with lichen covering. The colours of the outcrops of such rock are often similar to that of limestone outcrops.

Based on above knowledge, a training area with 15 × 15 pixels was selected from the known alteration zones to generate a standard 3×3 template histogram of the pattern (Table 6-5). The THMC was then executed by image scanning with a 3 × 3 window. In the resulting image (Figure 6-6), the alteration zones are identified as a new class (class 24). The pixels of the new classes are mainly from class 5 as well as class 2 and 4, as shown in the column 2 and 3 of Table 6-6.

Smoothing and small class merging

As further steps of spatial re-classification, the iterative majority filtering (IMF) and small class merging (SCM) were applied to smooth the classification image (Figure 6-6) resulted from THMC. After five IMF iterations with the criterion for majority classes as 5, the spatial continuity of the image was significantly improved and a well smoothed classification image was achieved. Then SCM was performed to merge the classes with less than 500 pixels into its spatially and spectrally nearest larger classes. As the result, class 13 was deleted (Table 6-6). Finally the image shown in Figure 6-7 was produced, in which the major classes are presented much more clearly and concisely and coincide with the lithology in the published 1:50000 scale geological maps (ref. Figure 6-2) and field check more precisely than those in the original classification image (Figure 6-5). The accuracy of the lithological classification is somewhat improved in this way. Generally, if the criterion for small classes in SCM processing is appropriate, there will be almost no visual difference between the images with and without SCM processing. The only difference is that the small classes are deleted from the class label list after SCM processing.

Boundary detection and colour editing

After spatial post processing, class boundary detection using CBD technique and colour editing using IPAINT programme were applied to produce an imagery classification map. The class boundaries were detected and added into the smoothed classification image and the class key box were also inserted (ref. Figure 5-3) by a program, CBDKB (Appendix A), integrating the CBD technique and key box function. Then the image was painted by IPAINT programme in two ways. Firstly, the data file of class mean vectors were used as colour codes (the portion of red, green and blue) of the classes; thus the classification map was painted to resemble the HRGB composite of the three

Table 6-6: The class pixel numbers of spectral classification (FSIC), templet histogram matching classification (THMC), iterative majority filtering (IMF) and small class merging (SCM). The class 0 is the sea area not involved in the classification

Class	Pixel numbers			
	FSIC	THMC	IMF	SCM
0	78597	78597	79097	79097
1	2408	2408	2501	2727
2	13424	13208	17793	17803
3	2677	2677	1188	1188
4	6088	5889	2042	2052
5	39244	36018	44507	45191
6	1931	1931	1922	1922
7	18573	18573	20956	20956
8	4523	4523	5213	5213
9	3110	3110	2684	2648
10	6345	6345	6920	6920
11	5718	5718	4783	4783
12	2959	2959	1826	2187
13	1426	1426	433	deleted
14	3758	3758	1205	1205
15	11837	11873	15132	15176
16	5062	5062	3649	3649
17	2945	2945	1093	1121
18	16378	16378	17413	17413
19	2973	2973	1051	1051
20	6673	6673	6057	6057
21	14317	14317	14256	14256
22	6557	6557	3855	3855
23	4677	4677	3594	3594
24	none	3621	930	930

hue images used for classification (Figure 6-8). Painting in such a way can show the spectral relationships among different classes directly because the spectrally similar classes will be in similar colours. The colours of some classes may be too similar to be distinguished. This is a disadvantage if the spectrally similar classes represent different terrain types. Thus, further colour editing is needed to permit the user to supervise the final colour presentation of the classification for thematic mapping based on their expert knowledge. Colour editing is a very important procedure for automatic lithological mapping. Two general rules were applied to editing:

1. Paint the classes representing similar lithologies and terrain types in similar but distinctive colours, *e.g.* all andesite rock types were painted in reds.

2. Paint different lithologies and terrain types in different colour series, *e.g.* andesites in reds, limestones in yellows, vegetation in greens, *etc.*.

The colour scheme of the existing geological maps can be used as a reference for colour assignments.

Figure 6-9 was produced by interactive colour editing following above rules. Different classes are clearly illustrated and the spatial relationship of many similar classes are well presented. Several classes can be painted in the same colour if we know that they represent the same lithology and the spectral variations are caused by non-lithological factors. An imagery lithological map that is much simpler and more concise than Figure 6-9 can be produced by repainting those classes identified as the same lithologies (or terrain types) in the same colours after class lithological identification (see section 6.5). It might be better to keep Figure 6-8, 6-9 as the original version of the image classification for lithological mapping so as to maintain the evidence for further investigation.

To illustrate the spectral classification and post-classification processing, all the classification images resulted in previous stages were also painted using the

same data files of colour codes as Figure 6-8.

Intensity modulation

It is difficult to locate the geographic positions of lithological units in the imagery classification map (Figure 6-8, 6-9) because of the lack of topographic information. The intensity modulation technique was used to add the topography back to the classification image. Modulated versions of Figure 6-8, 6-9 are shown in Figure 6-10, 6-11.

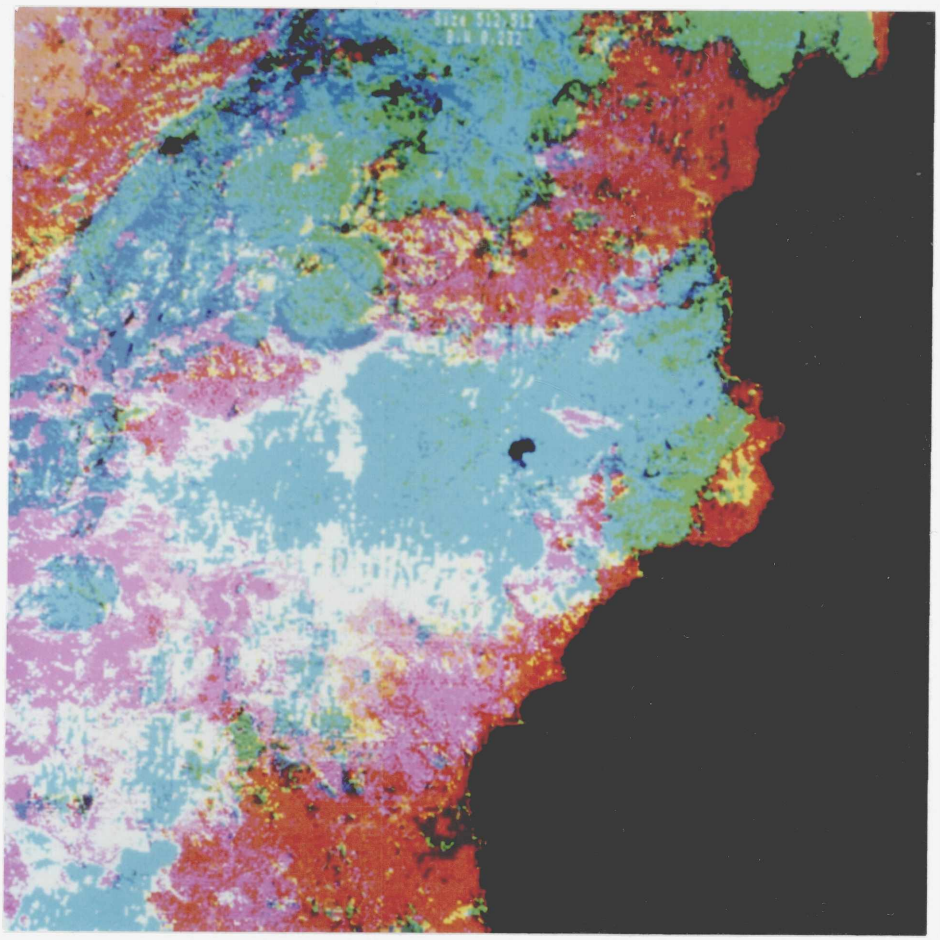


Figure 6-5: Classification image of the test site produced by 3D-FSIC.

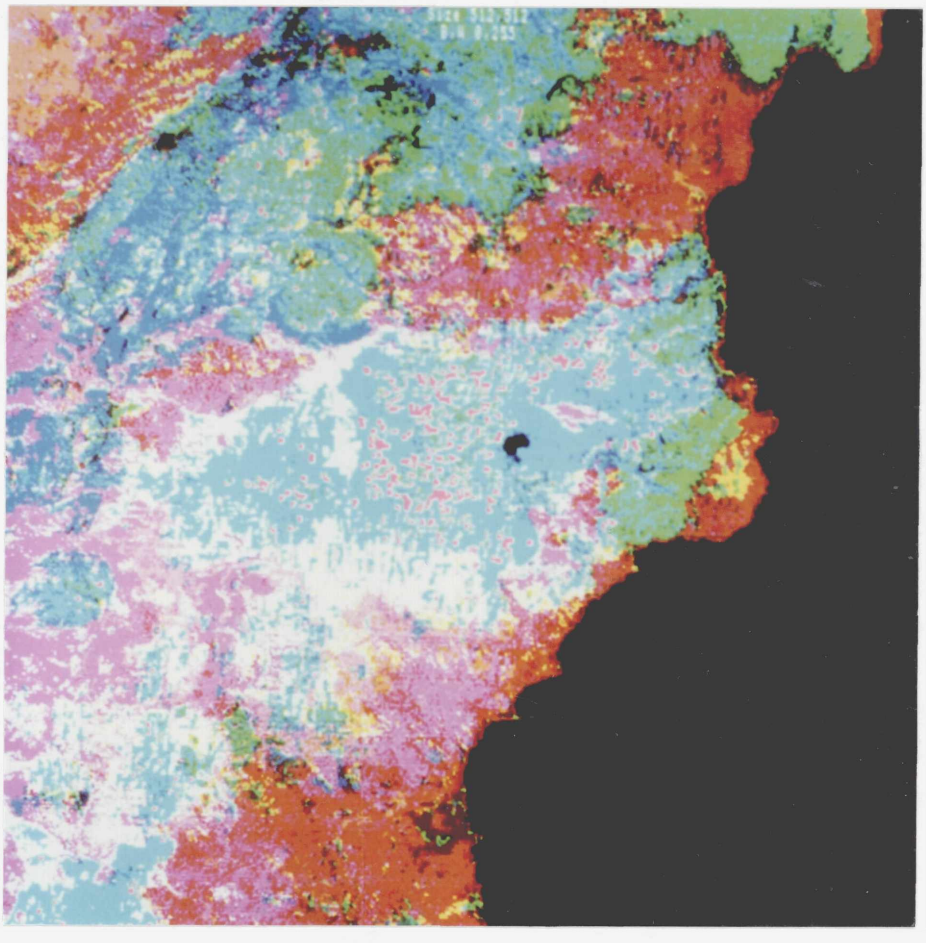


Figure 6-6: Classification image of the test site after THMC processing.

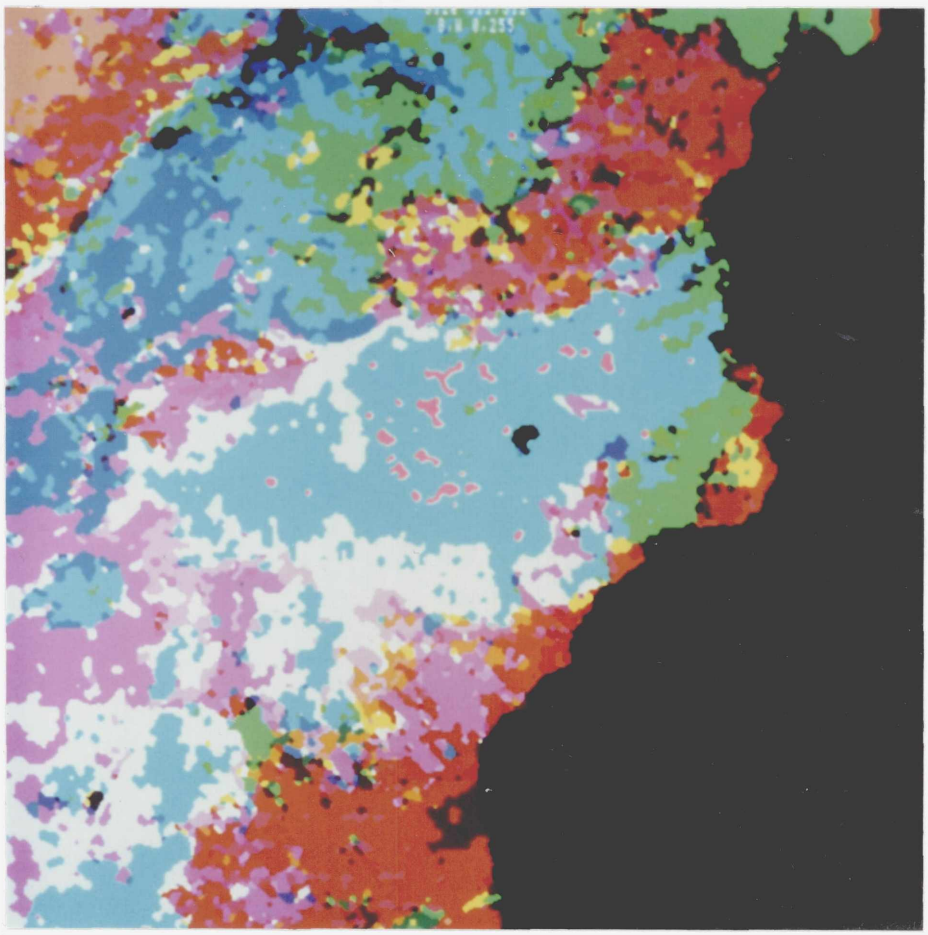


Figure 6-7: Smoothed classification image of the test site produced by IMF and SCM.

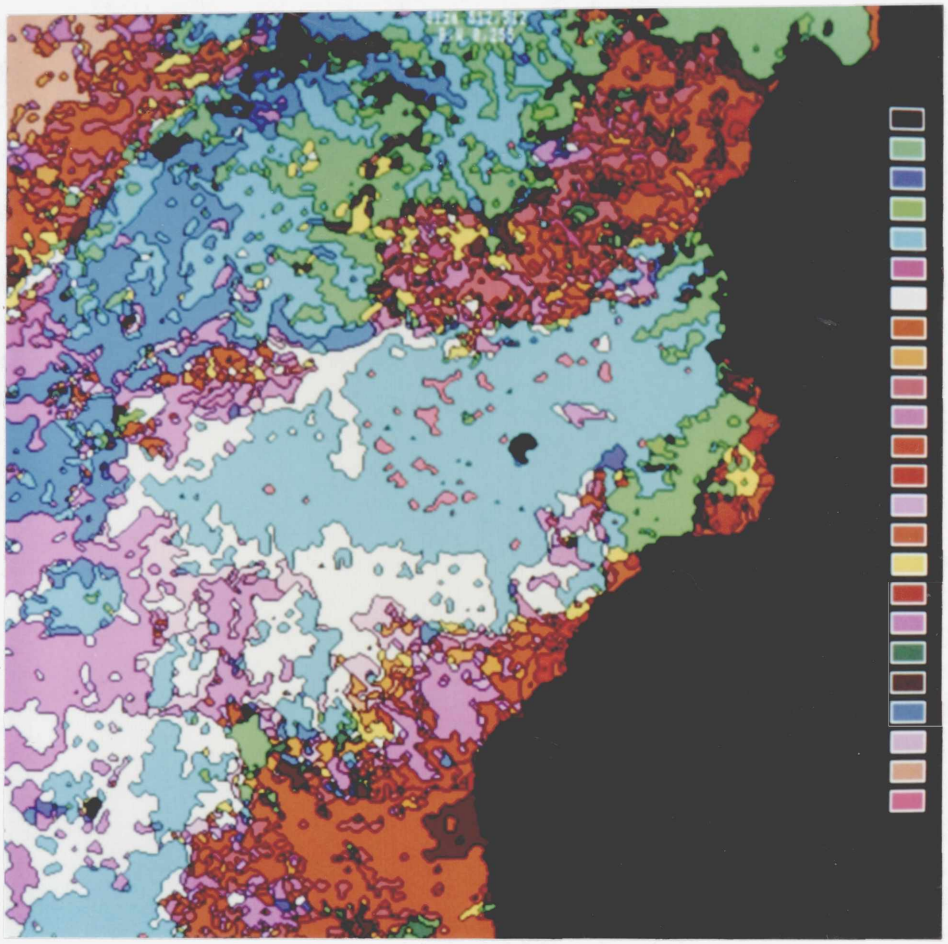


Figure 6-8: The imagery classification map of the test site painted based on the mean vectors of spectral classes.

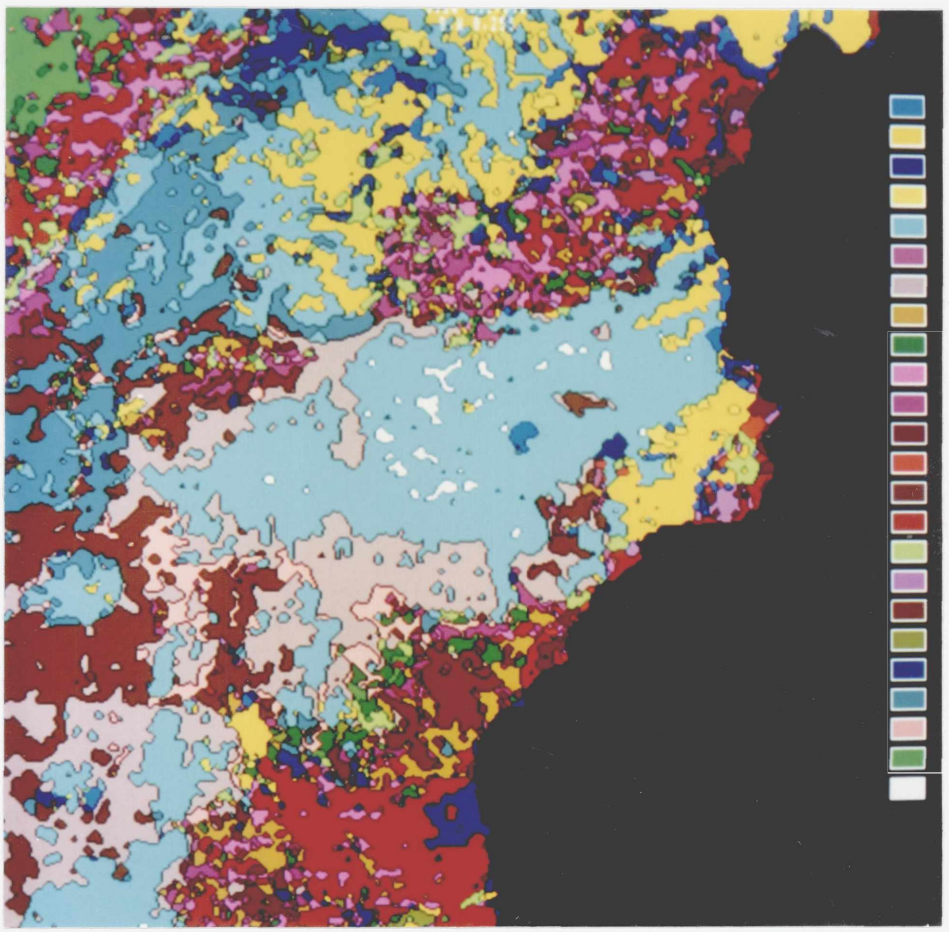


Figure 6-9: The imagery classification map of the test site Painted by interactive colour editing.

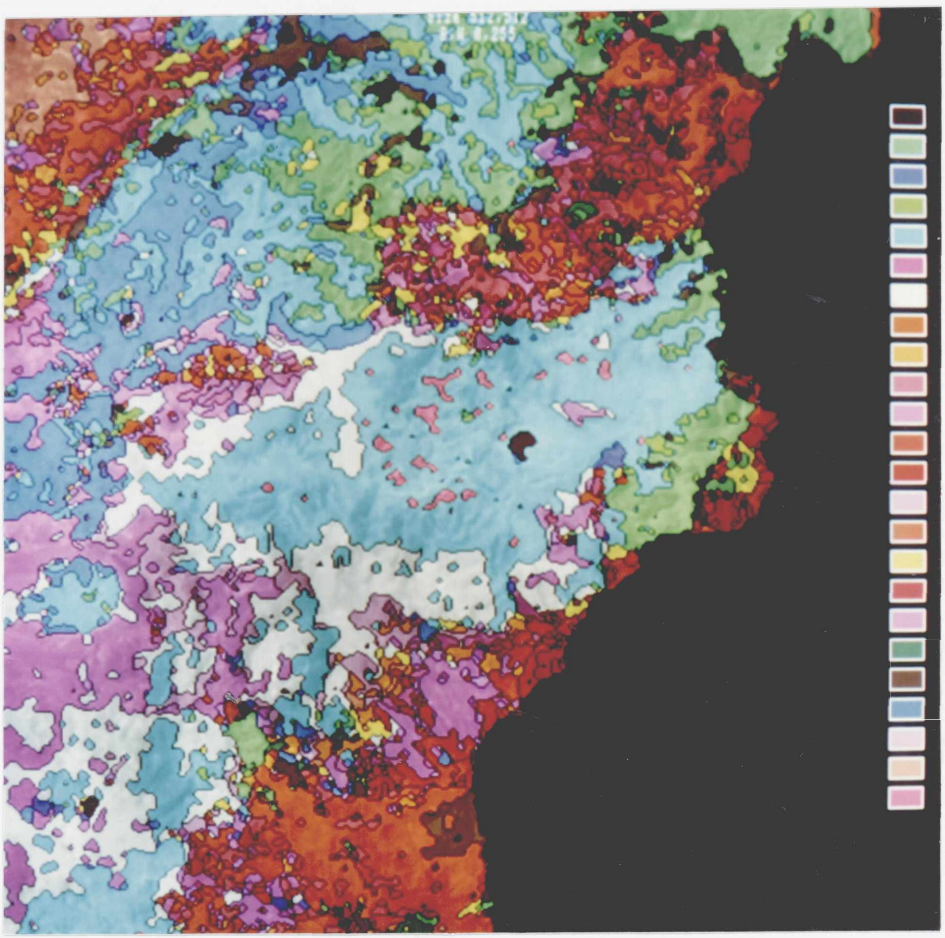


Figure 6-10: Modulated version of Figure 6-8.

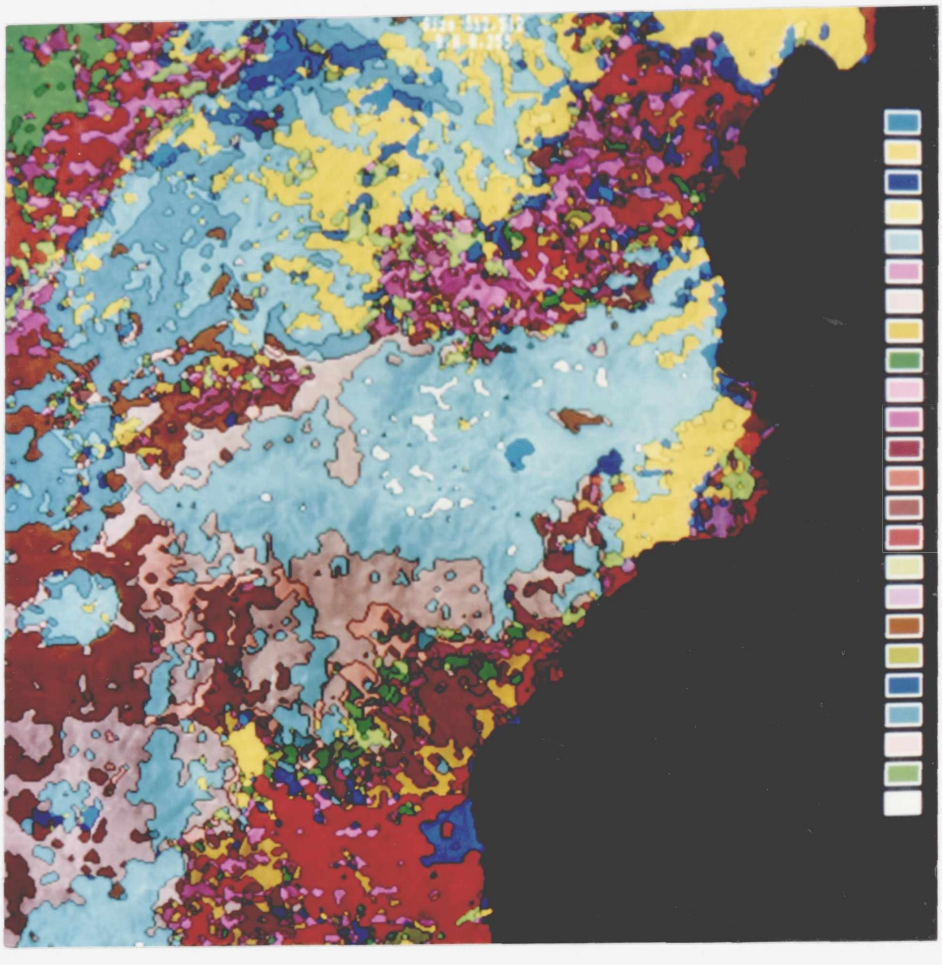


Figure 6-11: Modulated version of Figure 6-9.

6.5 Class Identification and Appraisal of the Lithological Mapping

The imagery classification map (Figure 6-8 or Figure 6-9) cannot be called a lithological map until the classes are correctly identified for their relevant lithologies. The class identification was based on field information, spectral analysis and published 1:50000 scale geological maps together with large scale images such as aerial photographs. As lithological mapping using remotely sensed data is really necessary only for those areas without geological maps or poorly mapped, a practical software for automatic lithological mapping should be able to implement the task without the aid of geological maps. To simulate the situation in this study, the geological maps were used only as a reference for class identification and quality assessment.

The identification and field check for the major lithologies in the area was relatively easy. The same task for those classes with limited distribution was much more difficult as the orientation and accession to the few occurrences of those classes were not alway possible. In this case, spectral analysis is a very useful tool for class identification. The seven TM band spectral shapes of all the classes in the classification map were plotted based on seven TM band mean values of these classes by program CLSMV.

The imagery classification maps painted in the two ways mentioned in previous section were both useful for class identification. The classes representing the same terrain types were grouped according to the spectral similarity shown in Figure 6-8, spatial co-occurrence shown in Figure 6-9 and the analysis of spectral shapes. The details of the class identification and quality appraisal for each rock and terrain types are given below.

1. Andesite (class 10, 12, 15, 17)

Andesite is a major volcanic rock type in the area. It occurs along the east

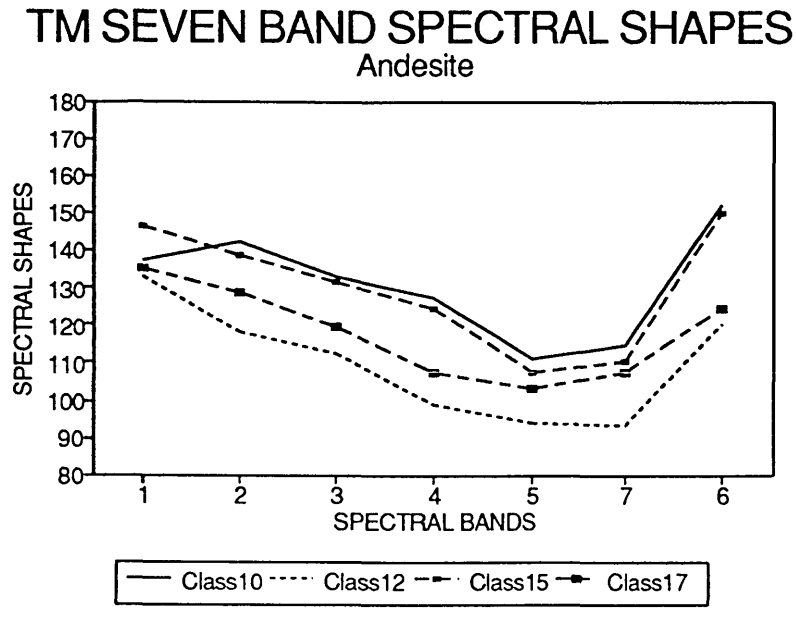


Figure 6-12: TM seven band spectral shape of andesite

coast and in the northwestern corner of the test site. Great variation of this lithology can be seen both in field and on TM imagery. Class 15 and 10 are the major classes (Table 6-6) representing andesite volcanics. The spectral shapes of the two classes are almost identical except in band 1 (Figure 6-12); the difference suggests that the andesite of class 10 is a little bit brownish while that of class 15 is grey blue. Class 12 and 17, both are small classes, have spectral shapes similar to those of class 10 and 15 but with much lower albedo. They may represent darker and more basic andesite such as basaltic andesite. Basically, the spectral shapes of the four classes are quite similar. Their colours in Figure 6-8 are almost identical. They are painted in slightly different colours in Figure 6-9 to display the varieties of andesite. The field check at the major outcrops along the east coast confirmed that these classes were correctly identified. The distribution of these classes in the classification map show very high agreement with the published 1:50000 geological maps (Figure 6-2). The automatic mapping provided the details of the variation of andesitic lithology (four different classes), which need to be further investigated.

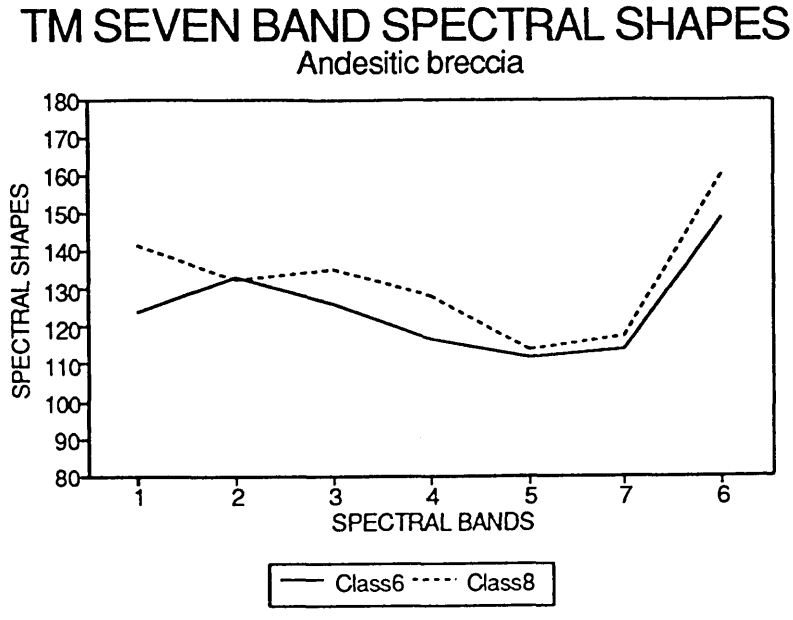


Figure 6-13: TM seven band spectral shape of andesite breccia

2. Andesite breccia (class 6, 8)

Class 6 and 8 both are small classes (Table 6-6) distributing as scattered patches within the andesite terrain. Their spectral shapes (Figure 6-12) correspond to the basic spectral feature of andesite. The field check west of La Isleta indicated that class 8 is andesite breccia with tuff. It was difficult to locate class 6 in the field because the outcrops are small. This class has a similar spectral shape to class 8 and is spatially associated with andesite. These classes are much less wide spread than the breccia presented in the geological maps (Figure 6-2), but the class locations generally coincide with breccia outcrops.

3. Dacite (class 7, 22)

Economically, dacite is a very important lithology in the test site, and is concentrated in the central part of the subscene. Most dacite in the area is altered to some degree. Classes 7 and 22 represent the relatively unaltered dacite surrounding the altered dacite. The spectral shapes of the two classes generally coincide with a little difference in TM bands 4, 5 and 7 (Figure 6-14). The higher reflectance in TM4 and lower reflectance in TM5 and TM7 of class 22 may be caused by vegetation. The distribution of dacite classes generally

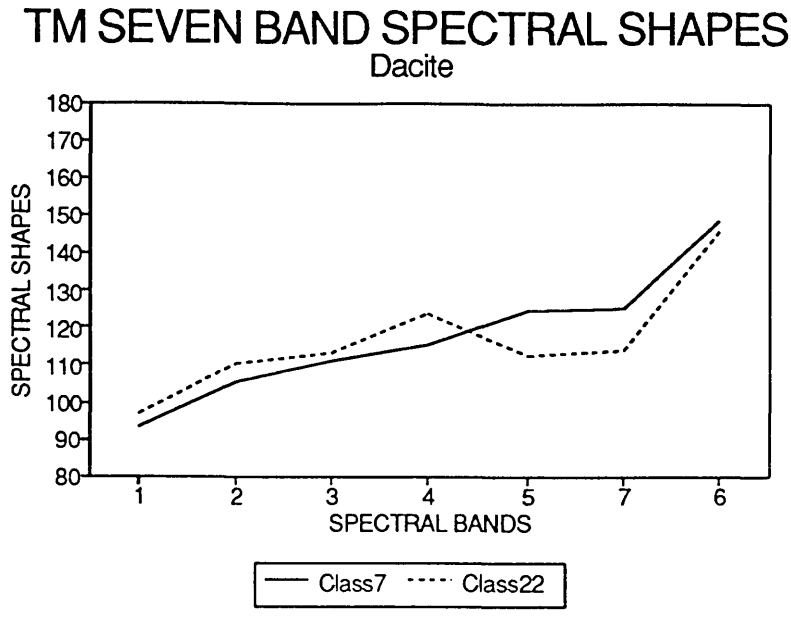


Figure 6-14: TM seven band spectral shape of dacite

agrees with the published geological maps (Figure 6-2) and was verified by field check. In the wide valleys among the hills of altered dacite, class 7 coincides with the red residual soil derived from dacite.

4. Altered volcanics (class 5)

Class 5 defines silicified dacite with kaolinite and illite alteration. This is the host rock of epithermal gold deposits within the dacite terrain in Rodalquilar area. Class 5 also shows the silicified andesite in the southwestern corner of the subscene. The coincidence between class 5 and the altered volcanics in the published geological maps (Figure 6-2) is significant. The peak in TM5 and high reflectance in TM7 of the spectral shape of class 5 (Figure 6-15) indicate the concentration of clay minerals and quartz and is explained by silicification and kaolinization in the dacite and andesite defined by class 5. The higher reflectance in TM3 than in TM1 and TM2 implies that the terrain types represented by class 5 is quite reddish and iron rich on surface. This is true for the altered volcanics in this area according to the field observation. Class 5 shows rather low agreement to the geological maps (Figure 6-2) in the basin area, in the northwestern part of the test site, where the class coincides with

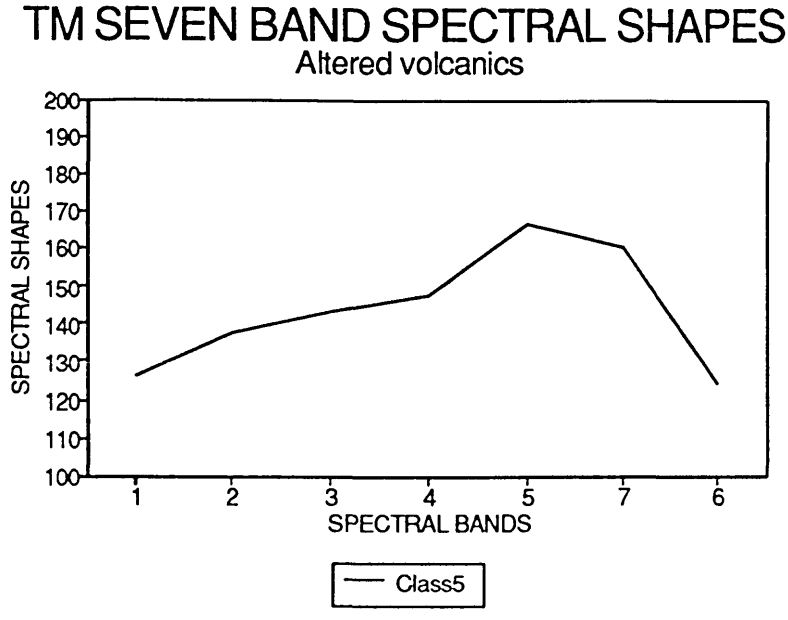


Figure 6-15: TM seven band spectral shape of altered volcanics

some quartz and iron rich alluvial deposits.

5. Epithermal alteration zones (class 24)

This class is a textural class detected by THMC. It corresponds to the active gold mining area and epithermal alteration zone. The scattered patches of class 24 form a circular feature (west of Rodalquilar) surrounded by class 5 (altered dacite) with class 7 and 22 (unaltered dacite) marking its periphery. This three ring concentric structure implies that class 24 may define an hydrothermal centre in dacitic volcanics. The information confirms the opinion of geologists (P. Hernandez, 1989).

6. Limestone (class 2, 4)

Miocene limestone formed after the main volcanic eruption period is another major rock type in the test site. It spreads in the north and east part of the area, sometimes occurs as caps on the top of volcanic hills. Class 2 and 4 show the distribution of limestone very accurately and match the geological map (Figure 6-2) very precisely. Class 2 is the major class representing limestone. Class 4 commonly occurs at the margins of limestone and other

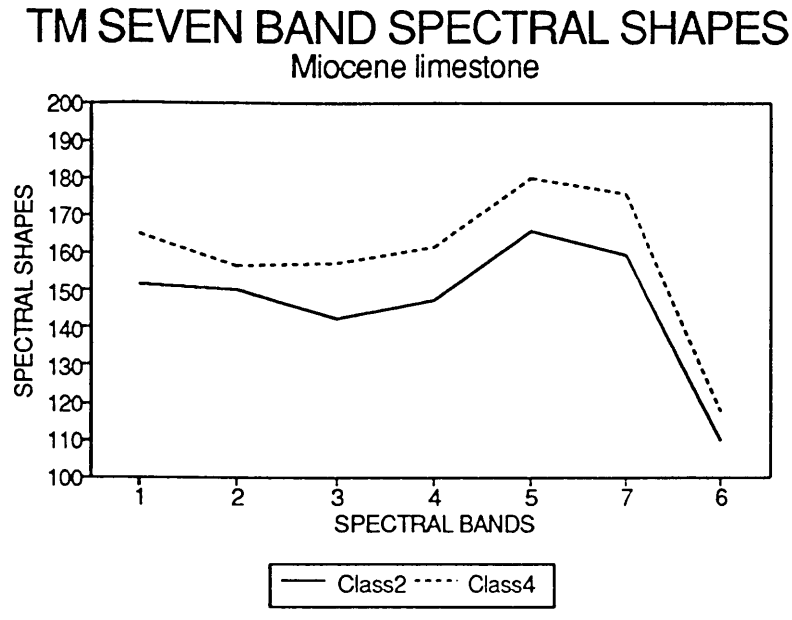


Figure 6-16: TM seven band spectral shape of limestone

lithologies and spectrally resembles class 2 with slightly brighter albedo (Figure 6-16). The field check for limestone was easy. The class 2 and 4 were fully confirmed as limestone with the only exception in the valley at the south side of Rellana Gata (the major crater in the image) where the ground truth of class 2 is bentonitic volcanic tuff. This small area is incorrectly mapped as colluvial deposit in the published geological map (IGME, P0330 Frailes [1060]).

7. Carbonate calcrete (class 16)

With lower albedo, the spectral shape of class 16 (Figure 6-17) agree with the general trend of the spectral shape of class 2 except in TM6 where class 16 shows high emissivity. The phenomenon implies that the material represented by class 16 has a similar mineral composition to limestone but darker appearance. Occurrences of this class are often associated with volcanic rocks even though it resembles limestone spectrally. In the field check on the top of Puntazo de Piedra Negra, the class was found to be carbonate calcrete (duricrust) on the surface of jointed andesite (Figure 6-18). It is thus reasonable to consider class 16 as carbonate calcrete. Further field work is needed to confirm fully of the distribution of this class.

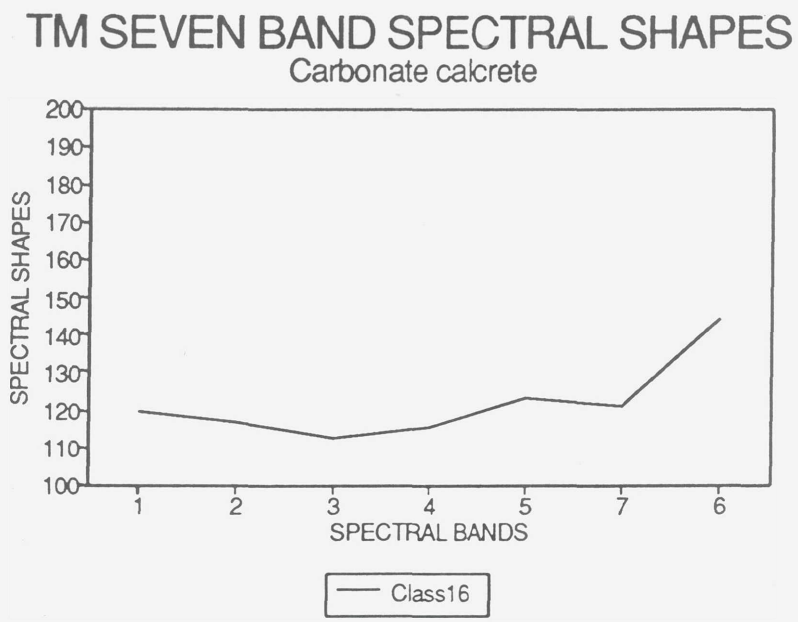


Figure 6-17: TM seven band spectral shape of carbonate calcrete



Figure 6-18: Outcrop of andesite with carbonate calcrete surface. Taken on the top of Puntazo de Piedra Negra

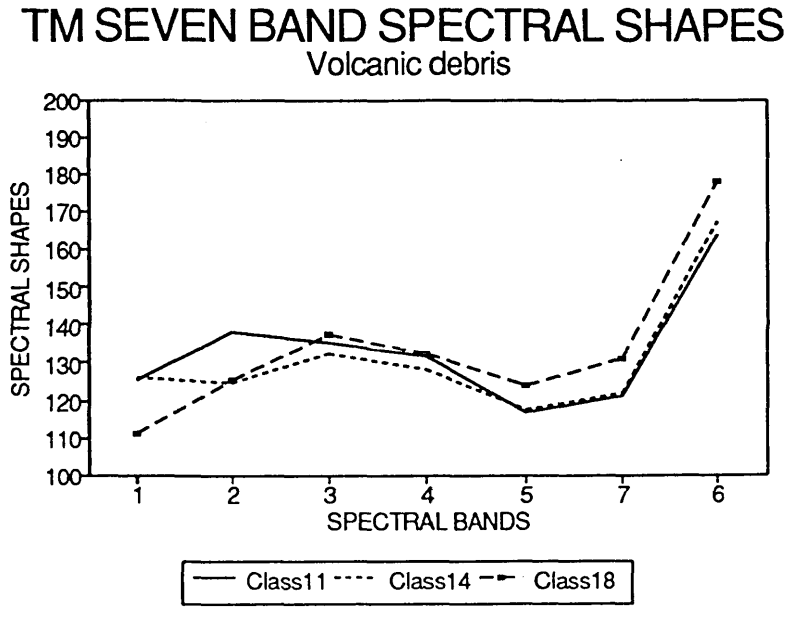


Figure 6-19: TM seven band spectral shape of volcanic debris

8. Volcanic debris (class 11, 14, 18)

Apart from small differences, the spectral shapes of class 11, 14 and 18 are generally similar (Figure 6-19) and the spatial occurrences of them are associated. Class 18 is the major class of this group (Table 6-6). These classes occur mainly on the slopes surrounding volcanic hills coinciding with the mapped colluvial volcanic debris. The field check on the east slope of Rellana crater and around Cerro Blanco confirmed this identification. The volcanic debris is reddish, on dry flat slopes (class 18 and 11) and dark grey in valleys (class 14).

9. Old alluvial sedimentary (class 3 and 21)

Class 3 is a very small class (Table 6-6) and considered as a similar terrain type to class 21 according to its spectral shape (Figure 6-20) and spatial association. Class 21 is mainly in the basin area in the northwestern part of the subscene. The geomorphological position and spatial shape of the class indicate that it is related to the superficial deposits. Field checks confirmed that class 21 and class 3 represent old alluvial gravels, sands and clays forming river terraces and slope washes.

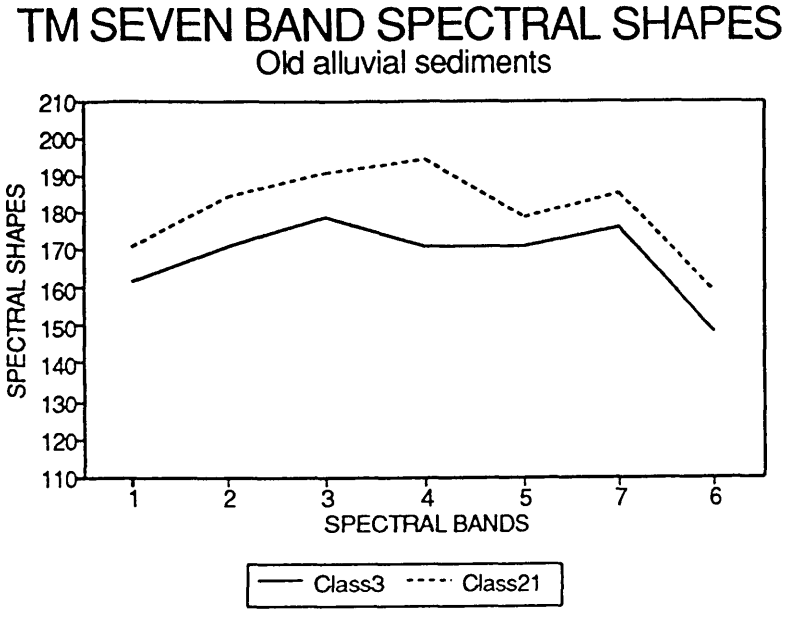


Figure 6-20: TM seven band spectral shape of old alluvial sediments

10. Recent alluvial sedimentary (class 19 and 20)

The spectral shapes of the two classes are almost identical in infrared and thermal bands. Class 20 is brighter than class 19 in the three visible bands (Figure 6-21). The two classes usually occur together. They coincide with water channels and debris aprons in both field checks and geological maps. The recent alluvial sediments composed of sands and gravels are often moist or near a stream and thus support healthier vegetation than other terrain types in this semi-arid area. This is demonstrated by the dip in TM3 and peak in TM4 in the spectral shape of classes 19.

11. Fine sand (class 1)

Class 1 shows the sand beaches, dry river beds and the abundant mining tailing at Rodalquilar very precisely. Its spectral shape explains bright appearance caused by high concentration of quartz in sand (Figure 6-22).

12. Vegetation (class 9, 23)

The spectral shapes of the two classes (Figure 6-23) show the main characteristics of the generalized spectral signature of vegetation (Figure 6-24). This

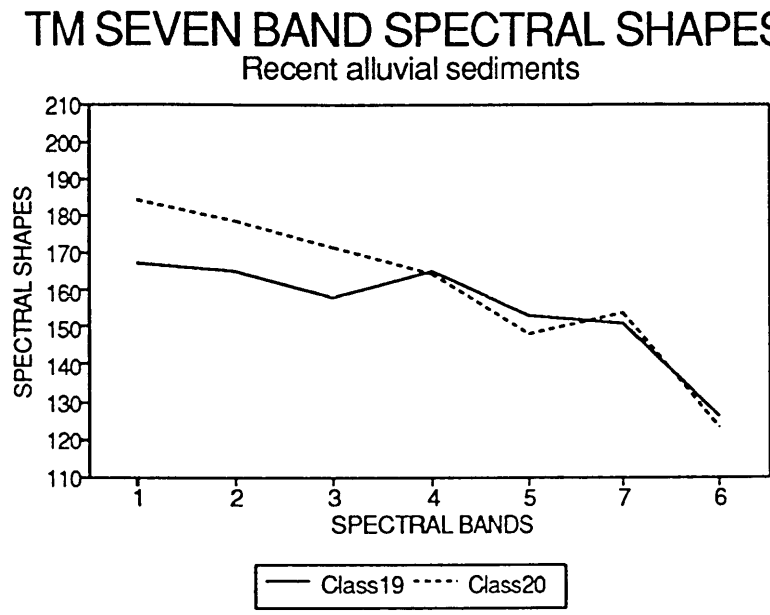


Figure 6-21: TM seven band spectral shape of recent alluvial sediments

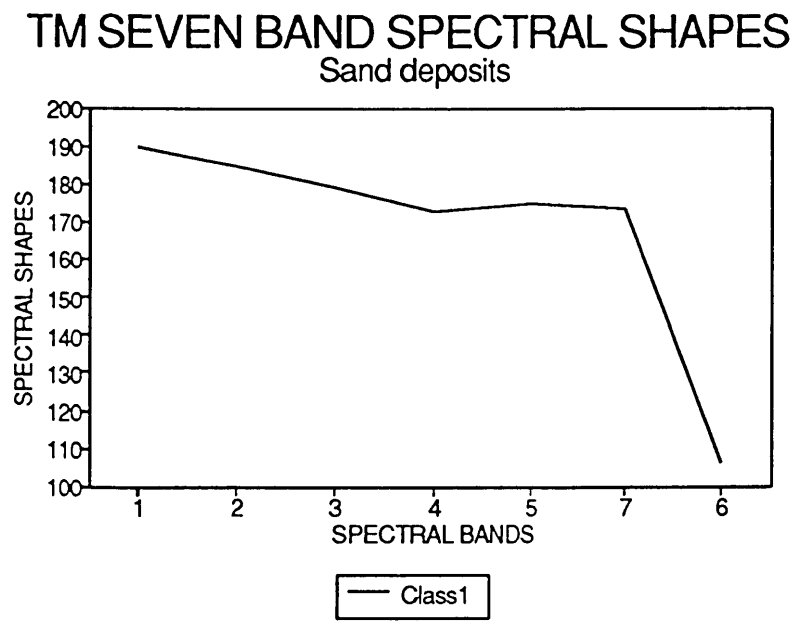


Figure 6-22: TM seven band spectral shape of fine sand

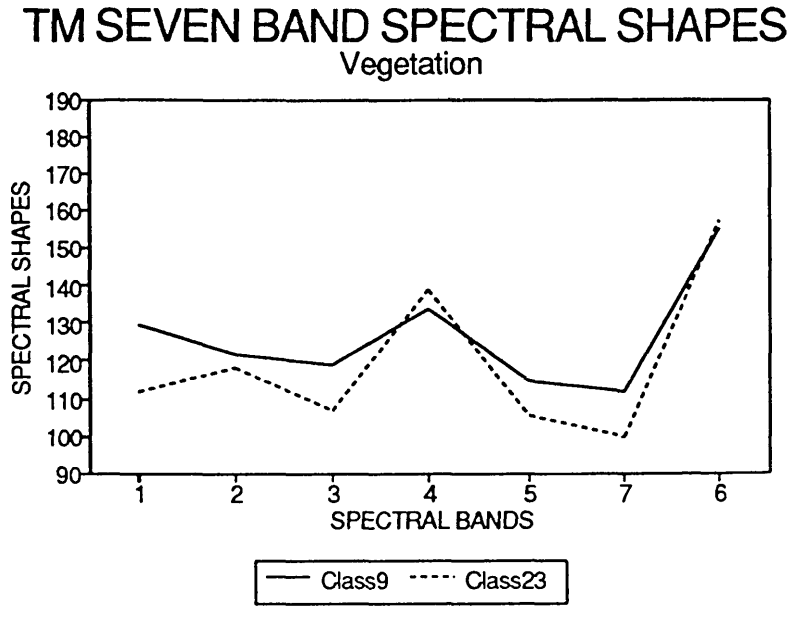


Figure 6-23: TM seven band spectral shape of vegetation

includes peaks in TM2 (green) and TM4 (near infrared), although they are not directly comparable with laboratory curves. Class 9 defines the horticulture area in the NW corner of the subscene. The plastic sheeting used to cover the horticultural areas causes higher reflectance in blue band (TM1) than in green and red bands (TM2 and TM3) in the spectral shape of class 9. Class 23 indicates concentrated natural vegetation, such as bushes and trees in valleys.

After class identification, the imagery classification map (Figure 6-8) was further simplified by uniting the classes identified as the same lithologies. The processing of boundary detection and colour editing (conventional colour scheme for geological maps was used as reference) as well as intensity modulation was then re-performed. Finally, a concise and informative imagery lithological map (Figure 6-25) and its intensity modulated version (Figure 6-26) were achieved, in which 11 lithologies (7 solid rock types and 4 superficial deposits) and vegetation are well illustrated (Table 6-7).

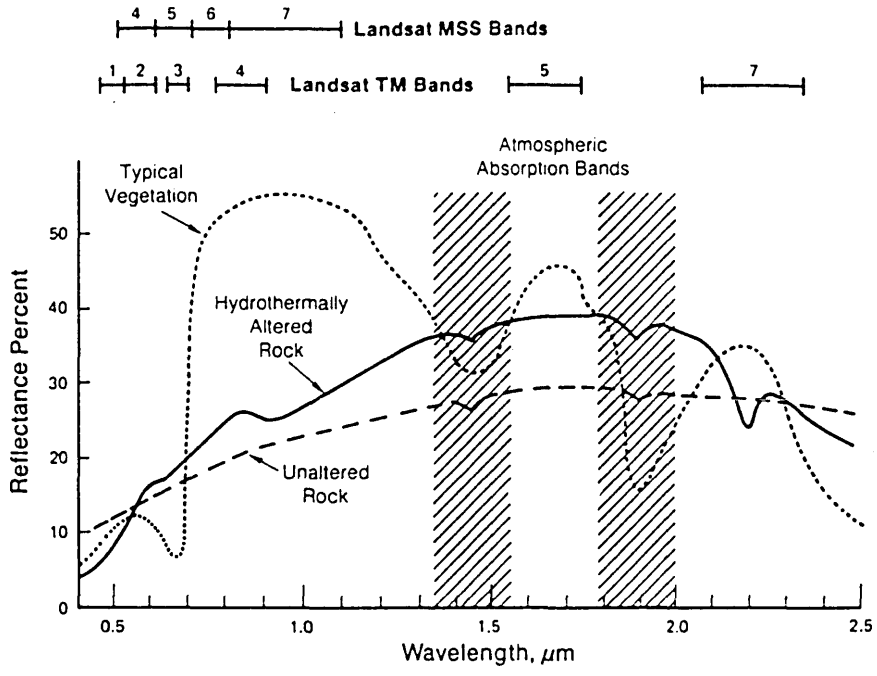


Figure 6-24: Generalized spectral signatures of vegetation, soil, rock and alteration. (Quot. from Sabins, 1986)

Table 6-7: Pixel numbers of lithologies and vegetation in the imagery lithological map of the test site.

Label	Description	Pixels
0	Sea (not classified)	80000
1	Andesite	2744
2	Andesite breccia	17982
3	Dacite	1200
4	Altered dacite	2071
5	Epithermal alteration zones	45327
6	Limestone	1939
7	Carbonate concrete	21073
8	Volcanic debris	5222
9	Old alluvial sedimentary	2720
10	Recent alluvial sedimentary	6953
11	Fine sand deposits	4815
12	Vegetation	2197

Figure 6-25: The imagery lithological map of the test site.

Figure 6-26: The imagery lithological map of the test site (with intensity modulation).

6.6 Summary

A 512 × 512 TM subscene of Cabo de Gata area in SE Spain was selected as a test area for experimental automatic lithological mapping. This included the following steps:

1. **Pre-classification enhancement** Band-triplets: 6 7 5, 5 4 3 and 3 2 1 were selected, based on IOBS and experiment, for hue image derivation. BCET was used to eliminate colour bias in the colour composites of the three band-triplets as a preparation of HRGB colour composition. Finally, a shadow free HRGB image with good spectral discrimination of lithologies was produced.

2. **Spectral classification** Unsupervised spectral classification were performed by 3D-FSIC to classify the image pixels of the TM subscene into spectral classes according to their hue values in the three hue images forming the HRGB image. The classification started with 20 seeds (the data points with highest frequence in the 3D scattergram of the three hue images selected by ASST programme) and ended with 23 spectral classes after 6 iterations.

3. **Post-processing of spectral classification**

   - Supervised textural re-classification using THMC. The epithermal alteration zones with gold deposits, which is characterized by a class spatial pattern: class 5 as background with spots of class 2 and 4, were effectively detected as class 24.

   - Smoothing and small class merging. The classification image was spatially smoothed by IFM. The classes with less than 500 pixels were then merged into the spatially and spectrally nearest larger classes by SCM. As the result, class 13 was deleted.

   - Boundary detection. Class boundaries were detected and added into the smoothed classification image by CBD technique. The key boxes were

added.

- Colour editing. The classification was initially painted in the colours encoded by the mean vectors of the spectral classes. Further colour editing was carried out to display similar terrain types in similar but distinct colours.

4. **Class identification and assessment** With the processing above, a classification map with 22 spectral classes and one textural class was produced. The classes were then grouped and identified as terrain types using field evidence, spectral analysis and published 1:50000 geological maps. As the result, the 23 classes were identified as 7 solid rock lithologies, 4 superficial deposit types, and vegetation. Finally, an imagery lithological map illustrating 11 lithologies and vegetation was produced after further simplification and re-performing the boundary detection and colour editing procedure. The lithological map shows high agreement with the published geological maps and has been verified by field checking.

Chapter 7

Regional Lithological Mapping in SE Spain

After the experiment of automatic lithological mapping of the 512×512 TM subscene test site, the same techniques were applied to a larger TM subscene of 1792×1536 pixels (Figure 7-1) extracted from the same TM quarter scene image of SE Spain. This larger subscene includes the test site, thus the image processing parameters used in the experimental processing can be used directly or as references. Information provided by the lithological mapping of the test site was applied to monitor and control the image processing of the larger subscene.

There are many more lithologies in this larger area than in the test site. They include metamorphic, volcanic and sedimentary rocks, and superficial deposits. The area is lithologically representative of SE Spain and a suitable test of the effectiveness of the techniques developed in this project, for the automatic lithological mapping of semi-arid areas.

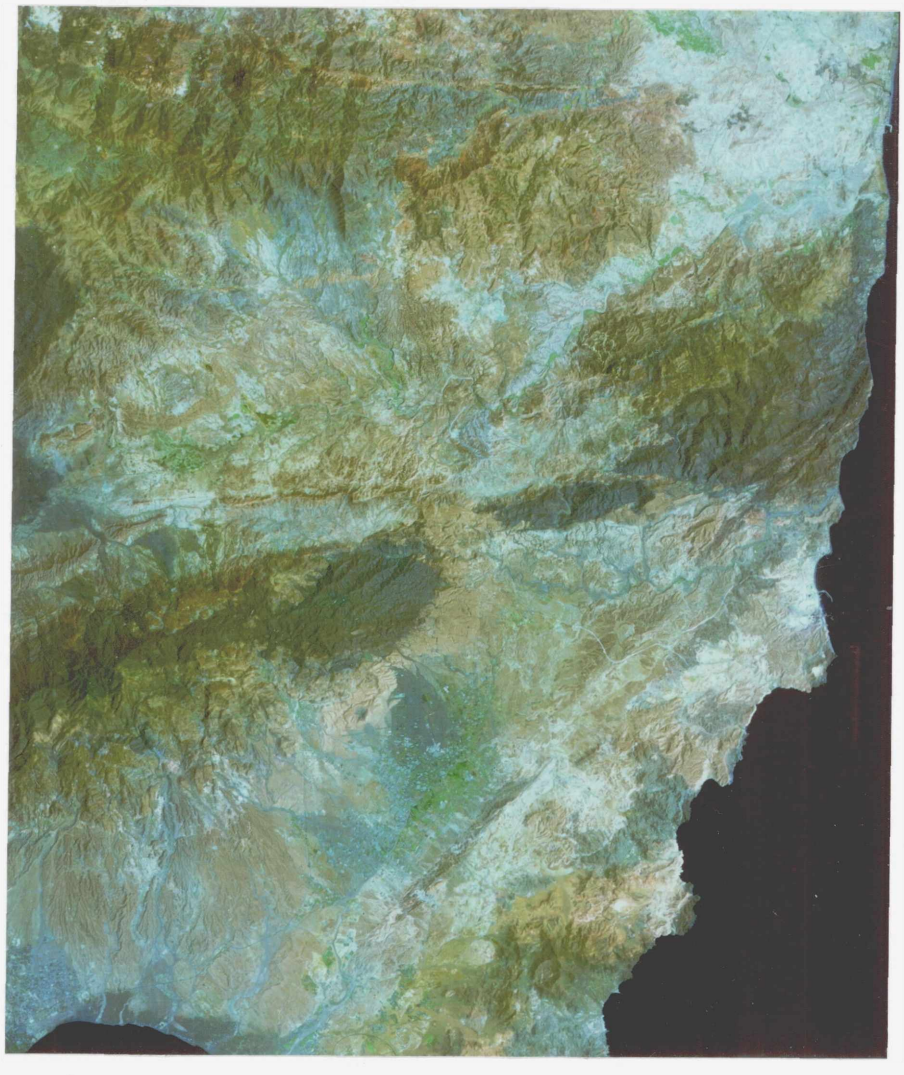


Figure 7-1: A Landsat TM colour composite image of the study area in SE Spain. TM5 in red, TM4 in green and TM1 in blue.

7.1 Introduction to the Regional Geology of the Area

The 1792 × 1536 pixel TM subscene covers an area of about $2477km^2$ in Almeria Province, Spain (Figure 6-1). It extends from the west end of Sierra de Alhamilla to the east coast facing the Mediterranean Sea and from Vera basin in the north to El Alquian in the south. The area is represented in parts of ten 1:50000 scale geological maps as shown in Figure 1-3.

The area is composed of mountain ranges and inter-montane basins elongated WSW-ENE in the southern unit of the Betic Cordillera. It contains several tectonic units (Crosta, 1989): the Nevado-Filabrede Complex, the Alpujarride Complex, late Tertiary basins and a Tertiary volcanic complex.

The Nevado-Filabride Complex is the basal unit of the Betic tectonic sequence and forms the core of the mountain ranges in the area. It comprises a Hercynian and Alpine metamorphic nappe complex of great thickness. Mica-schists, quartzites and gneiss are the major rock types of this unit.

The Alpujarride tectonic unit is the major Alpine nappe complex of the Betic Cordillera (Ager, 1980). It contains Lower Paleozoic units of mica-schists and quartzites and Permo-Triassic phyllites, quartzites and dolomites, forming mantles on the flanks of the Nevado-Filibride metamorphic mountain ranges.

The Tertiary basins between the mountain ranges were formed by extension on re-activated faults of the wrench thrust and oblique slip system created during the Alpine collisional orogeny. The uplift mountains and basins subsidence caused rapid erosion and marine incursion. This resulted in thick molasse and marine sedimentary deposits in the basins. Volcanic eruptions along the south east coast formed the Cabo de Gata volcanic complex which may also related to the extensional activity.

The mountains and basins in the area from south to north are briefly described as follows (Figure 6-1).

Tertiary volcanics formed Sierra de Gata extending along the south east coast from Carboneras SW toward to Cabo de Gata. Andesite, dacite and breccia are the major rock types of this volcanic belt. The volcanic belt is bounded in its northwestern side by a NE trending fault zone, the Carboneras fault.

Another mountain belt, Sierra de Alhamilla and Sierra Cabrera, in the central part of the subscene is a thrust block of Mesozoic and pre-Mesozoic strata raised during Alpine tectonic movement. The block is composed of two stratigraphic units: phyllites, quartzites, dolomite and gypsum in Permo - Triassic unit; and carbonaceous mica-schists, mica-schists, gneiss and marble of the Nevado-Filibride unit.

The Almeria - Carboneras basin lies in the corridor between the above two mountain ranges with both ends open to sea, extending in to the WSW-ENE direction. The basin is filled by Miocene to Pliocene marine deposits, limestone, dolomite and marls, with a covering of Quaternary alluvial deposits.

The major mountain range, Sierra de Filabres, appears in the north of the subscene. The mountains are composed of metamorphic strata including Permo - Triassic phyllite, quartzites, dolomite, marble and gypsum and Pre-Cambrian to Paleozoic mica-schist and gneiss.

Between Sierra de Filabres and Sierra de Alhamilla as well as Sierra Cabrera, there is another narrow inter-montane basin, the Tabernas-Sorbas basin. The basin contains Miocene molasse deposits and Pliocene alluvial deposits.

Raised by Alpine tectonic movement after Miocene, the molasse formed high level terraces that were then intensively eroded producing bad land erosional terrain. The Pliocene deposits are mainly semi-consolidated sand and gravel cemented by mud and calcite.

North east to the east end of Sierra de Filabres, is Vera basin also containing marine deposits and recent river deposits.

The economic mineral deposits in the area include the gold deposit in volcanic belt described in last chapter, massive gypsum layers in Miocene strata and marble in metamorphic mountain areas together with abandoned small iron and other metallic mineral deposits.

7.2 Image Processing

The image processing of this subscene is basically the same as that of the test site. The discussion will focus on those aspects that are different. The illustrations shown in this chapter were all taken from re-sampled 897 $\times$ 768 display by camera except the colour composite of TM band-triplet 5 4 1, the HRGB image and the final imagery lithological maps that were a product of photo writing with full resolution.

7.2.1 Pre-classification image enhancement

The band-triplet selections for HRGB are the same as those of test site as shown in Table 3-8.

As mentioned in section 3.2.4 of Chapter 3, the colour balance of a colour composite is scene dependent. Therefore, the colours of the test site in a colour

composite of the large TM subscene are not exactly the same as the colours of the same colour composite of the 512 × 512 subscene of the test site even if the same parameters are used in BCET processing. The spectral character of the wide-spread metamorphic rocks changes the colour balance of the large subscene. As a result, the HRGB imagery DN value range of altered dacite (that is a major terrain type in test site but a minor one in large subscene) is narrowed and resembles Miocene limestone so that effective discrimination of these two important rock types becomes very difficult for 3D-FSIC. To solve the problem, the local BCET (LBCET, Appendix A) was used instead of general BCET. In this case, BCET functions for each of seven TM bands were derived from the test site and then applied to the whole large subscene. With LBCET, the colour composites of the large subscene may not be really colour balanced. However good spectral discrimination between altered dacite and Miocene limestone achieved in the 512 × 512 subscene of the test site is well preserved.

After LBCET processing, HRGB images were derived from the band-triplets shown in Table 3-8 by RGB-IHS transformation (Figure 7-2).

7.2.2 Spectral classification

17 seeds (Table 7-1) were selected from the 3D scattergram of the three hue images of the large subscene by ASST program. Then the unsupervised clustering classification was performed by 3D-FSIC. A cosmetically good result (Figure 7-3) was obtained by using the following parameters:

SPLIT=10, UNITE=4, ITERATION: 1 Euclidean, 8 Euclidean OMPR.

The iteration information is given in Table 7-2. 39 spectral classes were resulted (Table 7-3).

The Gaussian OMPR decision rule was not used in this case because the low processing speed prevented testing many different parameter sets to achieve the best discrimination of lithologies in the subscene.

7.2.3 Post-classification processing

The THMC was not applied to the large subscene. The spectral classification image was smoothed by IMF (8 iterations and majority=5). As shown in Table 7-4, several classes which had significant numbers of pixels became very small after IMF because most pixels of these classes are scattered and isolated points representing noise. Thus SMC was used to eliminate such small classes. The classes with less than 5060 pixels were merged. the criterion 5060 was deliberately selected to delete six small classes (class 7, 22, 24, 30, 34 and 38) having a scattered appearance in Figure 7-3, but retain the class 15 with 5188 pixels, which is distributed in concentration and shows the mine tailings in Rodalquilar. The number of classes was reduced to 33 by SCM. The IMF and SCM processing effectively eliminated the noise in the classification image and produced a well smoothed image (Figure 7-4). The class labels and pixel numbers before and after IMF and SCM are shown in Table 7-4.

The smoothed classification image was further treated by two class editing techniques after the spectral classes had been identified in terms of lithology and terrain types. Firstly, the classes corresponding to more than one rock and terrain types were edited by CRED programme. A class representing different rock and terrain types in different regions was spilt into several classes by CRED according to the regions where the pixels of the class appear. As a result, the total class number increased to 37. The CGR programme was then applied to merge two or more classes corresponding the same rock or terrain type.

Finally, the class boundaries were detected and added, with key boxes, to the classification image by programme CBDKB (Appendix A) followed by colour painting. The interactive colour editing cannot be performed on the scene larger than 512×512 on the image processing system used in this project. Thus, for this large subscene, the interactive painting was firstly performed on the 512×512 re-sampled scene of the classification image by IPAINT. Then the colour code file generated by interactive painting was used to produce three images from the classification image by PAINT programme (Appendix A). The colour composite of the three images will display the classification image as it is painted in the re-sampled 512×512 scene.

Intensity modulation was also applied to add topography back to the final product.

7.3 Class Identification for Lithological Mapping

The identification of the spectral classes in terms of lithology was based on field work, published 1:50000 scale geological maps and the analysis of class spectral shapes.

The correlation between terrain types and spectral classes in this large subscene is not simple. The class identification was carried out with the aid of CRED and CGR. The 33 spectral classes in the classification image were regionally split into 37 classes and then merged into 24 classes corresponding to different lithologies and terrain types.

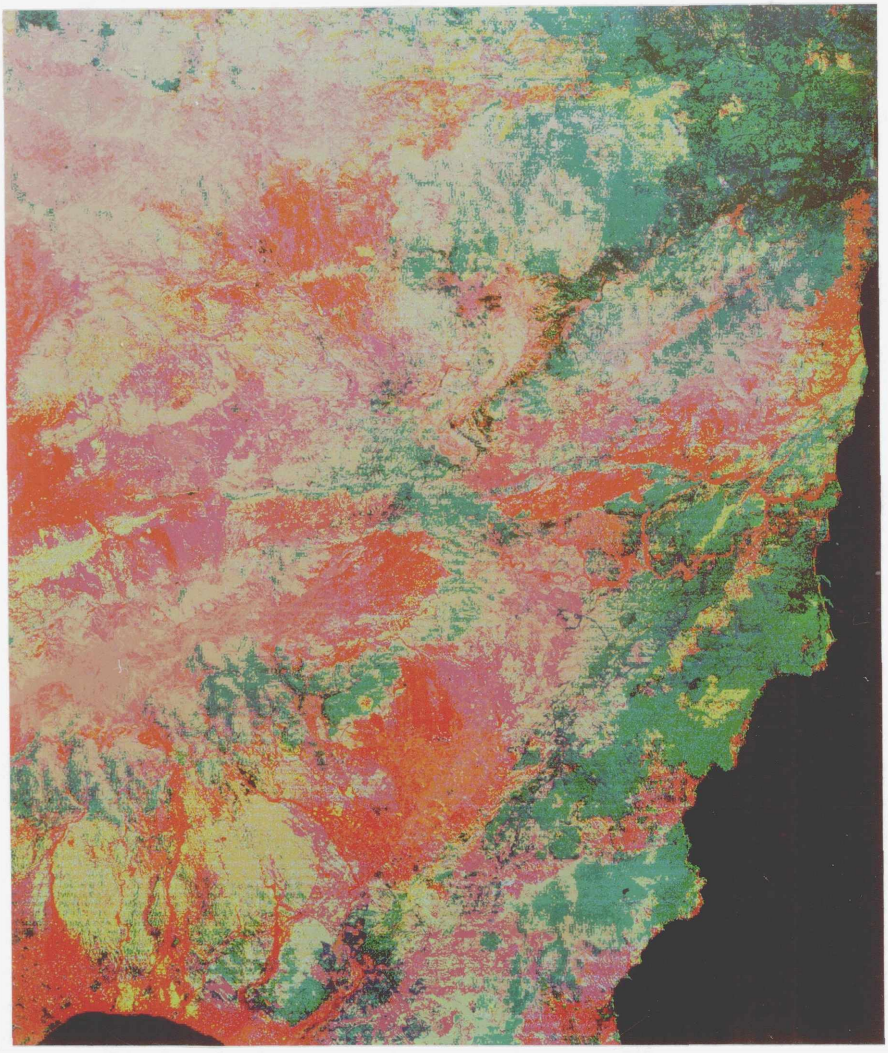


Figure 7-2: The HRGB image of the study area.

Table 7-1: Hue DN values of the initial centres for clustering classification based on the HRGB image of the study area.

	PIXEL VALUES OF SEEDS FOR CLUSTER		
	Hue675	Hue543	Hue321
1	174.00	130.00	130.00
2	174.00	138.00	130.00
3	170.00	26.00	26.00
4	170.00	22.00	26.00
5	174.00	106.00	130.00
6	170.00	30.00	26.00
7	174.00	150.00	130.00
8	174.00	126.00	130.00
9	174.00	114.00	130.00
10	174.00	122.00	130.00
11	174.00	118.00	130.00
12	170.00	30.00	30.00
13	174.00	94.00	130.00
14	170.00	26.00	22.00
15	174.00	98.00	130.00
16	170.00	22.00	18.00
17	170.00	26.00	38.00

Table 7-2: Iteration information of the clustering classification using three hue images (the HRGB image) of the study area.

Decision rules	Iteration times	Class born	Class died	Total class	Maximum migration
Seed file	0	-	-	17	-
Euclidean	1	16	7	26	15.8090
Euclidean OMPR	2	5	0	31	10.8904
	3	5	0	36	3.8893
	4	2	0	38	6.4763
	5	1	0	39	2.7513
	6	0	0	39	2.8081
	7	0	0	39	2.1717
	8	0	0	39	1.6372
	9	0	0	39	1.2030

Table 7-3: Statistics of the clustering classification of the study area

STATISTICAL DATA OF CLASSIFICATION

No.	MEAN VALUES			SD			CORRELATION			PIXEL
	H675	H543	H321	H675	H543	H321	CR_{12}	CR_{13}	CR_{23}	
1	182.3	129.1	89.6	21.1	13.3	14.6	0.26	0.002	-0.11	77805
2	181.4	142.0	130.6	18.0	10.4	11.2	0.09	-0.01	-0.05	246492
3	123.8	27.3	33.0	16.3	14.2	18.1	-0.05	-0.04	0.08	21157
4	168.4	23.7	46.0	7.9	10.1	11.0	-0.02	0.02	0.16	102704
5	170.2	70.8	122.7	9.8	11.6	13.1	0.02	0.01	0.02	131367
6	180.1	97.2	28.4	18.8	16.7	15.6	-0.05	0.05	0.02	37107
7	166.4	216.6	228.5	19.8	23.0	21.4	-0.06	0.04	-0.09	6972
8	174.8	77.1	75.8	14.4	14.1	12.9	0.10	-0.01	0.09	67057
9	172.0	52.8	34.3	10.3	9.7	13.4	0.02	-0.07	-0.16	77480
10	165.6	35.1	142.0	10.8	14.2	14.6	0.03	-0.06	0.07	157021
11	169.1	26.4	16.8	8.8	10.7	8.1	0.02	-0.03	-0.14	130023
12	177.5	106.9	130.9	13.5	10.6	12.2	-0.00	0.02	-0.07	189776
13	166.8	32.5	91.6	10.4	13.2	13.9	0.01	-0.03	-0.06	115999
14	41.5	131.5	81.3	16.9	13.5	14.8	-0.10	0.06	-0.08	33468
15	41.6	168.9	231.8	15.0	28.6	16.6	0.18	0.02	-0.03	17912
16	54.8	30.2	49.3	12.5	12.2	9.1	-0.03	-0.13	0.02	37695
17	60.3	41.2	119.9	19.4	16.2	11.9	0.04	-0.09	-0.08	31197
18	41.3	162.7	30.2	13.9	15.3	15.7	0.0	0.01	-0.01	65883
19	45.4	168.3	82.8	15.9	13.6	14.7	0.05	0.05	-0.02	66960
20	46.1	71.2	76.8	15.6	14.1	14.0	-0.12	-0.04	0.15	27865
21	38.0	93.4	35.4	15.4	15.6	16.2	0.07	-0.09	-0.07	20749
22	180.7	144.6	217.9	21.6	18.7	22.8	-0.02	-0.01	0.02	22730
23	49.8	45.4	19.8	14.6	11.3	12.1	-0.14	-0.04	0.18	24956
24	40.6	124.3	191.2	16.1	20.9	22.0	-0.07	0.00	-0.25	16940
25	47.4	14.3	20.7	14.9	8.6	10.8	-0.01	-0.08	-0.09	22250
26	52.9	28.2	82.5	12.3	12.8	11.0	0.04	-0.00	-0.08	37625
27	168.7	228.3	36.3	16.5	17.5	19.9	-0.01	-0.02	-.07	42234
28	34.9	146.8	124.9	14.9	11.4	12.9	0.01	-0.03	-0.20	98548
29	50.9	226.0	46.9	16.8	17.4	26.5	-0.01	0.04	0.07	32815
30	51.4	43.1	231.6	18.0	21.2	16.2	-0.19	0.01	-0.07	24047
31	43.7	99.5	130.6	19.2	15.6	15.0	0.07	-0.00	-0.01	36023
32	172.3	161.5	97.3	14.1	12.3	13.6	0.07	-0.01	-0.19	126660
33	49.9	177.2	145.9	19.2	22.7	16.5	-0.02	-0.21	-0.15	37182
34	166.4	34.9	233.6	14.7	15.1	16.7	0.11	0.10	0.14	47611
35	177.6	162.7	36.6	19.5	16.0	18.8	-0.05	-0.03	0.03	81331
36	62.5	41.4	161.8	21.1	18.1	15.8	-0.06	-0.09	0.11	24272
37	166.3	227.6	116.9	14.7	15.6	23.9	-0.08	-0.07	0.19	28542
38	173.2	71.2	198.1	16.3	19.0	22.6	0.11	0.15	0.21	28462
39	165.0	174.4	143.3	15.4	15.2	14.6	0.13	0.06	-0.04	45110
0	Pixels been masked off (Sea area)									312485

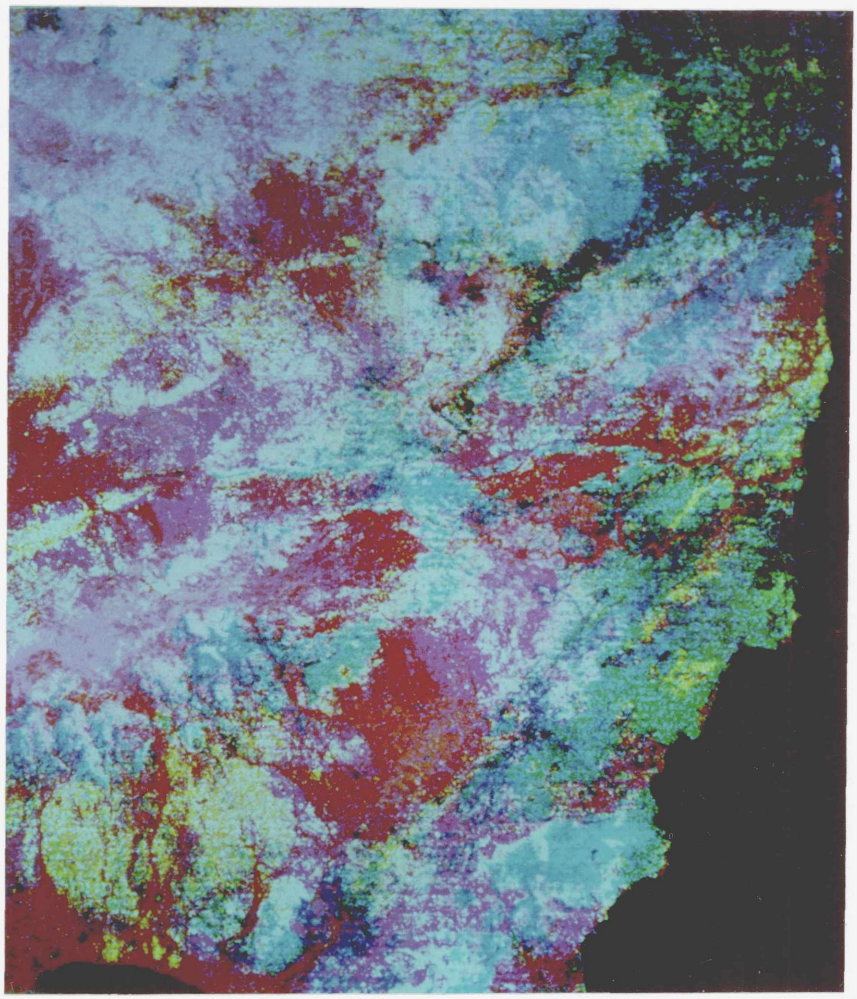


Figure 7-3: The classification image produced by 3D-FSIC from the HRGB image shown in Figure 7-2.

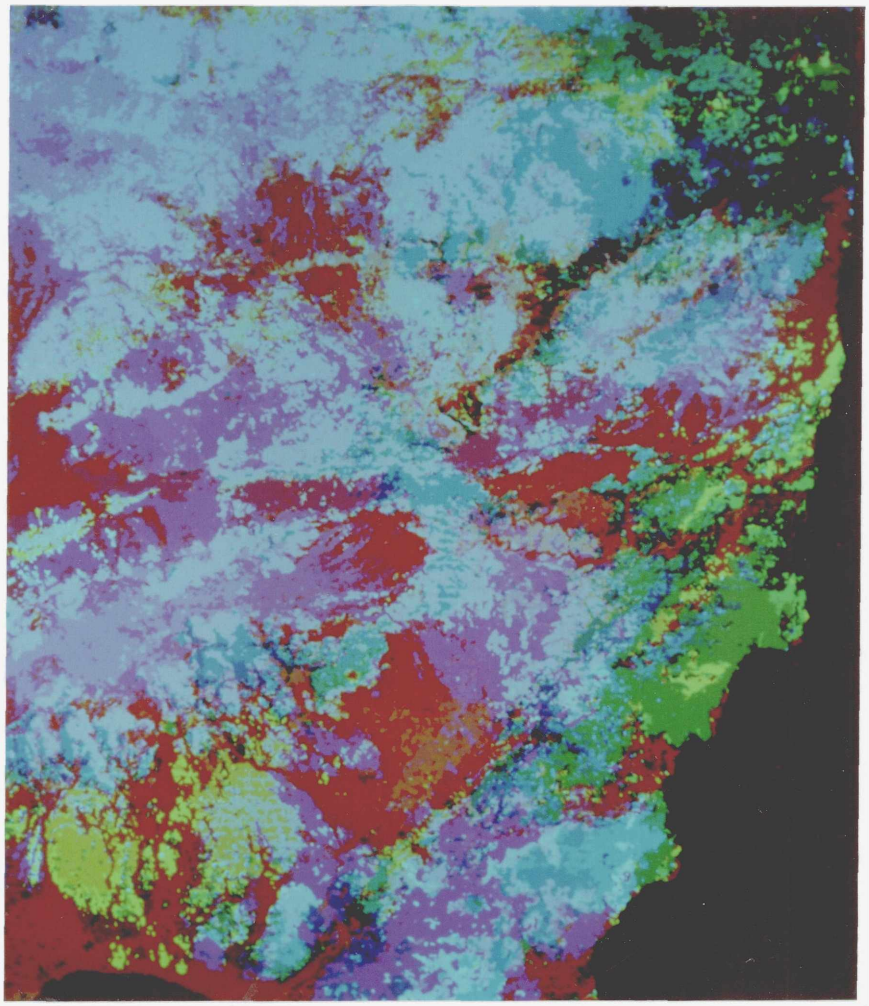


Figure 7-4: The smoothed classification image after IMF and SCM processing.

Table 7-4: Class pixel numbers of the spectral classification (FSIC), iterative majority filtering (IMF) and small class merging (SCM) of the study area.

Label	Pixel numbers			New
	FSIC	IMF	SCM	label
0	312485	314028	314028	0
1	77805	123568	123568	1
2	246492	355284	356011	2
3	21157	33902	33902	3
4	102704	136326	136326	4
5	131367	171285	171375	5
6	37107	27620	27625	6
7	6972	2075	deleted	
8	67057	55414	55416	7
9	77480	82261	82261	8
10	157021	193205	197817	9
11	130023	131430	131430	10
12	189776	165784	166651	11
13	115999	108187	108408	12
14	33468	40205	40205	13
15	17912	5188	7314	14
16	37695	54423	54423	15
17	31197	34882	36823	16
18	65883	92083	92083	17
19	66960	70972	71054	18
20	27865	23599	23606	19
21	20749	12748	12752	20
22	22730	1633	deleted	
23	24956	11447	11452	21
24	16940	1572	deleted	
25	22250	14568	14568	22
26	37625	32626	33060	23
27	42234	39327	39327	24
28	98548	113322	113627	25
29	32815	21080	21097	26
30	24047	2763	deleted	
31	36023	20589	21150	27
32	126660	125322	125715	28
33	37182	25123	25125	29
34	47611	5057	deleted	
35	81331	61040	61128	30
36	24272	8726	9141	31
37	28542	6086	6215	32
38	28462	550	deleted	
39	45110	20560	21177	33

7.3.1 Editing of multi-lithology classes

Three major spectral classes correspond to more than one lithology in the classification image, Figure 7-3. Thus CRED was applied to split these classes interactively. The class splitting performed by CRED is not based on the spectral character of a class but the districts where the class occurs. The information of the editing of multi-lithology classes is briefly shown in Table 7-5.

Class 4 and 10

The spectral shapes of class 4 and 10 are almost identical. The difference between them is caused by the wide striping in TM1. In a same region, the two classes always correspond to a same terrain type even they represent three different lithologies in different regions. Thus class 4 and 10 are treated as one class.

Class 4 and 10 correspond to carbonaceous mica-schist in metamorphic terrain, to andesite in volcanic terrain and to alluvial deposits and debris aprons on the south slope of Sierra de Alhamilla and along the south coast. These classes were re-labeled, by CRED, as class 34 in the region from south coast to the mountain foot of Sierra de Alhamilla and as class 35 in the volcanic belt along the east coast.

Class 25

Class 25 corresponds to marble and dolomite in metamorphic terrain and altered dacite in the south east part of the subscene where it was re-labeled as class 36 by CRED.

Table 7-5: New classes resulted by class regional editing (CRED)

Class	Region				Lithology	New class
	SL	SS	EL	ES		
4 & 10	1220	0	1792	800	Alluvial fans and delta	34
4 & 10					Andesite	35
25	1040	801	1792	1536	Highly altered dacite	36
12					Volcanic breccia	37

Class 12

Class 12 corresponds to molasse bad lands very precisely in the central part of the subscene but coincides with scattered occurrences of volcanic breccia in andesite terrain where it was re-labeled as class 37.

The classification image after CRED is shown in Figure 7-5.

7.3.2 Class grouping and identification

The 37 classes, after CRED processing, were merged into 24 terrain types corresponding to different lithologies, vegetation, *etc.* (Table 7-6) by CGR programme. The description of each class is given below in a sequence: metamorphic rock, volcanic rock, sedimentary rock, superficial deposits and others.

Metamorphic rock

The area involved intensive tectonic movement since Mesozoic, the Mesozoic and older rocks were all metamorphosed in some degree. In the published 1:50000 scale geological maps, the metamorphic rocks were mapped as many groups according to stratigraphy and tectonic units instead of lithology. Differ-

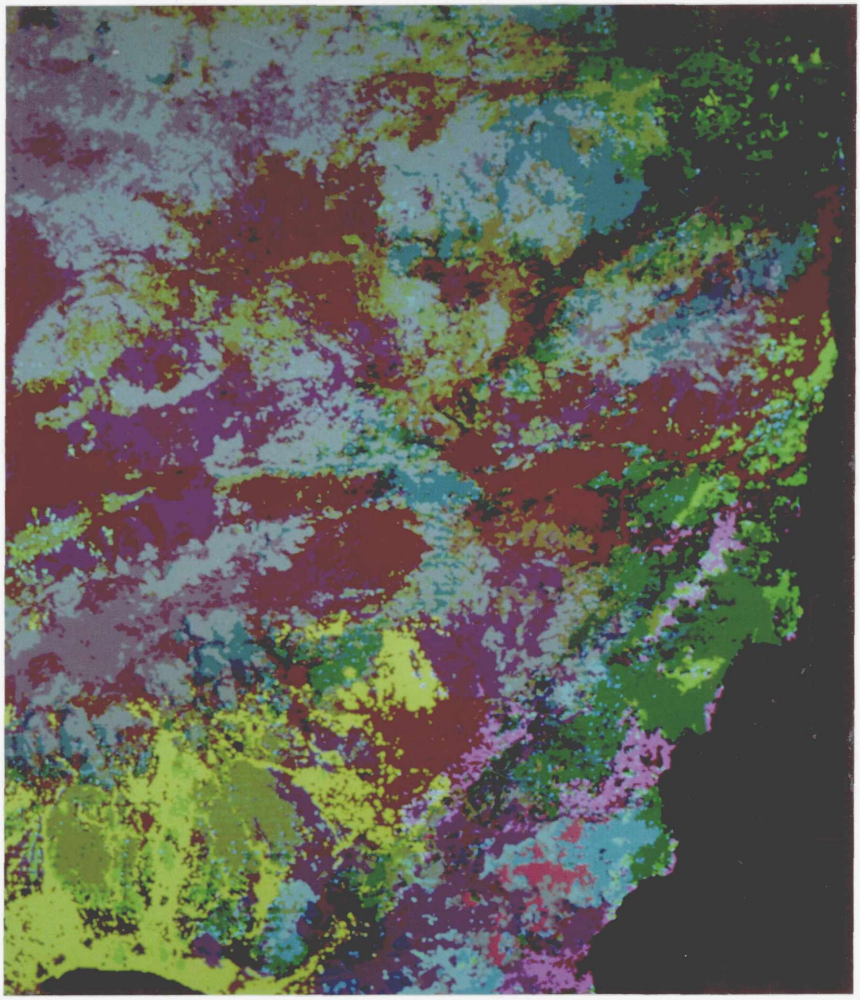


Figure 7-5: The classification image after CRED treatment.

Table 7-6: Terrain types in the imagery lithological map of the study area

Label	Description	Pixels
0	Sea (not classified)	316779
	Metamorphic rocks	
1	Carbonaceous mica-schist	116801
2	Mica-schist with gneiss	338481
3	Phyllite, quartzsite and gneiss	356414
4	Triassic dolomite and marble	100300
	Volcanic rocks	
5	Andesite	66077
6	Volcanic breccia and tuff	29843
7	Highly altered dacite	13397
8	Altered dacite with residual soil and debris	25136
	Sedimentary rocks	
9	Miocene limestone and dolomite	163287
10	Miocene molasse deposits	100107
11	Late Miocene to early Pliocene alluvial deposits	164084
12	Gypsum	82363
13	Pliocene limestone and marls	65926
14	Early Pleistocene alluvial deposits	187142
	Unconsolidated superficial deposits	
15	Slope washes	30436
16	Colluvial and residual debris of bed rock	197997
17	Sand deposits	14572
18	River beds	103613
19	Mine tailing and dry river beds	36920
20	Recent alluvial fans and debris aprons	124736
21	Red soil	21275
	Others	
22	Vegetation	83109
23	Open pits of mines	7357
24	Villages and small towns	6360

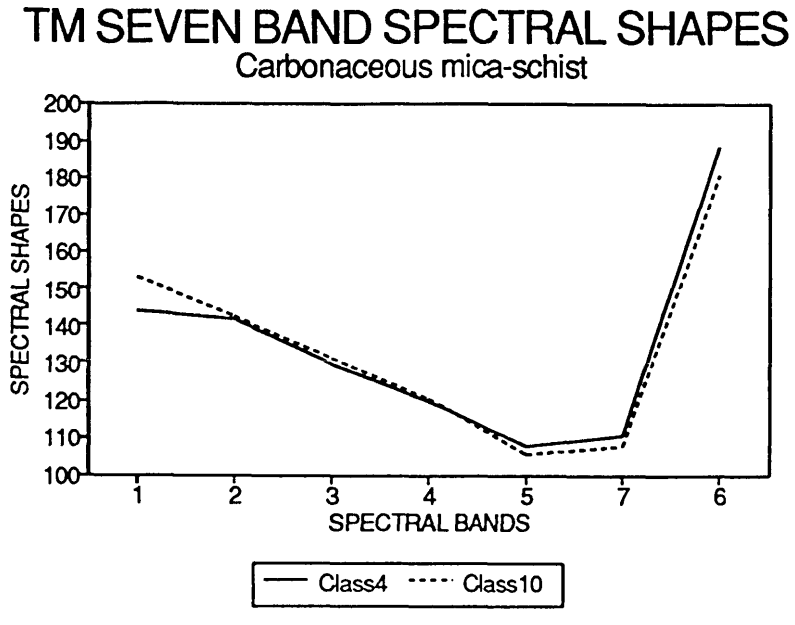


Figure 7-6: TM seven band spectral shape of terrain type 1

ent rock types may occur in the same group and similar rock types may exist in different tectonic units. For the lithological mapping based on the classification imagery in this study, the metamorphic terrain was divided into four rock types. Comparing with the 1:50000 geological maps, the lithological composition of each stratigraphic group can be illustrated by the imagery lithological map produced.

1. Carbonaceous mica-schist (class 4,10)

As mentioned above, classes 4 and 10 are treated as one class defining the carbonaceous mica-schist in the cores of the Sierra Cabrera and eastern part of Sierra de Alhamilla ranges. Field observation on two sections along the road crossing the two mountains confirms the lithology and accuracy of the boundary between carbonaceous mica-schist and other lithologies. The very dark appearance (almost black) of this rock types explain the high emissivity in thermal band (TM6) shown by the spectral shapes of class 4 and 10 (Figure 7-6).

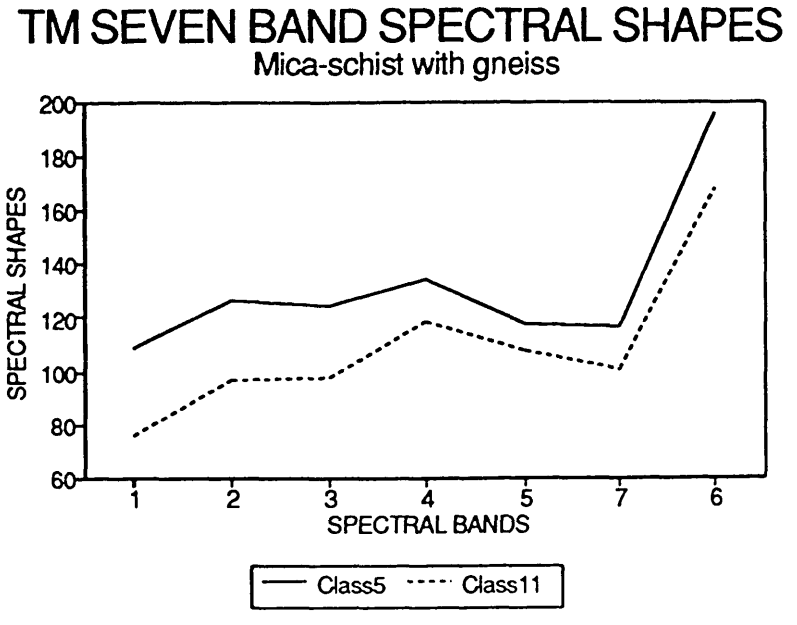


Figure 7-7: TM seven band spectral shape of terrain type 2

2. Mica-schist with gneiss (class 5 and 11)

Class 5 and 11 are spectrally very similar (Figure 7-7) and spatially related. Both classes correspond to mica-schist with gneiss in the western Sierra de Alhamilla. This rock type, in grey to dark grey, is brighter than carbonaceous mica-schist. In the classification image (Figure 7-3), Sierra de Alhamilla is composed of two major rock types, carbonaceous mica-schist in the east and mica-schist with gneiss in the west. This phenomenon is not well shown in the published geological maps but was confirmed by field observation.

3. Phyllite, quartzite, gneiss and granite gneiss (class 2)

Class 2 (Figure 7-8) is the largest spectral class in the classification image of the study area. It generally corresponds to bright metamorphic rock types, such as phyllite, quartzite and gneiss in the metamorphic mountains in the central and northern part of the subscene. A circular feature of class 2 west to the Vera basin coincides with granite gneiss.

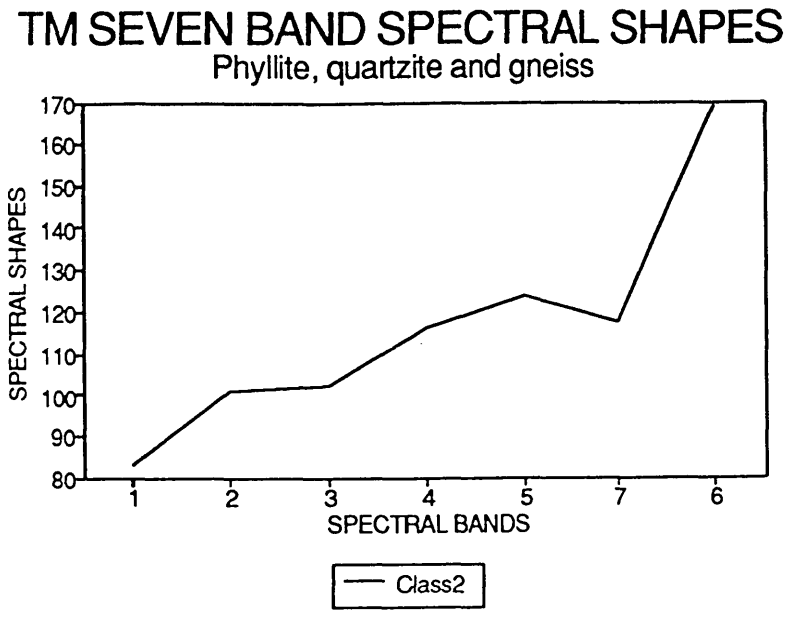


Figure 7-8: TM seven band spectral shape of terrain type 3

4. Triassic dolomite and marble (class 25)

The carbonate rocks such as dolomite and marble are effectively defined by class 25 (Figure 7-9) in metamorphic terrain. This rock type is found in Triassic strata along the flank of major metamorphic mountain ranges as the mantle above the mica-schists forming the mountain cores. The distribution of this class in the image compares well with Triassic dolomite and marble on 1:50000 scale geological maps.

Volcanic rock

Tertiary volcanic rock in the area forms the mountain belt of Sierra de Gata along the southeast coast. Andesite, dacite and volcanic breccia are the dominant rock types.

5. Andesite (class 24, 35)

Class 35 is regionally split from class 4 and 10 by CRED. Both Class 35 and 24 represent andesite lava and agglomerate lava. Class 24 (Figure 7-10) defines the andesite containing large hornblende crystals near Carboneras. Class 35

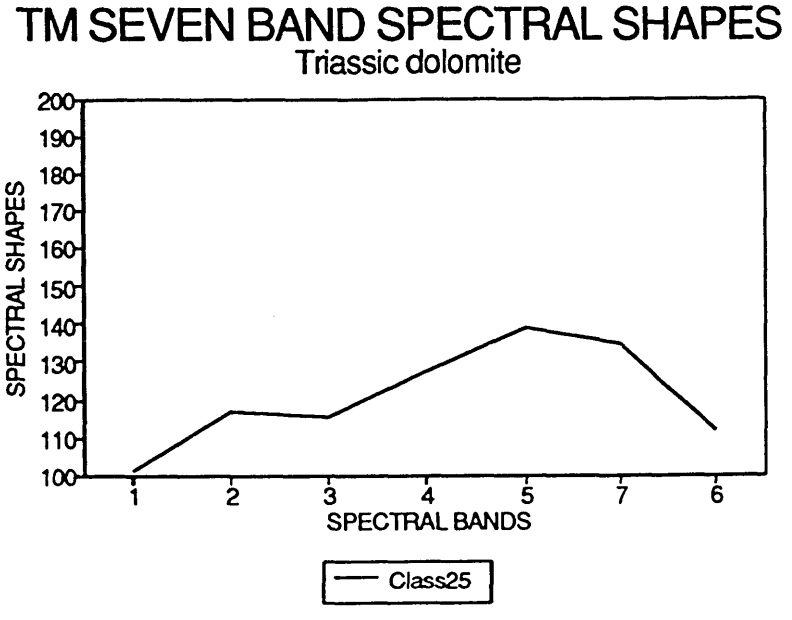


Figure 7-9: TM seven band spectral shape of terrain type 4

corresponds to the very dark basaltic andesite in Las Negras, Punta de la Polacra and La Isleta area.

6. Volcanic breccia and tuff (class 26, 37)

The spectral shape of class 26 corresponds to the general spectral character of class 24 except in the thermal band (Figure 7-11). The very low thermal emissivity of this class suggests a similar rock type to andesite but rather brighter than andesite. It may represent andesitic breccia and tuff, but this provisional identification was not verified because of the difficulty of locating this scattered class in the field. Class 37, regionally split from class 12, is spectrally similar to class 35 (andesite), and coincides with breccia and tuff in basaltic andesite regions according to published 1:50000 scale geological maps and field observations.

7. Highly altered dacite (class 36)

This class is regionally split from class 25. It corresponds to highly silicified and kaolinized dacite with epithermal gold deposits in the Rodalquilar area. As discussed in last chapter, such altered dacite is spectrally very similar to

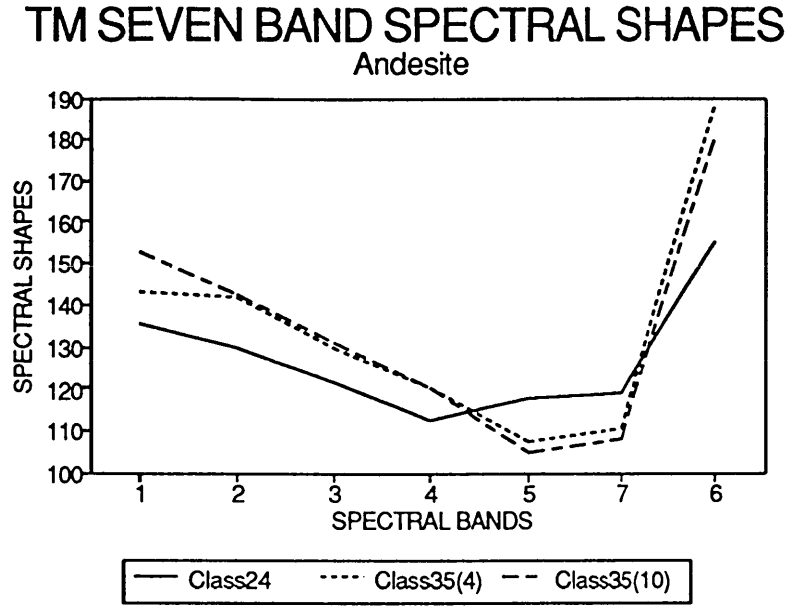


Figure 7-10: TM seven band spectral shape of terrain type 5

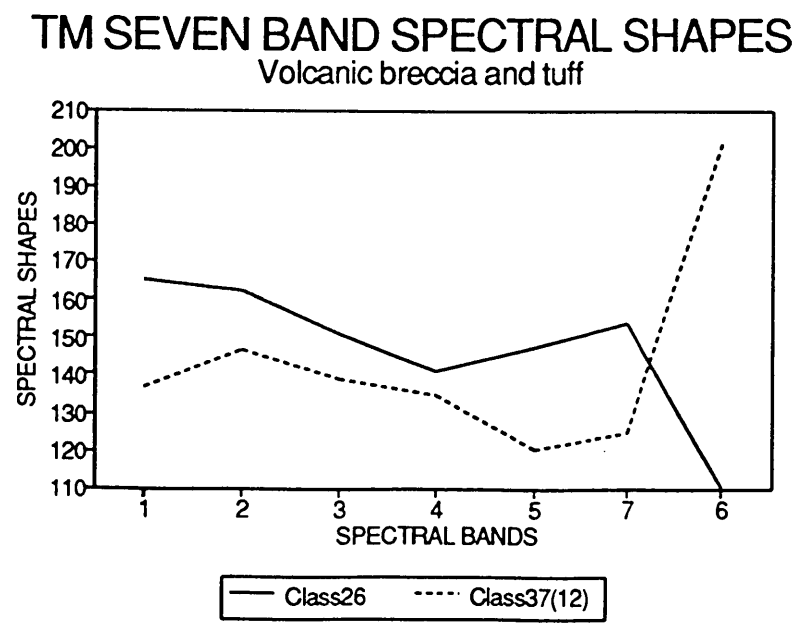


Figure 7-11: TM seven band spectral shape of terrain type 6

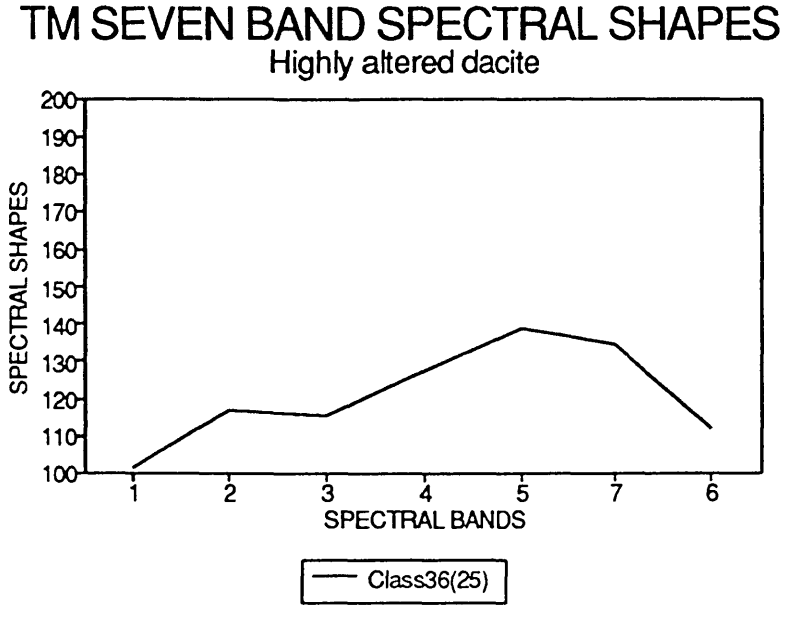


Figure 7-12: TM seven band spectral shape of terrain type 7

carbonate rock, thus is classified as the same spectral class (Triassic dolomite). The reflectance peak in TM5 (Figure 7-12) corresponds to the clay minerals related to epithermal alteration. The detailed field check in the Rodalquilar area confirmed that class 36 is highly altered dacite.

8. Altered dacite covered by residual soil and debris (class 29)

With similar spectral shape to class 36 (25) (Figure 7-13), class 29 is lightly altered softer dacite partly covered by residual soil and debris. The identification of this class was verified by field checks around Rodalquilar.

Sedimentary rock

The sedimentary rocks of the area are mostly of Tertiary age from Miocene to Pliocene. In some regions, the early Pleistocene (Q_1) deposit cemented by calcite is also consolidated as rock. For sedimentary rocks, different classes seem to correspond to layers of different age as well as lithology because the colour of Tertiary sediments was influenced by climatic conditions.

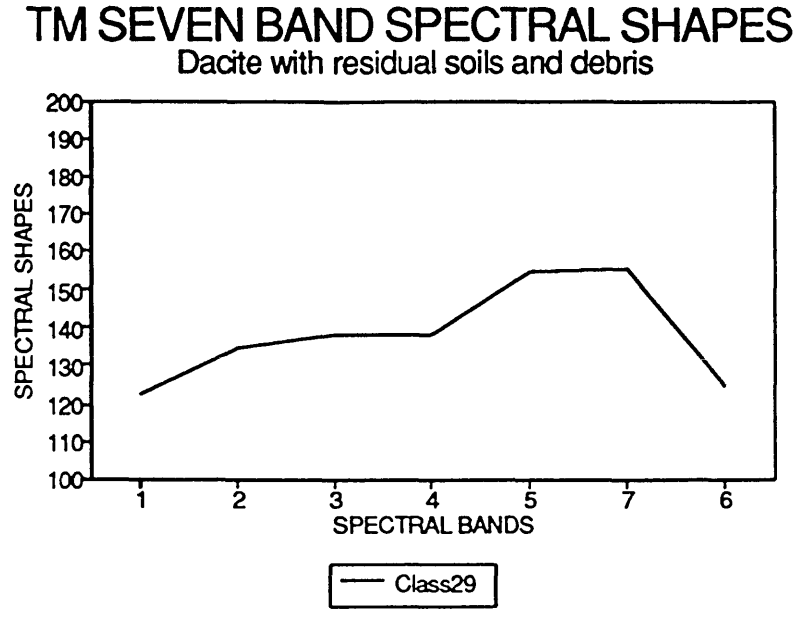


Figure 7-13: TM seven band spectral shape of terrain type 8

9. Miocene limestone and dolomite (class 17, 18)

These two classes are equivalent to classes 2 and 4 in the test site. With similar spectral shape (Figure 7-14), they both correspond to well consolidated Miocene limestone and dolomite layers in the Almeria - Carboneras basin.

10. Miocene molasse deposits (class 12)

Class 12 (Figure 7-15) defines the Miocene molasse deposits in the Tabernas - Sorbas basin along the north slope of Sierra de Alhamilla and Sierra Cabrera. The molasse deposits are composed of sandstone, conglomerate and marls and form a very spectacular badland landscape.

11. Late Miocene to early Pliocene alluvial deposits (class 1, 13)

The spectral shapes (Figure 7-16) of the two classes are almost identical except in band TM6 where class 1 shows high emissivity while class 13 low. Thus class 13 may represent similar material but brighter than that of class 1. The two classes, distributed mainly in Vera basin, correspond to the consolidated alluvial deposits, such as sand and gravel beds cemented by calcite.

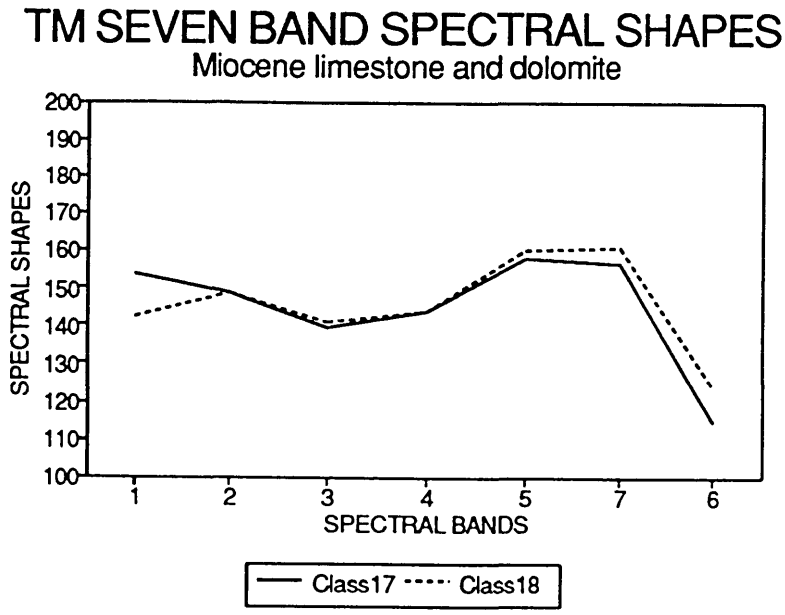


Figure 7-14: TM seven band spectral shape of terrain type 9

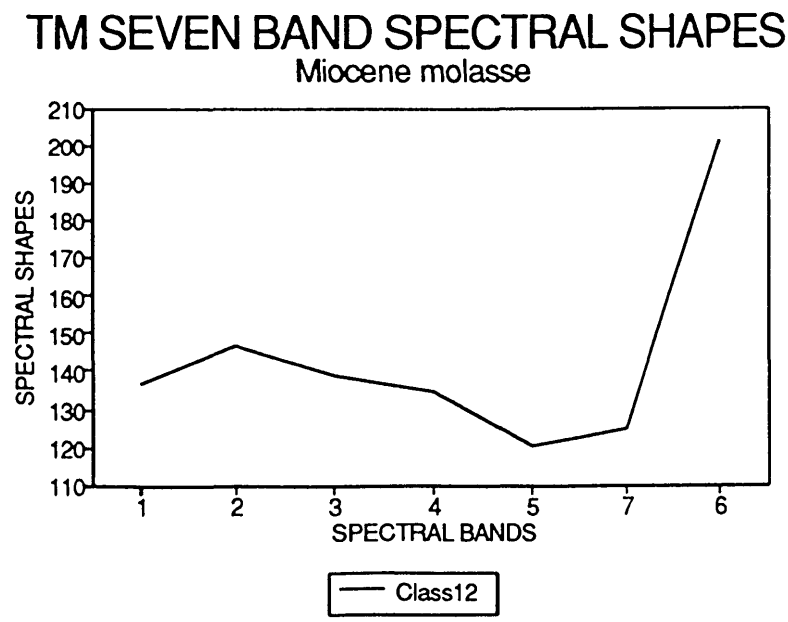


Figure 7-15: TM seven band spectral shape of terrain type 10

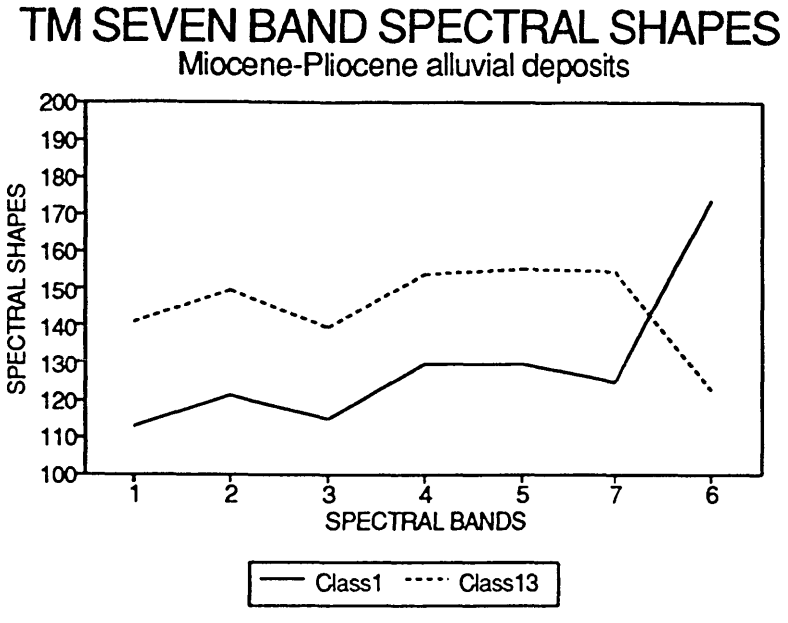


Figure 7-16: TM seven band spectral shape of terrain type 11

12. Gypsum (class 8)

Class 8 (Figure 7-17) shows up the Miocene gypsum layers quite effectively. The massive gypsum layer on the southern pediment of Sierra Cabrera, containing a large gypsum mine, is effectively located by class 8. The class also detects the gypsum in the metamorphosed Triassic strata. In Nijar area, the recent diluvial fan is also classified as class 8. This may be caused by the gypsum crust or debris on the land surface.

13. Pliocene limestone and marls (class 15, 21)

Class 15 and 21 are considered to represent the same lithology because of their spectral identity (Figure 7-18) and coincident distribution. They coincide with Pliocene limestone and marls in the east coast region.

14. Early Pleistocene alluvial deposits (class28, 30)

The slight spectral difference between class 28 and 30 (Figure 7-19) is caused by the striping noise in TM1 as in the case of classes 4 and 10. The two classes occur mainly in the alluvial plain on the south flank of the Sierra Alhamilla and correspond to early Pleistocene alluvial deposits composed of sands and

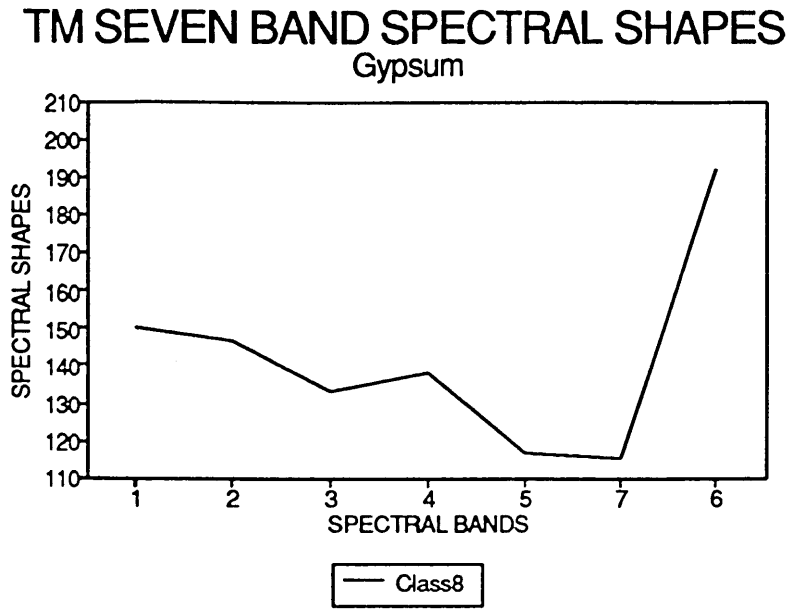


Figure 7-17: TM seven band spectral shape of terrain type 12

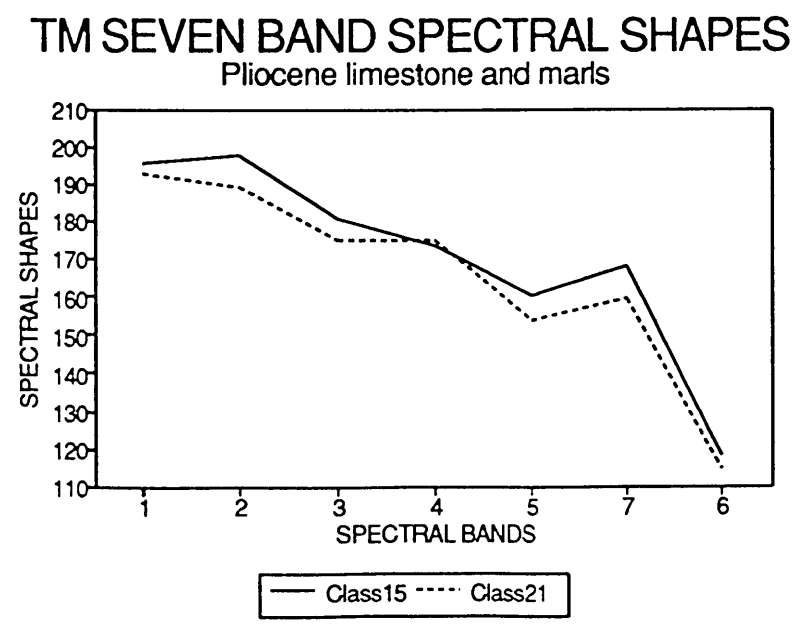


Figure 7-18: TM seven band spectral shape of terrain type 13

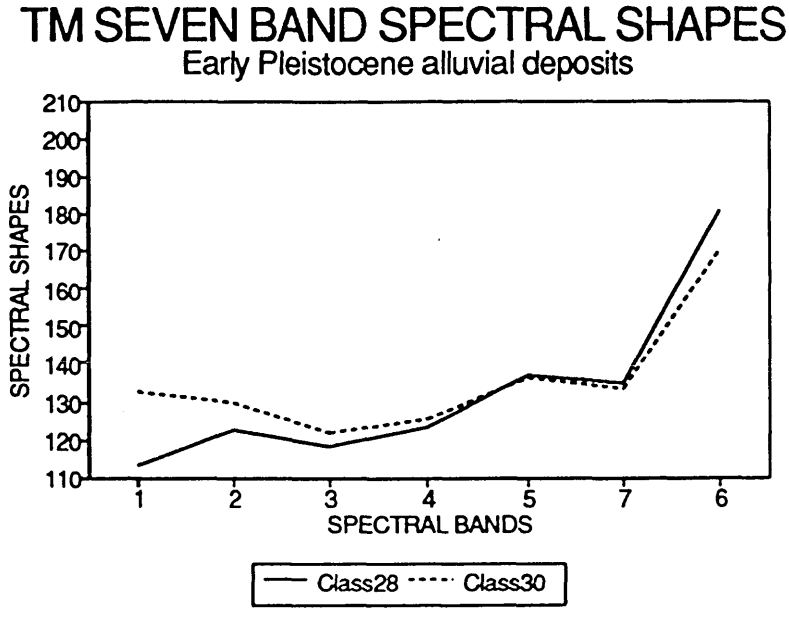


Figure 7-19: TM seven band spectral shape of terrain type 14

gravels cemented by calcite.

Unconsolidated superficial deposits

15. Slope washes (class 27, 31)

Slope washes surrounding hills are not represented in the published 1:50000 geological maps. They are however very well shown by class 27. Class 31 commonly occurs with class 27 and has very similar spectral shape but with higher albedo (Figure 7-20). It may also represent slope washes.

16. Colluvial and residual debris of bed rock (class 9)

This class is equivalent to the class 18 of the test site. It corresponds to the colluvial and residual debris covering bed rock that forms gentle slopes in mountain and hilly regions. The material is usually reddish and dark as shown by the relative high reflectance in band TM3 and high thermal emissivity in TM6 (Figure 7-21).

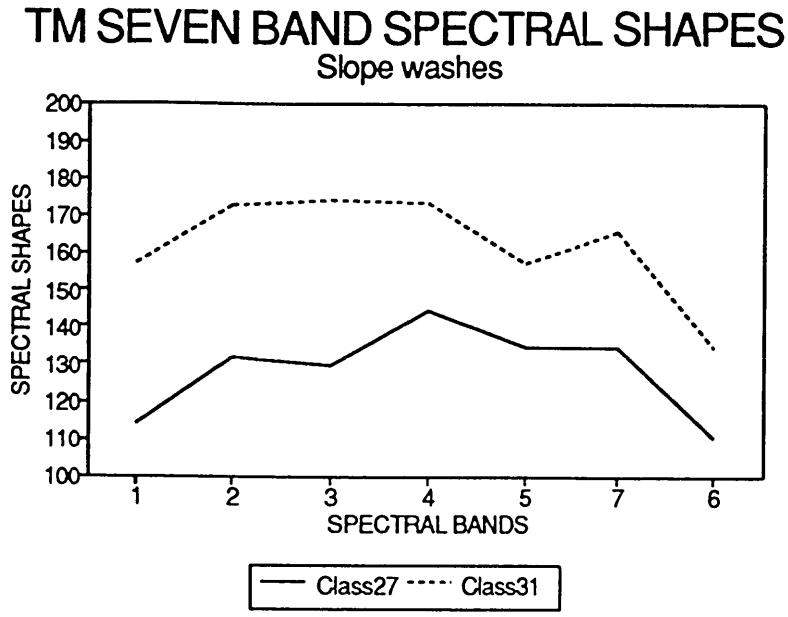


Figure 7-20: TM seven band spectral shape of terrain type 15

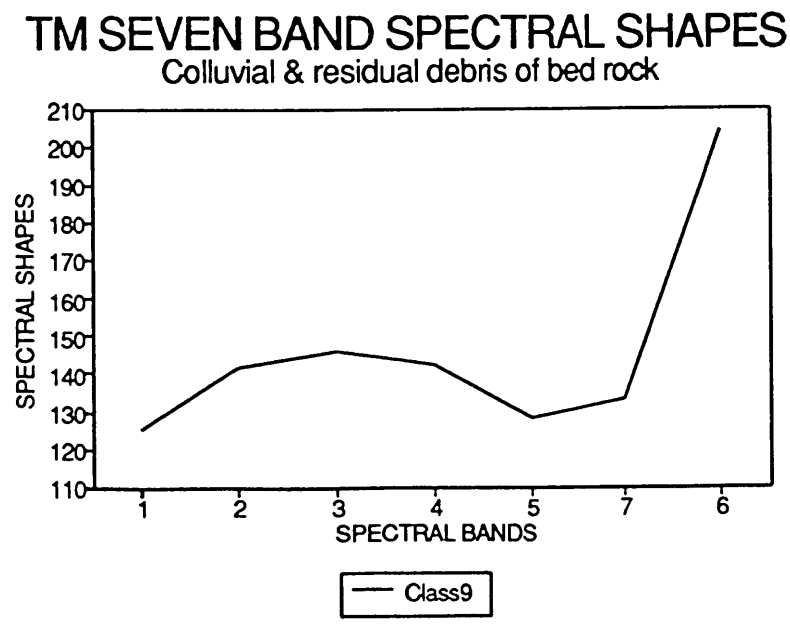


Figure 7-21: TM seven band spectral shape of terrain type 16

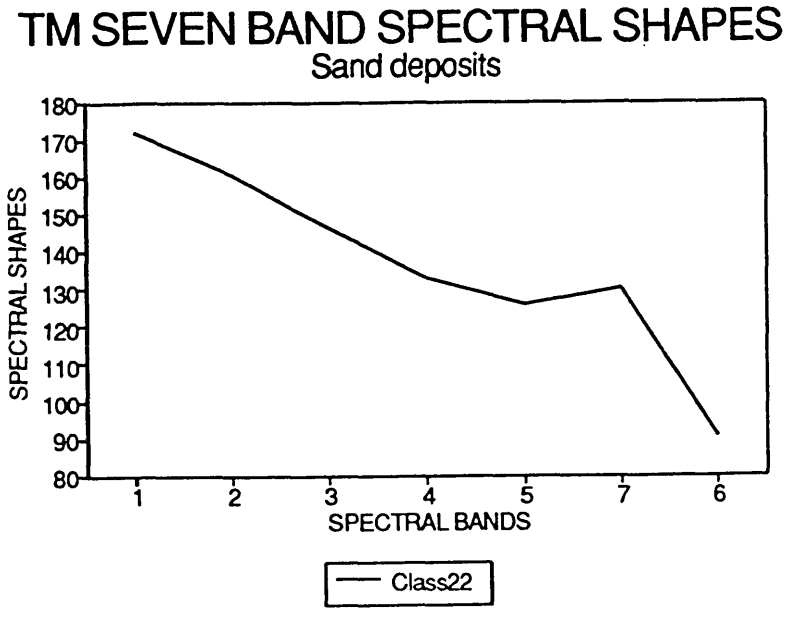


Figure 7-22: TM seven band spectral shape of terrain type 17

17. Sand deposits (class 22)

The recent sand deposits of beaches and river banks are well illustrated by class 22. With similar spectral shape (Figure 7-22), this class is equivalent to the class 1 in the test site. The very high reflectance in visible bands and very low thermal emissivity in TM6 correspond to the bright appearance of sand. The relatively high reflectance in TM7 explains the high content of quartz in sand.

18. River beds (class 3, 19, 20, 23)

The four classes usually have continuous curved forms in the classification image (Figure 7-3). Comparing with the 1:50000 scale geological maps and field checks, these classes correspond to the active drainage channels (river beds). The material along river beds varies widely with the locations, the source areas and the erosion patterns. The spectral character of the material is further varied by the vegetation along river beds. It is therefore not surprising for so many spectral classes to correspond to river beds. All these classes except class 3 have very low thermal emissivity in TM6 (Figure 7-23) because water increases thermal inertia significantly and makes the relevant pixels much cooler

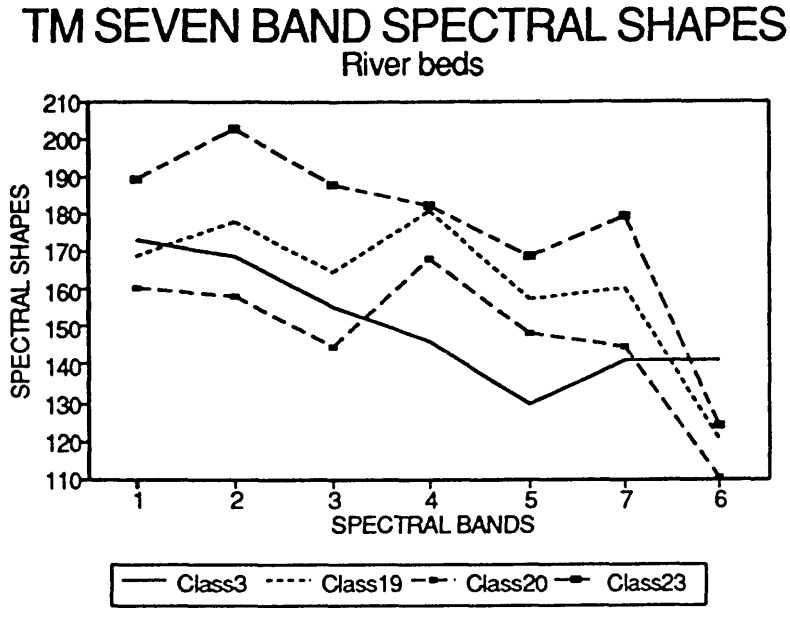


Figure 7-23: TM seven band spectral shape of terrain type 18

than other pixels in day time. Class 3 is spectrally slightly different from but spatially related to the other three and may represent the river terraces rather than active drainage channels.

19. Mine tailings and dry river beds (class 16)

The spectral shape of class 16 (Figure 7-24) is not very different from those of the classes of river beds. It is considered separately because it highlights the abundant mine tailings of the gold mine in Rodalquilar. The class corresponds to dry river beds in other places.

20. Recent (Q_4) alluvial fans and debris aprons (class 34)

Class 34 is regionally split from class 4 and 10. It defines the recent alluvial fans on the south slope of Sierra de Alhamilla and wide debris aprons forming the south coast region. The recent deposits in this region are dominated by rock debris of carbonaceous mica-schist and mica-schist from the Sierra de Alhamilla source area. They show the same spectral character as the carbonaceous mica-schist (Figure 7-25).

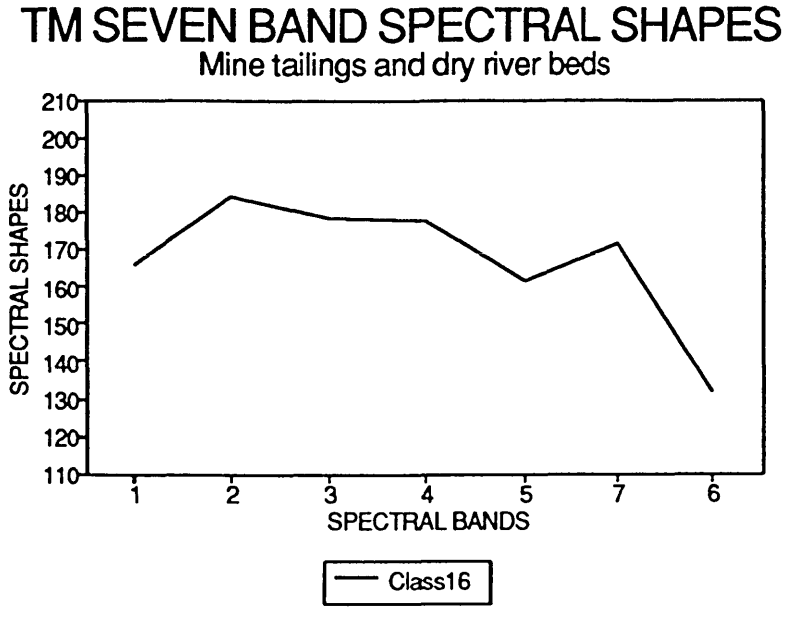


Figure 7-24: TM seven band spectral shape of terrain type 19

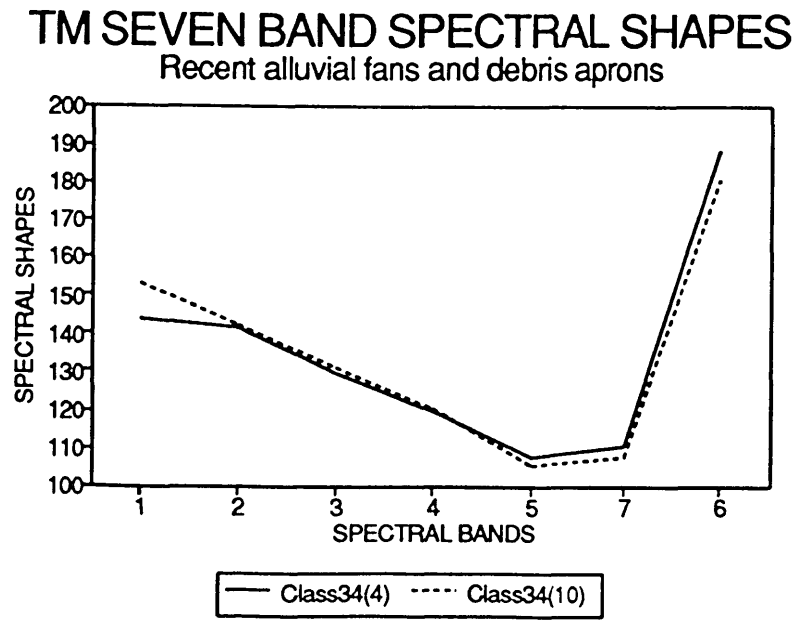


Figure 7-25: TM seven band spectral shape of terrain type 20

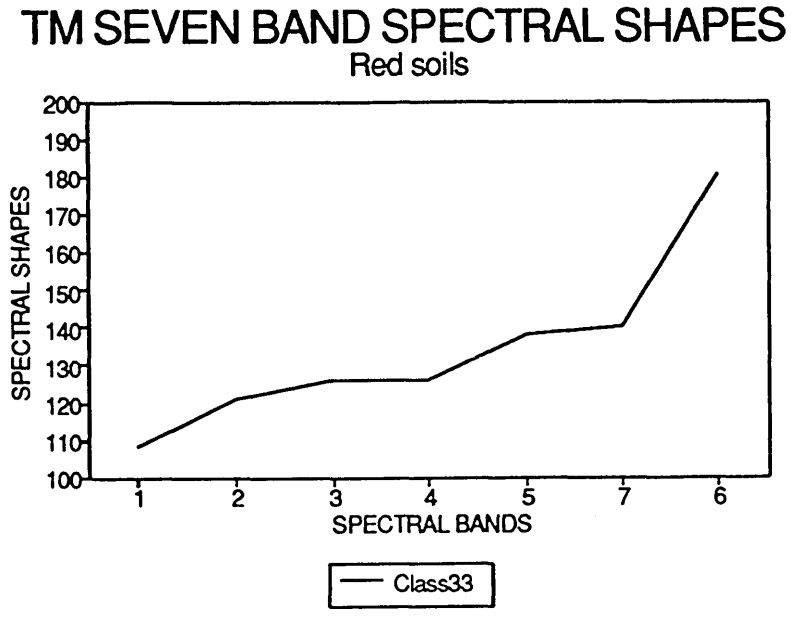


Figure 7-26: TM seven band spectral shape of terrain type 21

21. Red soil (class 33)

Red soil is very precisely defined by class 33 and was fully verified by field checking in the southeastern part of the subscene. The reddish appearance of the soil is characterized by the high reflectance in red band TM3 of the spectral shape of this class (Figure 7-26).

Others

22. Vegetation (class 6, 7)

With similar spectral shapes (Figure 7-27), the two classes represent vegetation. The green colour and high reflectance in near infrared band TM4 of vegetation are well presented by the spectral shapes of these classes. The class identification as vegetation was easily checked in the field.

23. Open pits of mines (class 14)

Class 14 (Figure 7-28) appears to be concentrated on the active gold mine near by Rodalquilar and closely matches the patterns of open pits. However, further field work is needed to explain the identification of this class in other

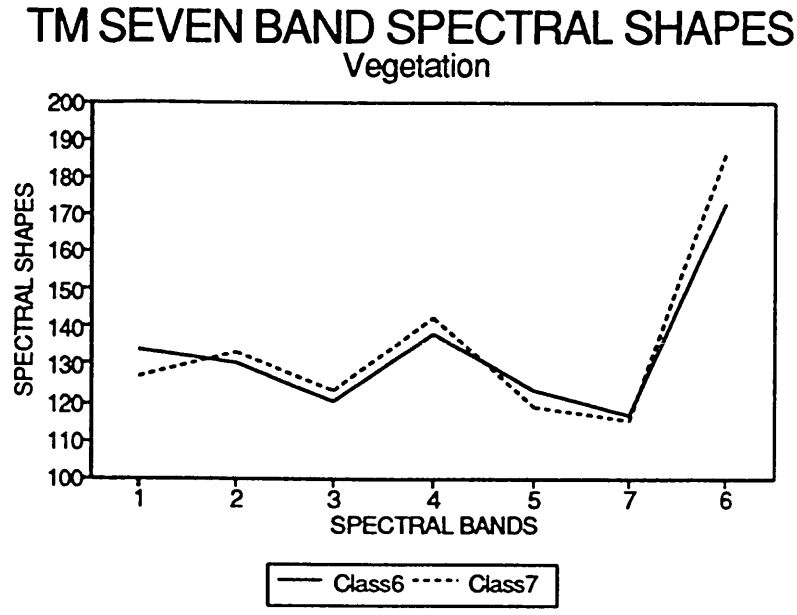


Figure 7-27: TM seven band spectral shape of terrain type 22

areas.

24. Villages and small towns (class 32)

The scattered and tiny occurrence of class 32 (Figure 7-29) makes field checking difficult. Limited field observations in Carboneras, Nijar, *etc.*, seems to indicate that this class corresponds to the tiled roofs of buildings and streets of villages and small towns.

After class identification, an imagery lithological map (Figure 7-30) with 24 terrain types and its intensity modulated version (Figure 7-31) were finally produced.

7.4 Discussion and Assessment of the Regional Lithological Mapping

Regional lithological mapping based on unsupervised classification in the large TM subscene is much more difficult than that in the 512 × 512 test site

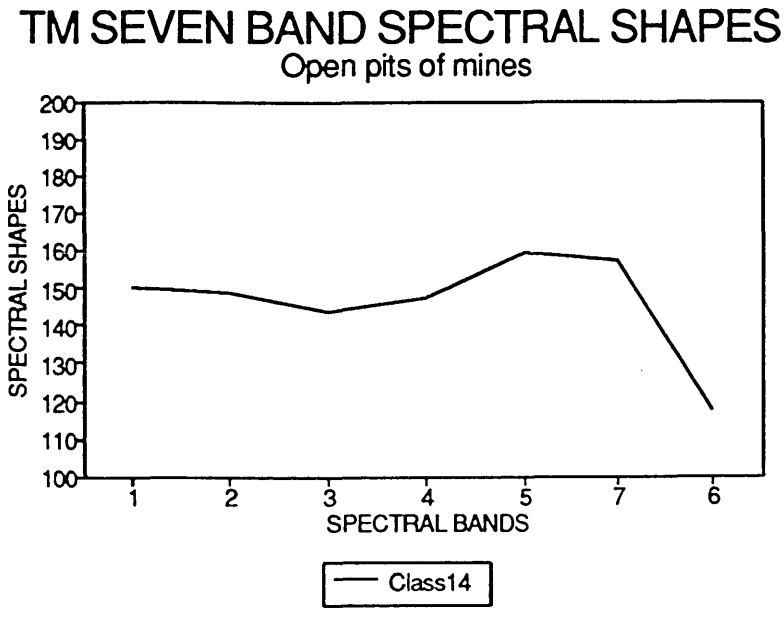


Figure 7-28: TM seven band spectral shape of terrain type 23

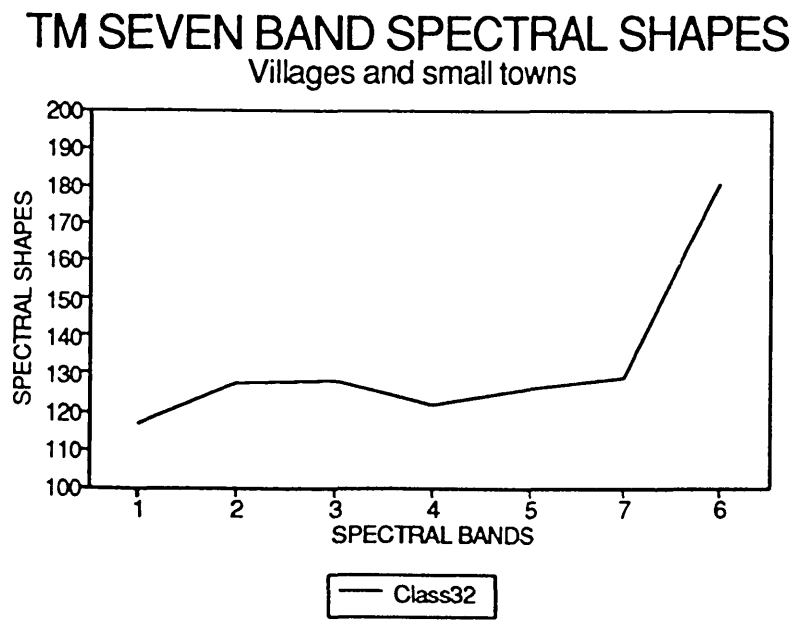


Figure 7-29: TM seven band spectral shape of terrain type 24

because separation of many terrain types may be beyond the spectral discrimination capacity of TM imagery. In fact, the size of an image for classification is a kind of regional control. The smaller the image, the less terrain types will be involved and the simpler is the spectral classification. Thus small image size means better regional control for unsupervised classification.

Nevertheless, the imagery lithological map resulting from automatic lithological mapping based on the 1792×1536 TM subscene (Figure 7-30, 31) shows reasonable agreement with the published 1:50000 scale geological maps and can be used for field reconnaissance.

Several classes, class 4, 10, 8, 12 and 25, in the original classification correspond to more than one terrain types. Confusion in the spectral classification occurs in following cases:

- The spectral signatures of several terrain types are very similar within the spectral bands of the imagery used, such as altered dacite and metamorphosed dolomite. This means that the spectral properties of these terrain types are beyond the spectral resolution of the imagery and the discriminating ability of the classification algorithm used.

- Spectral classification cannot distinguish the terrain types composed of similar material but with different textures or formed by different geological processes, such as the carbonaceous mica-schist and the alluvial deposits composed of carbonaceous mica-schist debris.

The confusion caused by above cases can be reduced by class editing using CRED. This supervised regional class splitting technique sub-divides a spectral class on the basis of its regional occurrence.

For the Rodalquilar test site, the lithological discrimination in the 1792×1536 subscene (Figure 7-30) is much better than was achieved in the 512×512 subscene (Figure 6-25). In Figure 7-30, the altered dacite is more precisely

defined by terrain type 7, the less altered dacite with residual debris and soils is identified as another class (terrain type 8), the open pits of the gold mine are detected as a distinct class (terrain type 23) without using the textural technique (THMC) and red soil is more accurately recognized (as terrain type 21). The possible reasons of the improvement of classification of the test site in the large subscene are:

- The locations of the "seeds" to start a clustering classification influence the final classification result because the iterative clustering can only converge to a local optimum even though the class splitting and uniting functions are installed (Devijver and Kittler, 1982).
- The data distribution of the large subscene is different from that of the test site. Thus the local optimum of the two subscenes are also different.
- For the large subscene, only the Euclidean and Euclidean OMPR decision rules were used in 3D-FSIC. These decision rules are less effective than the Gaussian OMPR for classes with Gaussian distributions, but may be more suitable for those classes not having Gaussian distributions.

7.5 Summary

After the experimental processing of the 512 × 512 subscene of the test site, the similar processing procedure was applied to a much larger TM subscene with 1792 × 1536 pixels including various lithologies, such as metamorphic rocks, volcanic rocks, sedimentary rocks and superficial deposits.

Firstly, a smoothed classification image with 33 spectral classes was produced. The spectral classes which correspond to more than one terrain types were then regionally split based on prior knowledge of the area. The

total number of classes was thus increased to 37. Finally, the 37 classes were grouped and identified as 24 terrain types based on field work, published 1:50000 scale geological maps and spectral analysis.

The limitations of the processing on a more diverse set of terrain types are discussed.

The final imagery lithological map illustrates the major rock types, superficial drift lithologies and other terrain types (*e.g.* vegetation) with reasonable accuracy. It can be used directly for field reconnaissance and is also useful for comparison of lithological composition among stratigraphic units represented on 1:50000 scale geological maps.

Figure 7-30: The imagery lithological map of SE Spain. (Derived from Landsat TM imagery). **Note:** An enlargement of the map is in the pocket inside the back cover.

Figure 7-31: The imagery lithological map (with topographic background) of SE Spain. (Derived from Landsat TM imagery).

Chapter 8

Conclusions, Comments and Recommendations

This chapter summarizes the software package developed in this research project and its application to lithological mapping and proposes the further development of practical image based automatic lithological mapping. All the techniques and programs annotated by capital letter abbreviations are cataloged in Appendix A.

The major contributions of this research project are twofold:

1. A software package with new image processing techniques for automatic lithological mapping;

2. Results of the application of the software package to the automatic lithological mapping of the study area in SE Spain using a TM image.

8.1 Techniques and Software Development

The image processing procedure for automatic lithological mapping in this study is composed of three sequential stages: pre-classification enhancement, spectral classification and post-classification processing. More than thirty For-

tran 77 programs (Appendix A) have been developed to perform different processing functions for lithological mapping, which form a sub-package within the I2S/TAE image processing system used in this study. Among these programs, are many based on new techniques developed in this research project, together with improved versions of several well established techniques, and several routine functions to perform simple processing tasks (such as making a mask by thresholding) which cannot be done easily in the TAE system. Processing speed is an important consideration in software development. The high processing speed of the most programs in Appendix A is achieved by efficient software structures and concise mathematical models.

8.1.1 Pre-processing techniques

A package of new techniques for pre-classification image enhancement is a main theme of the thesis. The Index of Optimal Band-triplet Selection (IOBS), Balance Contrast Enhancement Technique (BCET) and Hue image Red, Green and Blue colour composition (HRGB) have been designed to produce shadow free HRGB colour composites from seven TM bands. Such well prepared images can significantly improve spectral discrimination. Although in this project, these techniques were used sequentially as pre-classification enhancements, they are individual techniques in their own right and can be used independently.

The IOBS is based on a geometric model of inter-band correlation, which predicts the band-triplet with minimum inter-band correlation as the band triplet containing the maximum information among all the band-triplets of a multi-spectral image. Such a band-triplet tends to produce a high quality colour composite after BCET enhancement processing.

BCET is an effective and convenient contrast enhancement technique. By using parabolic or cubic functions, it can eliminate colour bias and significantly

improve the quality of colour composite images.

RGB-IHS transformation is the foundation of HRGB. An HRGB image is achieved simply by displaying three hue images derived from three band-triplets in red, green and blue. Such an image can condense spectral information from up to nine image bands and eliminate shadow effects. The resulting image is suitable for spectral classification although it may not always be good for visual interpretation.

8.1.2 Unsupervised classification algorithm

Spectral classification is the fundamental basis of automatic lithological mapping. A three Dimensional Feature Space Iterative Clustering (3D-FSIC) method was designed to realize the iterative clustering using Optimal Multiple Point Re-assignment (OMPR) decision rule with an acceptable speed. The OMPR takes pixel frequence and cluster size into account in re-assigning an image data point in image feature space from one cluster to another. Thus the accuracy of classification can be improved.

An important new feature of 3D-FSIC is a cluster splitting function that splits an elongated cluster based on the first principal component of the cluster. Another development related to classification is an Automatic Seed Selection Technique (ASST) that locates the high frequency data points in the 3D scattergram of a three channel image as the initial cluster centres to start a clustering classification using 3D-FSIC.

8.1.3 Post-processing techniques

Post-processing and analysis of spectral classification is a necessary step in producing a practical thematic map based on spectral classification of multi-

band imagery. Several techniques related to this topic have been discussed in this thesis. These techniques can be divided into those for spatial reclassification and smoothing and those for class editing, boundary detection and spectral analysis.

Several new techniques have been introduced, such as the Template Histogram Matching Classification (THMC) technique for detecting the textures and patterns formed by certain spatial arrangement of several classes in a classification image; the Small Class Merging (SCM) technique to merge small classes into their spatially and spectrally nearest larger classes; and the Class Boundary Detection (CBD), a very simple and effective technique for detecting class boundaries. Iterative Majority Filtering (IMF), interactive class editing (CRED and CGR) and colour painting (IPAINT) techniques, intensity modulation and methods for deriving class spectral shapes are also discussed.

8.2 Applications: Automatic Lithological Mapping in SE Spain

The automatic lithological mapping of the study area in SE Spain, using a Landsat TM image, was carried out by the software package (without reference to published geological maps).

8.2.1 Processing procedure

The generalized processing procedure is as following:

1. Select three band-triplets with low inter-band correlation and least band re-use from the multi-spectral image. For TM imagery, band-triplets: 3 2 1, 5 4 3 and 6 7 5 are recommended.

2. Perform balance contrast enhancement by BCET to stretch all image bands to an equal value range and mean. The processing optimizes the

contrast of each band and removes the colour bias that may occur in the colour composites of these band-triplets. As the result, the hue images derived from these band-triplets will have wide value ranges.

3. Derive a hue image from each band-triplet by RGB-IHS transformation. Then display the three hue images in red, green and blue to produce a HRGB colour composite.

4. Perform unsupervised clustering classification by 3D-FSIC on the three hue images forming the HRGB colour composite. The clustering is started from the seeds located by ASST.

5. THMC Spatial re-classification can be applied to the image produced by spectral classification to detect interesting class texture/patterns as new classes if necessary.

6. Smooth the classification image either with or without THMC processing by IMF and SCM. SCM should always be used after IMF.

7. Class identification in terms of lithology and other terrain types based on field knowledge, analysis of class spectral shapes and reference to published geological maps.

8. Interactive class editing. Classes which represent different lithologies in different regions are regionally split by CRED. CGR groups those classes corresponding to a same lithology or terrain type into one class. After class editing, the classes in the classification image will be termed terrain types rather than spectral classes as each of them corresponds to a unique terrain type.

9. Detect terrain type boundaries by CBD and add key boxes to the final classification image. The two tasks can be done by one program, CBDKB.

10. Execute interactive colour painting on the image produced in step 9 by IPAINT on a 512×512 display system. If the image is larger than $512 \times$

512, perform interactive colour painting by IPAINT on 512 × 512 resampled display first and then generate three images to restore the colour painting to full resolution by PAINT based on the file of colour codes output by IPAINT. The result of this step is finally a imagery lithological map.

11. As an optional step, topographic background can be added back into the imagery lithological map by intensity modulation using an average image of image bands used (except the thermal band).

8.2.2 Experimental lithological mapping of test site

Experimental lithological mapping was performed on a 512 × 512 TM subscene of the test site. The subscene locates a $15.36 \times 15.36 km^2$ area in Cabo de Gata. The imagery lithological map produced by the software package illustrates 7 rock types, 3 types of superficial deposits and vegetation. The distribution of the major rock types, andesite, altered dacite and limestone, is clearly and accurately defined on the map image. The epithermal alteration zones associated with gold deposits in dacite areas are detected, by textural reclassification, as a textural class characterized by a spatial pattern of three spectral classes.

8.2.3 Regional lithological mapping of the study area

Regional lithological mapping of the study area in SE Spain was carried out based on a 1792 × 1536 TM subscene. The subscene covers a $53.76 \times 46.08 km^2$ area in Almeria Province including the test site. Twenty-four terrain types were discriminated by the automatic lithological mapping, among which, twenty-one correspond to various lithologies and three are related to vegetation, open pits of mines and villages or small towns. The lithologies identified include four types of metamorphic rocks, four types of volcanic rocks and their alteration

products, five sedimentary rock types and eight types of unconsolidated superficial deposits. The classification of the large subscene is much more difficult than that of the small subscene test site as the larger scene means the less regional control. The case of several classes corresponding to one terrain types and, even worse, the case of one class representing several terrain types were encountered. These cases were well handled by interactive class editing programs, CRED and CGR, which impose functions equivalent to regional control (supervision) based on user knowledge. The final imagery lithological map of the study area produced from TM data presents the major lithologies in a clear and concise way with remarkable accuracy. The map image provides more detailed lithological information than the published 1:200000 scale geological map of the area and shows many details comparable with 1:50000 scale geological maps. The imagery lithological map can be used directly for field work of geological reconnaissance and as the base for large scale geological survey.

8.3 Comments on Application of the Software Package

This research project concentrated on automatic lithological mapping, but most techniques and the relevant software were developed to handle any spectral information and perform general mapping tasks. The techniques were designed and used in a systematic way to achieve a high quality classification result that is a good foundation for terrain analysis applications, *e.g.* land use/cover, forest, soil, *etc.*. The software package is therefore suitable for general thematic mapping based on spectral information.

The most important requirement for lithological mapping based on spectral information is that rock information must be represented by surface spectral signatures. This means either the rocks are well exposed or there is a direct

relation between surface cover and bed rock. For example, residual soils and debris or vegetation types controlled by particular rock types. This condition is generally satisfied in arid to semi-arid areas. The software package is therefore an effective tool for the lithological mapping in such terrain.

The software package can utilize the information from up to nine bands at low cost, high speed and acceptable accuracy. It is therefore particularly suitable for regional lithological mapping (scale no larger than 1:50000) based on seven band Landsat TM imagery. The technique can also be used at a more detailed scale based on eleven bands ATM data. For imagery with very high spectral resolution, such as AVIRIS, *etc.*, the software package cannot fully utilize the spectral information simultaneously. However, with careful band selection, it is still a powerful mapping tool for particular terrain types. The enhancement techniques, such as IOBS, BCET and HRGB are certainly very useful for spectral enhancement of such imagery data.

8.4 Recommendations for Future Study

8.4.1 Utilization of textural information

The THMC introduced in Chapter 5 is a simple and effective technique to identify simple spatial patterns when it is used on a classification image instead of on the original image. The patterns identified are equivalent to various colour mixtures on the original image colour composites. Unfortunately, this simple technique is not adequate for more complex textural patterns formed by topographic shadow of micro-geomorphological features which are useful for the discrimination of many rock types. In order to use spectral information for effective classification in this study, topographic shadow was deliberately suppressed by the HRGB technique. Such pre-processing improved the spectral classification, but at the cost of textural information loss. As a result, the

spectral classification failed to discriminate some bed rocks and the superficial deposits derived from these rocks in several cases as shown in Chapter 7 because superficial deposits are often different from their relevant bed rocks in texture rather than in spectral signatures. Interactive regional class editing (CRED) was used to remedy the problem. The fundamental solution, however, may lie in the effective utilization of spatial information.

As reviewed in Chapter 2, much effort has been expended on research into textural classification. The complexity and low processing speed of most textural techniques limit their practical applications. To improve the situation, more effective techniques and an efficient strategy for their application are needed. Promising results may be achieved at reasonable computer cost by applying computationally expensive but effective textural techniques, after spectral classification, only to the spectrally similar but texturally different terrain types or terrain types characterized by spatial patterns of several spectral classes.

8.4.2 Knowledge based class identification

The lithological mapping procedure presented in this study is a classification followed by class identification based on user lithological knowledge, spectral analysis and published geological map information. The mapping is therefore not fully automatic. It seems a good idea to perform the class identification automatically using a geological expert system but in most cases, an expert system based on experts' knowledge can hardly compete with an expert himself in either speed or accuracy for sophisticated data analysis and comprehensive decisions. Even a regionally usable expert system for automatic lithological identification is not normally practicable because the natural factors influencing the image features of lithologies are very complex and expensive to model by computers.

The purpose of this study was to develop a software package for experts rather than an expert system. The software can automatically produce a imagery classification map but the meaning of the imagery map is entirely subject to users' judgement. Simple class editing functions (CRED and CGR) in the software package provide an easy way to convey user knowledge for class identification interactively. Further technical and software development of interactive image editing could provide a more versatile and friendly interface for users. One simple automatic approach is to use the classification of a large area as a regional control mask. Then re-classify those classes each corresponding to more than one terrain type. Such a approach will be more objective than CRED.

The software is designed to be able to perform lithological mapping, supported by limited field work, in arid to semi-arid areas where no geological maps are available. For geologically well mapped areas, maps can be improved by automatic lithological mapping based on remotely sensed data. This can be done by using the automatic lithological mapping software with a GIS system. After digitizing geological maps into a raster (imagery) data set, overlay and logical operations as well as interactive image editing can be applied for either using data set of geological maps to conduct the lithological identification of a classification image or using the classification image to improve the geological data set. Data obtained from field work can also be stored in either raster or vector format to direct class identification or amend data sets of geological maps. Automatic lithological mapping based on TM imagery data provides a cheap, convenient and flexible data base for further geological mapping for those areas without geological maps and an efficient tool for improving the lithological content of existing geological maps.

8.5 Conclusions

The research of this thesis has concentrated on image processing for automatic lithological mapping based on Landsat TM imagery. It has generated two products. The first is a software package comprising a series of image processing techniques intended to assist geologists to produce practical lithological maps based on Landsat TM imagery data. Although the software package performs lithological mapping based on unsupervised automatic classification, it should always be used in conjunction with user field knowledge control. The second product are demonstrations of the techniques on a 512×512 subscene test site with limited rock types, and the subsequent application to a larger study area (1792×1536 pixels) with more varied rock types and less detailed field control. The conclusion from these applications is that the image processing techniques can be used to provide lithological information for geological mapping of regional scale (1:200000) at low cost and high efficiency. On limited scale, the techniques are applicable to improving the quality of 1:50000 scale geological maps. The research indicates themes for an extension of the study towards incorporation of textural data and knowledge basis in more refined mapping procedures.

Appendix A

Image Processing Fortran 77 Programmes Developed in the Research Project

The names and functions of 35 image processing programmes developed in this research project are listed below in alphabetic sequence. All the programmes are written in Fortran 77 under a general frame of Transportable Applications Executive (TAE) image processing software system installed in a I2S/VAX computer system.

ASST 25-APR-1990 Automatic seed selection technique.

AVERAGE 24-JUN-1989 Calculate an average image of several image bands.

BCETC 27-OCT-1989 Balance contrast enhancement technique using a cubic function.

BCETL 5-MAR-1990 Local balance contrast enhancement technique.

BCETP 15-FEB-1990 Balance contrast enhancement technique using a parabolic function.

CBDKB 12-JUN-1990 Function to detect class boundaries and add key boxes.

BIM 3-JAN-1989 Function to generate a binary image for masking certain DN value range.

CBD 18-MAR-1990 Class boundary detection technique.

CGR 18-SEP-1990 Class grouping program.

CLSMV 2-Mar-1990 Calculate classes mean vectors based on a classification image and image bands directly or indirectly used for the classification.

CRATM 6-FEB-1990 Program to correct column mis-interlacement of ATM data.

CRED 9-OCT-1990 Class regional editing function.

DYTHRSHD 25-FEB-1990 Dynamic multi-level thresholding based on statistics and context.

FSIC 13-JUN-1990 Three dimensional feature space iterative clustering.

HS 4-MAR-1990 Technique to generate a fully saturated colour composite from three image bands.

HUE 10-JUN-1989 Program to perform RGB-IHS transformation but only generate a hue image as output.

IMF 4-APR-1990 Iterative majority filtering.

IOBS11 14-FEB-1990 Index of optimal band-triplet selection of up to 11 bands.

IOBS7 18-DEC-1989 Index of optimal band-triplet selection of up to 7 bands.

IPAINT 3-APR-1990 Interactive image colour painting program.

HSI 11-JUN-1989 RGB-IHS transformation.

KEY 20-AUG-1989 Function for adding key boxes to an image.

LGR 22-JUN-1989 Function to generate a logarithm residual image.

MDCL 18-JAN-1990 Mini-distance classification (ISODATA) program.

MFT 21-FEB-1990 Median filtering.

MFTV 21-FEB-1990 Vertical median filtering.

MODUL 19-JUN-1990 Program to multiply two images and then scale the product image to 0-255 value range for image modulation.

MODUL1 19-JUN-1990 Program to perform modulation of two images of different sizes.

MULTI 22-FEB-1990 Image multiplication without scaling. Used for image masking.

PAINT 14-JUN-1990 Generate a colour composite of a classification image based on a class colour code file.

RMBDL 28-FEB-1990 Replace a bad image line by its neighbour line.

SCM 14-JUN-1990 Small class merging technique.

SPECT 3-SEP-1990 Program to derive data of spectral shapes from the three hue values of an HRGB colour composite.

THMC 8-AUG-1989 Template histogram matching classification technique.

WATER 30-JAN-1989 Ratio technique for detecting surface water bodies.

References

Abrams , M.J., Ashley, R.P., Rowan, L.C., Goetz A.F.H. and Kahle, A.B., 1977, Mapping of hydrothermal alteration in the Cuprite Mining District, Nevada, using aircraft scanner images for the spectral regions $0.46 - 2.36\mu m$. *Geology*, 5, 713-718.

Abrams , M.J., 1980. Lithologic Mapping. Chapter 13 in: *Remote Sensing in Geology*, edited by Barry S. Siegal and Alan R. Gillespie. (New York: John Wiley & Sons).

Abrams , M.J., 1984. Landsat-4 Thematic Mapper simulator data for a porphyry copper deposit. *Photogrammetric Engineering & Remote Sensing*, 50, 1171-1173.

Abrams , M.J., 1986. Mapping the Oman ophiolite using TM data. In: *Proc. of the 5th Thematic Conference on Remote Sensing for Exploration Geology*, Reno, Nevada, 29 Sept.- 2 Oct., 1986 (ERIM, Ann Arbor, Michigan), pp. 85-95.

Abrams , M.J., Rothery, D.A. and Pontual, A., 1988. Mapping in the Oman ophiolite using enhanced Landsat Thematic Mapper images. *Tectonics*, 151(1988)387-401.

Allum , J.A.E., 1966. Photogeology and Regional Mapping (Oxford: Pergamon).

Amdasun , M., 1988. Analysis Method for Cost Efficient Scene Interpretation (PhD thesis). Electrical Engineering Dept., Imperial College of Science, Technology and Medicine, London.

Amos , B.J. and Greenbaum, D., 1989. alteration detection using TM imagery - The effects of supergene weathering in arid climate. *International Journal of Remote Sensing*, 10, 515-527.

Anderberg , M.R., 1973. Cluster Analysis for Application (New York and London: Academic Press), pp.157-176.

Anderson , T.W., 1984. An Introduction to Multivariate Statistical Analysis, 2nd edition (New York: John Wiley & Sons).

Anon , Landsat 4 Data Users Handbook. NOAA, US Geological Survey, Washington DC, USA, 1984.

Arribas , A.,Jr., Rytuba, J.J., Rye, R.O., Cunningham, C.G., Podwysocki, M.H., Kelly, W.C., McKee E.H. and Smith, J.G., 1989. Preliminary study of the ore deposits and alteration of the Rodalquilar caldera complex, southeastern Spain. US Geological Survey, Open file Report 89-327, 39p.

Ball , G.H., 1965. Data analysis in the social sciences: what about details? In: *Proc. Fall Joint Computer Conference*, 1965, pp.533-539.

Ball , G.H. and Hall, D.J., 1967. A clustering technique for summarizing multivariable data. *Behavioral Science*, Vol.12, pp.153-155.

Barker , J.L. and Gunther, F.L., 1983. Landsat-4 sensor performance. In: *Proc. 8th W.T. Pecora Memorial Remote Sensing Symposium, Land Remote Sensing Advances for the Eighties*, US Geological Survey, Sioux Falls, South Dakota, pp.46-74.

Berman , M., 1985. the statistical properties of three noise removal procedures for multichannel remotely sensed data. CSIRO Div. of Mathematics and Statistics, Consulting Report. NSW/85/31/MB9.

Billingsley , F.C., 1972. Computer-generated color image display of lunar spectral reflectance ratios. *Photo. Gramm. Sci. Eng.*, 16: 51-57.

Blodget , H.W., Brown G.F. and Mock, J.G., 1975. Geological mapping in Northeastern Saudi Arabia using Landsat multispectral techniques. In: *Proc. American Society of Photogrammetry 41st annual Meeting*, Washington DC, pp.971-980.

Campos-Marquetti , R., Jr. and Rockwell, B., 1989. Quantitative lithologic mapping in spectral ratio feature space: Volcanic, sedimentary and metamorphic terrains. In: *Proc. 7th Thematic Conference on Remote Sensing for Exploration Geology*, 2 - 6 Oct., 1989, Calgary, Alberta, Canada. (ERIM, Ann Arbor, Michigan). Vol.1, pp.471-484.

Cañas , A.A.D. and Barnett, M.E., 1985. The generation and interpretation of false colour composite principal component images. *International Journal of Remote Sensing*, 6, 867-881.

Carrere , V., 1989. Mapping alteration in the Goldfield Mining District, Nevada, with the Airborne Visible/Infrared Imaging Spectrometer (AVIRIS). In: *Proc. 7th Thematic Conference on Remote Sensing for Exploration Geology*, 2 - 6 Oct., 1989, Calgary, Alberta, Canada. (ERIM, Ann Arbor, Michigan). Vol.1, pp.365-378.

Castleman , K.R., 1979. Digital Image Processing (Englewood Cliffs, New Jersey: Prentice-Hall, Inc.) 429p.

Chalmers , A.I. and Harris, R., 1981. Band ratios in multispectral analysis of Landsat digital data. In: *Geological and Terrain Analysis Studies by Remote Sensing.* Edited by J.A. Allan and M. Brandshaw (UK: Remote Sensing Society), pp.139-146.

Chavez , P.S., Jr., Berlin, G.L. and Sowers, L.B., 1982. Statistical method for selecting Landsat MSS ratios. *Journal of Appl. Photo. Eng.*, 8, 23-30.

Chavez , P.S., Jr., Guptill, S.C. and Bowell, J., 1984. Image processing techniques for Thematic Mapper data. In: *Proc. 50th Annual ASP-*

ACSM Symposium, American Society of Photogrammetry, Washington DC, pp.728-743.

Chavez , P.S., Jr. and Kwarteng, A.Y., 1989. Extracting spectral contrast in Landsat Thematic Mapper image data using selective principal component analysis. *Photogrammetry Engineering and Remote Sensing*, 55, 339-348.

Chow , C.K. and Kaneko, T., 1972. Automatic boundary detection of the left ventricle from cineangiograms. *Comp. and Biomed. Res.*, 5, 388-410.

Crippen , R.E., 1986. Image display of four dimensional spectral data. In: *Summary of 6th Thematic Conference on Remote Sensing for Exploration Geology*, 16-19 May, 1988, Houston, Texas (ERIM, Ann Arbor, Michigan), pp.130-131.

Crippen , R.E., Blom, R.G. and Heyada, J.R., 1988. Directed band ratioing for the retention of perceptually-independent topographic expression in chromaticity-enhanced imagery. *International Journal of Remote Sensing*, 9, 749-765.

Crippen , R.E., 1989. Selection of Landsat TM band and band-ratio combinations to maximize lithologic information in colour composite displays. In: *Proc. 7th Thematic Conference on Remote Sensing for Exploration Geology*, 2 - 6 Oct., 1989, Calgary, Alberta, Canada. (ERIM, Ann Arbor, Michigan). Vol.2, pp.917-921.

Crosta , A. and Moore, J. McM., 1989. Enhancement of Thematic Mapper imagery for residual soil mapping in SW Minas Gerais State, Brazil: A prospecting case history in greenstone belt terrain. In: *Proc. 7th Thematic Conference on Remote Sensing for Exploration Geology*, 2 - 6 Oct., 1989, Calgary, Alberta, Canada. (ERIM, Ann Arbor, Michigan). Vol.2, pp.1173-1187.

Crosta , A.P. and Moore, J. McM., 1989. Geological mapping using Landsat Thematic Mapper Imagery in Almeria Province, southeast Spain. *International Journal of Remote Sensing*, 10, 505-514.

Cutts , J.A., 1971. Martian Spectral reflectivity properties from Mariner 7 observations (PhD dissertation). Calf. Inst. of Tech., Pasadena, CA91125. 92p.

Davis , W.A. and Peet, F.G., 1977. A method for smoothing digital thematic maps. *Remote Sensing of Environment*, 6, 45-49.

Davis , P.A., Berlin, G.L. and Chavez, P.S., Jr., 1987. Discrimination of altered basaltic rocks in the southwestern United States by analysis of Landsat Thematic Mapper data. *Photogrammetric Engineering and Remote Sensing*, 53, 45-55.

Devijver , P.A. and Kittler, J., 1982. Pattern Recognition - A statistical Approach (London: Prentice-Hall International, Inc.), pp.382-420.

Diday , E. and Simon, J.C., 1976. Cluster Analysis. In: *Digital Pattern Recognition*, edited by K.S. Fu (Berlin, Heidelberg, New York: Springer- Verlag). pp.47-94.

Drury , S.A., 1987. Image Interpretation in Geology (London:Allen & Unwin), pp.135-140.

Drury , S.A. and Hunt, G.A., 1988. Remote sensing of laterized archean greenstone terrain: Marshall Pool area, northeastern Yigarn Block, Western Australia. *Photogrammetric Engineering & Remote Sensing*, 54, 1717-1725.

Duda , R.O. and Hart, P.E., 1973. Pattern Classification and Scene Analysis (New York: John Wiley & Sons). pp.263-297.

Elvidge , C.D., 1988. Vegetation reflectance features in AVIRIS data. In: *Proc. 6th Thematic Conference on Remote Sensing for Exploration Geology*, 16-19 May, 1988, Houston, Texas (ERIM, Ann Arbor, Michigan), pp.1969-1982.

Forster , B.C., 1985. Principle(sic) and rotated components analysis of urban surface reflectance. *Photogrammetric Engineering and Remote Sensing*, 51, 475-477.

Fram , J.R. and Deutsch, E.S., 1975. On the quantitative evaluation of edge detection schemes and their comparison with human performance. *IEEE Trans. Computers*, C-24, 616-628.

Fu , K.S., Gonzalez, R.C. and Lee, C.S.G., 1987. Robotics: Control, Sensing, Vision, and Intelligence (New York: McGraw-Hill).

Gesú , V. D., 1984. A system for the analysis of the boundaries of a shape. In: *Digital Image Analysis*, edited by S. Levialdi (London: Pitman Publishing Limited). pp.144-148.

Gillespie , A.R., 1975. Colour manipulation of digital images. In: *Proc. Society of Photo-graphic Scientists and Engineers Symposium IV, Unconventional Photographic Systems*, 20-21 November, Washington DC, pp.35-37.

Gillespie , A.R., 1980. Digital techniques of image enhancement. Chapter 6 in: *Remote Sensing in Geology*, edited by B.S. Siegal and A.R. Gillespie (New York: Wiley).

Gillespie , A.R., Kahle, A.B. and Palluconi, F.D., 1984. Mapping alluvial fans in Death Valley, California, using multispectral thermal infrared images. *Geophys. Res. Lett.*, 11, 1153-1156.

Gillespie , A.R., Kahle, A.B. and Walker, R.E., 1986. Colour enhancement of highly correlated images. I. Decorrelation and HSI contrast stretches.

Remote Sensing of Environment, 20, 209-235.

Gillespie , A.R., Kahle, A.B. and Walker, R.E., 1986. Colour enhancement of highly correlated images. II. Channel ratio and "chromaticity" transformation technique. *Remote Sensing of Environment*, 22, 343-365.

Goetz , A.F.H., Billingsley, F.C., Elston, D.P., Luchitta, I. and Shoemaker, E.M., 1973. Application of ERTS to geological problems on the Colorado Plateau, Arizona. In: *Proc. 3rd ERTS Investigation Symposium*, 10-14 Dec., 1973, Washington DC, pp.719-744.

Goetz , A.F.H., Billingsley, F.C., Gillespie, A.R., Abrams, M.J., Squires, R.L., Sheomaker, E.M., Luchitta, I. and Elston, D.P., 1975. Application of ERTS images and image processing to regional geologic problems and geologic mapping in northern Arizona, Appendix B, NASA TR32-1597, JJPL, Pasadena, CA91109. pp. 131-171.

Goetz , A.F.H., 1987. Remote sensing for non-renewable resources: Satellite and airborne multiband scanners for mineral exploration. In: *Proc. Symposium on Remote Sensing for Resources Development and Environmental management*, August, 1986, Enschede (Rotterdam: Balkema), pp.1009-1014.

Goldberg , M., Goodenough, D. and Shlien, S., 1975. Classification methods and error estimation for multispectral scanner data. In: *Proc. 3rd Canadian Symposium on Remote Sensing*, Sept., 1975. PP. 125-143.

Gonzalez , R.C. and Fittes, 1977. Gray-level transformations for interactive image enhancement. *Mechanism and Machine Theory*, 12, 111-122.

Gonzalez , R.C. and Wintz, P., 1987. Digital Image Processing, 2nd Edition (Reading, Massachusetts: Addison-Wesley Publishing Company, Inc.).

Green , A.A. and Craig, M.D., 1985. Analysis of aircraft spectrometer data with logarithmic residuals. In: *Proc. Airborne Imaging Spectrometer Data Analysis Workshop.* 8-10 April, 1985, JPL Pub., pp.85-41.

Green , A.A., Berman, M., Switzer, P. and Craig, M.D., 1988. A transformation for ordering multispectral data in terms of image quality with implications for noise removal. *IEEE Trans. Geoscience and Remote Sensing*, 26, 65-74.

Gurney , C.M. and Townshend, J.R.C., 1983. The use of textural information in the classification of remotely sensed data. *Photogrammetric Engineering and Remote Sensing*, 49, 55-64.

Hall , E.L., *et al.*, 1971. A survey of preprocessing and feature extraction techniques for radiographic images. *IEEE Trans. Computers*, C-20, 1032-1044.

Hall , E.L., 1974. Almost uniform distributions for computer enhancement. *IEEE Trans. Computers*, C-23, 207-208.

Haralick , R.M. and Shanmugam, K.S., 1973. Combined spectral and spatial processing of ERTS images. In: *Proc. Symposium on Significant Results Obtained from Earth Resources Technology Satellite-1*, NASA SP-327, Washington DC, pp.1219-1228.

Haralick , R.M. and Dinstein, I., 1975. A spatial clustering procedure for multi- image data. *IEEE Trans. Circuits and Systems*, CAS-22, 440-450.

Harris , J. and Murray, R., 1989. IHS transformation for the integration of radar imagery with geophysical data. In: *Proc. IGARSS'89/12th Canadian Symposium on Remote Sensing*, July, 1989, Vancouver, BC. pp.923-926.

Harris , J., 1989. Data integration for gold exploration in eastern Nova Scotia using GIS. In: *Proc. 7th Thematic Conference on Remote Sensing for Exploration Geology*, 2 - 6 Oct., 1989, Calgary, Alberta, Canada. (ERIM, Ann Arbor, Michigan). Vol.1, pp.233-249.

Harris , R., 1981. An experiment in probabilistic relaxation for terrain cover classification of Kuwait from Landsat imagery. In: *Proc. 15th International Conference on Remote Sensing of Environment*, ERIM, Ann Arbor, Michigan, pp. 1245-1252.

Harris , R., 1985. Contextual classification post-processing of Landsat data using a probabilistic relaxation model. *International Journal of Remote Sensing*, 6, 847-866.

Haydan , R., 1981. the application of a colour transformation for the enhancement of multispectral images and for the combination of multisensor data. In: *Summaries of International Symposium on Remote Sensing of the Environment, "Remote Sensing of Arid and Semi-arid Lands"*, 3-9 November, 1981, Cairo, Egypt. pp.78.

Haydan , R., Dalke, G.W., Henkel, J. and Bare, J.E., 1982. Application of the IHS colour transformation to the processing of multisensor data and image enhancement. In: *Proc. International Symposium on Remote Sensing of the Environment, "Remote Sensing of Arid and Semi-arid Lands"*, January, 1982, Cairo, Egypt. pp.599-616.

Haydan , R. and Youssef, M., 1984. The application of processed Landsat imagery in photo-interpretation. In: *Proc. International Geosciences and Remote Sensing Symposium*, June, 1984, Munich, Germany, Vol.1, pp.TP-9.5.

Hernandez , P.A., Garcia-Estrada, P.A. and Cowley, P.N., 1989. Geological Setting, alteration and lithogeochemistry of the Transaction epithermal

gold deposit, Rodalquilar mining district, southeast Spain. *Transactions of Institute of Mining and Metallurgy*, London, 98. B. 78-80.

Huckerby , J.A., Magee, R.W., Moore, J. McM. and Coates, D., 1986. Thematic Mapper applied to alteration zone mapping for gold exploration in southeast Spain. In: *Proc. 5th Thematic Conference on Remote Sensing for Exploration Geology*, 29 Sept.-2 Oct., 1986, Reno, Nevada, USA. (ERIM, Ann Arbor, Michigan). pp. 591-599.

Hummel , R.A., 1974. Histogram Modification Techniques, Technical Report TR-329, F-44620-72C-0062. Computer Science Center, University of Maryland, College Park, Maryland.

Hunt , G.A., Drury, S.A. and Rothery, D.A., 1986. Techniques for choosing the optimal channel combinations for lithological mapping in semi-arid terrains. In: *Proc. Symposium: Mapping from Modern Imagery*, Edinburgh, Remote Sensing / ISPRS Commission, London, VIII. pp.637-646.

Justice , C.O., Townshend, J.R.G., Holben, B.N. and Tucker, C.J., 1985. Analysis of the phenology of global vegetation using meteorological satellites. *International Journal of Remote Sensing*, 6, 1271-1318.

Kahle , A.B. and Rowan, L.C., 1980. Evaluation of multispectral middle infrared images for lithologic mapping in East Tintic Mountains, Utah. *Geology*, 8, 234-239.

Kahle , A.B. and Goetz, A.F.H., 1983. Mineralogic information from a new airborne thermal infrared multispectral scanner. *Science*, 222, 24-27.

Kaufmann , H., 1988. Mineral exploration along the Aqaba-Levant Structure by use of TM data concepts, processing and results. *International Journal of Remote Sensing*, 9, 1639-1658.

Ketcham , D.J., 1976. Real time image enhancement techniques. In: *Proc. Soc. Photo-Optical Instum. Eng.*, 74, 120-125.

Kittler , J., 1983. Image processing for remote sensing. *Philosophical Transactions of the Royal Society*, London, Series A, 309, 323-335.

Kittler , J. and Figlein, J., 1984. contextual classification of multispectral pixel data. *Image and Vision Computing*, 2, 13-29.

Kittler , J. and Pairman, D., 1988. Optimality of reassignment rules in dynamic clustering. *Pattern Recognition*, 21, 169-174.

Kowalik , W.S., Lyon, R.J.P. and Switzer, P., 1983. The effects of additive radiance terms on ratios of Landsat data. *Photogrammetric Engineering and Remote Sensing*, 49, 659-669.

Kreigler , F.J., Malila, W.A., Nalepka, R.F. and Richandson, W., 1969. Preprocessing transformations and their effects on multispectral recognition. In: *Proc. 6th International Symposium on Remote Sensing of Environment.* Ann Arbor: University of Michigan, pp.97-131.

Kruse , F.A., Calvin, W.M. and Seznec, O., 1988. Automated extraction of absorbtion features from Airborne Visible/Infrared Imaging Spectrometer (AVIRIS) and Geophysical Environmental Research Imaging Spectrometer (GERIS) Data. In: *Proc. AVIRIS Performance Evaluation Workshop*, JPL publication 83-38, JPL, Pasadena, California. pp.26-75.

Kruse , F.A., Kierein-Young, K.S. and Boardman, J.W., 1990. Mineral mapping at Cuprite, Nevada with a 63-Channel Imaging Spectrometer. *Photogrammetric Engineering and Remote Sensing*, 56, 83-92.

Lee , J.B., Woodyatt, A.S. and Berman, M., 1990. Enhancement of high spectral resolution remote sensing data by a noise-adjusted principal com-

ponents Transform. *IEEE Trans. Geoscience and Remote Sensing*, 28, 295-304.

Lee , K. and Weimer, R., 1975. Geological interpretation of Skylab photographs: Remote Sensing Report, 1975-1976, Colorado School of Mines, Golden, Colorado, 77p.

Letts , P.A., 1978. Unsupervised classification in the Aries image analysis system. In: *Proc. 5th Canadian Symp. on Remote Sensing*, pp.61-71.

Lillesand , T.M. and Kiefer, R.W., 1987. Remote Sensing and Image Interpretation, 2nd Edition (New York: John Wiley and Sons), 721p.

Liu Jian Guo and Moore, J. McM., 1989. Colour enhancement and shadow suppression technique for TM images. In: *Proc. 7th Thematic Conference on Remote Sensing for Exploration Geology*, 2 - 6 Oct., 1989, Calgary, Alberta, Canada. (ERIM, Ann Arbor, Michigan). Vol.2, pp.901-915.

Liu Jian Guo and Haigh, J.D., 1990. A three dimensional feature space iterative clustering method for multi-spectral image classification. In: *Remote Sensing for the Nineties - Proc. 10th Annual International Geoscience and Remote Sensing Symposium*, 20 - 24 May, 1990, University of Maryland, Washington DC, USA. Vol.3, pp. 2367-2370.

Liu Jian Guo, 1990. Hue image colour composition - a simple technique for shadow suppression and spectral enhancement. *International Journal of Remote Sensing*, 11, 1521-1530.

Liu Jian Guo, 1991. Balance Contrast Enhancement Technique and its application in image colour composition. *International Journal of Remote Sensing*, in press.

Lo , C.P., 1986. Applied Remote Sensing (New York: Longman Scientific & Technical, Longman Group UK Limited), 393p.

MacQueen , J., 1967. Some methods for classification and analysis of multivariate observations. In: *Proc. 5th Berkeley Symposium on Mathematics, Statistics and Probability*, (Berkeley and Los Angeles, Calif: University of California Press), pp.281-299.

Magee , R.W., Moore, J. McM. and Brunner, J., 1986. Thematic Mapper applied to mapping hydrothermal Alteration in southwest New Mexico. In: *Proc. 5th Thematic Conference on Remote Sensing for Exploration Geology*, 29 Sept.-2 Oct., 1986, Reno, Nevada, USA. (ERIM, Ann Arbor, Michigan). pp. 373-382.

Marr , D., 1982. Vision (San Francisco, California: Freeman).

Martelli , A., 1972. Edge detection using heuristic search methods. In: *Computer Graphics Image Proceedings*, Vol.1, pp.169-182.

Martelli , A., 1976. An application of heuristic search method to edge and contour detection. *Comm. ACM*, 19, 73-83.

Mather , P.M., 1987. Computer Processing of Remotely Sensed Images - An Introduction (Chichester, New York: John Wiley & Sons), 352p.

Mazer , A.S., Martin, M., Lee, M. and Solomon, J.E., 1987. Image processing software for imaging spectrometry. In: *Proc. 31st Annual International Technical Symposium, Society of Photo-Optical Instrumentation Engineers*, 16-21 August, 1987. Vol.834, pp.136-139.

Mazer , A.S., *et al.*, 1988. Image processing software for imaging spectrometry data analysis. *Remote Sensing of Environment*, 24, 201-210.

Mekel , J.F.M., 1972. The geological interpretation of radar images, ITC textbook of photo-interpretation, Vol. VIII-2. Enschede, Netherland.

Mekel , J.F.M., 1978. The use of aerial photographs and other images in geological mapping, ITC, Enschede, Netherland.

Miller , V.C., 1961. Photogeology (New York: McGraw-Hill).

Moore , J. McM. and Liu Jian Guo, 1990. Image enhancement of epithermal gold deposit alteration zones in southeast Spain. In: *Remote Sensing: an operational technology for the mining and petroleum industries*, 15-17 Nov., 1989, Institute of Mining and Metallurgy, London, UK, pp.49-58.

Narendra , P.M. and Fitch, R.C., 1981. Real-time adaptive contrast enhancement. *IEEE Trans. Pattern Anal. Mach. Intel.*, PAMI-3, 655-661.

Niblack , W., 1986, An Introduction to Digital Image Processing (London: Prentice- Hall International(UK) Ltd), pp.23-67.

Pairman , D., 1986. Image Processing in Geophysics (Ph.D. Thesis), Department of Atmospheric Physics, Clarendon Laboratory, University of Oxford. 150p.

Peleg , S., 1980. A new probabilistic relaxation scheme. *IEEE Transactions on Pattern Analysis and Machine Intelligence*, PAMI-2, 362-369.

Perry , C.R. and Lautenschlager, L.F., 1984. Functional equivalence of spectral vegetation indices. *Remote Sensing of Environment*, 14, 169-182.

Raines , G.L., 1977. Digital color analysis of color-ratio composite Landsat scenes. In: *Proc. 11th International Symposium on Remote Sensing of Environment*, pp.1463-1472.

Ray , R.G., 1960. Aerial Photographs in Geologic Interpretation and Mapping (Washington, D.C.: United States Government Print Office).

Richard , J.A., 1986. Remote Sensing Digital Image Analysis - An Introduction (Berlin, Heidelberg, New York: Springer-Verlag).

Robert , D.A., Yamaguchi, Y. and Lyon, R.J.P., 1985. Calibration of airborne imaging spectrometer data to percent reflectance using field spectral mea-

surements. In: *Proc. 19th International Symposium on Remote Sensing of Environment*, Ann Arbor, Michigan, 21-25 October, 1985.

Robinson , G.S., 1976. Detection and coding of edges using directional masks. Image Processing Institute, University of Southern California, Report No.660.

Rosenfeld , A., 1976. Interactive methods in image analysis. *Pattern Recognition*, 10, 181-187.

Rosenfeld , A. and Kak, A.C., 1982. Digital Picture Processing, 2nd Edition (New York: Academic Press).

Rothery , D.A. and Milton, E.J., 1981. Lithological discrimination in an ophiolite terrain: Landsat MSS imagery and reflectance. In: *Geological and Terrain Analysis Studies by Remote Sensing*, edited by J.A. Allan and M. Brandshaw, the Remote Sensing Society, UK. pp.3-23.

Rothery , D.A., 1987a. Improved discrimination of rock units using Landsat Thematic Mapper imagery of the Oman ophiolite. *Journal of Geological Society*, London. 144, 587-597.

Rothery , D.A., 1987b. Decorrelation stretching as an aid to image interpretation. *International Journal of Remote Sensing*, 8, 1253-1254.

Rowan , L.C., Wetlaufer, P.H., Goetz, A.F.H. and Stewart, J.H., 1974. Discrimination of hydrothermally altered areas and of rock types using computer enhanced ERTS images, south central Nevada. U.S. Geological Survey Professional paper 883.

Ruiz , R.M., Elliott, D.A., Yagi, G.M., Pomphrey, R.B., Power, M.A., Farrell, K.W., Jr., Lorre, J.J., Benton, W.D., Dewar, R.E. and Cullen, L.E., 1977. IPL processing of the Viking Orbiter images of Mars. *J. Geophys. Res.*, 82, 4189-4202.

Sabins , F.F.,Jr., 1986. Remote Sensing: Principles and Interpretation, Second Edition, (New York: W.H. Freeman and Company), 449p.

Saeb0 , H.V., Braten, K., Hjort, N.L., Llewelly, B. and Mohn, E., 1985. Contextual classification of remotely sensed data. In: *Statistical method and development of a system*, Report No.768, Nowegian Computing Center (Norsk Regnesentral), Oslo.

Schowengerdt , R.A., 1983. Techniques for Image Processing and Classification in Remote Sensing (New York, London: Academic Press), 249p.

Sclove , S.L., 1983. Application of the conditional population-mixture model to image segmentation. *IEEE Trans. on Pattern Analysis and Machine Intelligence*, PAMI-5, 428-433.

Segal , D.B., 1983. Use of Landsat Multispectral Scanner data for the definition of limonitic exposures in heavily vegetated areas. *Economic Geology*, 78, 711-722.

Sheffield , C., 1985. Selecting band combinations from multispectral data. *Photogrammetric Engineering and Remote Sensing*, 51, 681-687.

Smith , A.R., 1978. Colour Gamut Transform Pairs. In: *Proc. SIGGRAPH'78 Conference*, 23-25 August, 1978, Atlanta, USA. (New York: Association of Computing Machinery), pp.12-19.

Soha , J.M., Gillespie, A.R., Abrams, M.J. and Madura, D.P., 1976. Computer techniques for geological applications. In: *Proc. Caltech/JPL Conference on Image Processing Technology, Data Sources and Software for Commercial and Scientific Applications*, California Institute of Technology, Pasadena, CA.

Soha , J.M. and Schwartz, A.A., 1978. Multispectral histogram normalization contrast enhancement. In: *Proc. 5th Canadian Symposium on Remote*

Sensing, 28-31 August, 1978, Victoria, BC, Canada. pp.86-93.

Swain , P. H., 1978. Fundamentals of pattern recognition in remote sensing. Chapter 3 in: *Remote Sensing: the Quantitative Approach*, edited by P.H. Swain (New York: McGraw-Hill), pp.176.

Suits , G.H., 1983. The Nature of Electromagnetic Radiation. In: *Manual of Remote Sensing*, Second Edition, edited by Robert N. Colwell, (Falls Church: American Society of Photogrammetry), pp.37-60.

Taylor , M.M., 1973. Principal Components Colour Display of ERTS Imagery. In: *Proc. 3rd Earth Resources Technology Satellite-1 Symp.*, NASA SP-351, pp1877-1897.

Thamas , J.O., 1977. Texture analysis in imagery processing. In: *Proc. British Pattern Recognition Society/Remote Sensing Society Joint Meeting on Texture Analysis*, University of Nottingham, 1-43.

Thomas , I.L., 1980. Spatial post processing of spectrally classified Landsat data. *Photogrammetric Engineering and Remote Sensing*, 46, 1201-1206.

Townsend , F., 1986. The enhancement of computer classifications by logical smoothing. *Photogrammetric Engineering and Remote Sensing*, 52, 213-221.

Tucker , C.J., 1979. Red and photographic infrared linear combinations for monitoring vegetation. *Remote Sensing of Environment*, 10, 127-150.

Viljoen , R.P., Viljoen, M.J., Grootenboer, J. and Longshaw, T.G., 1975. ERTS-1 imagery: an appraisal of applications in geology and mineral exploration. *Minerals Sci. Eng.*, 7, 132-168.

Vincent , R.K., 1977. Geochemical mapping by spectral ratioing. Chapter 10 in: *Remote Sensing Applications for Mineral Exploration*, edited by W.L. Smith (Stroudsburg, Pennsylvania: Dowden, Hutchinson and Ross).

Von , B.H.F., 1962. Aerogeology (Houston, Texas: Gulf Publishing Company).

Wang , L. and He, D.C., 1990. A new statistical approach for texture analysis. *Photogrammetric Engineering and Remote Sensing*, 56, 61-66.

Wang , L. and He, D.C., 1990. Recognition of lithological units in airborne SAR images using new texture features. In: *Remote Sensing for the Nineties - Proc. 10th Annual International Geoscience and Remote Sensing Symposium*, 20 - 24 May, 1990, University of Maryland, Washington DC, USA. Vol.2, pp.991-994.

Weska , J.S., 1978. A survey of threshold selection techniques. In: *Computer Graphics Image Proc.*, Vol.7, pp.259-265.

Wharton , S.W., 1980. A contextual classification method for recognizing land use patterns in high-resolution remotely-sensed data. *Pattern Recognition*, 15, 317-324.

White , J.M. and Rohrer, G.D., 1983. Image thresholding for optical character recognition and other applications requiring character image extraction. *IBM Journal of Research Development*, 27, 400-411.

Williams , R.S, Jr., 1983. Geological Application. Chapter 31 in: *Manual of Remote Sensing*, 2nd Edition, American Society of photogrammetry, Vol.2, pp.1667-2100.

Woods , R.E. and Gonzalez, R.C., 1981. Real-time digital image enhancement. *IEEE Trans. Pattern Anal. Mach. Intel.*, PAMI-3, 643-654.

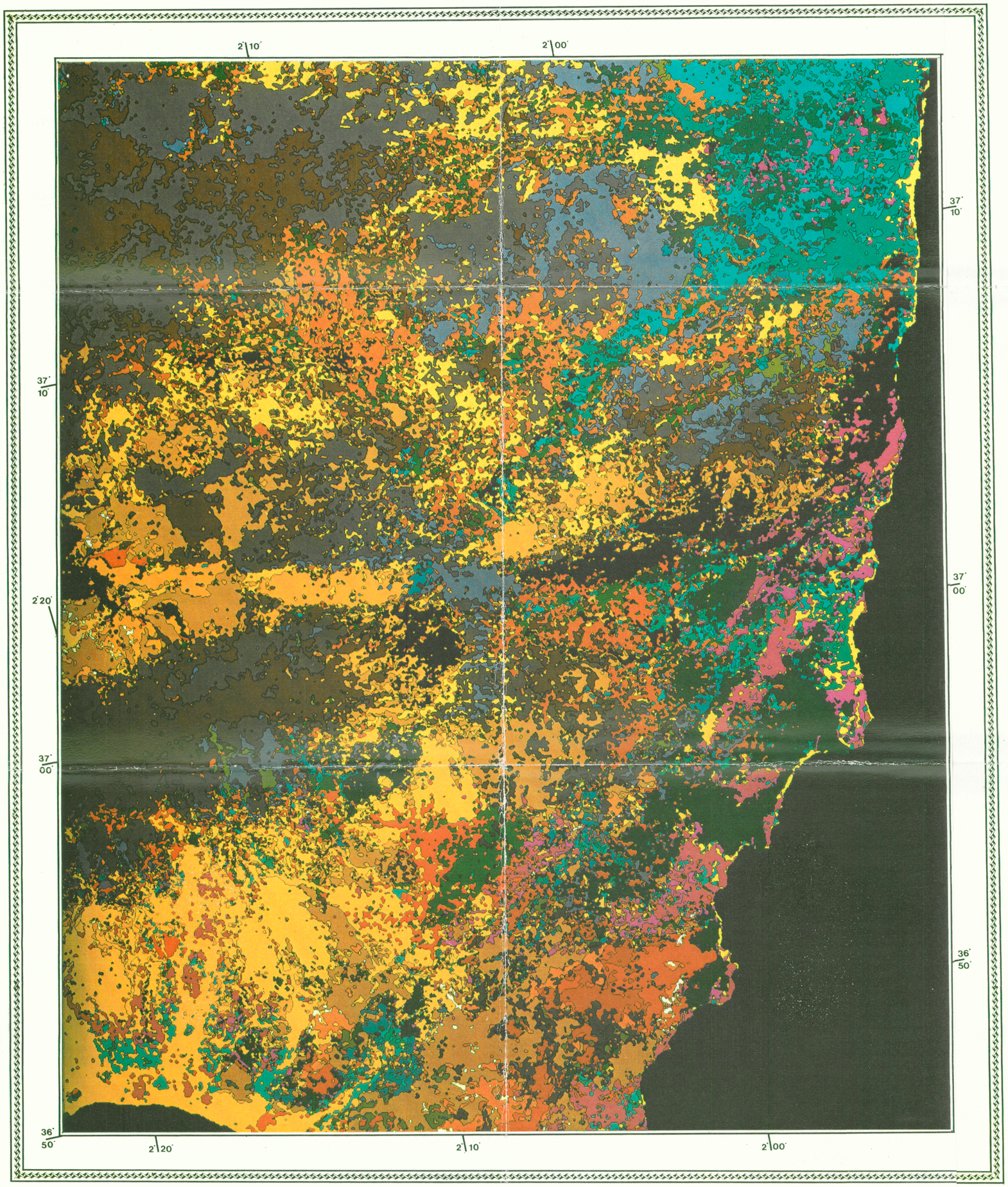
Yamaguchi , Y., 1987. Possible techniques for lithologic discrimination using the short-wavelength-infrared bands of the Japanese ERS-1. *Remote Sensing of Environment*, 23, 117-129.

Yamaguchi , Y., 1988. Spectral indices for vegetation and rock type discrimination using optical sensor of the Japanese ERS-1. In: *Proc. 6th Thematic*

Conference on Remote Sensing for Exploration Geology, 16-19 May, 1988, Houston, Texas (ERIM, Ann Arbor, Michigan), pp.159-168.

Yamaguchi , Y., 1989. Application of GEOSCAN AMSS MKI data to lithologic mapping in Queensland, Australia. In: *Proc. 7th Thematic Conference on Remote Sensing for Exploration Geology*, 2 - 6 Oct., 1989, Calgary, Alberta, Canada. (ERIM, Ann Arbor, Michigan). Vol.1, pp.395-409.

IMAGERY LITHOLOGICAL MAP OF SE SPAIN



Legend

1 Carbonaceous mica-schist
2 Mica-schist with gneiss
3 Phyllite, quartzsite and gneiss
4 Triassic dolomite and marble
5 Andesite
6 Volcanic breccia and tuff
7 Highly altered dacite
8 Altered dacite with residual soil and debris
9 Miocene limestone and dolomite
10 Miocene molasse deposits
11 Late Miocene to early Pliocene alluvial deposits
12 Gypsum
13 Pliocene limestone and marls
14 Early Pleistocene alluvial deposits
15 Slope washes
16 Colluvial and residual debris of bed rock
17 Sand deposits
18 River beds
19 Mine tilling and dry river beds
20 Recent alluvial fans and debris aprons
21 Red soil
22 Vegetation
23 Open pits of mines
24 Villages and small towns

This map is produced from the classification of an HRGB image derived from the seven bands of a 1792×1536 TM subscene.

Liu Jian Guo
Centre for Remote Sensing
Imperial College of Science, Technology and Medicine
London SW7 2BZ, UK

10 April, 1991

SCALE
0 4 8 12 16 Km